N° d'ordre NNT : 2020LYSEI122

THÈSE DE DOCTORAT DE L'UNIVERSITÉ DE LYON

opérée au sein de

l'Institut National des Sciences Appliquées de Lyon

École doctorale N°162

Mécanique, Énergétique, Génie Civil, Acoustique

Spécialité/ discipline de doctorat :

Génie Mécanique

Soutenue à huis clos le 27/11/2020 par :

Zi Kang LOW

MATÉRIAUX CELLULAIRES ISOLANTS HAUTE TEMPÉRATURE :

RELATION MICROSTRUCTURE–PROPRIÉTÉS

Devant le jury composé de :

FOREST, Samuel	Directeur de Recherche, CNRS	Président
HAUSSENER, Sophia	Professeure Associée, EPFL	Rapportrice
RÉMY, Benjamin	Professeur, Univ. Lorraine	Rapporteur
PIERROT, Laurent	Directeur R&D, SGR Provence	Examinateur
BAILLIS, Dominique	Professeure, INSA Lyon	Directrice de thèse
BLAL, Nawfal	Maître de Conférences, INSA Lyon	Co-directeur de thèse
SAN MIGUEL, Laurie	R&D Portfolio Manager, SGR Provence	Invitée
MEULEMANS, Johann	Ingénieur de Recherche, SGR Paris	Invité
DE SOUSA MENESES, Domingos	Professeur, Univ. Orléans	Invité

CONFIDENTIEL

MATÉRIAUX CELLULAIRES ISOLANTS HAUTE TEMPÉRATURE :

RELATION MICROSTRUCTURE–PROPRIÉTÉS

High temperature insulating cellular materials :
Microstructure–property relationships

ZI KANG LOW

Département FEDORA – INSA Lyon - Ecoles Doctorales – Quinquennal 2016-2020

SIGLE	ECOLE DOCTORALE	NOM ET COORDONNEES DU RESPONSABLE
CHIMIE	**CHIMIE DE LYON** **http://www.edchimie-lyon.fr** Sec. : Renée EL MELHEM Bât. Blaise PASCAL, 3e étage **secretariat@edchimie-lyon.fr** INSA : R. GOURDON	**M. Stéphane DANIELE** Institut de recherches sur la catalyse et l'environnement de Lyon IRCELYON-UMR 5256 Équipe CDFA 2 Avenue Albert EINSTEIN 69 626 Villeurbanne CEDEX **directeur@edchimie-lyon.fr**
E.E.A.	**ÉLECTRONIQUE, ÉLECTROTECHNIQUE, AUTOMATIQUE** **http://edeea.ec-lyon.fr** Sec. : M.C. HAVGOUDOUKIAN **ecole-doctorale.eea@ec-lyon.fr**	**M. Gérard SCORLETTI** École Centrale de Lyon 36 Avenue Guy DE COLLONGUE 69 134 Écully Tél : 04.72.18.60.97 Fax 04.78.43.37.17 **gerard.scorletti@ec-lyon.fr**
E2M2	**ÉVOLUTION, ÉCOSYSTÈME, MICROBIOLOGIE, MODÉLISATION** **http://e2m2.universite-lyon.fr** Sec. : Sylvie ROBERJOT Bât. Atrium, UCB Lyon 1 Tél : 04.72.44.83.62 INSA : H. CHARLES **secretariat.e2m2@univ-lyon1.fr**	**M. Philippe NORMAND** UMR 5557 Lab. d'Ecologie Microbienne Université Claude Bernard Lyon 1 Bâtiment Mendel 43, boulevard du 11 Novembre 1918 69 622 Villeurbanne CEDEX **philippe.normand@univ-lyon1.fr**
EDISS	**INTERDISCIPLINAIRE SCIENCES-SANTÉ** **http://www.ediss-lyon.fr** Sec. : Sylvie ROBERJOT Bât. Atrium, UCB Lyon 1 Tél : 04.72.44.83.62 INSA : M. LAGARDE **secretariat.ediss@univ-lyon1.fr**	**Mme Sylvie RICARD-BLUM** Institut de Chimie et Biochimie Moléculaires et Supramoléculaires (ICBMS) - UMR 5246 CNRS - Université Lyon 1 Bâtiment Curien - 3ème étage Nord 43 Boulevard du 11 novembre 1918 69622 Villeurbanne Cedex Tel : +33(0)4 72 44 82 32 **sylvie.ricard-blum@univ-lyon1.fr**
INFOMATHS	**INFORMATIQUE ET MATHÉMATIQUES** **http://edinfomaths.universite-lyon.fr** Sec. : Renée EL MELHEM Bât. Blaise PASCAL, 3e étage Tél : 04.72.43.80.46 **infomaths@univ-lyon1.fr**	**M. Hamamache KHEDDOUCI** Bât. Nautibus 43, Boulevard du 11 novembre 1918 69 622 Villeurbanne Cedex France Tel : 04.72.44.83.69 **hamamache.kheddouci@univ-lyon1.fr**
Matériaux	**MATÉRIAUX DE LYON** **http://ed34.universite-lyon.fr** Sec. : Stéphanie CAUVIN Tél : 04.72.43.71.70 Bât. Direction **ed.materiaux@insa-lyon.fr**	**M. Jean-Yves BUFFIÈRE** INSA de Lyon MATEIS - Bât. Saint-Exupéry 7 Avenue Jean CAPELLE 69 621 Villeurbanne CEDEX Tél : 04.72.43.71.70 Fax : 04.72.43.85.28 **jean-yves.buffiere@insa-lyon.fr**
MEGA	**MÉCANIQUE, ÉNERGÉTIQUE, GÉNIE CIVIL, ACOUSTIQUE** **http://edmega.universite-lyon.fr** Sec. : Stéphanie CAUVIN Tél : 04.72.43.71.70 Bât. Direction **mega@insa-lyon.fr**	**M. Jocelyn BONJOUR** INSA de Lyon Laboratoire CETHIL Bâtiment Sadi-Carnot 9, rue de la Physique 69 621 Villeurbanne CEDEX **jocelyn.bonjour@insa-lyon.fr**
ScSo	**ScSo*** **http://ed483.univ-lyon2.fr** Sec. : Véronique GUICHARD INSA : J.Y. TOUSSAINT Tél : 04.78.69.72.76 **veronique.cervantes@univ-lyon2.fr**	**M. Christian MONTES** Université Lyon 2 86 Rue Pasteur 69 365 Lyon CEDEX 07 **christian.montes@univ-lyon2.fr**

*ScSo : Histoire, Géographie, Aménagement, Urbanisme, Archéologie, Science politique, Sociologie, Anthropologie

À mes mentors

Remerciements

La réalisation de cette thèse a été un bond de géant pour moi, même si elle ne représente probablement qu'un tout petit pas pour l'humanité... Cette aventure professionnelle et humaine n'aurait pas été possible sans un certain nombre de personnes qui m'ont formé, soutenu et inspiré. Les mots ne suffisent certes pas pour leur exprimer toute ma gratitude, mais je vais quand même essayer !

La place d'honneur va naturellement à mes cinq directeurs et encadrants de thèse : Dominique Baillis et Nawfal Blal du LaMCoS, Laurie San Miguel et Laurent Pierrot de SGR Provence, et Johann Meulemans de SGR Paris pour la confiance et la bienveillance qu'ils m'ont témoignées ces trois dernières années. Dominique, je te remercie pour les discussions enrichissantes et pleines de surprises sur le rayonnement thermique, ainsi que ta disponibilité et tes encouragements tout au long de ma thèse, surtout pendant les derniers mois de rédaction qui furent difficiles ! Nawfal, merci de ta pédagogie et ton éternelle bonne humeur ! Je retiendrai nos agréables échanges autour de la multitude de sujets qui nous animent : mécanique, voyage, administration française... Laurie, tu m'as fait découvrir le monde passionnant des céramiques réfractaires à travers le joli matériau qu'est le NorFoam. Grâce à toi, j'ai pu construire mon réseau, améliorer mes points faibles et ainsi réussir mes premiers pas dans la R&D industrielle (ou au moins en sortir vivant) ; pour cela je te serai toujours reconnaissant. Laurent, je souhaite te remercier pour ta forte implication non seulement dans le suivi de mes travaux, mais aussi dans mon développement professionnel pendant et après la thèse. Tu m'as toujours poussé à me dépasser tout en me rappelant de garder mes pieds sur terre, ce qui a été très formateur. Johann, tu m'as montré par ton exemple comment se frayer un chemin entre les mondes industriel et académique. Merci beaucoup de ta patience, de ta perspicacité, et surtout de m'avoir initié aux arcanes de la métrologie thermique !

Je tiens à remercier sincèrement Sophia Haussener du LRESE et Benjamin Rémy du LEMTA pour les échanges que nous avons pu avoir en début de ma thèse, et d'avoir accepté de rapporter mes travaux à leur conclusion. Je remercie également Samuel Forest du Centre des Matériaux d'avoir présidé mon jury de thèse. Merci beaucoup pour la qualité de notre discussion et pour vos retours extrêmement constructifs.

Tout au long de cette thèse, j'ai aussi eu l'immense chance de bénéficier de l'expertise de nombreux collaborateurs. J'adresse un grand merci à Domingos De Sousa Meneses et Alexey Novikov du CEMHTI, ainsi que Yves Jannot et Vincent Schick du LEMTA pour vos contributions expérimentales qui ont énormément enrichi ce travail. Merci en particulier à Domingos pour les passionnants échanges et pour ta participation à mon jury de thèse. Je remercie aussi Rémi Coquard (EC2 Modélisation) et Salvatore Cunsolo (ex-LaMCoS) pour les discussions extrêmement instructives sur la modélisation numérique du transfert radiatif dans les mousses. Merci également

à Naïm Naouar (LaMCoS) et Jérôme Adrien (Mateis) pour leur aide précieuse lors des campagnes de tomographie à rayons X et d'analyse d'images. Je n'oublie pas ceux avec qui j'ai été en contact lors de mes/nos petites quêtes infructueuses : Wouter Van De Walle et Hans Janssen (KU Leuven), Denis Rochais (CEA Le Ripault), Laurent Gremillard (Mateis), Bernard Ménaert (Institut Néel) et Ana-Maria Trunfio-Sfarghiu (LaMCoS), merci d'y avoir consacré de votre temps.

Passons ensuite aux collègues de SGR Provence : je ne saurais commencer autrement qu'en remerciant Yannick "Mimi" Millot, technicien R&D et grand œnologue. Mimi, en plus d'avoir réalisé tous mes échantillons (même les plus exotiques) avec rigueur et panache, tu as toujours su trouver du temps pour répondre à mes questions, avec ton sourire que rien ne semble pouvoir effacer. Merci à toi ! Je remercie également Robert Germar, directeur de SGR Provence et Yves Boussant-Roux, directeur R&D des Matériaux Céramiques, ainsi que l'ensemble du personnel technique et administratif du centre de m'avoir permis de réaliser cette thèse dans de bonnes conditions. Merci en particulier au reste de l'équipe PCR – Marianne, Frédéric, Nicolas, Aurélie, Alexandre, Alexandre, Jérôme, Jérôme, Mathieu, Matthieu, Najih, Adrien, Xavier, Olivier, Klaus, Mangesh, Clémence et Camille – pour leur accueil chaleureux ; à Éric, Zoé et Angélique de ZirPro pour leur aide lors de mon détour dans le monde de la zircone ; à Paul, Magaly, Arnaud, Laurent, Didier, Jean-François, Jean-Michel, Patrick et Jean-Marc des CRL pour leur aide dans les essais, usinages et analyses ; et à Caroline, Sylvain et Michaela du LSFC pour les nombreux échanges intéressants. Je remercie au passage les équipes de Taxi Aurélie et de l'Hôtel du Parc pour leur service impeccable lors de mes séjours dans le pays de melon.

Du côté du LaMCoS, je remercie en premier lieu Isabelle Comby et Sophie De Oliveira, gestionnaires de l'équipe MIMESIS et du laboratoire, pour leurs amabilité et efficacité sans pareils. J'associe à ces remerciements les ingénieurs et techniciens du laboratoire : Arnaud Duval, Jean-Michel Dumont, Christelle Dumont et Alain Thivillier pour la gestion de l'infrastructure et du matériel informatiques indispensables au quotidien de numéricien, et Philippe Chaudet, Lionel Lafarge et Jean-Pascal Guilhermond pour leur assistance sur l'usinage de mes mousses. Merci également à l'équipe du Bar et à la commission QVT d'œuvrer pour la bonne ambiance au laboratoire. En parlant de la QVT, je souhaite remercier chaleureusement Alain de m'avoir invité à participer à l'organisation de la Semaine Asiatique du laboratoire, ainsi que tous les organisateurs et participants qui ont fait de ce moment une magnifique expérience humaine pour moi.

Ce partenariat entre SGR Provence et le LaMCoS n'aurait certainement pas vu le jour sans le soutien financier de Saint-Gobain et du Ministère de l'Enseignement Supérieur via le dispositif CIFRE, dont la mise en place a aussi nécessité l'implication de nombreux autres acteurs : ANRT, INSAVALOR... Je souhaite ici leur assurer de ma profonde gratitude.

Il est maintenant temps d'entamer un tournant personnel dans ces remerciements. Je m'adresse d'abord aux camarades doctorants au LaMCoS avec qui j'ai passé tant de bons moments ces trois dernières années : Tristan (Abaqos user se transformant en topologie optimisée avec 8 manas), Thomas (la générosité incarnée), Marie (maman chat forte et indépendante), Médéric (Celui-Dont-On-Massacra-Le-Prénom), Bonetto-san (Shazam et 9GAG 2-en-1), Karine (et son extrême gentillesse), Zhaofeng (meilleur compagnon de road-trip), Ethel (le slalomeur), Efoe (pop star en cachette), Nicolas, Haoming, Alexis, Yvan, Quanshangze, Florian, Zineb, Raphaël, Pierre, Noël (Team Algeco), Meng, Panico, Thibaut, Sergent, Jin, Renzi, Xiaowen, Yvan, Tarek, Meriem, Ye, Arthur, Wenqi, Shuai, Deqi, Wenjun, Chao, Alexia, Guillaume, Thibault, Étienne, Matthieu, Mou-

hamadou, et peut-être quelques autres que j'ai oubliés malgré moi (et qui j'espère m'excuseront). Merci à vous, vos +1 et/ou vos colocs (un petit clin d'œil à Félix, Carron et Merlette) pour l'entraide, les soirées jeux, les conférences, les pots de thèse, les gâteaux du vendredi, les blagues privées nulles, les pétages de câble ... Je pense aussi aux doctorants et chercheurs de l'univers Saint-Gobain – Claire, Hassan, Sidanth, Giang, Alejandra, Julien, Adrien, Marielle, Mathilda, Julie et Helena. Merci des pauses-café, des workshops, et de m'avoir fait découvrir vos mondes si fascinants !

Un grand merci également à mes chers amis qui m'ont aidé à garder un minimum d'équilibre mental pendant ces trois années : les Rhinos/Sommeliers Gaby, Coline, Emma, Sysy rend l'argent, Pierre et ses B-52, Jojo, Marion, Mathieu, Nico, Gaëtan, Vithya, Lucas, Anne-Lise, Dorian, Justine, Amandine ; les Lyonnais (oui c'est original) Sébastien, Élodie + Zéphyr, Guillaume, Paul, Edgar, Valentine et Édouard ; le "Groupe Kinabalu" Edmund, Clement, Teck Wan, Ze Ying, Vincent, Grace, Eri, Eswaren, William, Sharvin, Ziwei et Heeran ; et quelques autres en vrac : Vivian, Mimi, Liên, Jonathan, Livia, Sophie, Caijing, Alexandra, Majda, Ling et Ege.

Puisque faire une thèse nécessite avant tout une formation scientifique de qualité, je remercie tous mes professeurs du département Génie Mécanique (autrefois GMC) de l'INSA de Lyon ainsi que les encadrants que j'ai eus en échange ou en stage, en particulier ceux qui m'ont donné le goût de la modélisation numérique et de la recherche : dr.ir. Jim Kok (UTwente), Adèle Caron et Charles-André Lemarié (ex-Hamon d'Hondt), et surtout la "dream team" Abaqus-PreciSo-Inconel718, composée de Thibaut Chaise, Didier Bardel, Sophie Cazottes, Daniel Nélias et Michel Perez. La conclusion de cette thèse symbolise aussi l'aboutissement d'un long chemin d'intégration culturelle qui ne serait pas possible sans les personnes suivantes : Philippe Velex et Siobhan Wegeler, directeurs de SCAN ainsi que l'ensemble d'enseignants de cette filière dont Romaric Pujol, Suzanne Cawston, Lionel Manin, Frédéric Lortie, Lucien Roiban et Christian Olagnon ; mes formidables professeurs de français Laurence, Lise, Hugues et Aurore ; et Antony Woaye-Hune (Framatome) dont l'accompagnement m'a permis de m'affirmer et m'épanouir. Merci aussi à Chew Lihong (ex-SCAN), Tan Chin Guan (ex-HCI), Alexis Richard (Michelin) et le personnel de Campus France de Singapour et de Malaisie pour leur précieux conseils avant même que j'aie décidé de sauter le pas et m'expatrier en France.

Il semble approprié de passer ici de la langue de Molière à celle de Shakespeare pour le bénéfice de mes plus proches. Fresh off this sudden switch in language, I would like to thank all my teachers from my formative years at Hwa Chong Institution and Chen Moh Primary School, especially Mr. Ong Jek Yaw, Mr. Tang Koon Loon and Mrs. Teo Chin Chew for having inspired me to continue doing science, Mr. Chua Khang Jye for his encouragement when I most needed it, and Messrs. Jeffrey Lim and Ng Seaw Choon for their care and guidance.

Thanks to all my aunts, uncles, cousins, and in-laws for showering me with love and kindness everytime we meet, especially Cabie, the undisputed best cousin ever ! And a huge thank you to my dear friends back home, especially those who are practically family – you know who you are :)

A tip of the hat to the late Jonathan Larson, for having written the soundtrack of my thesis.

Finally, but most importantly :

I thank my parents, my first teachers, for making me who I am ;

I thank my brother, my first and always friend, for going through thick and thin with me ;

I thank Pumpkin, my companion and muse, for reminding me of what really matters in life ;

And I thank Theresa, the love of my life, for her unwavering affection, trust, and support.

Ce qui est simple est toujours faux. Ce qui ne l'est pas est inutilisable.

– Paul Valéry

Résumé

Cette thèse CIFRE réalisée en collaboration avec Saint-Gobain Research Provence porte sur la modélisation des propriétés thermiques d'une mousse d'alumine NorFoam XPure®, conçue pour l'isolation thermique haute température (1200 °C–1700 °C). L'objectif est de développer et valider des modèles numériques multiéchelles pour calculer le transfert de chaleur par conduction et rayonnement dans cette mousse, à partir des microstructures 3D tomographiées et des propriétés intrinsèques des composants. La mousse étant composée des cellules ouvertes et d'un squelette solide lui-même poreux, la prise en compte de l'influence de cette double porosité est particulièrement novatrice.

Dans un premier temps, le transfert thermique par conduction à travers la mousse est modélisé avec des techniques d'homogénéisation par éléments finis. Il est démontré que des conditions aux limites périodiques couramment utilisées ne sont pas adaptées aux mousses tomographiées, et qu'un jeu de conditions aux limites mixtes permet d'obtenir des résultats plus précis sur ces dernières.

Quant au transfert radiatif à travers le squelette poreux, qui présente une forte diffusion volumique avec des phénomènes ondulatoires, le développement d'une nouvelle approche de modélisation basée sur l'approximation dipolaire discrète permet de prendre en compte l'influence desdits phénomènes.

Les propriétés radiatives de la mousse sont ensuite calculées par méthode de lancer de rayons en tenant compte du comportement radiatif complexe du squelette poreux. L'influence des phénomènes de réflexion et réfraction non-spéculaires aux interfaces entre le squelette et les cellules a été étudiée. Enfin, une modélisation numérique basée sur les techniques d'homogénéisation permet de calculer le transfert thermique à travers la mousse, avec couplage de la conduction et du rayonnement.

Le bon accord entre les résultats issus de chaque modèle et les mesures thermiques et optiques réalisées sur la mousse et le squelette poreux confirme le caractère prédictif des modèles développés.

Mots clés : Mousse céramique, Conductivité thermique haute température, Homogénéisation numérique, Optique physique, Couplage conduction-rayonnement

Abstract

This CIFRE doctoral study, performed in collaboration with Saint-Gobain Research Provence, aims to model the thermal properties of NorFoam XPure®, an alumina foam designed for high temperature thermal insulation (1200 °C–1700 °C). The goal is to develop and validate multiscale numerical models to compute the conductive and radiative heat transfer through the foam from 3D tomography-reconstructed microstructures and the intrinsic properties of each constituent phase. Specific attention is given to the complex porosity in the studied foam : in addition to the open-cell network, smaller pores are also found within the foam skeleton. Novel approaches are proposed in the present work to take into account the influence of this dual-scale porosity.

Firstly, effective heat conduction through the foam is modeled with finite element homogenization techniques. It is demonstrated that the commonly used periodic boundary conditions are unsuitable for tomography-reconstructed foams, and that a set of mixed boundary conditions gives more accurate and precise results for such foams.

As radiative transfer through the porous foam skeleton is characterized by high volume scattering and significant wave effects, a novel physical optics approach based on the discrete dipole approximation is next developed to model the influence of these phenomena.

The radiative properties of the foam are then determined through a ray tracing method that takes into account the complex radiative behavior of the porous foam skeleton. The influence of non-specular reflection and refraction at the interfaces between the foam cells and skeleton is studied. Finally, the homogenized properties are applied to simulate the coupled conductive and radiative heat transfer through the foam.

The model predictions are systematically compared to thermal and spectroscopic measurements performed on samples of the foam and the foam skeleton material. The good agreement between numerical and experimental results confirms the predictive capabilities of the models developed in this study.

KEYWORDS: Ceramic foam, High temperature thermal conductivity, Computational homogenization, Physical optics, Conduction-radiation coupling

Table des matières

Introduction générale

Depuis le début de la vie sur Terre, la nature a su exploiter les propriétés remarquables des matériaux cellulaires : alliant légèreté, rigidité, et fonctionnalité, ces derniers permettent aux oiseaux de voler, à *homo sapiens* de marcher sur deux pieds, et aux arbres de monter jusqu'au ciel. La porosité, à l'origine de ces merveilles, a toutefois été pendant longtemps le fléau des ingénieurs cherchant à réaliser des matériaux de haute performance. Ce paradigme semble aujourd'hui être en pleine mutation. Les céramiques cellulaires de type mousse ont notamment connu un fort développement ces dernières années dans de nombreux domaines où les transferts thermiques à haute température jouent un rôle important, tels que la récupération d'énergie solaire [1–3], la catalyse thermochimique [4], ou la combustion industrielle [5, 6]. La bonne connaissance des propriétés thermiques de ces matériaux, dont la conductivité thermique, est indispensable pour la maîtrise de la performance, la consommation énergétique, et la sûreté des systèmes qu'ils composent.

Cette thèse réalisée en partenariat avec Saint-Gobain Research (SGR) Provence porte sur l'étude du transfert thermique dans NorFoam XPure®, une mousse d'alumine pure développée par Saint-Gobain pour l'isolation thermique de 1200 °C à 1700 °C [7]. La caractérisation de NorFoam par tomographie à rayons X (Figure 1) révèle la présence d'une double porosité : la structure de la mousse est composée d'un réseau de cellules sphéroïdales ouvertes des tailles de l'ordre des 100 µm, et d'un squelette lui-même poreux avec des pores tortueux de tailles microniques. La porosité totale nominale de la mousse, tous types de pores confondus, est de 82%. À cette porosité et ces températures, les modes de transfert thermique principaux dans NorFoam sont la conduction et le rayonnement (la convection est généralement négligée lorsque les pores sont au-dessous du mm [8]). La conductivité thermique n'est alors plus intrinsèque car elle comportera aussi le transfert radiatif qui fait intervenir des phénomènes complexes de diffusion, d'absorption et d'émission. On l'appelle par la suite conductivité thermique *apparente*. La compréhension de la relation entre la microstructure complexe et la conductivité thermique apparente aux températures d'intérêt représente un enjeu important pour l'optimisation du produit. La quantification de la contribution de chaque mode de transfert thermique est particulièrement intéressante, or, son identification par l'approche expérimentale-inverse est très délicate, surtout aux températures d'intérêt [2, 9–11].

Dans cette thèse, on développe une approche numérique qu'on juge plus versatile car elle permet de prédire le transfert conducto-radiatif à partir des microstructures 3D. Pour la mousse NorFoam, la porosité hiérarchique justifie l'adoption d'une approche multiéchelle : le squelette poreux est simulé comme une phase homogène équivalente lorsque l'on souhaite étudier les transferts à l'échelle de la mousse, qui elle est simulée comme un milieu homogène équivalent quand il s'agit d'étudier le transfert conducto-radiatif à travers les pièces ou les systèmes qu'elle compose

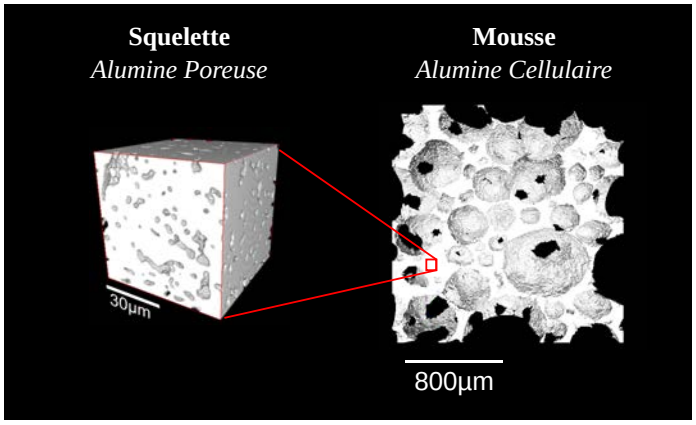

FIGURE 1 – Microstructure à double porosité de NorFoam XPure®.

(échelle "macroscopique"). Les échelles sont alors découplées et reliées entre-elles uniquement par des propriétés *effectives* [1]. Afin que ces propriétés effectives traduisent fidèlement l'influence de la porosité à plus petites échelles, elles doivent être simulées avec des modèles physiques et conditions aux limites judicieusement choisis.

Le caractère prédictif des modèles est vérifié en comparant les résultats numériques obtenus sur des microstructures réelles tomographiées aux mesures réalisées sur des échantillons de mousse et squelette. En effet, des collaborations entre SGR Provence et SGR Paris ainsi que les laboratoires LEMTA (Nancy) et CEMHTI (Orléans) ont permis d'avoir accès aux données d'entrées et données expérimentales de validation jusqu'à haute température. Notamment, pour caractériser les propriétés thermiques et radiatives du squelette, des échantillons de microstructure équivalente ont été fabriqués sous forme des disques d'alumine poreuse de 33 mm de diamètre et 2 mm d'épaisseur.

L'approche est schématisée sur la FIGURE 2 et expliquée ci-dessous. Malgré les nombreuses études passés sur ce sujet [1, 3, 12–15], un certain nombre de verrous ont dû être levés afin de prendre en compte des spécificités liées à la modélisation de NorFoam. Les travaux entrepris dans cette thèse ont été intégralement résumés sous forme de quatre papiers en anglais (dont un paru dans *International Journal of Heat Transfer* [16]), organisés en trois chapitres comme suit :

Le Chapitre I traite la simulation de la conductivité thermique effective de NorFoam à partir de sa microstructure tomographiée. Pour ce faire, la technique d'homogénéisation numérique destinée aux composites biphasiques (ici cellule et squelette) est souvent appliquée. Or les conditions aux limites à utiliser ne font pas l'unanimité dans la littérature. Ces différents jeux de conditions aux limites peuvent conduire à des écarts importants, notamment dans le cas des mousses tomographiées. Une comparaison systématique a permis de conclure qu'un jeu de conditions aux limites mixtes (et non les conditions aux limites périodiques couramment utilisées) permet de donner des estimations de conductivité effective plus justes et précises sur

1. On appelle propriété *effective* une propriété intrinsèque du matériau hétérogène à une microstructure donnée, cette propriété doit donc être indépendante vis-à-vis de la géométrie et la configuration aux échelles beaucoup plus grandes que celle de la variation microstructurale, où le matériau est modélisé comme un milieu homogène équivalent. La conductivité thermique *effective*, qui décrit uniquement le transfert thermique par conduction, est donc à distinguer de la conductivité thermique *apparente* qui décrit le transfert conducto-radiatif, par nature extrinsèque.

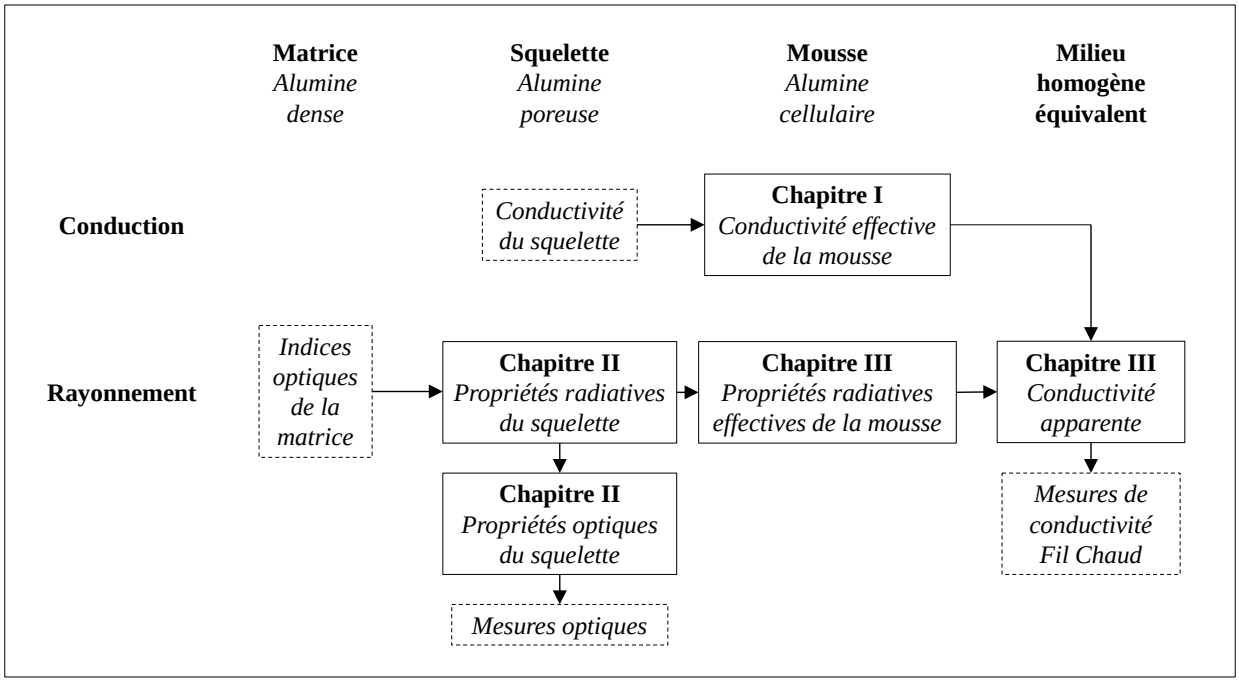

Figure 2 – Approche numérique développée et validée dans le cadre de cette thèse. Cadres continus : Modélisation numérique (travail du doctorant), Cadres pointillés : Mesures utilisées comme données d'entrée ou données de validation.

des mousses tomographiées [16]. Ce modèle de conductivité effective modélise le squelette par une phase homogène équivalente, et prend comme donnée d'entrée la conductivité effective du squelette (caractérisée par méthode Flash à SGR Paris sur les disques d'alumine poreuse). Les pores dans le squelette n'étant pas représentés à cette échelle, la porosité observée est uniquement celle des cellules ($74 \pm 2\%$).

Le Chapitre II est composé de deux papiers traitant la simulation et validation des propriétés radiatives effectives du squelette de NorFoam. Contrairement à la plupart des mousses étudiées dans le passé qui ont des squelettes opaques, le squelette de NorFoam est semi-transparent et peu absorbant. Les méthodes actuelles n'arrivent pas à prédire la haute diffusion volumique [4, 6, 12] au sein du squelette de NorFoam liée aux phénomènes de l'optique physique. Dans le premier papier de ce chapitre, une nouvelle méthode de calcul basée sur l'approximation dipolaire discrète (DDA en anglais) est proposée, validée sur des géométries de référence, puis appliquée à la simulation des propriétés radiatives effectives du squelette de NorFoam (à partir des images tomographiées et l'indice de réfraction complexe de l'alumine dense). Dans le second papier, ces propriétés radiatives sont appliquées à la simulation de la réflectance, transmitance et émettance des plaques composées du même matériau que le squelette de NorFoam, pour des températures allant jusqu'à 1300 °C. En parallèle, des mesures spectroscopiques de réflectance et transmittance à l'ambiante ainsi que d'émettance normale jusqu'à 1300 °C sont mesurées au laboratoire CEMHTI sur les disques d'alumine poreuse. Les résultats numériques affichent un très bon accord avec les mesures spectroscopiques, ce qui valide les propriétés radiatives

calculées par l'approximation dipolaire discrète.

Le Chapitre III traite la simulation des propriétés radiatives de mousse, puis la résolution du couplage conduction-rayonnement afin de calculer la conductivité apparente de la mousse NorFoam. Les propriétés radiatives de mousses sont calculées par méthode de lancer de rayons sur des mousses tomographiées, adaptée pour tenir compte des propriétés radiatives du squelette calculées dans le Chapitre 2. Les propriétés radiatives effectives de la mousse sont ensuite appliquées avec la conductivité effective calculée dans le Chapitre 1, à la simulation de la conductivité thermique apparente sous l'hypothèse d'un transfert thermique conducto-radiatif unidirectionnel en régime stationnaire. L'influence des phénomènes de réflexion et réfraction non-spéculaires à l'interface cellules-squelette a été étudiée. La comparaison des résultats numériques avec des mesures de fil chaud parallèle jusqu'à 1000 °C valide la capacité de notre modèle à fournir des prédictions justes du transfert conducto-radiatif au sein de NorFoam.

Il est à noter que chaque chapitre commence par une présentation de l'état de l'art de la littérature pour le type de modélisation qu'il traite, et possède ses propres table des symboles, bibliographie et, le cas échéant, annexe(s).

Chapitre I

Modélisation de la conductivité thermique effective des mousses

Sommaire

Influence of boundary conditions on computation of the effective thermal conductivity of foams

Z.K. Low[a,b,*], N. Blal[a], N. Naouar[a], D. Baillis[a]

[a] *Univ Lyon, INSA-Lyon, CNRS UMR5259, LaMCoS, F-69621 Villeurbanne, France.*
[b] *Saint-Gobain Research Provence, F-84306 Cavaillon, France.*

Abstract

Accurate numerical simulation of the effective thermal conductivity (ETC) of 3D pore-scale foam models requires a judicious choice of boundary conditions, as the computational domains are often smaller than the representative volume element, giving rise to considerable edge effects. Within the finite element homogenization framework, a set of mixed boundary conditions are considered alongside the usual uniform and periodic boundary conditions. Validity criteria and order relations, demonstrated from entropy-based principles, are numerically verified on unit cell-based geometries, random virtual periodic foams, and non-periodic tomography-reconstructed foams of equivalent microstructure. A statistical treatment based on the integral range provides confidence intervals for the estimated ETC. For foam samples with random homogeneous porosity, the mixed boundary conditions are shown to fulfill the macrohomogeneity condition and thus provide thermodynamically valid ETC estimates. For periodic foams with irregular microstructure, the ETC is very slightly underestimated under the mixed boundary conditions. For non-periodic geometries, it is shown that periodic boundary conditions–commonly viewed as the reference–underestimate the ETC due to boundary geometry mismatch, while the mixed boundary conditions give a more accurate and precise estimate.

Keywords: Foam, Thermal conductivity, Homogenization, Boundary conditions, Finite elements

1. Introduction

Cellular foam materials are a source of interest in many fields [1–3] as they combine attractive thermal properties with good strength-to-weight ratio [4]. Accurate modeling of the foam effective thermal conductivity (ETC) is important on account of the difficulties in performing precise measurements under service conditions (e.g., refractory ceramic foams with service temperatures up to 1700 °C [5]). While analytical relations between the ETC and microstructural parameters are abundant in the literature [6, 7], most still require calibration or validation against empirical data [7] before they may be applied to particular classes of materials. As such, many recent studies have focused on 3D pore-scale numerical simulations on either regular unit cell geometries [8], digitally

*Corresponding author
Email address: zi.low@insa-lyon.fr (Z.K. Low)

Int. J. Heat Mass Transfer 155 (2020) 119781. DOI: 10.1016/j.ijheatmasstransfer.2020.119781

Nomenclature

Scalars are written in *regular italic* font, while first- and second-order tensors are denoted with ***bold face italics***.

Latin

A	Area
C	Covariance
e	Basis vector
F	Macroscopic heat flux
f	Volume fraction
G	Macroscopic temperature gradient
h	Distance
J	Integral range
j	Direction index
k	Thermal conductivity
L	Length
N	Number
n	Normal direction
Q	Heat flow
q	Heat flux
R	Rotation
r	Residual
T	Absolute temperature
V	Volume
x	Position
ℓ	Micro-scale characteristic length
$\mathbb{P}$	Probability
$\mathbb{R}^3$	Cartesian frame
$\mathcal{S}$	Entropy functional

Greek

Δ	Difference
ϵ	Precision, error
μ	Mean
σ	Standard deviation
θ	Relative temperature
Ω	Domain

Superscripts and Subscripts

+/–	Opposite sides on the boundary
0	Reference, Arbitrary, Constant
c	Complementary
D	Diagonal
p	Pore
s	Solid
adm	Admissible
app	Apparent
eff	Effective
sol	Solution

Operators and accents

∇	Del operator
$\cdot$	Dot product (single tensor contraction)
∂	Boundary
$\langle\bullet\rangle$	Volume average
$\langle\langle\bullet\rangle\rangle$	Stochastic mean
$[\bullet]$	Matrix representation
$\dot{\bullet}$	Time derivative
$\hat{\bullet}$	Imposed values
$\tilde{\bullet}$	Fluctuating component

Acronyms

ATC	Apparent thermal conductivity
ETC	Effective thermal conductivity
MBC	Mixed boundary conditions
PBC	Periodic boundary conditions
PSD	Pore size distribution
RVE	Representative volume element
SSA	Specific surface area
UHF	Uniform heat flux
UTG	Uniform temperature gradient

generated random periodic foams [9–11], or tomography-reconstructed real foam models [1, 2, 12–15].

Finite element-based computational homogenization [16–19] has been used to accurately predict the ETC tensor of heterogeneous materials such as composites [11] and porous media [20, 21] from microstructural descriptions of the material. In this scheme, the ETC is classically obtained by resolving uniform heat flux (UHF) and uniform temperature gradient (UTG) boundary value problems [22] on computational domains of increasing size, until the resulting apparent thermal conductivities (ATC) converge to the same value: the ETC. The domain at which convergence is reached is then defined as a representative volume element (RVE). By this definition, the ETC satisfies the macrohomogeneity condition[1], i.e., fundamental thermodynamic quantities (entropy in the case of heat conduction) are conserved during scale transition [23]. However, real porous media such as foams can have prohibitively large RVE sizes due to the random microstructure and high contrast in phase properties [20, 21, 24]. Therefore, it is often necessary to estimate the ETC using computational domains smaller than the RVE (for example, with statistical treatments based on the integral range [20]). Contrary to the ETC which is intrinsic to the material, the ATC of such domains may be highly sensitive to boundary conditions due to edge effects, even when convective and radiative heat transfer are neglected [20, 24].

With their roots in the pioneering works on asymptotic homogenization [25–27], periodic boundary conditions (PBC)[2] have been shown to satisfy the macrohomogeneity condition, and to directly yield the ETC when applied to single periodic unit cells [17, 24]. Even though the PBC implicitly assume a periodic computational geometry, they have also been applied in numerous instances to non-periodic geometries such as tomography-reconstructed microstructures [14, 15, 20, 21, 30]. The commonly held view is that the PBC provide the best possible ETC estimate even for non-periodic geometries [16, 19], and that the error due to geometrical non-periodicity [30] would vanish if the computational domain is sufficiently large [29]. However, no evidence has been found to support this view in the case of highly porous real foam models obtained by tomographic reconstruction, which are often smaller than the RVE.

Much past work involving numerical modeling on tomography-reconstructed foams (e.g., [1, 2, 13, 31]) used instead a set of mixed boundary conditions (MBC) that simulates steady-state experimental configurations such as the guarded hot plate method [32]. With a parallelepipedic domain of the sample material, uniform temperatures are fixed on two plane-parallel faces with a small temperature difference $\Delta\theta$ between them, while adiabatic conditions are applied to the four other faces. If the macroscopic material behavior is isotropic or orthotropic [2, 31], a unidirectionnal heat flow Q exists within the sample, and a scalar apparent conductivity k_{1D} is computed:

$$k_{1D} = -\left(\frac{Q}{A}\right)\left(\frac{\Delta L}{\Delta\theta}\right) \tag{1}$$

with A being the surface area of the hot and cold faces, and ΔL being the distance between

[1]The analogous condition in the mechanical case is commonly called Hill's lemma or the Hill-Mandel condition, and is based on conservation of the mechanical strain energy during scale transitions.

[2]Periodic boundary conditions are also used in the volume averaging scheme [28], which gives the same result as asymptotic homogenization under equivalent assumptions despite being theoretically distinct [29].

them. Despite their widespread use by the porous media community (e.g., [1, 2, 13, 31]), to the present authors' knowledge, these MBC have only been sporadically used within the computational homogenization framework [21, 24]. This is likely due to the uncertainty on whether the resulting ATC satisfies the macrohomogeneity condition, especially for anisotropic microstructures. The accuracy and precision of the MBC results relative to those given by the uniform and periodic boundary conditions are also unclear, save for a few specific cases: Jiang et al. [24] found that the MBC and PBC gave equally accurate results for 2D isotropic unit cells, and Dirrenberger et al. [21] found that for stochastic fibrous samples, larger sample volumes were required to achieve the same precision with the MBC than with the UTG. For foam geometries smaller than the RVE, these questions remain open.

Through theoretical demonstrations verified with numerical results, the present work investigates the validity, accuracy, and precision of the ETC of foams estimated via computational homogenization under uniform, periodic and mixed boundary conditions. The aim is to clarify the most appropriate boundary conditions for different types of 3D foam models (unit cell-based geometries, virtual periodic foams, and tomography-reconstructed real foams), so as to pave the way for more accurate predictions of microstructure-property relations. Section 2 describes the characterization of tomography-reconstructed real foams through image analysis and the generation of periodic foams of equivalent microstructure. Section 3 formalizes the homogenization problem and theoretically demonstrates validity criteria and order relations for the different ATC using entropy-based principles. Section 4 presents the computational strategy, clarifies the concepts of validity, accuracy, and precision of the ETC estimates, and describes the statistical treatment used to account for the stochastic real foam microstructure. Results for the different numerical case studies are then discussed in section 5.

1.1. Mathematical notation

Tensorial notation is used in the equations, with scalars in *regular italic* font, and first- and second-order tensors denoted with ***bold face italics***. Tensors expressed as vectors or matrices (denoted with square brackets [•]) are given with respect to the Cartesian reference frame $\{\boldsymbol{e}_1, \boldsymbol{e}_2, \boldsymbol{e}_3\}$, unless otherwise specified.

2. Characterization and modeling of foam morphology

This section describes the characterization and modeling of the different types of foams studied in this work. Two types of random foam models are considered: tomography-reconstructed samples of a reference ceramic foam which provide the most realistic description of the pore scale morphology, and digitally generated periodic foams of equivalent microstructure. In addition, non-periodic regular structures were also created from an orthotropic unit cell for a preliminary study (described further in subsection 5.1).

2.1. 3D imaging and reconstruction of real foam samples

The reference material for this study is NorFoam XPure® by Saint-Gobain, a high-purity alumina foam for high temperature thermal insulation [5]. X-ray micro-computed tomography of the reference material was performed using the *Phoenix v|tome|x s* by GE. A cubic volume

of 92.04 mm^3 was scanned and stored as a grayscale image stack. Automatic thresholding and denoising were performed using the Fiji software [33] (see Figures 1(a) to (c)) to obtain a binary image stack containing 516 × 516 × 516 voxels with a voxel size of 8.75 µm). The porosity of the reconstructed real foam is 74 ± 2 %, which agrees well with the measured apparent density of the physical samples (the uncertainty reflects the sensitivity towards the image processing parameters).

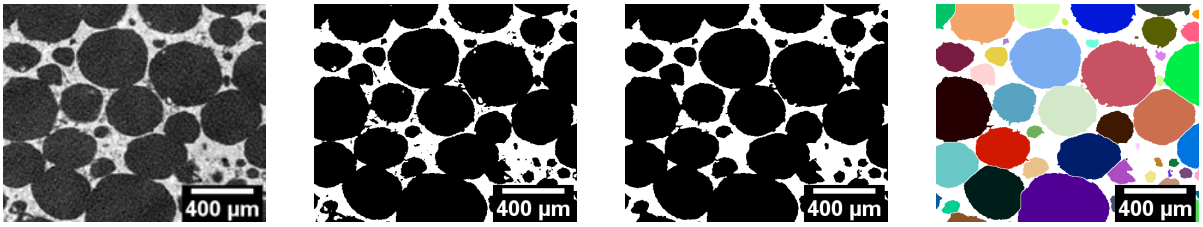

(a) Initial image. (b) Thresholding. (c) Denoising. (d) Segmentation.

Figure 1: Image processing steps.

2.2. *Quantitative analysis of microstructural parameters*

Pore size distribution. The reference alumina foam has a predominantly open-cell foam structure with interconnected spheroidal pores. The principal microstructural parameter is taken as the pore size distribution (PSD), with pore size defined as the diameter of an equal-volume sphere. Segmentation of the pore phase is performed with a watershed algorithm based on a maximal ball approach implemented in the iMorph software [34]. In Figure 2(a), the PSD based on pore count (with the diameter in µm) is shown to follow a lognormal distribution of parameters $\mu = 4.5$ and $\sigma = 0.97$ representing the mean and standard deviation of the diameter's logarithm respectively. The median diameter is 140 µm based on pore count, and 590 µm based on pore volume.

Pore connectivity. Once segmentation of the pore phase is performed, the pore network can be obtained by connecting the barycenter of each pore to those of its closest neighbors. The pore connectivity is then described by the mean number of neighboring pores in contact with any given pore, i.e., those having at least 1 voxel in common. This parameter is often considered in relation to heat and mass transport through the pore phase.

Specific surface area (SSA). The specific surface area is the total foam surface area per unit apparent volume, and represents the area available for heat exchange between the pore and solid phase. iMorph uses a marching cubes algorithm [34] to generate a surface mesh of the pore-solid interface constituted of triangular elements; the specific surface area is then estimated using the sum of the elements' areas.

Covariance range. The morphological covariance characterizes the geometrical dispersion within the foam sample [20]. Let $\mathbf{x}$ be a point in the sample. Denoting Ω_p the set of all points belonging to the pore phase and $\boldsymbol{h} \in \mathbb{R}^3$ an arbitrary distance vector, the morphological covariance $C(\boldsymbol{h})$ is an even function describing the probability that both points $\mathbf{x}$ and $\mathbf{x} + \boldsymbol{h}$ belong to the pore phase:

$$C(\boldsymbol{h}) = \mathbb{P}\left(\left\{\mathbf{x} \in \Omega_p\right\} \cap \left\{\mathbf{x} + \boldsymbol{h} \in \Omega_p\right\}\right) = C(-\boldsymbol{h}) \tag{2}$$

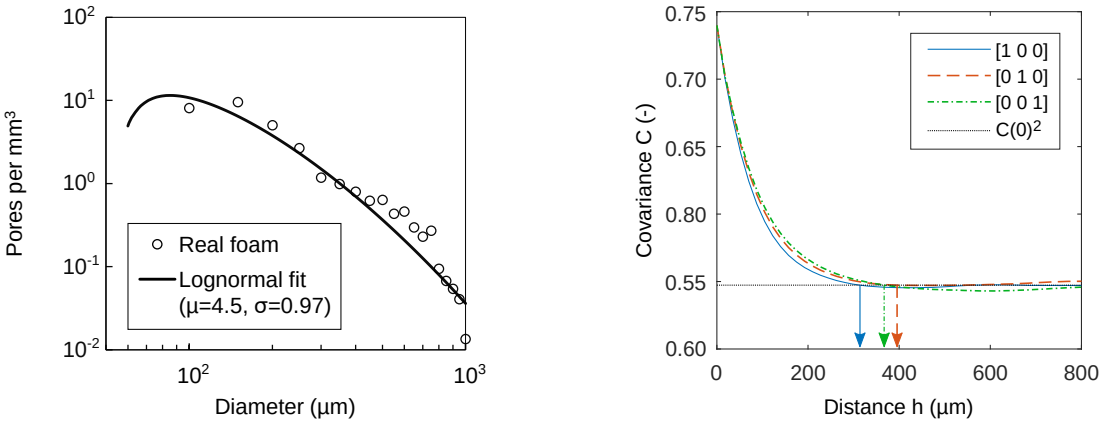

(a) Pore size distribution (PSD).

(b) Covariance along the principal directions.

Figure 2: Microstructural characteristics of the real foam.

When $\boldsymbol{h} = \mathbf{0}$, the covariance is simply equal to the porosity f_p. As $|\boldsymbol{h}| \to \infty$, $C(\boldsymbol{h})$ tends to the theoretical asymptotic value f_p^2 (two points infinitely far apart are uncorrelated). In most cases, there exists a finite distance called the covariance range at which this asymptotic value is reached. The covariance range depends on the size and arrangement of pores, and thus represents the characteristic length ℓ of the micro-scale in a given direction [20]. Points at distances larger than this range are considered statistically independent in terms of their microstructure. In Figure 2(b), the covariance ranges along the principal directions of the cubic geometry vary from 333 µm to 373 µm, which is approximately 3 times the median pore diameter of 140 µm. The tiny variation along the different principal directions suggests a very slight anisotropy in the material.

2.3. Generation of equivalent periodic foam models

Recent studies on pore-scale foam modeling have increasingly favored the use of digitally generated random polydisperse foam models over traditional unit cell descriptions [35], with Voronoi-based tessellations often used to simulate the distinctively skeletal structure of ultra-low density foams (usually having porosities of over 90%) [4, 9, 10, 36]. However, for ceramic foams of slightly lower porosity (approximately between 60% and 85%) fabricated by direct foaming of a ceramic slurry, spheroidal pores tend to be observed instead [37], as is the case with NorFoam XPure®. For this class of foams, the foam structure is more closely simulated as a solid matrix with packed spherical inclusions [10, 38]. The method of Cunsolo et al. [10] chosen to generate the virtual foams in this work will be briefly described in this subsection.

Four microstructural parameters are given as input: the target porosity f_p, the standard deviation σ of the diameter's logarithm, the edge length L of the cubic domain, and the number of pores in the domain. Figure 3 summarizes the foam generation workflow. The process starts with the generation of a random periodic packing of non-overlapping spheres, with relative diameters following a normalized lognormal PSD of parameter σ. The spheres are first inflated with their relative size unchanged, allowing intersections, to roughly match the target porosity. The structure is then converted into binary voxel format. A Gaussian blur filter followed by grayscale thresholding allows fine-tuning of the porosity while softening sharp edges in the foam structure, giving results

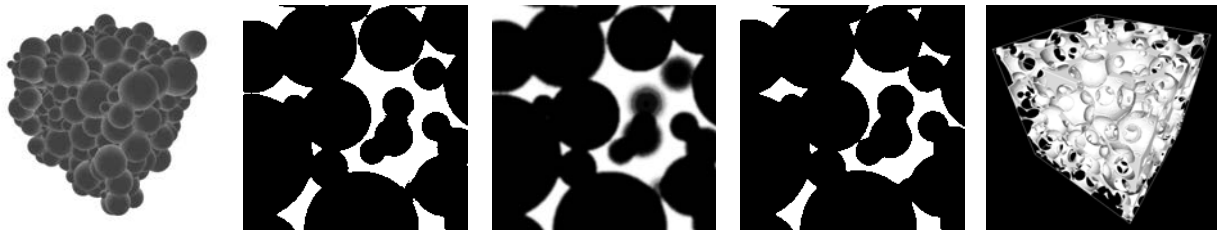

(a) Sphere packing. (b) Inflation. (c) Gaussian filter. (d) Thresholding. (e) Periodic foam.

Figure 3: Generation of periodic foam models with the algorithm of Cunsolo et al. [10].

Foam type & volume (mm^3)	PSD: Pores per mm^3 vs. diameter (µm)	Pore connectivity	SSA (mm^{-1})	Covariance range (µm)
Real foam ○ (V = 92.04)	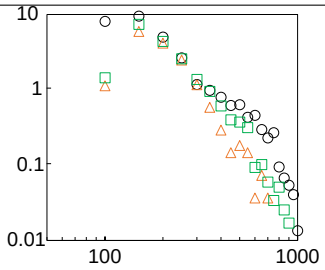	3.93	10.7	353 ± 20
Virtual foam △ (V = 2.74)		3.5 ± 0.7	9.7 ± 0.5	429 ± 184
Virtual foam □ (V = 11.78)		3.9 ± 0.4	8.4 ± 0.3	696 ± 345

Table 1: Comparison of key microstructural parameters between the real and virtual foams: pore size distribution (PSD), pore connectivity, specific surface area (SSA), and covariance range. For the virtual foams, the mean and standard deviations across 10 realizations are given.

similar to more sophisticated but computationally demanding approaches (e.g., the discrete element approach of Dyck and Straatman [38]).

Virtual foams of 6 distinct volumes ranging from 2.74 mm^3 to 11.78 mm^3 with 10 realizations for each volume are generated. The target porosity of 74% is achieved within voxel precision for all virtual foams. The same microstructural analysis described in subsection 2.2 is then applied to the virtual foams, with the results for the smallest and largest foams summarized in Table 1. The PSD, connectivity and SSA of the virtual foams agree remarkably well with those of the real foam, especially given that the absolute pore sizes were not fixed during the generation procedure. The higher mean covariance range in the virtual foams with a wider scatter suggests a less random pore arrangement in the virtual foam resulting from the periodicity constraint, with a higher degree of geometrical anisotropy within certain realizations due to the presence of a few extremely large pores. As the covariance ranges remain smaller than the cubic edge length L, the separation of micro- and macro-scales is upheld, and the realizations are statistically independent of one another.

2.4. Creation of non-periodic unit cell-based structures

For the preliminary study described in subsection 5.1, regular geometries that possess the key characteristics of the tomography-reconstructed foams (non-periodicity, anisotropy, high porosity) are created according to the method described below.

A reference orthotropic unit cell is first built, starting from a motif comprised of a body-centered cubic arrangement of overlapping spheres (Figure 4(a)). An oblong $4 \times 2 \times 1$ tessellation of said

motif is created (Figure 4(b)), then compressed into a cube, resulting in an orthotropic tessellation of overlapping ellipsoids. Finally, the inverse of this tessellation (Figure 4(c)) gives a periodic, orthotropic unit cell with interconnected ellipsoidal pores. The porosity of $f_p = 71.3\%$ is in the same range as the studied foams.

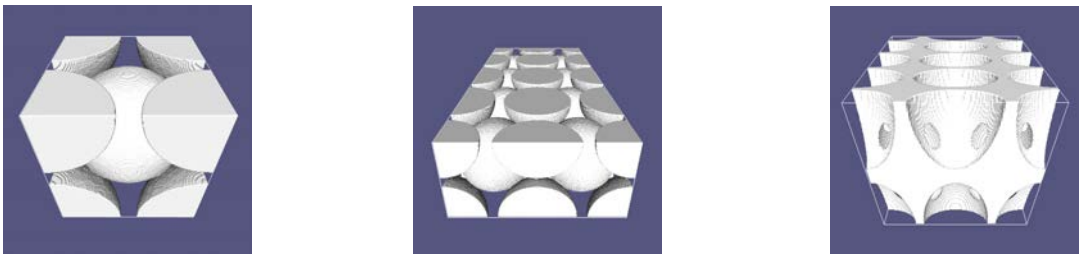

(a) Initial motif. (b) $4 \times 2 \times 1$ tessellation. (c) Orthotropic unit cell.

Figure 4: Generation of the orthotropic unit cell.

Non-periodic anisotropic geometries are then created as follows: a large 3D tessellation of the orthotropic unit cell is created, an arbitrary rotation is applied to the tessellation, then a cube is cut according to the initial Cartesian reference frame to give the final geometry. They are then used for the preliminary study described in subsection 5.1; notably, Table 2 contains examples of the anisotropic geometries obtained with the present method.

3. Theoretical study on boundary conditions

Heat transfer within engineering parts or structures made of foams typically occur over length scales much greater than the characteristic sizes of the foams' heterogeneities. Applying the principle of scale separation, two distinct scales can be considered. At the macro-scale, one is concerned with the thermal loading and response of the engineering structure, and the behavior of the foam may be represented by an effective thermal conductivity (ETC) tensor $\boldsymbol{k}_{\text{eff}}$. While a phenomenological model for $\boldsymbol{k}_{\text{eff}}$ can be derived from experimental measurements, this approach is generally cumbersome. Computational homogenization provides a more versatile way to deduce $\boldsymbol{k}_{\text{eff}}$ by simulating heat transfer at the micro-scale on explicit representations of the foam morphology (see Figure 5). The chosen micro-scale boundary conditions should satisfy the so-called "macrohomogeneity condition" to ensure fundamental thermodynamic quantities remain consistent during scale transition.

Four boundary conditions for the micro-scale problem are examined in this work: uniform heat flux (UHF), uniform temperature gradient (UTG), periodic (PBC) and mixed (MBC) boundary conditions. Assuming they satisfy the macrohomogeneity condition, these boundary conditions should predict the same macro-scale behavior when the computational geometry is large enough to be considered a representative volume element (RVE) of the foam. However, as most foam geometries are smaller than the RVE, different boundary conditions generally generally give different apparent thermal conductivity (ATC) tensors $\boldsymbol{k}_{\text{app}}$ which are more or less accurate estimates of the ETC.

The governing equations of the two-scale problem are first provided in subsection 3.1. The different boundary conditions are then examined in subsection 3.2. In particular, validity criteria for the MBC are developed with respect to the macrohomogeneity condition. The maximum entropy principle is then used in subsection 3.3 to establish analytical order relations between the ATC computed under different boundary conditions.

3.1. Governing equations

3.1.1. Macro-scale problem

At the macro-scale, the foam may be approximated as an equivalent homogeneous medium with a second-order effective thermal conductivity (ETC) tensor $\boldsymbol{k}_{\text{eff}}$. In the absence of volumetric heat sources, steady-state heat transfer is described by the macro-scale Fourier's law:

$$\boldsymbol{F} = -\boldsymbol{k}_{\text{eff}} \cdot \boldsymbol{G} \quad \text{with} \quad \boldsymbol{\nabla} \cdot \boldsymbol{F} = 0 \tag{3}$$

where $\boldsymbol{F}$ and $\boldsymbol{G}$ are the macroscopic heat flux and temperature gradient vectors respectively.

If $\boldsymbol{k}_{\text{eff}}$ is known, the heat flux and temperature fields across the entire macroscopic domain can be computed for any well-posed loading case. One way to obtain $\boldsymbol{k}_{\text{eff}}$ is through the computational homogenization approach presented in the next subsection.

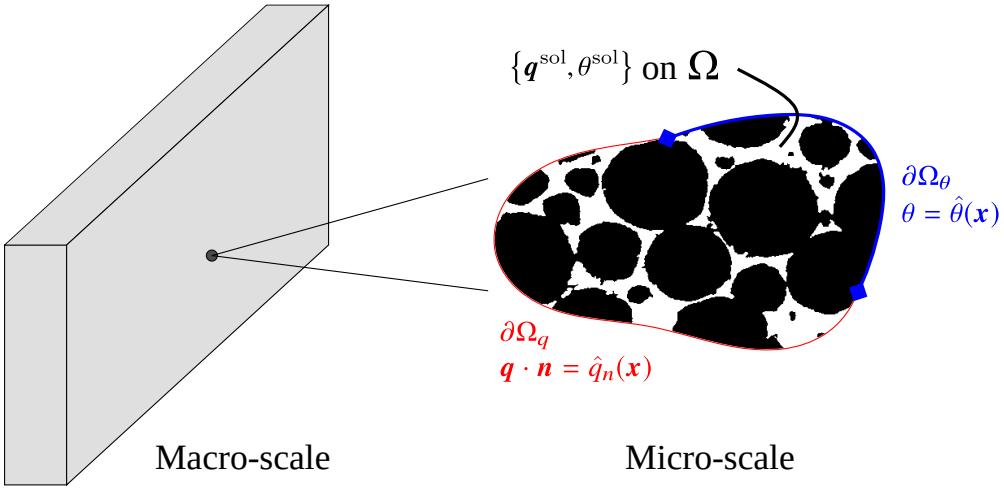

Figure 5: An illustration of two-scale problem. At the micro-scale, boundary temperatures $\hat{\theta}$ and normal heat fluxes $\hat{q}_n$ are prescribed on parts of the boundary $\partial\Omega_q$ and $\partial\Omega_\theta$ respectively, giving solution fields q^{sol} and θ^{sol} over the entire domain Ω.

3.1.2. Micro-scale problem and maximum entropy principle

The micro-scale problem considers the foam as a two-phase domain Ω with boundary $\partial\Omega$, sufficiently large compared to the characteristic microscopic length scale ℓ, yet sufficiently small compared to the macroscopic length scale (see Figure 5). As such, the temperature variations within Ω are small: $T = T_0 + \theta \approx T_0$, with T_0 being the reference temperature and θ the relative temperature. The second-order local thermal conductivity tensor $\boldsymbol{k}$ is then assumed constant with respect to temperature.

Under steady-state heat conduction with no volumetric heat generation, the micro-scale heat flux vector $\boldsymbol{q}$ and relative temperature θ are linked by the micro-scale Fourier's law:

$$\boldsymbol{q} = -\boldsymbol{k} \cdot \boldsymbol{\nabla}\theta \quad \text{with} \quad \boldsymbol{\nabla} \cdot \boldsymbol{q} = 0 \tag{4}$$

Given a set of micro-scale boundary conditions on $\partial\Omega$, the heat flux and temperature fields over Ω may be provided by the "maximum entropy principle" introduced by Onsager [39] and formalized in the next paragraph.

Maximum entropy principle. For a set of boundary conditions applied to the domain Ω, it is possible to define the disjoint parts of the boundary $\partial\Omega_q$ and $\partial\Omega_\theta$ on which the boundary normal heat flux $\hat{q}_n$ and temperature $\hat{\theta}$ are prescribed respectively (see Figure 5). The resulting solution heat flux and temperature fields are denoted q^{sol} and θ^{sol}.

An "admissible" solution for the heat flux field q^{adm} is a field that satisfies the boundary heat flux conditions, while possibly differing from the "true" solution q^{sol} elsewhere. The maximum entropy principle states that q^{sol} maximizes the rate of entropy increase minus the dissipation-rate [39], which for small temperature variations ($T \approx T_0$ on Ω) is written using the functional $\mathcal{S}$:

$$\forall \boldsymbol{q} \in \left\{\boldsymbol{q}^{\text{adm}}\right\}, \quad \mathcal{S}(\boldsymbol{q}) = \frac{1}{T_0^2}\left(-\int_{\partial\Omega_\theta} (\boldsymbol{q}\cdot\mathbf{n})\hat{\theta}\,\mathrm{d}A - \frac{1}{2}\int_\Omega \boldsymbol{q}\cdot(\boldsymbol{k}^{-1}\cdot\boldsymbol{q})\,\mathrm{d}V\right) \leq \mathcal{S}(\boldsymbol{q}^{\text{sol}}) \tag{5}$$

where $\hat{\theta}$ is the boundary temperature prescribed on $\partial\Omega_\theta$.

Similarly, an "admissible" solution θ^{adm} for the temperature field satisfies the temperature boundary conditions, but may differ from the "true" solution θ^{sol} elsewhere. The complementary statement of the maximum entropy principle is written as:

$$\forall \theta \in \left\{\theta^{\text{adm}}\right\}, \quad \mathcal{S}_c(\theta) = \frac{1}{T_0^2}\left(-\int_{\partial\Omega_q} \hat{q}_n\theta\,\mathrm{d}A - \frac{1}{2}\int_\Omega (\boldsymbol{k}\cdot\boldsymbol{\nabla}\theta)\cdot\boldsymbol{\nabla}\theta\,\mathrm{d}V\right) \leq \mathcal{S}_c(\theta^{\text{sol}}) \tag{6}$$

where $\hat{q}_n$ is the boundary normal heat flux prescribed on $\partial\Omega_q$.

Note that for a given set of boundary conditions and the resulting solution fields $\left\{\boldsymbol{q}^{\text{sol}}, \theta^{\text{sol}}\right\}$, the following property may be proven with the divergence theorem (equation (A.1)):

$$\begin{aligned} \mathcal{S}(\boldsymbol{q}^{\text{sol}}) + \mathcal{S}_c(\theta^{\text{sol}}) = \frac{1}{T_0^2}\left(-\int_{\partial\Omega} (\boldsymbol{q}^{\text{sol}}\cdot\mathbf{n})\theta^{\text{sol}}\,\mathrm{d}A + \int_\Omega \boldsymbol{q}^{\text{sol}}\cdot\boldsymbol{\nabla}\theta^{\text{sol}}\,\mathrm{d}V\right) = 0 \\ \iff \quad \mathcal{S}(\boldsymbol{q}^{\text{sol}}) = -\mathcal{S}_c(\theta^{\text{sol}}) \end{aligned} \tag{7}$$

3.1.3. Micro-macro scale transition and macrohomogeneity condition

The following averaging relation is proposed for any given scalar or vector field defined over Ω:

$$\langle \bullet \rangle = \frac{1}{V}\int_\Omega \bullet\,\mathrm{d}V \tag{8}$$

Having obtained the solution heat flux and temperature fields, the micro-macro scale transition is achieved by assigning $\boldsymbol{F} \equiv \langle \boldsymbol{q} \rangle$ and $\boldsymbol{G} \equiv \langle \boldsymbol{\nabla}\theta \rangle$ [18, 19]. The terms "mean" and "macroscopic"

are henceforth used interchangeably. It is then possible to identify a second-order apparent thermal conductivity (ATC) tensor $\boldsymbol{k}_{\text{app}}$ linking $\boldsymbol{F}$ and $\boldsymbol{G}$, using the macroscopic Fourier's law (given here in both tensorial notation and vector/matrix form with respect to the Cartesian frame):

$$\boldsymbol{F} = -\boldsymbol{k}_{\text{app}} \cdot \boldsymbol{G} \quad \equiv \quad \begin{bmatrix} F_1 \\ F_2 \\ F_3 \end{bmatrix} = - \begin{bmatrix} k_{11}^{\text{app}} & k_{12}^{\text{app}} & k_{13}^{\text{app}} \\ k_{21}^{\text{app}} & k_{22}^{\text{app}} & k_{23}^{\text{app}} \\ k_{31}^{\text{app}} & k_{32}^{\text{app}} & k_{33}^{\text{app}} \end{bmatrix} \begin{bmatrix} G_1 \\ G_2 \\ G_3 \end{bmatrix} \tag{9}$$

As $\boldsymbol{k}_{\text{app}}$ may vary depending on the choice of micro-scale boundary conditions and the size of Ω, it is generally different from $\boldsymbol{k}_{\text{eff}}$, which should be intrinsic to the homogenized medium. The chosen micro-scale boundary conditions to compute $\boldsymbol{k}_{\text{app}}$ should ensure consistency of fundamental thermodynamic quantities between the micro- and macro-scales. This "macrohomogeneity condition" is detailed below.

Macrohomogeneity condition. The following quantity represents the micro-scale specific entropy production rate due to the irreversibility of heat conduction, and is obtained by expressing the second law of thermodynamics in the form of the Clausius-Duhem inequality [39, 40]:

$$-\boldsymbol{q} \cdot \frac{\boldsymbol{\nabla} T}{T^2} \geq 0 \tag{10}$$

where $T = T_0 + \theta$. Note that the same quantity appears in the statements of the maximum entropy principle (equations (5) and (6)).

The macrohomogeneity condition states that the specific entropy production rate should be conserved between the micro- and macro-scales [19, 23]. For small temperature variations ($T \approx T_0$) across Ω, this condition can be simplified to:

$$\left\langle -\boldsymbol{q} \cdot \frac{\boldsymbol{\nabla} T}{T^2} \right\rangle \approx \left\langle -\boldsymbol{q} \cdot \frac{\boldsymbol{\nabla} \theta}{T_0^2} \right\rangle = -\boldsymbol{F} \cdot \frac{\boldsymbol{G}}{T_0^2} \quad \Longleftrightarrow \quad \langle \boldsymbol{q} \cdot \boldsymbol{\nabla} \theta \rangle \approx \boldsymbol{F} \cdot \boldsymbol{G} \tag{11}$$

Schindler et al. [23] showed that this simplification is indeed valid, inducing an error of 0.18% when the maximal temperature variation over the domain is 1 K for $273\ \text{K} \leq T_0 \leq 775\ \text{K}$.

As the divergence theorem links the averages $\langle \boldsymbol{q} \rangle$, $\langle \boldsymbol{\nabla} \theta \rangle$, and $\langle \boldsymbol{q} \cdot \boldsymbol{\nabla} \theta \rangle$ to their boundary values (see equation (A.1)), the applied boundary conditions have a direct influence on whether the macrohomogeneity condition is satisfied.

3.2. Boundary conditions

The different sets of boundary conditions considered in this work are presented in this section, and their validity with respect to the macrohomogeneity condition is examined. For mathematical details, readers may refer to Appendix A.

3.2.1. Uniform and periodic boundary conditions

The usual uniform and periodic boundary conditions encountered in the literature on computational homogenization (e.g., [19, 27]) are first discussed.

Uniform heat flux (UHF). Denoting $\boldsymbol{F_0}$ an arbitrary heat flux vector constant with respect to $\mathbf{x}$, the normal component of the heat flux $q_n = \boldsymbol{q} \cdot \mathbf{n}$ at all points on the boundary is fixed:

$$\forall \mathbf{x} \in \partial\Omega, \quad q_n = \boldsymbol{F_0} \cdot \mathbf{n} \tag{12}$$

These conditions can be applied to computational domains of any geometry, and lead to: $\langle \boldsymbol{q} \rangle = \boldsymbol{F_0}$. Application of these boundary conditions automatically satisfies the simplified macrohomogeneity condition (11).

Uniform temperature gradient (UTG). Denoting $\boldsymbol{G_0}$ an arbitrary temperature gradient vector constant with respect to $\mathbf{x}$, the temperature θ at all points on the boundary is fixed:

$$\forall \mathbf{x} \in \partial\Omega, \quad \theta = \boldsymbol{G_0} \cdot \mathbf{x} \tag{13}$$

As with the UHF, these conditions can be applied to computational domains of any geometry, and lead to: $\langle \boldsymbol{\nabla}\theta \rangle = \boldsymbol{G_0}$. Application of these boundary conditions also automatically satisfies the simplified macrohomogeneity condition (11).

Periodic boundary conditions (PBC). These conditions are based on splitting the temperature field over the entire domain into $\theta = \boldsymbol{G_0} \cdot \mathbf{x} + \tilde{\theta}$, and imposing the periodicity on $\tilde{\theta}$ (which represents the fluctuations due to the heterogeneities). In practice, for cuboidal domains, the boundary temperature is specified as:

$$\forall \{\mathbf{x}^+, \mathbf{x}^-\} \in \partial\Omega, \quad \theta(\mathbf{x}^+) = \theta(\mathbf{x}^-) + \boldsymbol{G_0} \cdot (\mathbf{x}^+ - \mathbf{x}^-) \tag{14}$$

where $\mathbf{x}^+$ and $\mathbf{x}^-$ are two homologous points on the boundary $\partial\Omega$, i.e., one point is obtained by projecting the other along the normal vector onto the opposite face. If a variational approach such as the finite element method is used to resolve the temperature and heat flux fields within the domain, application of the PBC automatically results in antiperiodic normal heat fluxes ($q_n(\mathbf{x}^+) = -q_n(\mathbf{x}^-)$) on the boundary [41]. If that is not the case, this needs to be specified as an additional constraint (e.g., in [14]).

Application of the PBC also automatically satisfies the simplified macrohomogeneity condition (11). The PBC as defined do not explicitly impose any restriction (e.g, periodicity) on the geometry of the computational domain [19]. However, their use on non-periodic microstructures such as real foam models reconstructed with X-ray tomography could lead to errors in the computed ATC [30].

3.2.2. Mixed boundary conditions and validity criteria

Unlike uniform and periodic boundary conditions, mixed boundary conditions (MBC) do not generally satisfy the macrohomogenity condition (equation (11)), and are thus rarely considered within the computational homogenization framework. In this subsection, the validity of a set of MBC commonly encountered in past work on porous media [1, 2, 13, 31] and sporadically used in computational homogenization [21, 24] is analysed with respect to the macrohomogeneity condition.

Definition of the MBC. Consider a cuboidal domain Ω centered at the origin of the Cartesian frame, with boundary normal vectors $\mathbf{n}$ aligned to the Cartesian axes $\{\boldsymbol{e}_1, \boldsymbol{e}_2, \boldsymbol{e}_3\}$ (see Figure 6). The lengths of the cuboid along the $\boldsymbol{e}_1$, $\boldsymbol{e}_2$ and $\boldsymbol{e}_3$ directions are denoted L_1, L_2 and L_3 respectively. Assuming $\boldsymbol{G_0} = G_0\boldsymbol{e}_1$, the MBC are defined as follows (the cases with $\boldsymbol{e}_1$ replaced by $\boldsymbol{e}_2$ and $\boldsymbol{e}_3$ are obtained trivially by index permutation):

$$\forall \mathbf{x} \in \partial\Omega, \quad \begin{cases} \theta = \boldsymbol{G_0} \cdot \mathbf{x} = G_0 x_1 & \text{if} \quad \mathbf{n} \parallel \boldsymbol{G_0} \\ q_n = 0 & \text{if} \quad \mathbf{n} \perp \boldsymbol{G_0} \end{cases} \tag{15}$$

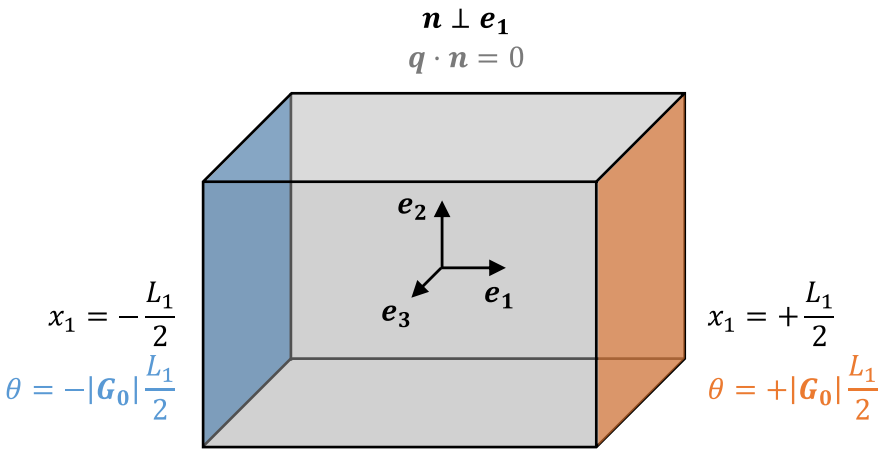

Figure 6: Schema of the mixed boundary conditions (MBC) applied to a cuboidal domain.

To simplify the expressions for the macroscopic fields, the following notations are defined:

$$\forall j \in \{1,2,3\}, \quad \begin{cases} \partial\Omega_j^+ = \left\{\mathbf{x} \in \partial\Omega \mid \mathbf{n} = +\boldsymbol{e}_j\right\} \\ \partial\Omega_j^- = \left\{\mathbf{x} \in \partial\Omega \mid \mathbf{n} = -\boldsymbol{e}_j\right\} \\ \partial\Omega_j = \partial\Omega_j^+ \cup \partial\Omega_j^- \end{cases} \tag{16}$$

The macroscopic fields are obtained by directly applying their definitions in boundary integral form (equations (A.3) to (A.5) in Appendix A). The macroscopic heat flux vector is expressed as:

$$[\boldsymbol{F}] = \begin{bmatrix} F_1 = \dfrac{1}{V}\left(\displaystyle\int_{\partial\Omega_1^+} q_1 \frac{L_1}{2}\,\mathrm{d}x_2\,\mathrm{d}x_3 - \int_{\partial\Omega_1^-} q_1\left(-\frac{L_1}{2}\right)\mathrm{d}x_2\,\mathrm{d}x_3\right) \\ F_2 = \dfrac{1}{V}\left(\displaystyle\int_{\partial\Omega_1^+} q_1 x_2\,\mathrm{d}x_2\,\mathrm{d}x_3 - \int_{\partial\Omega_1^-} q_1 x_2\,\mathrm{d}x_2\,\mathrm{d}x_3\right) \\ F_3 = \dfrac{1}{V}\left(\displaystyle\int_{\partial\Omega_1^+} q_1 x_3\,\mathrm{d}x_2\,\mathrm{d}x_3 - \int_{\partial\Omega_1^-} q_1 x_3\,\mathrm{d}x_2\,\mathrm{d}x_3\right) \end{bmatrix} \tag{17}$$

The macroscopic temperature gradient is expressed as:

$$[\boldsymbol{G}] = \begin{bmatrix} G_1 = \dfrac{G_0}{V}\left(\displaystyle\int_{\partial\Omega_1^+} \frac{L_1}{2}\,\mathrm{d}x_2\,\mathrm{d}x_3 - \int_{\partial\Omega_1^-}\left(-\frac{L_1}{2}\right)\mathrm{d}x_2\,\mathrm{d}x_3\right) = G_0 \\ G_2 = \dfrac{1}{V}\left(\displaystyle\int_{\partial\Omega_2^+} \theta\,\mathrm{d}x_1\,\mathrm{d}x_3 - \int_{\partial\Omega_2^-}\theta\,\mathrm{d}x_1\,\mathrm{d}x_3\right) \\ G_3 = \dfrac{1}{V}\left(\displaystyle\int_{\partial\Omega_3^+} \theta\,\mathrm{d}x_1\,\mathrm{d}x_2 - \int_{\partial\Omega_3^-}\theta\,\mathrm{d}x_1\,\mathrm{d}x_2\right) \end{bmatrix} \tag{18}$$

The macroscopic specific entropy production rate is expressed as:

$$\langle \boldsymbol{q}\cdot\boldsymbol{\nabla}\theta\rangle = \frac{G_0}{V}\left(\int_{\partial\Omega_1^+} q_1\frac{L_1}{2}\,\mathrm{d}x_2\,\mathrm{d}x_3 - \int_{\partial\Omega_1^-} q_1\left(-\frac{L_1}{2}\right)\mathrm{d}x_2\,\mathrm{d}x_3\right) = F_1G_1 \tag{19}$$

Validity criteria. Recall that the MBC do not necessarily satisfy the macrohomogeneity condition given in equation (11), which based on equations (17) to (19) can be rewritten as:

$$\boldsymbol{F}\cdot\boldsymbol{G} - \langle \boldsymbol{q}\cdot\boldsymbol{\nabla}\theta\rangle = 0 \quad\Longleftrightarrow\quad F_2G_2 + F_3G_3 = 0 \tag{20}$$

While equation (20) can be systematically verified *a posteriori*, it is often desirable to be able to deduce *a priori* if the macrohomogeneity condition is satisfied based on the given microstructure. To begin with, one may observe that a sufficient condition for equation (20) to be satisfied is if the mean temperature difference between any two pairs of opposite lateral faces are zero, which from equation (18) gives:

$$G_2 = G_3 = 0 \tag{21}$$

Equation (21) is hereafter called the sufficient condition for macrohomogeneity of the MBC. For non-periodic foam structures, it can be postulated that if the pores are distributed in space in a statistically homogeneous manner, the macroscopic temperature gradient will deviate little from the $\boldsymbol{e}_1$ direction: the temperature fields on opposite lateral faces will then be similar, i.e., the sufficient condition (21) will be satisfied. This postulate will be confirmed by numerical modeling on real and virtual microstructures in subsection 5.4.

Note also that if condition (21) holds, the expression for k_{11}^{app} is consistent with the scalar $k_{1\mathrm{D}}$ in equation (1) computed with the 1D simplification to Fourier's law:

$$G_2 = G_3 = 0 \Longrightarrow \quad k_{11}^{\mathrm{app}} = -\frac{F_1}{G_1} = -\underbrace{\frac{L_1}{V}}_{1/A}\underbrace{\frac{1}{2}\left(\int_{\partial\Omega_1} q_1\,\mathrm{d}x_2\,\mathrm{d}x_3\right)}_{Q}\underbrace{\frac{1}{G_0}}_{\Delta L/\Delta\theta} \tag{22}$$

This alone by no means implies that $\boldsymbol{k}_{\mathrm{app}}$ is orthotropic, since F_2 and F_3 are not necessarily zero.

3.3. Influence of boundary conditions on the apparent thermal conductivity

If the computational domain chosen for the micro-scale problem is a representative volume element (RVE) of the foam material, the apparent thermal conductivity (ATC, $\boldsymbol{k}_{\text{app}}$) should then be equal to the effective thermal conductivity (ETC, $\boldsymbol{k}_{\text{eff}}$) under any set of boundary conditions satisfying the macrohomogeneity condition. However, as the RVE may be prohibitively large for real porous media, it is often necessary to estimate the ETC from smaller, non-representative computational domains. As such, the ATC may vary greatly depending on the boundary conditions used due to edge effects [20, 21, 24].

For foam domains Ω smaller than the RVE, the values of $\boldsymbol{k}_{\text{app}}$ under different boundary conditions are compared analytically using the maximum entropy principle [39] presented in section 3.1.2. The uniform heat flux (UHF), uniform temperature gradient (UTG), periodic (PBC) and mixed (MBC) boundary conditions presented in subsection 3.2 are considered. The objective is to establish order relations between the four values of $\boldsymbol{k}_{\text{app}}$. As the thermal conductivity tensor is necessarily positive semi-definite [40], any two thermal conductivity tensors $\boldsymbol{k}_A$ and $\boldsymbol{k}_B$ may be compared based on their quadratic form:

$$\begin{aligned} \boldsymbol{k}_A \leq \boldsymbol{k}_B \quad &\equiv \quad (\boldsymbol{k}_A \cdot \boldsymbol{G_0}) \cdot \boldsymbol{G_0} \;\leq\; (\boldsymbol{k}_B \cdot \boldsymbol{G_0}) \cdot \boldsymbol{G_0} \qquad \forall \boldsymbol{G_0} \\ &\equiv \quad \boldsymbol{F_0} \cdot \left(\boldsymbol{k}_A^{-1} \cdot \boldsymbol{F_0}\right) \;\geq\; \boldsymbol{F_0} \cdot \left(\boldsymbol{k}_B^{-1} \cdot \boldsymbol{F_0}\right) \qquad \forall \boldsymbol{F_0} \end{aligned} \tag{23}$$

The discussion is hereinafter restricted to cuboidal domains Ω comprised between points $-[L_1\ L_2\ L_3]/2$ and $+[L_1\ L_2\ L_3]/2$ in the Cartesian frame $\{\boldsymbol{e}_1, \boldsymbol{e}_2, \boldsymbol{e}_3\}$, as illustrated in Figure 6, with the arbitrary heat flux and temperature gradient vectors $\boldsymbol{F_0} = F_0\boldsymbol{e}_1$ and $\boldsymbol{G_0} = G_0\boldsymbol{e}_1$ (the cases with $\boldsymbol{e}_1$ replaced with $\boldsymbol{e}_2$ and $\boldsymbol{e}_3$ can be obtained trivially by index permutation). The same reference temperature T_0 is adopted for all four boundary value problems. It is first assumed that application of the MBC satisfies the macrohomogeneity condition (20) (but not necessarily condition (21), the sufficient condition for macrohomogeneity).

3.3.1. Known order relations

Key results from the literature [17, 19, 22, 24, 42] are summarized below, with complete demonstrations included in Appendix B. These are based on the observation that any heat flux $\boldsymbol{q}$ defined over Ω is an admissible solution heat flux field to the UTG problem, since no boundary heat fluxes are prescribed ($\partial\Omega_q = \emptyset$). Conversely, any temperature θ defined over Ω is an admissible solution temperature field to the UHF problem since no boundary temperatures are defined ($\partial\Omega_\theta = \emptyset$). The maximum entropy principle (5) and its complementary statement (6) then give:

$$\forall \boldsymbol{q}, \quad \mathcal{S}^{\text{UTG}}(\boldsymbol{q}) \;\leq\; \mathcal{S}^{\text{UTG}}(\boldsymbol{q}^{\text{UTG}}) \tag{24a}$$

$$\forall \theta, \quad \mathcal{S}_c^{\text{UHF}}(\theta) \;\leq\; \mathcal{S}_c^{\text{UHF}}(\theta^{\text{UHF}}) \tag{24b}$$

Firstly, considering the true solutions to the PBC problem $\boldsymbol{q}^{\text{PBC}}$ and θ^{PBC} as admissible solutions to the UTG and UHF problems respectively, equations (24) gives a well-known result [17, 19, 24]

the demonstration of which is found in Appendix B:

$$\begin{cases} \mathcal{S}^{\mathrm{UTG}}(\boldsymbol{q}^{\mathrm{PBC}}) \leq \mathcal{S}^{\mathrm{UTG}}(\boldsymbol{q}^{\mathrm{UTG}}) \\ \mathcal{S}_c^{\mathrm{UHF}}(\theta^{\mathrm{PBC}}) \leq \mathcal{S}_c^{\mathrm{UHF}}(\theta^{\mathrm{UHF}}) \end{cases} \iff \boldsymbol{k}_{\mathrm{app}}^{\mathrm{UHF}} \leq \boldsymbol{k}_{\mathrm{app}}^{\mathrm{PBC}} \leq \boldsymbol{k}_{\mathrm{app}}^{\mathrm{UTG}} \tag{25}$$

Secondly, considering the true solutions to the MBC problem $\boldsymbol{q}^{\mathrm{MBC}}$ and θ^{MBC} as admissible solutions to the UTG and UHF problems respectively, a development based on the work of Hazanov and Huet [42] gives the following result, which is also demonstrated in Appendix B:

$$\begin{cases} \mathcal{S}^{\mathrm{UTG}}(\boldsymbol{q}^{\mathrm{MBC}}) \leq \mathcal{S}^{\mathrm{UTG}}(\boldsymbol{q}^{\mathrm{UTG}}) \\ \mathcal{S}_c^{\mathrm{UHF}}(\theta^{\mathrm{MBC}}) \leq \mathcal{S}_c^{\mathrm{UHF}}(\theta^{\mathrm{UHF}}) \end{cases} \iff \boldsymbol{k}_{\mathrm{app}}^{\mathrm{UHF}} \leq \boldsymbol{k}_{\mathrm{app}}^{\mathrm{MBC}} \leq \boldsymbol{k}_{\mathrm{app}}^{\mathrm{UTG}} \tag{26}$$

Since $\boldsymbol{k}_{\mathrm{app}}^{\mathrm{UHF}} = \boldsymbol{k}_{\mathrm{eff}} = \boldsymbol{k}_{\mathrm{app}}^{\mathrm{UTG}}$ when $V \to \infty$ according to Hill [22], the following relation necessarily holds for sufficiently large volumes:

$$\boldsymbol{k}_{\mathrm{app}}^{\mathrm{UHF}} \leq \boldsymbol{k}_{\mathrm{eff}} \leq \boldsymbol{k}_{\mathrm{app}}^{\mathrm{UTG}} \tag{27}$$

In summary, the existing literature agrees that the UTG and UHF yield upper- and lower-bound estimates respectively for $\boldsymbol{k}_{\mathrm{eff}}$, and for any given domain size, the PBC and MBC (assuming the macrohomogeneity condition (20) holds for the latter) provide equally good if not better estimates. However, no direct theoretical comparison has been made between the estimates obtained with the PBC and MBC, a gap which will be addressed presently.

3.3.2. Comparison between mixed and periodic boundary conditions

Assume for the purpose of the present demonstration that there exists a cubioidal domain Ω that, when subjected to the PBC, gives zero normal heat fluxes on the lateral faces (for foam geometries, this premise is in fact more general than it may seem at first glance, as will be explained following the demonstration). For the considered microstructure, $\boldsymbol{q}^{\mathrm{PBC}}$ is thus an admissible solution heat flux to the MBC problem, and one may write:

$$\begin{aligned} & \mathcal{S}^{\mathrm{MBC}}(\boldsymbol{q}^{\mathrm{PBC}}) \leq \mathcal{S}^{\mathrm{MBC}}(\boldsymbol{q}^{\mathrm{MBC}}) \\ \iff \quad & -\int_{\partial\Omega_1} (\boldsymbol{q}^{\mathrm{PBC}} \cdot \mathbf{n})(\boldsymbol{G_0} \cdot \mathbf{x}) \, \mathrm{d}A - \frac{V}{2} \langle \boldsymbol{q} \rangle^{\mathrm{PBC}} \cdot \left((\boldsymbol{k}_{\mathrm{app}}^{\mathrm{PBC}})^{-1} \cdot \langle \boldsymbol{q} \rangle^{\mathrm{PBC}} \right) \\ & \qquad \leq -\int_{\partial\Omega_1} (\boldsymbol{q}^{\mathrm{MBC}} \cdot \mathbf{n})(\boldsymbol{G_0} \cdot \mathbf{x}) \, \mathrm{d}A - \frac{V}{2} \langle \boldsymbol{q} \rangle^{\mathrm{MBC}} \cdot \left((\boldsymbol{k}_{\mathrm{app}}^{\mathrm{MBC}})^{-1} \cdot \langle \boldsymbol{q} \rangle^{\mathrm{MBC}} \right) \\ \iff \quad & -V \langle \boldsymbol{q} \rangle^{\mathrm{PBC}} \cdot \boldsymbol{G_0} + \frac{V}{2} \langle \boldsymbol{q} \rangle^{\mathrm{PBC}} \cdot \langle \boldsymbol{\nabla} \theta \rangle^{\mathrm{PBC}} \\ & \qquad \leq -V \langle \boldsymbol{q} \rangle^{\mathrm{MBC}} \cdot \boldsymbol{G_0} + \frac{V}{2} \langle \boldsymbol{q} \rangle^{\mathrm{MBC}} \cdot \langle \boldsymbol{\nabla} \theta \rangle^{\mathrm{MBC}} \end{aligned} \tag{28}$$

Assuming now that the sufficient condition for macrohomogeneity (21) holds for the MBC, i.e., $\langle \boldsymbol{\nabla} \theta \rangle^{\mathrm{MBC}} = \boldsymbol{G_0}$, and substituting $\langle \boldsymbol{q} \rangle = -\boldsymbol{k}_{\mathrm{app}} \cdot \langle \boldsymbol{\nabla} \theta \rangle$, the following inequality is obtained from

equation (28):

$$\begin{aligned} -\frac{V}{2}\langle \boldsymbol{q} \rangle^{\mathrm{PBC}} \cdot \boldsymbol{G_0} &\leq -\frac{V}{2}\langle \boldsymbol{q} \rangle^{\mathrm{MBC}} \cdot \boldsymbol{G_0} \\ \iff \quad \left(\boldsymbol{k}_{\mathrm{app}}^{\mathrm{PBC}} \cdot \boldsymbol{G_0}\right) \cdot \boldsymbol{G_0} &\leq \left(\boldsymbol{k}_{\mathrm{app}}^{\mathrm{MBC}} \cdot \boldsymbol{G_0}\right) \cdot \boldsymbol{G_0} \\ \iff \quad \boldsymbol{k}_{\mathrm{app}}^{\mathrm{PBC}} &\leq \boldsymbol{k}_{\mathrm{app}}^{\mathrm{MBC}} \end{aligned} \tag{29}$$

The premise of zero normal heat fluxes on the lateral faces ($q_n^{\mathrm{PBC}} = 0$ where $\mathbf{n} \perp \boldsymbol{G_0}$) required for equations (28) and (29) to hold can in fact be generalized to most types of foam geometries considered. It is trivially met for periodic microstructures for which the lateral boundaries are symmetry planes (e.g., unit cells such as in [24]). For non-periodic highly porous foam geometries, the following postulate can be offered: under the PBC, as q_n^{PBC} is anti-periodic, only opposite pairs of boundary points that both belong to the solid phase would have non-zero heat fluxes (in porous media, near-zero heat fluxes are found at points on the boundary where the pore phase is present and where the heat flux is not specified [24]). With increasing porosity, the rate of occurrence of such points decreases sharply, reducing the normal heat flux to zero everywhere on the lateral faces (save eventually for a few points).

In summary, for periodic geometries with boundary faces as symmetry planes and non-periodic foam models with sufficiently high boundary mismatch, the premise $q_n^{\mathrm{PBC}} = 0$ where $\mathbf{n} \perp \boldsymbol{G_0}$ should hold. These postulates will be examined through the numerical case studies (sections 5.2 and 5.4).

Combining equation (29) with the inequalities in equations (25) and (26) gives:

$$\boldsymbol{k}_{\mathrm{app}}^{\mathrm{UHF}} \leq \boldsymbol{k}_{\mathrm{app}}^{\mathrm{PBC}} \leq \boldsymbol{k}_{\mathrm{app}}^{\mathrm{MBC}} \leq \boldsymbol{k}_{\mathrm{app}}^{\mathrm{UTG}} \tag{30}$$

While $\boldsymbol{k}_{\mathrm{app}}^{\mathrm{PBC}}$ is equal to the effective thermal conductivity $\boldsymbol{k}_{\mathrm{eff}}$ in the case of periodic geometries, no rigorous ETC solution is available for non-periodic geometries, for which $\boldsymbol{k}_{\mathrm{app}}^{\mathrm{PBC}}$ and $\boldsymbol{k}_{\mathrm{app}}^{\mathrm{MBC}}$ can only be considered the best possible estimates of $\boldsymbol{k}_{\mathrm{eff}}$. One key goal of the numerical studies presented in the subsequent sections is to ascertain which of the two are more appropriate for the different types of foam geometries considered.

4. Numerical methods

Finite element modeling was performed on the different types of cubic foam geometries ($L_1 = L_2 = L_3 = L$) described in section 2 with two key goals:

- to investigate the validity, accuracy and precision of the effective thermal conductivity (ETC, $\boldsymbol{k}_{\mathrm{eff}}$) estimated with the apparent thermal conductivity (ATC, $\boldsymbol{k}_{\mathrm{app}}$) under different boundary conditions on foam geometries smaller than the representative volume element (RVE), and
- to verify the theoretical postulates of section 3 pertaining to the validity of the mixed boundary conditions (MBC) and to the comparison of its result and that obtained under periodic boundary conditions (PBC).

The finite element modeling procedure is described in subsection 4.1. The quantities of interest during post-processing (notably the concepts of validity, accuracy, and precision) are defined in

subsection 4.2. The precision of the estimated ETC for random microstructures can be evaluated with a statistical treatment based on the integral range [20], detailed in section 4.3.

4.1. Finite element modeling procedure

Initially represented in binary voxel format of equal voxel size (8.75 µm), the different cubic geometries were fully meshed with linear (P1) brick elements with a mesh density of one element per voxel (see Figure 7(a)); it was verified that further mesh refinement did not modify the computed ATC value by more than 1.6% on average. Each element was attributed a constant isotropic thermal conductivity corresponding to that of sintered alumina [43] or air [44] at a reference temperature $T_0 = 298$ K. The contrast between the solid and pore phase conductivities (k_s and k_p respectively) is indeed very high: $k_s/k_p = 539$.

Finite element modeling of 3D steady-state heat transfer over the entire computational domain was performed using the preconditioned Krylov-based iterative solver of Abaqus/Standard 2017 [45]. The governing variational statement of the finite element method [41, 45, 46] is mathematically equivalent to the maximum entropy principle [39] presented in section 3.1.2. From the computed temperature and heat flux fields (see example in Figures 7(b)–(c)), the mean temperature gradient, heat flux, and specific entropy production rate were calculated based on their respective definitions in Appendix A.

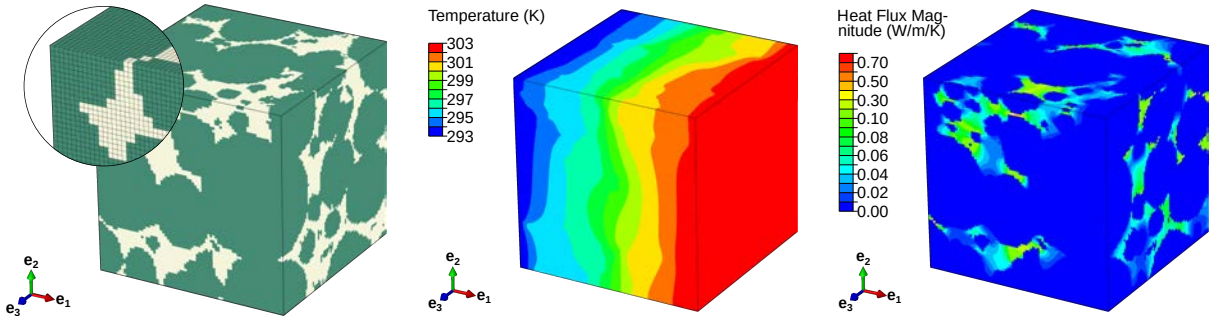

(a) Geometry and mesh. (b) Absolute temperature T. (c) Heat flux magnitude $|\boldsymbol{q}|$.

Figure 7: Application of the mixed boundary condition (MBC) on a 1.35 mm × 1.35 mm × 1.35 mm reconstructed foam model meshed with 3.65 million (154^3) elements. The $\partial\Omega_1^+$, $\partial\Omega_2^+$, and $\partial\Omega_3^+$ faces are shown.

To solve for $\boldsymbol{k}_{\text{app}}$, three orthogonal configurations were solved for each boundary value problem, i.e., the directions of $\boldsymbol{G_0} = G_0\boldsymbol{e_j}$ or $\boldsymbol{F_0} = F_0\boldsymbol{e_j}$ were permuted for $j \in \{1, 2, 3\}$. As equation (9) gives three equations linking $\boldsymbol{F} \equiv \langle \boldsymbol{q} \rangle$ and $\boldsymbol{G} \equiv \langle \boldsymbol{\nabla}\theta \rangle$ for each configuration, nine equations were thus obtained to solve for the nine unknowns in $\boldsymbol{k}_{\text{app}}$. With MPI-based parallelization on a quad-core processor with a clock speed of 2.20 GHz, computation of the complete ATC tensor for a domain with 8 million elements took approximately three hours, half of which was spent on post-processing.

4.2. Quantities of interest during post-processing

For each set of boundary conditions and each type of microstructure, four aspects of the computed ATC are studied:

Validity with respect to the macrohomogeneity condition. As small temperature variations are considered, the macrohomogeneity condition (11) should be satisfied by each set of boundary conditions used for the resulting ATC to be considered valid. An "entropy residual" r_S can be defined as follows:

$$r_S = \sqrt{\frac{1}{3}\sum_{j=1}^{3}\left(\frac{\langle \boldsymbol{q}\cdot\boldsymbol{\nabla}\theta\rangle - \boldsymbol{F}\cdot\boldsymbol{G}}{\boldsymbol{F}\cdot\boldsymbol{G}}\right)^2_{\boldsymbol{G_0}\|\boldsymbol{e_j}}} \tag{31}$$

A zero value of r_S means that the macrohomogeneity condition (11) is satisfied, i.e., the specific entropy production rate is consistent between the micro- and macro-scales.

Diagonalizability. Eigendecomposition of the ATC was performed to identify the principal directions of orthotropy (if they exist) and the ATC along these directions. Consider a cubic domain aligned to the Cartesian frame in which the ATC matrix $[\boldsymbol{k}_{\text{app}}]$ is computed. If the thermal conductivity of the underlying material is indeed orthotropic in another reference frame rotated with respect to the Cartesian frame by a matrix $[R]$, then $[\boldsymbol{k}_{\text{app}}]$ is diagonalizable and the diagonalized ATC matrix $[\boldsymbol{k}^D_{\text{app}}]$ can be written as:

$$\left[\boldsymbol{k}^D_{\text{app}}\right] = [R]^{-1}\left[\boldsymbol{k}_{\text{app}}\right][R] \quad \text{with} \quad \left[\boldsymbol{k}^D_{\text{app}}\right] = \begin{bmatrix} k_{\text{I}}^{\text{app}} & 0 & 0 \\ 0 & k_{\text{II}}^{\text{app}} & 0 \\ 0 & 0 & k_{\text{III}}^{\text{app}} \end{bmatrix} \tag{32}$$

where $k_{\text{I}}^{\text{app}}$, $k_{\text{II}}^{\text{app}}$ and $k_{\text{III}}^{\text{app}}$ are the real eigenvalues of $[\boldsymbol{k}_{\text{app}}]$, and the columns of $[R]$ are the corresponding eigenvectors.

Accuracy. For periodic geometries, the ATC obtained through application of the PBC is the reference ETC ($\boldsymbol{k}^{\text{PBC}}_{\text{app}} = \boldsymbol{k}_{\text{eff}}$), and was used to evaluate the accuracy of those obtained under the other boundary conditions (UHF, UTG, MBC). For non-periodic geometries, no rigorous reference ETC can be obtained in general, if convergence of the UHF and UTG bounds is not achieved.

Precision. While deterministic effective properties exist for regular geometries, for random microstructures, the variation between the ATC may not vanish even when the computational domain is extremely large. The ETC was therefore estimated using the stochastic mean ATC $\langle\langle \boldsymbol{k}_{\text{app}}\rangle\rangle$ of different samples of the material (or realizations, if digitally generated virtual geometries are considered). With N independent samples of equal volume V, the precision ϵ of the ij term of the mean ATC matrix was evaluated from the standard error [20]:

$$\epsilon = \frac{2\sigma_k}{\langle\langle k_{ij}^{\text{app}}\rangle\rangle\sqrt{N}} \tag{33}$$

where σ_k is the standard deviation of the ATC, which generally decreases with increasing V. To achieve a given precision ϵ, one may either work with a large number of small samples, or a small number of large samples.

4.3. Statistical treatment based on the integral range

In random foams of arbitrary size, the interplay between the variance of the ATC and sample volume depends not only on the regularity of the microstructure, but also on the type of property considered, the phase contrast, and the boundary conditions. To account for their influence, Kanit et al. [20] proposed the following power law model for the ATC variance σ_k^2:

$$\sigma_k^2 = f_p\left(1-f_p\right)\left(k_s-k_p\right)^2\left(\frac{J_k}{V}\right)^{\alpha} \quad \text{for} \quad V \gg J_k \tag{34}$$

where k_s and k_p are the conductivities of the solid and pore phases respectively, α is the power law exponent, and J_k is the integral range which can be interpreted as the scale of the phenomenon, V being the scale of observation. In practice, for a given set of boundary conditions and microstructure, J_k and α are estimated by first computing σ_k for a few different values of V, then performing a power law regression.

With equations (33) and (34), it is then possible to evaluate the precision ϵ of the estimated ETC even if computation of the standard deviation is impossible (e.g., when an insufficient number of samples are available). Alternatively, one may also define a target precision ϵ_0, and estimate the associated "statistical RVE size" as $V(\epsilon_0, N = 1)$.

It is important to note that application of the statistical treatment only accounts for the scatter due to the random microstructure; when working with geometries of sub-RVE sizes, due to edge effects, inaccuracies in the ETC estimate may still exist depending on the chosen boundary conditions.

5. Results and Discussion

The apparent thermal conductivity (ATC, $\boldsymbol{k}_{\text{app}}$) of three types of foam geometries are computed under four sets of boundary conditions: uniform heat flux (UHF), uniform temperature gradient (UTG), periodic (PBC) and mixed (MBC) boundary conditions. While a deterministic value of the effective thermal conductivity (ETC, $\boldsymbol{k}_{\text{eff}}$) intrinsic to the entire medium may be computed for regular periodic microstructures, for random microstructures, the mean ATC of several realizations was used as an estimate of the ETC.

Specific results corresponding to each type of foam geometry are first presented:

- Subsection 5.1 describes a preliminary study on unit cell-based geometries that highlights the effect of geometrical non-periodicity on the accuracy of the estimated ETC;
- Subsection 5.2 describes a study of the effect of random porosity on the accuracy of the ETC estimated under different boundary conditions in the case of periodic virtual foams;
- Subsection 5.3 describes a study of the accuracy and precision of the ETC estimated under different boundary conditions on non-periodic tomography-reconstructed real foams.

Last but not least, the theoretical postulates in section 3 pertaining to the validity of the MBC as well as the order relation between the MBC and PBC results are verified in subsection 5.4.

As was commonly done for porous media, the results were given in terms of the normalized ATC $\boldsymbol{k}_{\text{app}}/k_s$, which is generally only dependent on the microstructure and independent of the base

material properties due to the high phase contrast [6], allowing the discussion hereafter to be generalized to all foams of similar morphology whatever the base material.

Where appropriate, the results are compared to several well-known analytical models: the series and parallel models, also known as the Wiener or Voigt-Reuss bounds of the ETC of arbitrary mixtures; the Maxwell-Eucken models, also known as the Hashin-Shtrikman bounds for isotropic mixtures; and a power law solution to the "asymmetric" Bruggeman approximation for spherical inclusions of negligible conductivity, commonly named after Archie [47]. A thorough review of analytical models applicable to porous ceramics can be found in references [6] and [7].

5.1. Study on unit cell-based geometries: effect of geometrical non-periodicity

The ATC of the reference orthotropic unit cell (Figure 4(c)) was first calculated using different boundary conditions. Regardless of the boundary conditions used, the ATC matrix was indeed diagonal as expected. Results for two different tessellation sizes are shown in Figure 8. Larger tessellations were not considered to keep the size of the computational domain representative of typical reconstructed foam models.

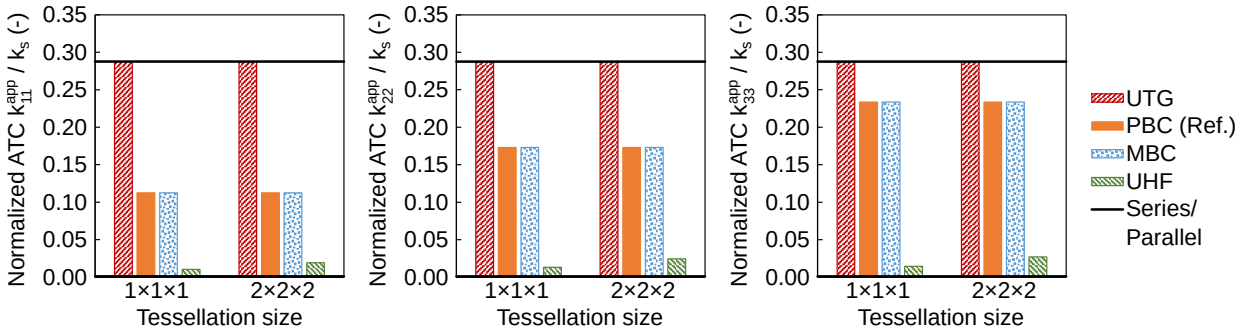

Figure 8: Diagonal values of the apparent thermal conductivity (ATC) matrix computed for two tessellations of the orthotropic unit cell with the uniform heat flux (UHF), uniform temperature gradient (UTG), periodic (PBC), and mixed (MBC) boundary conditions. The bounds given by the series and parallel models are also included; the lower bound (series model) is extremely close to zero.

As the geometry is periodic, the PBC result on a single unit cell directly gives the reference ETC of the whole medium. The conclusions regarding the other boundary conditions were in line with past findings [17, 20, 24]. The UHF and UTG provided lower- and upper-bound estimates of the ETC respectively; however the large difference between the bounds and their extremely slow size convergence due to the large phase contrast render their use impractical, and demonstrate that the RVE as defined by Hill [22] would be prohibitively large. Notably, the UTG result coincides exactly with the parallel model (upper Wiener bound) and seems insensitive to material orthotropy, a recurring observation in the following subsections. Similar to the results of Jiang et al. [24], the ATC of the orthotropic unit cell computed with the MBC is identical to that of the PBC within numerical accuracy.

With a $2 \times 2 \times 2$ tessellation of the orthotropic unit cell as the reference, two non-periodic, anisotropic geometries of the same volume are then created: a "low anisotropy" case through rotating the base material with respect to the Cartesian frame by 45° about the [0 0 1] axis, and a "high anisotropy" case by a rotation of 57.1° about the [–0.13 0.38 0.92] axis. As mentioned

in subsection 2.4, the diagonalized ATC matrices of all three geometries should be equal, i.e., they should have the same eigenvalues (equation (32)). Table 2 lists the eigenvalues of the ATC obtained with the PBC and MBC for the different anisotropic cases, and their mean errors with respect to those of the ETC matrix of the orthotropic unit cell calculated with the PBC.

Type of geometry	Normalized ATC matrix $[\boldsymbol{k}_{\text{app}}/k_s]$	Eigenvalues	Mean error
Reference:			
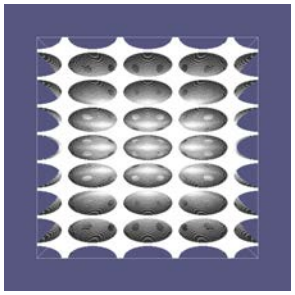	PBC: $\begin{bmatrix} 0.112 & 0 & 0 \\ 0 & 0.173 & 0 \\ 0 & 0 & 0.234 \end{bmatrix}$	$\begin{Bmatrix} 0.112 \\ 0.173 \\ 0.234 \end{Bmatrix}$	Ref.
	MBC: $\begin{bmatrix} 0.112 & 0 & 0 \\ 0 & 0.173 & 0 \\ 0 & 0 & 0.234 \end{bmatrix}$	$\begin{Bmatrix} 0.112 \\ 0.173 \\ 0.234 \end{Bmatrix}$	0.0%
Low anisotropy:			
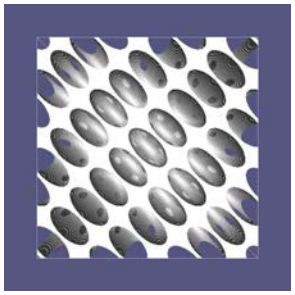	PBC: $\begin{bmatrix} 0.126 & -0.016 & 0 \\ -0.016 & 0.126 & 0 \\ 0 & 0 & 0.231 \end{bmatrix}$	$\begin{Bmatrix} 0.110 \\ 0.142 \\ 0.231 \end{Bmatrix}$	–7.3%
	MBC: $\begin{bmatrix} 0.141 & -0.030 & 0 \\ -0.030 & 0.141 & 0 \\ 0 & 0 & 0.230 \end{bmatrix}$	$\begin{Bmatrix} 0.111 \\ 0.171 \\ 0.230 \end{Bmatrix}$	–1.5%
High anisotropy:			
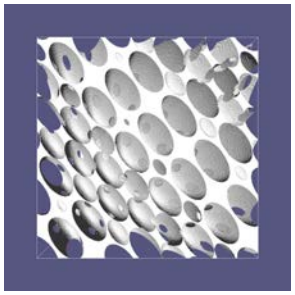	PBC: $\begin{bmatrix} 0.144 & -0.017 & 0.026 \\ -0.017 & 0.127 & 0.024 \\ 0.026 & 0.024 & 0.198 \end{bmatrix}$	$\begin{Bmatrix} 0.104 \\ 0.153 \\ 0.211 \end{Bmatrix}$	–9.5%
	MBC: $\begin{bmatrix} 0.112 & -0.020 & 0.027 \\ -0.020 & 0.136 & 0.030 \\ 0.027 & 0.030 & 0.211 \end{bmatrix}$	$\begin{Bmatrix} 0.107 \\ 0.166 \\ 0.226 \end{Bmatrix}$	–3.9%

Table 2: Normalized apparent thermal conductivity (ATC) matrices of anisotropic geometries computed with periodic (PBC) and mixed (MBC) boundary conditions, and the error of their eigenvalues relative to the reference (Ref.) values.

The negative errors show that the ETC is systematically underestimated by both the PBC and MBC due to boundary effects (linked to the zero lateral normal heat flux for the MBC, and to the geometrical mismatch for the PBC). The estimate obtained with the MBC is however significantly better than that given by the PBC, which contradicts the commonly held view that the PBC offer the best estimate for computational domains of sub-RVE sizes. This can be explained by the following: assuming the sufficient condition for macrohomogeneity (20) is fulfilled, the MBC can be seen as a

relaxed form of the PBC, in which the restriction of $\tilde{\theta}(\mathbf{x}^+) = \tilde{\theta}(\mathbf{x}^-)$ (local periodicity) on the lateral faces where $\mathbf{n} \perp \boldsymbol{G_0}$ is replaced with a weaker condition of $\int \tilde{\theta}(\mathbf{x}^+)\,\mathrm{d}A = \int \tilde{\theta}(\mathbf{x}^-)\,\mathrm{d}A$ ("macroscopic periodicity"). At the same time, without the condition of anti-periodicity of q_n on the faces with $\mathbf{n} \parallel \boldsymbol{G_0}$, the flux concentration is reduced on these faces. These lead to a lower error in the ETC estimation with the MBC than with the PBC.

5.2. Study on virtual periodic foam models: effect of random porosity

Virtual periodic foam models of six different volumes ranging from $V = 2.74\,\mathrm{mm}^3$ to $V = 11.78\,\mathrm{mm}^3$ were generated with the algorithm of Cunsolo et al. [10] (see subsection 2.3) and used to investigate the effect of random porosity on the estimated ETC. For each sample, rigorous reference values for the ATC can be obtained by applying the PBC; however a scatter in the ATC between different samples still exists due to the random microstructure.

For each given volume, the mean ATC over 10 virtual foam realizations was used to estimate the ETC of the entire medium. The mean ATC matrices in the Cartesian frame computed with the PBC, MBC and UHF are diagonal, with a slight orthotropy (±9% difference between the three eigenvalues). The orthotropy is expected from the large scatter observed in the covariance range (see Table 1 in subsection 2.3). The UTG result gives an isotropic matrix with diagonal values equal to the parallel model (upper Wiener bound).

Figure 9 compares the largest eigenvalue of the mean ATC ($k_{\max}^{\mathrm{app}} = \max\left\{k_{\mathrm{I}}^{\mathrm{app}}, k_{\mathrm{II}}^{\mathrm{app}}, k_{\mathrm{III}}^{\mathrm{app}}\right\}$) computed with the four sets of boundary conditions, with the precision ϵ indicated as error bands. The precision hovers around 2% for all cases, does not significantly decrease with increasing foam

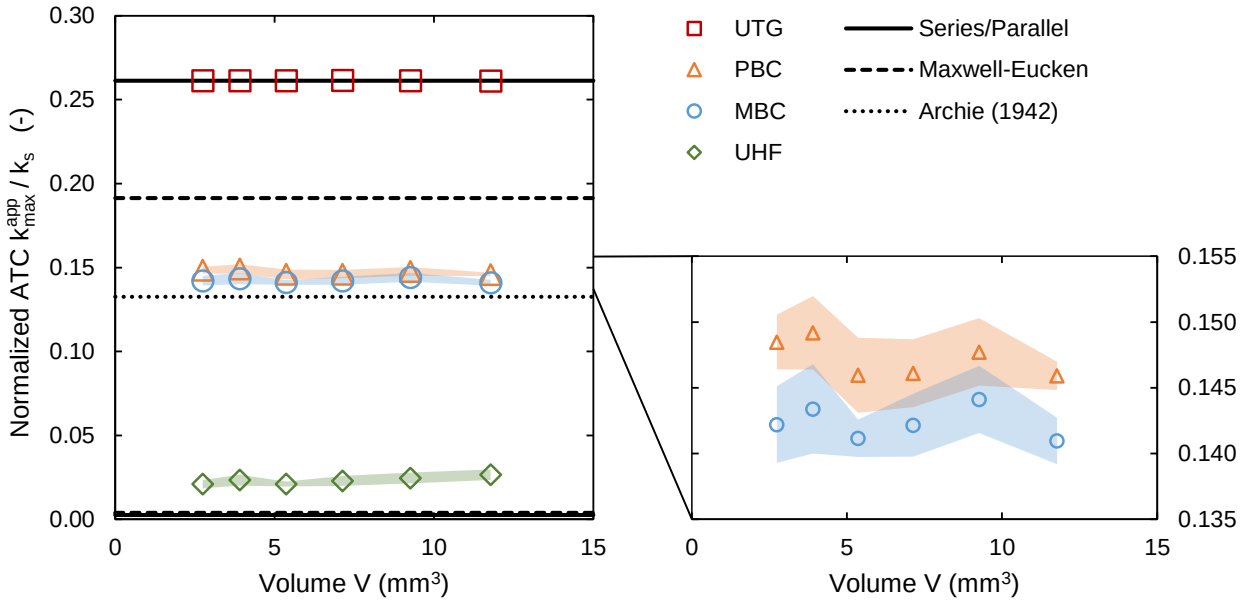

Figure 9: Mean normalized apparent thermal conductivity (ATC) of periodic virtual foams of increasing volume, under uniform heat flux (UHF), uniform temperature gradient (UTG), periodic (PBC) and mixed (MBC) boundary conditions. Comparison was shown for the largest eigenvalue of the ATC. The error bands indicate the standard error.

volume, and is only very slightly lower with the PBC than with the MBC. This is thanks to the

similarity in microstructure between the samples: the average over 10 samples of even the smallest volume ($V = 2.74\,\mathrm{mm}^3$) is sufficient to account for the random nature of the virtual foams. Further statistical treatment (e.g., with equation (34)) was thus considered unnecessary.

As the virtual foams are periodic, application of the PBC gives the reference ETC value. As with the orthotropic unit cell, the UTG and UHF yielded extremely wide and thus uninformative upper- and lower-bound estimates of the ETC. Unlike for the orthotropic unit cell, the MBC result is extremely close but systematically lower than the PBC result, which makes this type of geometry a counter-example to the order relation in equation (30). Indeed, the absence of symmetry planes due the irregularity of the pore arrangement means that the demonstration in subsection 3.3.2 does not apply to this type of microstructure.

One can thus conclude that for random periodic structures, the PBC result is unsurpassed by the MBC result, with the latter generally underestimating the ETC due to regions close to the boundary not participating in heat transfer as they would in an infinite medium. The difference between the MBC and PBC results in the present case is however very slight.

5.3. Estimation of the effective thermal conductivity of reconstructed real foams

For the tomography-reconstructed real foam models, no rigorous numerical solution of the ETC can be obtained due to the non-periodic geometry. As such, the mean ATC of non-overlapping cubic subdomains of the reconstructed foam is used as an ETC estimate. Volumes between $0.0117\,\mathrm{mm}^3$ and $11.5\,\mathrm{mm}^3$ were considered, with the number of samples for each volume recorded in Table 3. To ensure statistical independence of the samples, care was taken such that the dimensions L of the smallest subdomains remain greater than the real foam's covariance range.

Volume V (mm^3)	0.0942	0.318	0.754	1.47	2.54	6.03	11.5
Number of samples	125	125	64	64	27	8	8
Porosity f_p (%)	74 ± 9	74 ± 5	74 ± 3	74 ± 2	74 ± 1	73.8 ± 0.5	74.0 ± 0.5

Table 3: Number of samples and porosity (stochastic mean and standard deviation) for each considered subdomain volume.

Near-diagonal mean ATC matrices were obtained in all cases, with an approximate difference of $\pm 6\%$ between eigenvalues. For the volumes considered, the variance between the ATC of different subdomains are much higher than that obtained with the periodic foams. Indeed, while the periodic foams all have the same porosity and only differ in terms of pore arrangement, the real foam subdomains considered here can have vastly different porosities, which is the main factor influencing the ATC. The variance of the ATC computed with the UTG, PBC and MBC decreases sharply with sample volume, in excellent agreement with the power law (34) proposed by Kanit et al. [20] (Figure 10). On the other hand, the UHF estimate has a relatively stable variance that is of several orders of magnitude smaller, showing an insensitivity towards pore volume fraction at high porosities.

The integral range J_k and power law exponent α for the UTG, PBC and MBC identified from the numerical experiments are summarized in Table 4. The values of J_k confirm that the hypothesis $V \gg J_k$ for equation (34) holds, and also $\alpha \approx 1$ in line with the findings of Kanit et al. [20]. The statistical RVE sizes ($V_{N=1}$ for a target precision $\epsilon_0 = 2\%$) estimated through equations (33) and

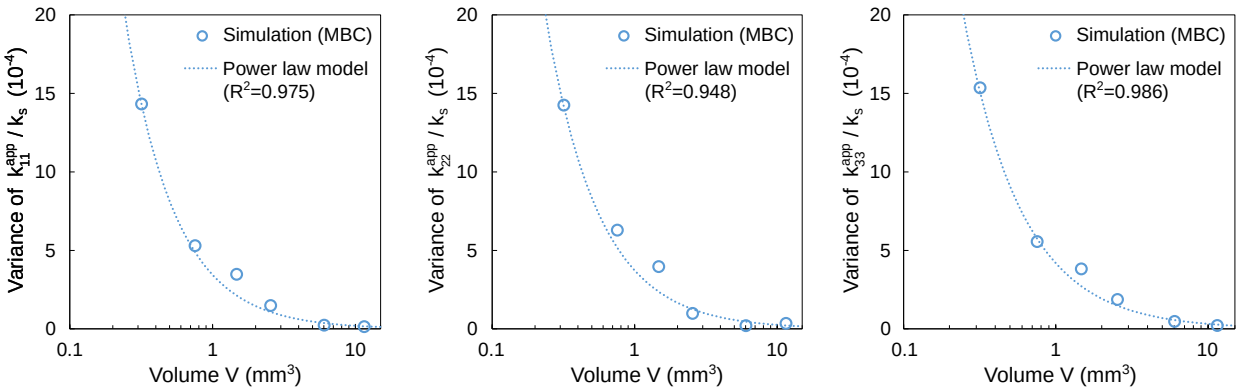

Figure 10: Variance of the normalized apparent thermal conductivity (ATC) of real foams of different volumes simulated with the mixed boundary conditions (MBC), with the power law fit proposed by Kanit et al. [20].

(34) using the identified parameters are also given, showing notably that the ETC estimated with the MBC stabilizes at smaller volumes than with the PBC.

	J_k of k_{jj}^{app}/k_s (10^{-3} mm^3)			α of k_{jj}^{app}/k_s (-)			$V_{N=1}$ (mm^3)
	$j=1$	$j=2$	$j=3$	$j=1$	$j=2$	$j=3$	$\epsilon_0 = 2\%$
UTG	9.490	9.490	9.490	1.255	1.255	1.255	33
MBC	6.116	4.670	4.137	1.240	1.163	1.117	125
PBC	1.339	4.309	2.602	0.934	1.153	1.028	505

Table 4: Integral range J_k and power law exponent α corresponding to the diagonal terms of the normalized apparent thermal conductivity $\boldsymbol{k}_{\text{app}}/k_s$ of the real foam, under uniform temperature gradient (UTG), mixed (MBC) and periodic (PBC) boundary conditions. The size of the statistical representative volume element $V_{N=1}$ for a precision of $\epsilon_0 = 2\%$ was also given.

The mean and precision of the largest eigenvalue of the ATC obtained using different boundary conditions on subdomains of increasing volumes are shown in Figure 11. As with the results obtained on periodic foams, comparison was made with the series and parallel (Weiner) bounds, Maxwell-Eucken bounds, and the power law of Archie [47]. Once again, the UTG and UHF results are extremely far apart and thus uninformative. For every subdomain, the UTG systematically gives the parallel model result (upper Wiener bound); the narrow error bands observed simply reflect the slight variation in porosity–and thus the parallel model result–between individual subdomains. The MBC results are slightly more precise than the PBC results, both in absolute and relative terms.

The estimate given by the PBC is now systematically and significantly inferior to the MBC result, in agreement with the order relation $\boldsymbol{k}_{\text{app}}^{\text{PBC}} \leq \boldsymbol{k}_{\text{app}}^{\text{MBC}}$ (30) demonstrated in subsection 3.3.2. While no rigorous reference ETC value exists, one can nonetheless see that the ETC estimated under the PBC slowly tends towards the MBC result (instead of the other way round), suggesting that the converged value is closer to the MBC result than it is to the PBC result. Coupled with the results from the preliminary study on unit cell-based geometries (see subsection 5.1), this observation gives strong evidence that the MBC give more accurate estimates of the ETC than the PBC for non-periodic foam microstructures.

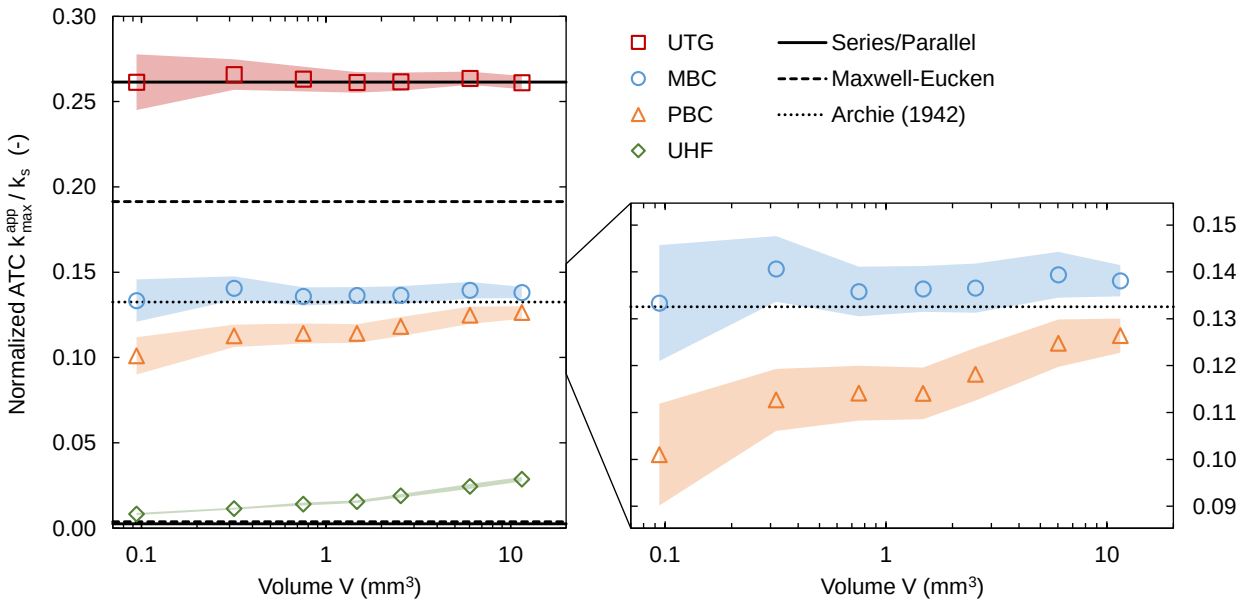

Figure 11: Mean normalized apparent thermal conductivity (ATC) of non-periodic real foam samples of increasing volume, under uniform heat flux (UHF), uniform temperature gradient (UTG), periodic (PBC) and mixed (MBC) boundary conditions. Comparison was shown for the largest eigenvalue of the ATC. The error bands indicate the standard error.

5.4. Verification of theoretical postulates

In the next subsections, the postulates in section 3 are verified with the results of the numerical case studies. Notably, the validity of the mixed boundary conditions (MBC) for statistically homogeneous foams and the order relation between the apparent thermal conductivities (ATC) computed under the MBC and periodic boundary conditions (PBC) are examined.

5.4.1. Macrohomogeneity condition and validity of the mixed boundary conditions

For all the considered cases, the entropy residual r_S (31) was systematically checked to ensure that the macrohomogeneity condition is satisfied. Figure 12 shows, for the tomography-reconstructed real foams, the evolution of the mean entropy residual with sample volume for different boundary conditions. The uniform temperature gradient (UTG) boundary conditions systematically gave a residual of exactly 0% showing that the macrohomogeneity condition was perfectly satisfied. However, a low, non-zero residual was found for the other cases, most likely due to the use of a "displacement-based" finite element solver [45] which introduces small discretization errors where exact temperature boundary conditions are not given.

At large domain sizes, the low residual ($r_S < 1\%$) shows that all the considered boundary conditions satisfy the macrohomogeneity condition. At small domain sizes, the residual obtained with the MBC rises sharply with a much larger scatter (compared to that obtained with the PBC, which only rises slightly due to the increased discretization error). This observation certainly supports the postulate made in subsection 3.2.2: that the MBC satisfy the sufficient condition for macrohomogeneity (21) as long the sample contains a statistically homogeneous spatial distribution of pores, since a smaller foam volume with respect to the characteristic pore size would imply a

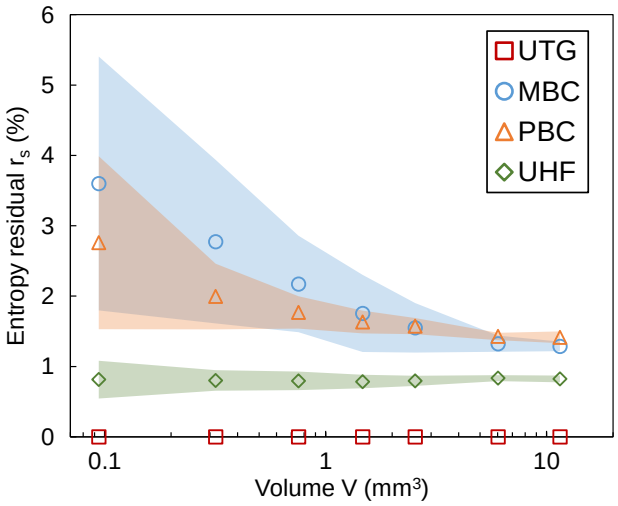

Figure 12: Mean entropy residual r_S as a function of real foam volume under uniform heat flux (UHF), uniform temperature gradient (UTG), periodic (PBC) and mixed (MBC) boundary conditions. The error bars indicate the standard deviation.

less homogeneous spatial distribution of pores within the sample. To illustrate this, the normalized temperature difference between opposite lateral faces ($\partial\Omega_3$) is compared in Figure 13 for two different volumes: the smaller sample ($V = 0.318\,\mathrm{mm}^3$, $L/\ell \approx 1.9$) has significantly larger differences between the temperature fields on opposite faces compared to the larger sample ($V = 2.54\,\mathrm{mm}^3$, $L/\ell \approx 3.9$) for which the difference is close to zero.

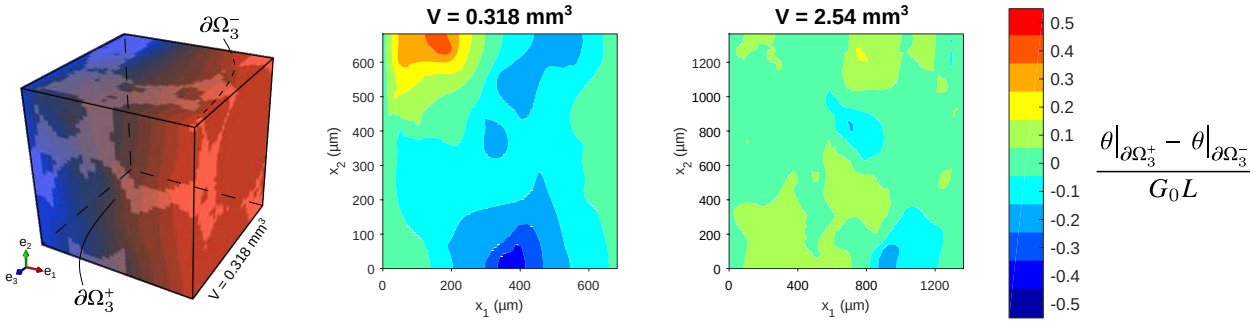

Figure 13: Normalized temperature difference on opposite pairs of lateral $\partial\Omega_3$ faces of non-periodic real foams of different volumes subjected to the mixed boundary conditions (MBC).

5.4.2. *Comparison of the apparent conductivities of non-periodic foams under periodic and mixed boundary conditions*

In subsection 3.3.2, the order relation $\boldsymbol{k}_{\mathrm{app}}^{\mathrm{PBC}} \leq \boldsymbol{k}_{\mathrm{app}}^{\mathrm{MBC}}$ (28) was demonstrated with the postulate that the boundary normal heat flux under the PBC vanishes on the lateral faces for non-periodic foams of high porosity, due to a combination of high phase contrast and high geometrical mismatch.

Figure 14 illustrates the normal heat flux q_n on the boundaries of a non-periodic real foam model subjected to the PBC, and compares it with the geometrical features on the corresponding

boundaries: for each pair of opposite boundary faces, the white regions show regions at which the solid phase is present on both faces, the black regions show regions at which the pore phase is present on both faces, and the gray regions indicate regions with boundary geometry mismatch.

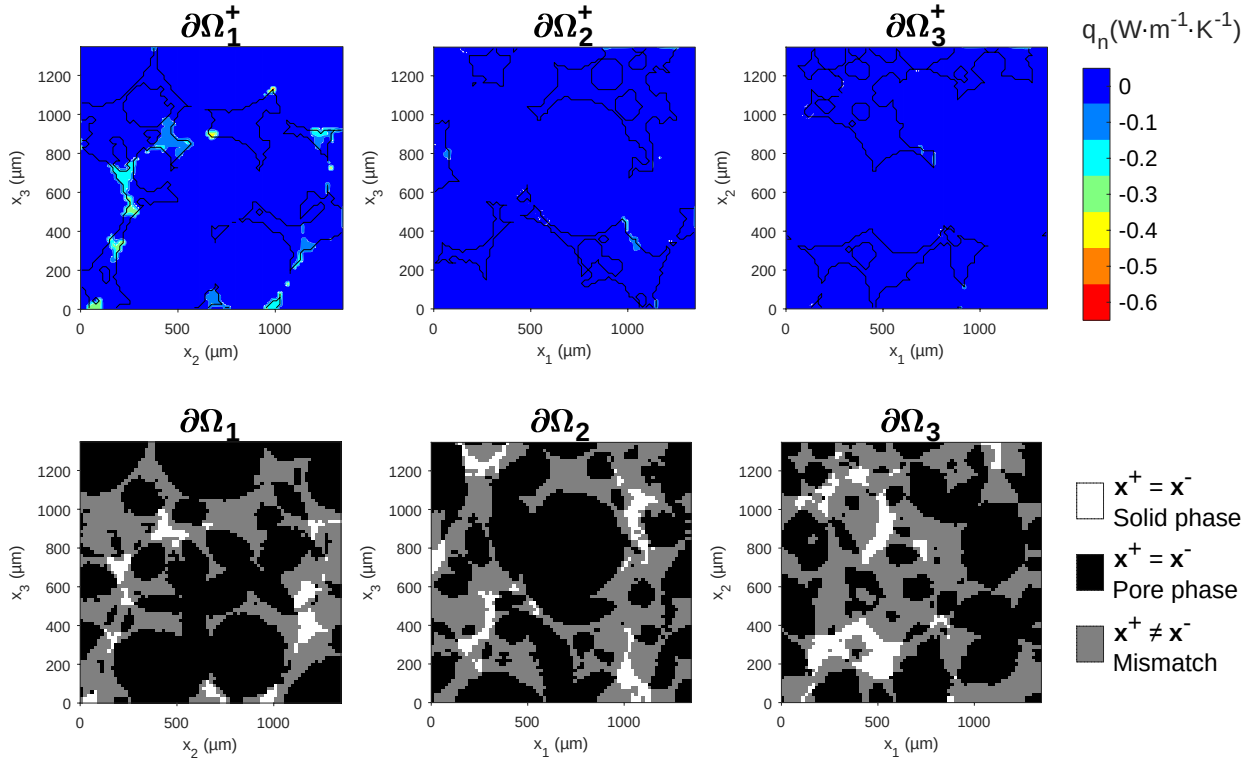

Figure 14: Comparison of the normal heat flux obtained using periodic boundary conditions (PBC) on a real foam of $V = 2.54\,\mathrm{mm}^3$, and the geometry mismatch on pairs of opposite faces (white: solid phase on both sides; black: pore phase on both sides; gray: different phases on both sides).

One sees that q_n^{PBC} is indeed non-zero on the boundaries only where the solid phase is present on both sides. While high values of q_n^{PBC} are seen on the $\partial\Omega_1$ faces perpendicular to the imposed temperature gradient, low values close to zero are generally seen on the lateral faces even when there is "continuity" of the solid phase across opposite lateral faces. This observation supports the postulate that the combined effect of geometrical mismatch on the lateral faces and high phase contrast reduces q_n^{PBC} to zero on lateral faces, confirming the theoretical status of the demonstrated order relation $\boldsymbol{k}_{\mathrm{app}}^{\mathrm{PBC}} \leq \boldsymbol{k}_{\mathrm{app}}^{\mathrm{MBC}}$ for non-periodic, highly porous foams.

6. Conclusion

In performing computational homogenization on microstructures smaller than the reprensentative volume element (RVE), the apparent thermal conductivity (ATC) under different boundary conditions are generally biased estimates of the effective thermal conductivity (ETC) of the entire medium due to edge effects. The present theoretical and numerical study clarified the influence of boundary conditions on the validity, precision and accuracy of the ETC thus estimated for open-cell foams of sub-RVE sizes with porosities close to 74%. Three different types of foam models

were considered: unit cell-based structures, digitally generated periodic foams, and tomography-reconstructed real foams. When the microstructure is random, the resulting scatter in the ATC is taken into account by averaging over several equivalent samples, and a statistical treatment proposed by Kanit et al. [20] based on the integral range was used to estimate the confidence interval, as well as the statistical RVE size associated with a given precision.

Due to the high porosity of the considered microstructures and the high contrast between the thermal conductivities of the solid and pore phases, an extremely wide gap was observed between the numerical lower and upper bounds given by the uniform heat flux (UHF) and uniform temperature gradient (UTG) boundary conditions respectively. The extremely slow convergence of these two bounds is evidence of the prohibitively large RVE size, and renders these boundary conditions impractical for estimating the ETC of foams. The UTG result can be particularly misleading as it systematically gives an isotropic ATC equal to the parallel model result (upper Wiener bound) for the considered computational volumes, even when significant orthotropy exists.

The set of mixed boundary conditions (MBC) considered in this work was shown to satisfy the macrohomogeneity condition for foam samples in which the pores are distributed homogeneously, and thus provide thermodynamically valid ETC estimates under the homogenization framework. While this rule of thumb may be used to determine *a priori* the types of microstructures on which the MBC can be used, it is still recommended to verify this point on a case-by-case basis (i.e., by computing the entropy residual r_S defined in equation (31)).

Contrary to the common view that periodic boundary conditions (PBC) give the best possible estimate of the ETC for any given microstructure, for non-periodic foam microstructures, the aforementioned MBC are shown to provide more accurate and precise ETC estimates. Indeed, the PBC significantly underestimate the ETC under the combined effect of high phase contrast and high geometrical mismatch on the lateral boundaries.

The reverse is true for periodic foams with irregular porosity: while the PBC directly give the reference ETC value, the MBC lead to an underestimation of the ETC, although in the present investigation, the confidence intervals of both results lay very close. Identical results are obtained for the MBC and PBC results for periodic structures in which symmetry planes exist for the geometry (e.g., the regular isotropic unit cells studied by [24]).

The guidelines established in this work should improve the accuracy and precision of foam microstructure-property relations predicted through direct pore-scale modeling. Future work could focus on numerical modeling on gigantic samples (using more appropriate alternatives such as FFT-based techniques [48, 49]) to attempt to reproduce the present results for foam sizes close to or exceeding the RVE. Also of interest is the development of more realistic, physics-based periodic foam generation techniques, which may eliminate the need for costly direct computation on tomography-reconstructed foam samples without sacrificing the accuracy of the morphological description and hence the estimated ETC. While the present study focuses on thermal conduction modeling in foams, extensions to other physical phenomena such as permeability, elasticity, and plasticity (with appropriate treatments to handle nonlinear behavior [16, 50]) are most certainly of interest for future investigations.

7. Acknowledgments

This research was supported by Saint-Gobain Research (SGR) Provence and the French National Association for Research and Technology (ANRT) through the CIFRE grant number 2017/0775. The authors would like to express their gratitude to L. San Miguel (SGR Provence), L. Pierrot (SGR Provence) and J. Meulemans (SGR Paris) for their insight and discussions that greatly assisted the research, to Y. Millot (SGR Provence) for the preparation of foam samples, and to J. Adrien (MATEIS laboratory) for assistance with X-ray tomography.

Appendix A. Mean field computation for different boundary value problems

For a volume Ω with boundary $\partial\Omega$ on which a differentiable scalar field ψ and a vector field $\boldsymbol{\Psi}$ are defined, the divergence theorem and its corollary state that:

$$\int_\Omega \boldsymbol{\nabla}\cdot\boldsymbol{\Psi}\,\mathrm{d}V = \int_{\partial\Omega}\boldsymbol{\Psi}\cdot\mathbf{n}\,\mathrm{d}A \tag{A.1a}$$

$$\int_\Omega \boldsymbol{\nabla}\psi\,\mathrm{d}V = \int_{\partial\Omega}\psi\mathbf{n}\,\mathrm{d}A \tag{A.1b}$$

The heat flux $\boldsymbol{q}$ can be expanded using the relations $\boldsymbol{\nabla}\mathbf{x} = \mathbf{1}$ (the identity tensor) and $\boldsymbol{\nabla}\cdot\boldsymbol{q} = 0$:

$$\boldsymbol{q} = \boldsymbol{q}\cdot\boldsymbol{\nabla}\mathbf{x} = \boldsymbol{\nabla}\cdot(\boldsymbol{q}\mathbf{x}) - \cancel{(\boldsymbol{\nabla}\cdot\boldsymbol{q})\mathbf{x}} \tag{A.2}$$

The mean heat flux $\langle\boldsymbol{q}\rangle$ is then written as a boundary integral:

$$\begin{aligned}\langle\boldsymbol{q}\rangle &= \frac{1}{V}\int_\Omega \boldsymbol{q}\,\mathrm{d}V = \frac{1}{V}\int_\Omega \boldsymbol{\nabla}\cdot(\boldsymbol{q}\mathbf{x})\,\mathrm{d}V\\ &= \frac{1}{V}\int_{\partial\Omega}(\boldsymbol{q}\mathbf{x})\cdot\mathbf{n}\,\mathrm{d}A = \frac{1}{V}\int_{\partial\Omega} q_n\mathbf{x}\,\mathrm{d}A\end{aligned} \tag{A.3}$$

Rewriting the mean temperature gradient $\langle\boldsymbol{\nabla}\theta\rangle$ as a boundary integral requires simple application of the divergence theorem (A.1):

$$\langle\boldsymbol{\nabla}\theta\rangle = \frac{1}{V}\int_\Omega \boldsymbol{\nabla}\theta\,\mathrm{d}V = \frac{1}{V}\int_{\partial\Omega}\theta\mathbf{n}\,\mathrm{d}A \tag{A.4}$$

As for the mean specific entropy production rate $\langle\boldsymbol{q}\cdot\boldsymbol{\nabla}\theta\rangle$, a similar development as in equation (A.3) is undertaken:

$$\begin{aligned}\langle\boldsymbol{q}\cdot\boldsymbol{\nabla}\theta\rangle &= \frac{1}{V}\int_\Omega \boldsymbol{q}\cdot\boldsymbol{\nabla}\theta\,\mathrm{d}V = \frac{1}{V}\int_\Omega \boldsymbol{\nabla}\cdot(\boldsymbol{q}\theta)\,\mathrm{d}V\\ &= \frac{1}{V}\int_{\partial\Omega}(\boldsymbol{q}\theta)\cdot\mathbf{n}\,\mathrm{d}A = \frac{1}{V}\int_{\partial\Omega} q_n\theta\,\mathrm{d}A\end{aligned} \tag{A.5}$$

Equations (A.3) to (A.5) are then applied to each boundary condition to demonstrate their validity with respect to the macrohomogeneity condition, as shown below.

Uniform heat flux (UHF). Using equation (12) as a starting point, the macroscopic heat flux $\boldsymbol{F} = \langle\boldsymbol{q}\rangle$ is computed:

$$\boldsymbol{F} = \frac{1}{V}\int_{\partial\Omega}\mathbf{x}(\boldsymbol{F_0}\cdot\mathbf{n})\,\mathrm{d}A = \frac{1}{V}\int_\Omega \boldsymbol{F_0}\,\mathrm{d}V = \boldsymbol{F_0} \tag{A.6}$$

From relation (A.5), it can then be shown that the macrohomogeneity condition in (11) is

automatically satisfied:

$$\langle \boldsymbol{q} \cdot \boldsymbol{\nabla}\theta \rangle = \frac{1}{V}\int_{\partial\Omega} (\boldsymbol{F_0}\cdot\mathbf{n})\theta \,\mathrm{d}A = \boldsymbol{F_0}\cdot\left(\frac{1}{V}\int_{\partial\Omega}\theta\mathbf{n}\,\mathrm{d}A\right) = \langle \boldsymbol{q}\rangle \cdot \langle \boldsymbol{\nabla}\theta\rangle \tag{A.7}$$

Uniform temperature gradient (UTG). Using equation (13) as a starting point, the macroscopic temperature gradient $\boldsymbol{G} = \langle \boldsymbol{\nabla}\theta\rangle$ can be computed (knowing that $\boldsymbol{\nabla}\mathbf{x} = \mathbf{1}$ the identity tensor):

$$\boldsymbol{G} = \frac{1}{V}\int_{\Omega} \boldsymbol{\nabla}(\boldsymbol{G_0}\cdot\mathbf{x})\,\mathrm{d}V = \frac{1}{V}\int_{\Omega} \boldsymbol{G_0}\cdot(\boldsymbol{\nabla}\mathbf{x})\,\mathrm{d}V = \boldsymbol{G_0} \tag{A.8}$$

The macrohomogeneity condition in (11) is also automatically satisfied:

$$\langle \boldsymbol{q} \cdot \boldsymbol{\nabla}\theta \rangle = \frac{1}{V}\int_{\partial\Omega} q_n(\boldsymbol{G_0}\cdot\mathbf{x})\,\mathrm{d}A = \left(\frac{1}{V}\int_{\partial\Omega} q_n\mathbf{x}\,\mathrm{d}A\right)\cdot\boldsymbol{G_0} = \langle \boldsymbol{q}\rangle \cdot \langle \boldsymbol{\nabla}\theta\rangle \tag{A.9}$$

Periodic boundary conditions (PBC). The temperature field over the domain is split as follows:

$$\forall \mathbf{x}\in\Omega, \quad \theta = \boldsymbol{G_0}\cdot\mathbf{x} + \tilde{\theta} \tag{A.10}$$

where $\tilde{\theta}$ is the fluctuation due to the micro-scale heterogeneities. The periodicity of $\tilde{\theta}$ is imposed in the PBC, as shown by rewriting equation (14):

$$\forall \mathbf{x}\in\partial\Omega, \quad \tilde{\theta}(\mathbf{x}^+) = \theta(\mathbf{x}^+) - \boldsymbol{G_0}\cdot\mathbf{x}^+ = \theta(\mathbf{x}^-) - \boldsymbol{G_0}\cdot\mathbf{x}^- = \tilde{\theta}(\mathbf{x}^-) \tag{A.11}$$

In the expression of the macroscopic temperature gradient $\boldsymbol{G} = \langle \boldsymbol{\nabla}\theta\rangle$, the boundary integral involving $\tilde{\theta}$ vanishes due to its periodicity:

$$\boldsymbol{G} = \frac{1}{V}\left(\int_{\Omega} \boldsymbol{\nabla}(\boldsymbol{G_0}\cdot\mathbf{x})\,\mathrm{d}V + \cancel{\int_{\partial\Omega} \tilde{\theta}\mathbf{n}\,\mathrm{d}A}\right) = \boldsymbol{G_0} \tag{A.12}$$

In a similar fashion, knowing that q_n is anti-periodic, the term involving $\tilde{\theta}$ in $\langle \boldsymbol{q}\cdot\boldsymbol{\nabla}\theta\rangle$ also vanishes, and the macrohomogeneity condition in (11) is satisfied:

$$\langle \boldsymbol{q} \cdot \boldsymbol{\nabla}\theta \rangle = \frac{1}{V}\left(\int_{\partial\Omega} q_n(\boldsymbol{G_0}\cdot\mathbf{x})\,\mathrm{d}A + \cancel{\int_{\partial\Omega} q_n\tilde{\theta}\,\mathrm{d}A}\right) = \langle \boldsymbol{q}\rangle \cdot \langle \boldsymbol{\nabla}\theta\rangle \tag{A.13}$$

Mixed boundary conditions (MBC). The mean fields are directly obtained from the application of equations (A.3)–(A.5), replacing with the boundary conditions in (15).

Appendix B. Proofs of known order relations between the ATC computed with different boundary conditions

Result #1. Comparison of the PBC and UTG results ($\boldsymbol{k}_{\mathrm{app}}^{\mathrm{PBC}} \leq \boldsymbol{k}_{\mathrm{app}}^{\mathrm{UTG}}$) in equation (25):

$$\mathcal{S}^{\mathrm{UTG}}(\boldsymbol{q}^{\mathrm{PBC}}) \leq \mathcal{S}^{\mathrm{UTG}}(\boldsymbol{q}^{\mathrm{UTG}}) \quad \Longleftrightarrow \quad \left(\boldsymbol{k}_{\mathrm{app}}^{\mathrm{PBC}}\cdot\boldsymbol{G_0}\right)\cdot\boldsymbol{G_0} \leq \left(\boldsymbol{k}_{\mathrm{app}}^{\mathrm{UTG}}\cdot\boldsymbol{G_0}\right)\cdot\boldsymbol{G_0} \tag{B.1}$$

Proof #1. The right hand side expands as follows:

$$\mathcal{S}^{\mathrm{UTG}}(\boldsymbol{q}^{\mathrm{UTG}}) = -\mathcal{S}_c^{\mathrm{UTG}}(\theta^{\mathrm{UTG}}) = \left(\boldsymbol{k}_{\mathrm{app}}^{\mathrm{UTG}} \cdot \langle \boldsymbol{\nabla}\theta \rangle^{\mathrm{UTG}}\right) \cdot \langle \boldsymbol{\nabla}\theta \rangle^{\mathrm{UTG}} = \left(\boldsymbol{k}_{\mathrm{app}}^{\mathrm{UTG}} \cdot \boldsymbol{G_0}\right) \cdot \boldsymbol{G_0} \tag{B.2}$$

The left hand side expands as follows:

$$\begin{aligned}
\mathcal{S}^{\mathrm{UTG}}(\boldsymbol{q}^{\mathrm{PBC}}) &= -\int_{\partial\Omega} (\boldsymbol{q}^{\mathrm{PBC}} \cdot \mathbf{n})\theta^{\mathrm{UTG}}\, \mathrm{d}A - \frac{V}{2} \langle \boldsymbol{q} \rangle^{\mathrm{PBC}} \cdot \left((\boldsymbol{k}_{\mathrm{app}}^{\mathrm{PBC}})^{-1} \cdot \langle \boldsymbol{q} \rangle^{\mathrm{PBC}}\right) \\
&= -\int_{\partial\Omega} (\boldsymbol{q}^{\mathrm{PBC}} \cdot \mathbf{n})(\boldsymbol{G_0} \cdot \mathbf{x})\, \mathrm{d}A - \frac{V}{2} \langle \boldsymbol{q} \rangle^{\mathrm{PBC}} \cdot \boldsymbol{G_0} \\
&= -V \langle \boldsymbol{q} \rangle^{\mathrm{PBC}} \cdot \boldsymbol{G_0} + \frac{V}{2} \langle \boldsymbol{q} \rangle^{\mathrm{PBC}} \cdot \boldsymbol{G_0} \\
&= \left(\boldsymbol{k}_{\mathrm{app}}^{\mathrm{PBC}} \cdot \boldsymbol{G_0}\right) \cdot \boldsymbol{G_0}
\end{aligned} \tag{B.3}$$

Result #2. Comparison of the PBC and UHF results ($\boldsymbol{k}_{\mathrm{app}}^{\mathrm{UHF}} \leq \boldsymbol{k}_{\mathrm{app}}^{\mathrm{PBC}}$) in equation (25):

$$\mathcal{S}_c^{\mathrm{UHF}}(\theta^{\mathrm{PBC}}) \leq \mathcal{S}_c^{\mathrm{UHF}}(\theta^{\mathrm{UHF}}) \iff \frac{V}{2}\boldsymbol{F_0} \cdot \left((\boldsymbol{k}_{\mathrm{app}}^{\mathrm{PBC}})^{-1} \cdot \boldsymbol{F_0}\right)' \leq \frac{V}{2}\boldsymbol{F_0} \cdot \left((\boldsymbol{k}_{\mathrm{app}}^{\mathrm{UHF}})^{-1} \cdot \boldsymbol{F_0}\right) \tag{B.4}$$

Proof #2. The right hand side expands as follows:

$$\mathcal{S}_c^{\mathrm{UHF}}(\theta^{\mathrm{UHF}}) = -\mathcal{S}^{\mathrm{UHF}}(\boldsymbol{q}^{\mathrm{UHF}}) = \frac{V}{2} \langle \boldsymbol{q} \rangle^{\mathrm{UHF}} \cdot \left((\boldsymbol{k}_{\mathrm{app}}^{\mathrm{UHF}})^{-1} \cdot \langle \boldsymbol{q} \rangle^{\mathrm{UHF}}\right) = \frac{V}{2}\boldsymbol{F_0} \cdot \left((\boldsymbol{k}_{\mathrm{app}}^{\mathrm{UHF}})^{-1} \cdot \boldsymbol{F_0}\right) \tag{B.5}$$

The left hand side expands as follows:

$$\begin{aligned}
\mathcal{S}_c^{\mathrm{UHF}}(\theta^{\mathrm{PBC}}) &= -\int_{\partial\Omega} (\boldsymbol{q}^{\mathrm{UHF}} \cdot \mathbf{n})\theta^{\mathrm{PBC}}\, \mathrm{d}A - \frac{V}{2}\left(\boldsymbol{k}_{\mathrm{app}}^{\mathrm{PBC}} \cdot \langle \boldsymbol{\nabla}\theta \rangle^{\mathrm{PBC}}\right) \cdot \langle \boldsymbol{\nabla}\theta \rangle^{\mathrm{PBC}} \\
&= -\int_{\partial\Omega} (\boldsymbol{F_0} \cdot \mathbf{n})\theta^{\mathrm{PBC}}\, \mathrm{d}A - \frac{V}{2} \langle \boldsymbol{q} \rangle^{\mathrm{PBC}} \cdot \langle \boldsymbol{\nabla}\theta \rangle^{\mathrm{PBC}} \\
&= -V\boldsymbol{F_0} \cdot \langle \boldsymbol{\nabla}\theta \rangle^{\mathrm{PBC}} - \frac{V}{2} \langle \boldsymbol{q} \rangle^{\mathrm{PBC}} \cdot \langle \boldsymbol{\nabla}\theta \rangle^{\mathrm{PBC}} \\
&= V\boldsymbol{F_0} \cdot \left((\boldsymbol{k}_{\mathrm{app}}^{\mathrm{PBC}})^{-1} \cdot \langle \boldsymbol{q} \rangle^{\mathrm{PBC}}\right) - \frac{V}{2} \langle \boldsymbol{q} \rangle^{\mathrm{PBC}} \cdot \left((\boldsymbol{k}_{\mathrm{app}}^{\mathrm{PBC}})^{-1} \cdot \langle \boldsymbol{q} \rangle^{\mathrm{PBC}}\right) \quad \equiv \Pi_c\left(\langle \boldsymbol{q} \rangle^{\mathrm{PBC}}\right)
\end{aligned} \tag{B.6}$$

Setting $\Pi_c\left(\langle \boldsymbol{q} \rangle^{\mathrm{PBC}}\right)$ to represent the expression on the last line, one can then deduce:

$$\begin{cases} \left.\dfrac{\partial \Pi_c}{\partial \langle \boldsymbol{q} \rangle^{\mathrm{PBC}}}\right|_{\langle \boldsymbol{q} \rangle^{\mathrm{PBC}} = \boldsymbol{F_0}} = V\boldsymbol{F_0} \cdot (\boldsymbol{k}_{\mathrm{app}}^{\mathrm{PBC}})^{-1} - V \langle \boldsymbol{q} \rangle^{\mathrm{PBC}} \cdot (\boldsymbol{k}_{\mathrm{app}}^{\mathrm{PBC}})^{-1} = \boldsymbol{0} \\ \dfrac{\partial^2 \Pi_c}{\left(\partial \langle \boldsymbol{q} \rangle^{\mathrm{PBC}}\right)^2} = -V(\boldsymbol{k}_{\mathrm{app}}^{\mathrm{PBC}})^{-1} \leq \boldsymbol{0} \qquad \forall \langle \boldsymbol{q} \rangle^{\mathrm{PBC}} \end{cases} \tag{B.7}$$

$$\iff \quad \max \mathcal{S}_c^{\mathrm{UHF}}(\theta^{\mathrm{PBC}}) = \max \Pi_c\left(\langle \boldsymbol{q} \rangle^{\mathrm{PBC}}\right) = \Pi_c(\boldsymbol{F_0}) = \frac{V}{2}\boldsymbol{F_0} \cdot \left((\boldsymbol{k}_{\mathrm{app}}^{\mathrm{PBC}})^{-1} \cdot \boldsymbol{F_0}\right)$$

Result #3. Comparison of the MBC and UTG results ($\boldsymbol{k}_{\mathrm{app}}^{\mathrm{MBC}} \leq \boldsymbol{k}_{\mathrm{app}}^{\mathrm{UTG}}$) in equation (26) according to the work of Hazanov and Huet [42]:

$$\mathcal{S}^{\mathrm{UTG}}(\boldsymbol{q}^{\mathrm{MBC}}) \leq \mathcal{S}^{\mathrm{UTG}}(\boldsymbol{q}^{\mathrm{UTG}}) \quad \iff \quad \frac{V}{2}\left(\boldsymbol{k}_{\mathrm{app}}^{\mathrm{MBC}} \cdot \boldsymbol{G_0}\right) \cdot \boldsymbol{G_0} \leq \frac{V}{2}\left(\boldsymbol{k}_{\mathrm{app}}^{\mathrm{UTG}} \cdot \boldsymbol{G_0}\right) \cdot \boldsymbol{G_0} \tag{B.8}$$

Proof #3. The right hand side expands as follows:

$$\mathcal{S}^{\mathrm{UTG}}(\boldsymbol{q}^{\mathrm{UTG}}) = -\mathcal{S}_c^{\mathrm{UTG}}(\theta^{\mathrm{UTG}}) = \frac{V}{2}\left(\boldsymbol{k}_{\mathrm{app}}^{\mathrm{UTG}} \cdot \langle \boldsymbol{\nabla}\theta \rangle^{\mathrm{UTG}}\right) \cdot \langle \boldsymbol{\nabla}\theta \rangle^{\mathrm{UTG}} = \frac{V}{2}\left(\boldsymbol{k}_{\mathrm{app}}^{\mathrm{UTG}} \cdot \boldsymbol{G_0}\right) \cdot \boldsymbol{G_0} \tag{B.9}$$

The left hand side expands as follows:

$$\begin{aligned} \mathcal{S}^{\mathrm{UTG}}(\boldsymbol{q}^{\mathrm{MBC}}) &= -\int_{\partial\Omega} (\boldsymbol{q}^{\mathrm{MBC}} \cdot \mathbf{n})\theta^{\mathrm{UTG}} \,\mathrm{d}A - \frac{V}{2} \langle \boldsymbol{q} \rangle^{\mathrm{MBC}} \cdot \left((\boldsymbol{k}_{\mathrm{app}}^{\mathrm{MBC}})^{-1} \cdot \langle \boldsymbol{q} \rangle^{\mathrm{MBC}}\right) \\ &= -\int_{\partial\Omega} (\boldsymbol{q}^{\mathrm{MBC}} \cdot \mathbf{n})(\boldsymbol{G_0} \cdot \mathbf{x}) \,\mathrm{d}A - \frac{V}{2} \langle \boldsymbol{q} \rangle^{\mathrm{MBC}} \cdot \left((\boldsymbol{k}_{\mathrm{app}}^{\mathrm{MBC}})^{-1} \cdot \langle \boldsymbol{q} \rangle^{\mathrm{MBC}}\right) \\ &= -V \langle \boldsymbol{q} \rangle^{\mathrm{MBC}} \cdot \boldsymbol{G_0} - \frac{V}{2} \langle \boldsymbol{q} \rangle^{\mathrm{MBC}} \cdot \left((\boldsymbol{k}_{\mathrm{app}}^{\mathrm{MBC}})^{-1} \cdot \langle \boldsymbol{q} \rangle^{\mathrm{MBC}}\right) \quad \equiv \Pi\left(\langle \boldsymbol{q} \rangle^{\mathrm{MBC}}\right) \end{aligned} \tag{B.10}$$

Setting $\Pi\left(\langle \boldsymbol{q} \rangle^{\mathrm{MBC}}\right)$ to represent the expression the last line, one can then deduce:

$$\begin{cases} \left.\dfrac{\partial \Pi}{\partial \langle \boldsymbol{q} \rangle^{\mathrm{MBC}}}\right|_{\langle \boldsymbol{q} \rangle^{\mathrm{MBC}} = -\boldsymbol{k}_{\mathrm{app}}^{\mathrm{MBC}} \cdot \boldsymbol{G_0}} = -V\boldsymbol{G_0} - V(\boldsymbol{k}_{\mathrm{app}}^{\mathrm{MBC}})^{-1} \cdot \langle \boldsymbol{q} \rangle^{\mathrm{MBC}} = \boldsymbol{0} \\ \dfrac{\partial^2 \Pi}{\left(\partial \langle \boldsymbol{q} \rangle^{\mathrm{MBC}}\right)^2} = -V(\boldsymbol{k}_{\mathrm{app}}^{\mathrm{MBC}})^{-1} \leq \boldsymbol{0} \qquad \forall \langle \boldsymbol{q} \rangle^{\mathrm{MBC}} \end{cases} \tag{B.11}$$

$$\iff \quad \max \mathcal{S}^{\mathrm{UTG}}(\boldsymbol{q}^{\mathrm{MBC}}) = \max \Pi\left(\langle \boldsymbol{q} \rangle^{\mathrm{MBC}}\right) = \Pi\left(-\boldsymbol{k}_{\mathrm{app}}^{\mathrm{MBC}} \cdot \boldsymbol{G_0}\right) = \frac{V}{2}\left(\boldsymbol{k}_{\mathrm{app}}^{\mathrm{MBC}} \cdot \boldsymbol{G_0}\right) \cdot \boldsymbol{G_0}$$

The comparison of the MBC and UHF results ($\boldsymbol{k}_{\mathrm{app}}^{\mathrm{UHF}} \leq \boldsymbol{k}_{\mathrm{app}}^{\mathrm{MBC}}$) in equation (26) can be demonstrated in the exact same manner as for result #3, by replacing all occurrences of 'PBC' with 'MBC'

in equations (B.4) and (B.5).

Data availability

The raw and processed data in this work cannot be made publicly available at this time as they are part of an ongoing study.

References

[1] S. Suter, A. Steinfeld, S. Haussener, Pore-level engineering of macroporous media for increased performance of solar-driven thermochemical fuel processing, International Journal of Heat and Mass Transfer 78 (2014) 688–698.
[2] J. Petrasch, B. Schrader, P. Wyss, A. Steinfeld, Tomography-based determination of the effective thermal conductivity of fluid-saturated reticulate porous ceramics, Journal of Heat Transfer 130 (2008) 032602.
[3] D. Baillis, R. Coquard, J. Randrianalisoa, L. A. Dombrovsky, R. Viskanta, Thermal Radiation Properties of Highly Porous Cellular Foams, Special Topics & Reviews in Porous Media - An International Journal 4 (2013) 111–136.
[4] W. Zhu, N. Blal, S. Cunsolo, D. Baillis, Micromechanical modeling of effective elastic properties of open-cell foam, International Journal of Solids and Structures 115-116 (2017) 61–72.
[5] M. Schumann, L. San Miguel, Fiber-Free Ceramic Insulation Foam for Highest Temperatures – a New Generation of HSE-friendly Refractory Products with Multiple Application Possibilities, refractories WORLDFORUM 9 (2017) 50–58.
[6] W. Pabst, E. Gregorová, Conductivity of porous materials with spheroidal pores, Journal of the European Ceramic Society 34 (2014) 2757–2766.
[7] P. Ranut, On the effective thermal conductivity of aluminum metal foams: Review and improvement of the available empirical and analytical models, Applied Thermal Engineering 101 (2016) 496–524.
[8] P. Kumar, F. Topin, J. Vicente, Determination of effective thermal conductivity from geometrical properties: Application to open cell foams, International Journal of Thermal Sciences 81 (2014) 13–28.
[9] D. Baillis, R. Coquard, S. Cunsolo, Effective conductivity of Voronoi's closed- and open-cell foams: analytical laws and numerical results, Journal of Materials Science 52 (2017) 11146–11167.
[10] S. Cunsolo, D. Baillis, N. Bianco, Improved Monte Carlo methods for computational modelling of thermal radiation applied to porous cellular materials, International Journal of Thermal Sciences 137 (2019) 161–179.
[11] W. Tian, L. Qi, X. Chao, J. Liang, M. Fu, Numerical evaluation on the effective thermal conductivity of the composites with discontinuous inclusions: Periodic boundary condition and its numerical algorithm, International Journal of Heat and Mass Transfer 134 (2019) 735–751.
[12] R. Coquard, D. Rochais, D. Baillis, Modeling of the Coupled Conductive and Radiative Heat Transfer in Nicral From Photothermal Measurements and X-Ray Tomography, Special Topics & Reviews in Porous Media - An International Journal 2 (2011) 249–265.
[13] M. A. Mendes, S. Ray, D. Trimis, A simple and efficient method for the evaluation of effective thermal conductivity of open-cell foam-like structures, International Journal of Heat and Mass Transfer 66 (2013) 412–422.
[14] J. Lux, A. Ahmadi, C. Gobbé, C. Delisée, Macroscopic thermal properties of real fibrous materials: Volume averaging method and 3D image analysis, International Journal of Heat and Mass Transfer 49 (2006) 1958–1973.
[15] F. Panerai, J. C. Ferguson, J. Lachaud, A. Martin, M. J. Gasch, N. N. Mansour, Micro-tomography based analysis of thermal conductivity, diffusivity and oxidation behavior of rigid and flexible fibrous insulators, International Journal of Heat and Mass Transfer 108 (2017) 801–811.
[16] M. G. Geers, V. G. Kouznetsova, W. A. Brekelmans, Multi-scale computational homogenization: Trends and challenges, Journal of Computational and Applied Mathematics 234 (2010) 2175–2182.
[17] J.-C. Michel, H. Moulinec, P. Suquet, Composites à microstructure périodique [Composites with periodic microstructures], in: M. Bornert, T. Bretheau, P. Gilormini (Eds.), Homogénéisation en mécanique des matériaux

1. Matériaux aléatoires élastiques et milieux périodiques, HERMES Science Europe Ltd, Paris, France, 2001, pp. 57–92.
[18] J. Qu, M. Cherkaoui, Fundamentals of Micromechanics of Solids, John Wiley & Sons, Inc, 2006.
[19] I. Özdemir, W. A. M. Brekelmans, M. G. D. Geers, Computational homogenization for heat conduction in heterogeneous solids, International Journal for Numerical Methods in Engineering 73 (2008) 185–204.
[20] T. Kanit, S. Forest, I. Galliet, V. Mounoury, D. Jeulin, Determination of the size of the representative volume element for random composites: Statistical and numerical approach, International Journal of Solids and Structures 40 (2003) 3647–3679.
[21] J. Dirrenberger, S. Forest, D. Jeulin, Towards gigantic RVE sizes for 3D stochastic fibrous networks, International Journal of Solids and Structures 51 (2014) 359–376.
[22] R. Hill, Elastic properties of reinforced solides: Some theoretical principles, Journal of the Mechanics and Physics of Solids 11 (1963) 357–372.
[23] S. Schindler, J. Mergheim, M. Zimmermann, J. C. Aurich, P. Steinmann, Numerical homogenization of elastic and thermal material properties for metal matrix composites (MMC), Continuum Mechanics and Thermodynamics 29 (2017) 51–75.
[24] M. Jiang, I. Jasiuk, M. Ostoja-Starzewski, Apparent thermal conductivity of periodic two-dimensional composites, Computational Materials Science 25 (2002) 329–338.
[25] A. Bensoussan, J.-L. Lions, G. Papanicolaou, Asymptotic Analysis for Periodic Structures, in: J.-L. Lions, G. Papanicolaou, R. Rockafellar (Eds.), Studies in Mathematics and its Applications, volume 5, North-Holland Publishing Company, Amsterdam, 1978, pp. 1–700. doi:10.1016/S0168-2024(08)70194-2.
[26] E. Sanchez-Palencia, Non-Homogeneous Media and Vibration Theory, volume 127 of *Lecture Notes in Physics*, Springer Berlin Heidelberg, Berlin, Heidelberg, 1980. URL: http://link.springer.com/10.1007/3-540-10000-8. doi:10.1007/3-540-10000-8.
[27] P. M. Suquet, Elements of Homogenization for Inelastic Solid Mechanics, in: E. Sanchez-Palencia, A. Zaoui (Eds.), Homogenization Techniques for Composite Media, Springer Nature, 1987, pp. 193–278.
[28] M. Quintard, S. Whitaker, Transport in ordered and disordered porous media: volume-averaged equations, closure problems, and comparison with experiment, Chemical Engineering Science 48 (1993) 2537–2564.
[29] Y. Davit, C. G. Bell, H. M. Byrne, L. A. Chapman, L. S. Kimpton, G. E. Lang, K. H. Leonard, J. M. Oliver, N. C. Pearson, R. J. Shipley, S. L. Waters, J. P. Whiteley, B. D. Wood, M. Quintard, Homogenization via formal multiscale asymptotics and volume averaging: How do the two techniques compare?, Advances in Water Resources 62 (2013) 178–206.
[30] A. Wiegmann, A. Zemitis, EJ-HEAT: A Fast Explicit Jump Harmonic Averaging Solver for the Effective Heat Conductivity of Composite Materials, Berichte des Fraunhofer ITWM 94 (2006).
[31] D. Baillis, R. Coquard, Radiative and Conductive Thermal Properties of Foams, in: Cellular and Porous Materials: Thermal Properties Simulation and Prediction, 2008, pp. 343–384. doi:10.1002/9783527621408.ch11.
[32] ISO 8302:1991, Thermal insulation – Determination of steady-state thermal resistance and related properties – Guarded hot plate apparatus, International Organization for Standardization, 1991.
[33] J. Schindelin, I. Arganda-Carreras, E. Frise, V. Kaynig, M. Longair, T. Pietzsch, S. Preibisch, C. Rueden, S. Saalfeld, B. Schmid, J.-Y. Tinevez, D. J. White, V. Hartenstein, K. Eliceiri, P. Tomancak, A. Cardona, Fiji: an open-source platform for biological-image analysis, Nature Methods 9 (2012) 676–682.
[34] E. Brun, J. Vicente, F. Topin, R. Occelli, iMorph: A 3D morphological tool to fully analyse all kind of cellular materials, Proceedings of the International Symposium on Cellular Metals for Structural and Functional Applications (CELLMET) (2008) 1–6.
[35] J. Randrianalisoa, D. Baillis, Thermal conductive and radiative properties of solid foams: Traditional and recent advanced modelling approaches, Comptes Rendus Physique 15 (2014) 683–695.
[36] W. Y. Jang, A. M. Kraynik, S. Kyriakides, On the microstructure of open-cell foams and its effect on elastic properties, International Journal of Solids and Structures 45 (2008) 1845–1875.
[37] P. Sepulveda, W. N. dos Santos, V. C. Pandolfelli, J. C. Bressiani, R. Taylor, Thermal Conductivity of Gelcast Porous Alumina, The American Ceramic Society Bulletin (1999).
[38] N. J. Dyck, A. G. Straatman, A new approach to digital generation of spherical void phase porous media microstructures, International Journal of Heat and Mass Transfer 81 (2015) 470–477.

[39] L. Onsager, Reciprocal Relations in Irreversible Processes. I, Physical Review 37 (1931) 405.
[40] J. M. Powers, On the necessity of positive semi-definite conductivity and onsager reciprocity in modeling heat conduction in anisotropic media, Journal of Heat Transfer 126 (2004) 670–675.
[41] S. Li, On the nature of periodic traction boundary conditions in micromechanical FE analyses of unit cells, IMA Journal of Applied Mathematics (Institute of Mathematics and Its Applications) 77 (2011) 441–450.
[42] S. Hazanov, C. Huet, Order relationships for boundary conditions effect in heterogeneous bodies smaller than the representative volume, Journal of the Mechanics and Physics of Solids 42 (1994) 1995–2011.
[43] D. S. Smith, S. Fayette, S. Grandjean, C. Martin, Thermal resistance of grain boundaries in alumina ceramics and refractories, American Ceramics Society 11 (2003) 105–111.
[44] R. Coquard, D. Baillis, Modeling of Heat Transfer in Low-Density EPS Foams, Journal of Heat Transfer 128 (2006) 538.
[45] Dassault Systèmes Simulia Corp., Abaqus Analysis User's Guide, in: Abaqus 2017 Documentation Collection, 2017.
[46] E. Mitsoulis, J. Vlachopoulos, The finite element method for flow and heat transfer analysis, Advances in Polymer Technology 4 (1984) 107–121.
[47] G. E. Archie, The Electrical Resistivity Log as an Aid in Determining Some Reservoir Characteristics, Petroleum Technology (1942) 54–62.
[48] H. Moulinec, P. Suquet, A numerical method for computing the overall response of nonlinear composites with complex microstructure, Computer Methods in Applied Mechanics and Engineering 157 (1998) 69–94.
[49] S. Brisard, K. Sab, L. Dormieux, New boundary conditions for the computation of the apparent stiffness of statistical volume elements, Journal of the Mechanics and Physics of Solids 61 (2013) 2638–2658.
[50] M. Ostoja-Starzewski, S. Kale, P. Karimi, A. Malyarenko, B. Raghavan, S. I. Ranganathan, J. Zhang, Scaling to RVE in Random Media, in: Advances in Applied Mechanics, 1 ed., Elsevier Inc., 2016, pp. 111–211. URL: http://dx.doi.org/10.1016/bs.aams.2016.07.001. doi:10.1016/bs.aams.2016.07.001.

Chapitre II

Modélisation des propriétés radiatives effectives du squelette et validation expérimentale

Sommaire

1– A physical optics approach to predict the radiative properties of semi-transparent porous ceramics

Z.K. Low[a,b,*], D. Baillis[a]

[a] *Univ Lyon, INSA-Lyon, CNRS UMR5259, LaMCoS, F-69621 Villeurbanne, France.*
[b] *Saint-Gobain Research Provence, F-84306 Cavaillon, France.*

Abstract

We propose a physical optics approach to compute the volume radiative properties and surface reflectivity of porous ceramics composed of a weakly absorbing solid matrix containing low fractions of heterogeneities (pores or particles). Our approach accounts for dependent scattering between heterogeneities that are small and close to each other compared to the wavelength, and only requires the 3D microstructure and complex refractive indexes of constituent phases as input. With our approach, we obtained an accuracy of within 5% on reference microstructures with known solutions. We then applied our models to compute the spectral volume and surface radiative properties of tomography-reconstructed porous alumina samples of various porosities up to 30%. Simulated results are compared to several analytical relations linking the effective radiative properties with the porosity, to assess their applicability in the studied material.

Keywords: Porous ceramics, Discrete dipole approximation (DDA), Radiative transfer equation (RTE), Volume radiative properties, Surface reflectivity

1. Introduction

Ceramics used in a wide array of high-temperature applications often contain heterogeneities in the volume and on the surface of the material, such as pores, cracks or bubbles formed during processing [1, 2] (see Figure 1) or scattering-absorbing particles added intentionally to modify the radiative properties of the base material [3]. Accurate knowledge of the influence of these heterogeneities on the radiative properties of the material is of paramount importance for the design of high-performance materials and systems. According to the scale separation principle, radiative transfer in materials containing small heterogeneities may be considered at two distinct scales: the micro-scale usually with characteristic length scales of several μm and below, at which the interaction of radiation with the heterogeneities is considered explicitly; and the macro-scale usually corresponding to mm- or cm-sized samples or parts, at which the material may be modeled as an equivalent homogeneous medium within the framework of the radiative transfer equation (RTE).

*Corresponding author
Email address: zi.low@insa-lyon.fr (Z.K. Low)

Preprint written as part of the doctoral thesis number 2020LYSEI122, INSA Lyon, France

Nomenclature

First- and second-order tensors ("vectors" and "matrices") are written in **bold face**.

Latin

A	Dipole interaction matrix
a	Radius
C	Cross section
D	Target diameter
d	Cell size
E	Electric field
e	Basis vector
f	Volume fraction
g	Scattering asymmetry
h	Target height
$\mathcal{I}$	Radiance
I	Intensity, $\int \mathcal{I}\,\mathrm{d}\Omega$
j, k	Dipole indexes
$\mathcal{k}$	Angular wavenumber, $2\pi/\lambda$
ℓ	Chord length
L	Target length
M	Mueller matrix
m	Complex refractive index, $n + i\kappa$
N	Number
n	Real refractive index; Normal vector
p	Parameter
P	Polarization
$\mathcal{R}$	Reflectivity
r	Distance
$\mathcal{T}$	Transmissivity
u	Direction
v, w	Target replica indexes
V	Target volume
x	Position
y	Discretization parameter
$\mathbb{Z}$	Integer

Greek

α	Polarizability
Δ	Difference
ε	Permittivity
ϕ	Scattering phase function
γ	Interaction cut-off parameter
κ	Absorption index
$\varkappa$	Absorption coefficient
λ	Wavelength
σ	Scattering coefficient
θ	Angle
χ	Mie size parameter, $\mathcal{k}a$
Ω	Solid angle

Superscripts and Subscripts

$'$	Modified quantity
0	Reference, *in vacuo*
abs	Absorption
amb	Ambient
diff	Diffuse
eff	Effective
ext	Extinction
Fr	Fresnel
$\hbar$	Hemispherical
inc	Incident
m	Matrix
p	Pore/Particle
sca	Scattering
spec	Specular
sub	Substrate
tr	Transport
V	Per unit volume

Operators and accents

∇	Del operator
$\cdot$	Dot product
$\langle\langle\bullet\rangle\rangle$	Stochastic mean
$\lvert\bullet\rvert$	Absolute value
$\bar{\bullet}$	Complex conjugate

Acronyms

BSDF	Bidirectional scattering distribution function
DDA	Discrete dipole approximation
FCD	Filtered Coupled Dipole
FDTD	Finite-difference-time-domain
LDR	Lattice Dispersion Relation
RMS	Root-mean-squared
RTE	Radiative transfer equation

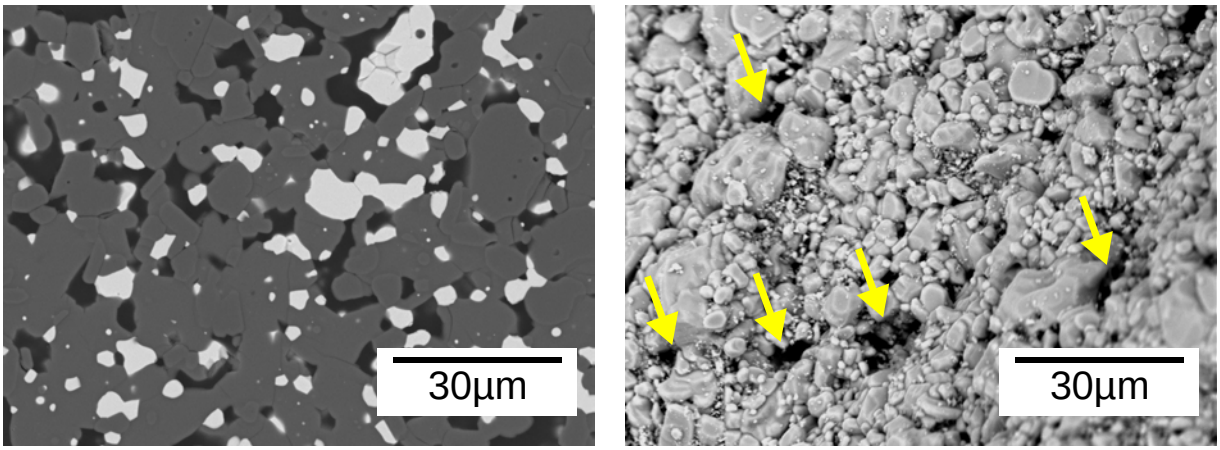

(a) Sectional view with pores (black) and particles (white). (b) Surface view with pores (indicated using arrows).

Figure 1: Scanning electron micrographs showing examples of porous ceramics.

While the effective macro-scale radiative properties have traditionally been identified from experimental data [4, 5], theoretical and numerical methods to predict the macro-scale properties from the micro-scale morphology have seen significant development. Past work in this area have focused on either semi-transparent solids containing low fractions of pores and particles [6, 7] or high-porosity materials such as foams [8], since the dominant phase in these types of materials may be considered as the host medium for radiative transfer and the secondary phases as absorbing or scattering heterogeneities. Purely theoretical predictions usually rely on known scattering and absorption properties of simple isolated geometries (e.g., spheres or infinite cylinders [9]), and invoke the independent scattering hypothesis [7] to calculate the effective properties of the material by summing the contributions of individual heterogeneities. This hypothesis usually fails when the volume fraction of heterogeneities exceed a few percent [10–13].

To model dependent scattering effects, Monte Carlo ray-tracing is a popular choice when characteristic length scales of the heterogeneities are larger than the wavelength, and has notably been performed on tomography-reconstructed or digitally generated porous ceramic microstructures [2, 14–17]. However, when the heterogeneities are small and close to each other compared to the wavelength, resolution of Maxwell's equations via numerical methods [18] is necessary to account for wave effects, though the high computational cost generally limits the geometry sizes that can be simulated. The discrete dipole approximation (DDA) [19, 20] has been used to compute the scattering and absorption properties by isolated particles or aggregates with complex geometry, which are then used to deduce the effective radiative properties under the independent scattering framework [3, 8, 21–23]. Recently, a hybrid direct-inverse approach was proposed by Chen et al. [1] for 2D microstructures of zirconia ceramics with porosities of 5% to 20%: the angular distribution of scattered radiation is first simulated via the finite-difference-time-domain (FDTD) method, then used to identify the effective radiative properties by iteratively solving the RTE on an equivalent homogeneous medium. To our knowledge, direct physical optics methods to obtain the effective radiative properties of 3D microstructures while accounting for dependent scattering between small heterogeneities have not been implemented.

Note that most past work on low-porosity ceramics [2, 4, 7, 14, 15, 17, 24] focused on the volume scattering and absorption behavior of the material, while the boundaries are assumed optically smooth with specular reflection and refraction according to Fresnel's equations [25]. However, the presence of surface asperities generally lead to non-specular boundary scattering behavior [26, 27], with potential wave effects at wavelengths close to the asperity sizes. While analytical electromagnetic scattering solutions have been developed for Gaussian or exponential surfaces [26, 28, 29], numerical methods such as the FDTD with periodic boundary conditions have recently been applied to simulate the reflectivity of porous semi-transparent periodic layers [30] and rough opaque surfaces [31] from their complex 3D microstructure.

In the present work, which is the first of two papers dealing with the characterization of the infrared radiative behavior of porous ceramics, we propose a new approach to predict the volume radiative properties and surface reflectivity of porous semi-transparent ceramics composed of a weakly absorbing solid matrix containing low volume fractions of pores or particles (around 20%) of sizes close to the wavelengths of interest. These characteristics are typical of sintered refractory ceramics with a high purity dominant metal oxide phase at the mid- to near-infrared range [32]. Our approach directly computes the effective radiative properties from the tomography-reconstructed 3D microstructure and the complex refractive indexes of the constituent phases by simulating the absorption and scattering by volume elements of the material using the DDA, which accounts for dependent scattering between small particles close to one another. After validation on several reference microstructures, we simulated the volume and surface radiative properties of a porous alumina ceramic by applying our approach to tomographic reconstructions, and compared our numerical results to several common analytical solutions.

Section 2 presents the radiative properties of interest and the analytical models commonly used to predict them, before introducing our numerical approach consisting of two DDA-based models. Section 3 assesses the influence of model parameters on results obtained on four reference microstructures. Section 4 describes the acquisition and characterization of the 3D microstructure of the studied porous alumina ceramic, and compares the numerically and analytically predicted effective radiative properties. In the second part of the study summarized in a companion paper [33], the predicted volume and surface radiative properties are applied to the simulation of the reflectance, transmittance, and emittance of thin slabs of the porous alumina ceramic. The numerical results are then validated with spectroscopic measurements.

1.1. Mathematical notation

Throughout this work, tensorial notation is used with first-order tensors ("vectors") and second-order tensors ("matrices") in bold face. Different quantities sharing the same symbol are distinguished by their styles (italic, cursive, or upright). The spectral dependence of energetic quantities and time dependence of electromagnetic fields are implied, and not denoted explicitly to improve readability.

2. Effective radiative properties modeling

In this section, we first introduce the effective volume and surface radiative properties of interest (section 2.1). Several analytical models commonly used to obtain these properties, along with their

limitations, are then presented in section 2.2. We then propose a new physical optics approach based on the discrete dipole approximation (DDA) to calculate the effective volume and surface radiative properties while taking into account wave effects and dependent scattering.

2.1. Definition of effective radiative properties

At the macro-scale, the heterogeneous material is modeled as an equivalent homogeneous semi-transparent medium, assumed isotropic with azimuthal asymmetry. The effective refractive index n_{eff} of the equivalent medium may be calculated analytically, for example with the volume-averaging definition [34]:

$$n_{\text{eff}}^2 = n_m^2 f_m + \sum_p n_p^2 f_p \tag{1}$$

where n is the refractive index and f is the volume fraction of the matrix (subscript m) and heterogeneities (subscript p for pores/particles) respectively.

The influence of the micro-scale heterogeneities on the macro-scale scattering and absorption behavior is represented through spectral effective properties, illustrated in Figure 2 and defined in this section. Note that the spectral dependence of all quantities is not denoted explicitly for readability.

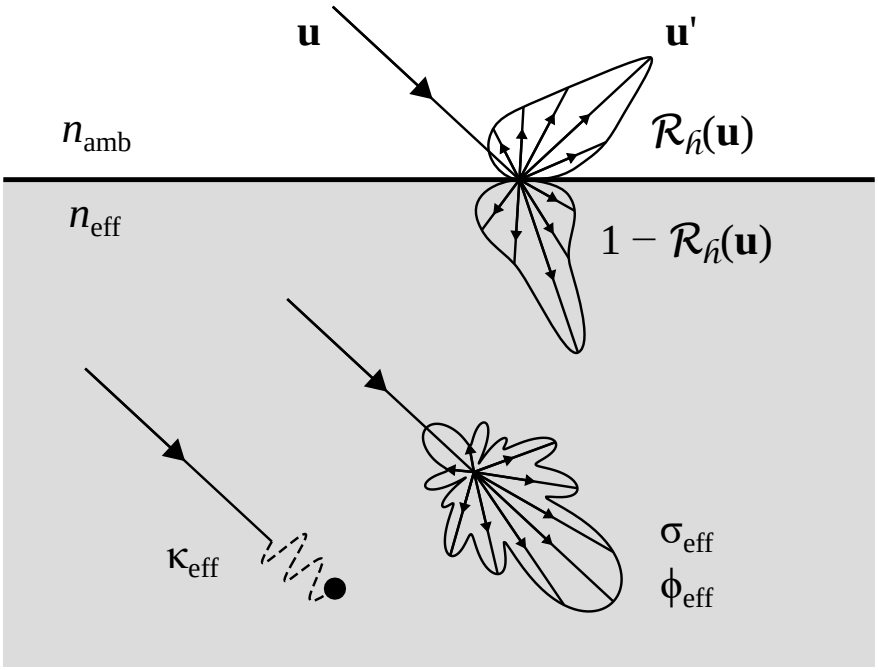

Figure 2: Schema of the equivalent homogeneous medium with its effective radiative properties.

Within the equivalent homogeneous medium, the radiance $\mathcal{I}$ in an elementary solid angle $\mathrm{d}\Omega$ associated with the unit direction vector $\mathbf{u}$ is modeled with the classic radiative transfer equation (RTE) [35]:

$$\mathbf{u} \cdot \boldsymbol{\nabla}\mathcal{I}(\mathbf{u}) = -[\sigma_{\text{eff}} + \kappa_{\text{eff}}]\mathcal{I}(\mathbf{u}) + n_{\text{eff}}^2 \kappa_{\text{eff}} \mathcal{B}(T) + \int_{4\pi} \sigma_{\text{eff}} \phi_{\text{eff}}(\mathbf{u}', \mathbf{u}) \mathcal{I}(\mathbf{u}')\, \mathrm{d}\Omega' \tag{2}$$

where σ_{eff} is the effective scattering coefficient, κ_{eff} is the effective absorption coefficient, and ϕ_{eff} is the effective scattering phase function describing the angular distribution of scattered energy. These three quantities are henceforth referred to as the effective volume radiative properties. Note that 4π is the solid angle of a sphere representing the entire angular space, and ϕ_{eff} is normalized such that:

$$\int_{4\pi} \phi_{\text{eff}}(\mathbf{u}, \mathbf{u}')\, \mathrm{d}\Omega' = 1 \tag{3}$$

Since azimuthal symmetry is assumed, $\phi_{\text{eff}}(\mathbf{u}, \mathbf{u}') = \phi_{\text{eff}}(\theta)$, with θ being the angle between the unit direction vectors $\mathbf{u}$ and $\mathbf{u}'$.

Light incident on the interface between the heterogeneous material and its surroundings (which we assume has a refractive index $n_{\text{amb}} < n_{\text{eff}}$) potentially undergoes complex interactions due to interface roughness effects [26]. At the macro-scale, this interface is modeled as sharp and non-absorbing. The effective interface scattering behavior may then be represented by a bidirectional scattering distribution function (BSDF), defined as the ratio between the scattered radiance $\mathcal{I}_{\text{sca}}$ along the direction $\mathbf{u}'$ and the incident intensity I_{inc} concentrated in a narrow solid angle $\Delta\Omega$ about the direction $\mathbf{u}$ [25]:

$$\text{BSDF}(\mathbf{u}, \mathbf{u}') \equiv \frac{\mathcal{I}_{\text{sca}}(\mathbf{u}')}{I_{\text{inc}}(\mathbf{u})|\mathbf{u}\cdot\mathbf{n}|} = \frac{\mathcal{I}_{\text{sca}}(\mathbf{u}')}{\int_{\Delta\Omega} \mathcal{I}_{\text{inc}}(\mathbf{u})|\mathbf{u}\cdot\mathbf{n}|\, \mathrm{d}\Omega} \tag{4}$$

where $\mathbf{n}$ is the outward-pointing interface normal vector. Complete characterization of the BSDF is onerous and not always necessary [25]. In this work, we focus on the the reflective behavior of the material surface under illumination from the surrounding medium (i.e., we only consider $\mathbf{u}$ for which $\mathbf{u}\cdot\mathbf{n} < 0$), which we represent by the bidirectional surface reflectivity $\mathcal{R}(\mathbf{u}, \mathbf{u}')$ defined for a finite number of scattered directions $\mathbf{u}'$:

$$\mathcal{R}(\mathbf{u}, \mathbf{u}') \equiv \frac{I_{\text{sca}}(\mathbf{u}')|\mathbf{u}'\cdot\mathbf{n}|}{I_{\text{inc}}(\mathbf{u})|\mathbf{u}\cdot\mathbf{n}|} = \int_{\Delta\Omega'} \text{BSDF}(\mathbf{u}, \mathbf{u}')|\mathbf{u}'\cdot\mathbf{n}|\, \mathrm{d}\Omega', \quad \mathbf{u}\cdot\mathbf{u}' < 0 \tag{5}$$

where $\Delta\Omega'$ is the solid angle associated with the scattered direction $\mathbf{u}'$. The directional-hemispherical surface reflectivity under external illumination $\mathcal{R}_{\text{fi}}(\mathbf{u})$ is then defined as follows:

$$\mathcal{R}_{\text{fi}}(\mathbf{u}) \equiv \int_{\mathbf{u}\cdot\mathbf{u}'<0} \text{BSDF}(\mathbf{u}, \mathbf{u}')|\mathbf{u}'\cdot\mathbf{n}|\, \mathrm{d}\Omega' = \sum_{\mathbf{u}\cdot\mathbf{u}'<0} \mathcal{R}(\mathbf{u}, \mathbf{u}') \tag{6}$$

In the absence of absorption at the interface, conservation of energy then gives the directional-hemispherical transmissivity from the surroundings into the material as $\mathcal{T}_{\text{fi}}(\mathbf{u}) = 1 - \mathcal{R}_{\text{fi}}(\mathbf{u})$.

2.2. Analytical modeling of effective radiative properties

We present here a few analytical models commonly used to calculate the effective volume and surface radiative properties (σ_{eff}, κ_{eff}, ϕ_{eff}, $\mathcal{R}(\mathbf{u}, \mathbf{u}')$), alongside their hypotheses and limitations.

Recall that we chose to focus on materials composed of a weakly absorbing solid matrix and heterogeneities (pores or particles) of comparable size to the wavelength. When the volume fraction of heterogeneities is low, the matrix phase may be considered as the host medium for radiative

transfer (e.g., [16]).

2.2.1. Volume absorption and scattering

The effective absorption coefficient κ_{eff} includes contributions of absorption by the matrix and the heterogeneities:

$$\kappa_{\text{eff}} = \kappa_{\text{eff},m} + \kappa_{\text{eff},p} \tag{7}$$

When the intrinsic absorptivity of the matrix is low, it can be assumed that absorption by the matrix does not depend on the morphology and spatial distribution of the scattering heterogeneities [6]. The following relation, proposed by Dombrovsky and Baillis [5], Dombrovsky et al. [6] for porous ceramics, may then be used to model absorption by the matrix:

$$\kappa_{\text{eff},m} = \frac{4\pi\kappa_m}{\lambda_0} f_m \tag{8}$$

where κ_m is the absorption index of the solid phase.

Likewise, when the matrix absorptivity is low, scattering and absorption by the heterogeneities may be considered as occurring within an infinite transparent host medium of refractive index n_m [6]. Analytical solutions for scattering and absorption by small objects are available only for isolated objects of simple geometry (e.g., Mie theory for spheres and cylinders [9]) in an infinite matrix. As such, the effective absorption and scattering behavior of a cluster of pores or particles ($\kappa_{\text{eff},p}$ and σ_{eff} in the present context) are often discussed in relation to the independent scattering hypothesis [3, 13]. This hypothesis assumes that each pore or particle is sufficiently far away from their closest neighbor such that it scatters and absorbs as if in isolation. As such, $\kappa_{\text{eff},p}$ and σ_{eff} may be computed as a sum of the contribution of individual heterogeneities.

For a material containing spherical pores/particles of equal radius a_p, $\kappa_{\text{eff},p}$ and σ_{eff} under the independent scattering hypothesis are then given as [36]:

$$\kappa_{\text{eff},p} = C_{\text{abs},p} N_V = \frac{C_{\text{abs},p} f_p}{\frac{4}{3}\pi a_p^3} \tag{9a}$$

$$\sigma_{\text{eff}} = C_{\text{sca},p} N_V = \frac{C_{\text{sca},p} f_p}{\frac{4}{3}\pi a_p^3} \tag{9b}$$

where $C_{\text{abs},p}$ and $C_{\text{sca},p}$ are the absorption and scattering cross sections of a single sphere given by Mie theory [9], and N_V is the number of spheres per unit volume. On the other hand, the effective scattering phase function ϕ_{eff} is simply taken as that of a single sphere [13, 36].

Many past investigations [10, 11, 13, 37, 38] have sought to establish validity criteria of the independent scattering hypothesis. Galy et al. [13] found that for equation (9b) to be valid, a minimal distance between each sphere is required: 5λ for $\chi_p > 2$, and 2λ for $\chi_p \leq 2$, where $\chi_p = k a_p = 2\pi a_p/\lambda$ is the Mie size parameter. Regarding the phase function, Mishchenko et al. [37] showed that the scattering phase function of a cluster of spheres is practically never equal to that of a single sphere, even at extremely low sphere fractions ($f_p << 1\%$), due to forward-scattering interference and coherent backscattering [11] phenomena.

2.2.2. Surface reflectivity under external illumination

Specular reflection of light by smooth surfaces is well-described by Fresnel's equations [25]. On the other hand, the scattering of light off a rough surface depends heavily on the sizes of surface asperities as well as the characteristic distances between them [26–28]. When surface asperities are large and far apart compared to the wavelength, the geometrical optics approximation may be applied [27] while assuming Fresnel's equations hold at every point on the surface, to model the reflectivity of arbitrary surface profiles and eventually account for multiple reflection [39]. A common simplification considers the effective reflection behavior of the surface as the sum of a perfectly specular and a perfectly diffuse component [25, 31, 40]:

$$\mathcal{R}_{\hbar} = \mathcal{R}_{\text{spec}} + \mathcal{R}_{\text{diff}} = \frac{\mathcal{R}_{\text{spec}}}{p_{\text{spec}}} \tag{10}$$

where p_{spec} is the so-called "specularity parameter" introduced by [40], who performed an inverse determination of this parameter based on measured reflectances and transmittances.

When the length scales of the surface asperities are of the same order as the wavelength, reflection should be considered within the electromagnetic scattering framework [28]. Purely physics-based solutions have been developed for light at near-normal incidence on locally smooth surfaces often assumed to follow a Gaussian height distribution and surface correlation function [28]; a well-known example, the Beckmann-Kirchhoff model [26], gives a closed-form expression for $\mathcal{R}_{\hbar}$ of the same form as equation (10). While a number of phenomenological corrections have been proposed in recent years to account for multiple scattering and shadowing [29], they still depend on analytical Gaussian or exponential roughness descriptions. Such descriptions are not necessarily suitable for the porous surfaces of interest in our study since pores are more accurately modeled as random defects instead of Gaussian-like fluctuations, and alternative Mie scattering or diffraction grating-based analytical models might be more appropriate instead [28]. Recently, Liu et al. [31] established phenomenological relations for $\mathcal{R}_{\hbar}$ and p_{spec} of a rough nickel surface based on numerical FDTD modeling on digitally generated surface samples.

Judging by the numerous physical and geometrical assumptions necessary in the existing analytical models, the development of physical-optics-based numerical methods to compute effective volume and surface radiative properties of arbitrary microstructures is clearly of great interest. In the next section, we propose two models based on the DDA to compute the effective volume radiative properties (σ_{eff}, κ_{eff}, ϕ_{eff}) and the bidirectional surface reflectivity under external illumination $\mathcal{R}(\mathbf{u}, \mathbf{u}')$ directly from the 3D microstructure and the refractive indexes of the constituent phases.

2.3. Physical optics computation of effective radiative properties with the discrete dipole approximation (DDA)

To take into account wave effects and dependent scattering, we propose a numerical approach that uses the Discrete Dipole Approximation (DDA) to solve Maxwell's equations on microstructural models of the heterogeneous material. The DDA calculates scattering and absorption of an incident monochromatic plane wave by an irregular heterogeneous target by approximating it as a finite array of point dipoles [19]. We first present the key governing equations of the DDA (section 2.3.1), then describe our proposed model configurations to compute the volume and surface

radiative properties (sections 2.3.2 and 2.3.3). We then end this section with an analysis on the main sources of uncertainty in our proposed approach (section 2.3.4).

2.3.1. Governing equations

The DDA is based on the volume integral form of the macroscopic Maxwell's equations (interested readers may consult the abundant literature on its theoretical derivation [18, 19, 41, 42]). Here, the formalism by Draine and Flatau [20] is used. We consider a dielectric target approximated by an array of N small volume cells on a regular cubic grid with cell size d. It is assumed that each cell j may be represented by a single dipole located at its center $\mathbf{x}_j$, with a complex refractive index $m_j = n_j + i\kappa_j$ assumed isotropic.The target dipole array is illuminated by a monochromatic plane wave $\mathbf{E}_{\text{inc}}$ of wavelength λ in the transparent ambient medium propagating in the direction $\mathbf{u}$, whose amplitude at $\mathbf{x}_j$ is of the form:

$$\mathbf{E}_{\text{inc}}(\mathbf{x}_j) = \mathbf{E}_0 \exp\left(i\mathcal{k}\mathbf{u}\cdot\mathbf{x}_j\right) \equiv \mathbf{E}_{\text{inc},j} \tag{11}$$

where $\mathbf{E}_0$ is a complex vector and $\mathcal{k} = 2\pi/\lambda$ is the angular wavenumber in the ambient medium. Not that the time dependence of electromagnetic fields are implicit. Each dipole acquires a dipole moment $\mathbf{P}_j \equiv \mathbf{P}(\mathbf{x}_j)$ in response to the local electric field $\mathbf{E}_j \equiv \mathbf{E}(\mathbf{x}_j)$:

$$\mathbf{P}_j = \boldsymbol{\alpha}_j \cdot \mathbf{E}_j \tag{12}$$

where $\boldsymbol{\alpha}_j \equiv \boldsymbol{\alpha}(\mathbf{x}_j, m_j, \mathcal{k}, d)$ is the polarizability matrix of the dipole, which we prescribe with the Lattice Dispersion Relation [43] based on our sensitivity study in section 3. Note that as radiative heat transfer usually considers unpolarized light, DDA computations are first obtained for two orthogonal incident polarizations then averaged.

The local electric field $\mathbf{E}_j$ is the sum of the incident field and the contribution from all the other dipoles:

$$\mathbf{E}_j = \mathbf{E}_{\text{inc},j} - \sum_{k=1}^{N} \mathbf{A}_{jk} \cdot \mathbf{P}_k \tag{13}$$

where $\mathbf{A}_{jk} \equiv \mathbf{A}(\mathbf{x}_j, \mathbf{x}_k, \mathcal{k})$ is a 3×3 complex matrix describing the influence of the dipole k on the local electric field $\mathbf{E}_j$. Expressions for $\mathbf{A}_{jk}$ will be given in the next two subsections.

Combining equations (12) and (13) gives the governing equation of the DDA:

$$\mathbf{E}_{\text{inc},j} = \boldsymbol{\alpha}_j^{-1} \cdot \mathbf{P}_j + \sum_{k=1}^{N} \mathbf{A}_{jk} \cdot \mathbf{P}_k \tag{14}$$

This reduces the scattering problem to a linear system of $3N$ complex equations with $\mathbf{P}$ as the unknown, as $\boldsymbol{\alpha}$ is prescribed and $\mathbf{E}_{\text{inc}}$ and $\mathbf{A}$ are computed directly from the target configuration. We solved for $\mathbf{P}$ iteratively using various complex conjugate gradient methods [44, 45] implemented in the open-source code DDSCAT (version 7.3.3, published on 10 July 2019 [20, 46, 47], double precision).

The next two subsections present the configurations used to compute the volume radiative properties (σ_{eff}, κ_{eff}, and ϕ_{eff}) and the bidirectional surface reflectivity under external illumination

$\mathcal{R}(\mathbf{u}, \mathbf{u}')$ respectively.

2.3.2. Volume radiative properties

Inspired by the approach of Coquard and Baillis [36], we propose to calculate the effective volume radiative properties (scattering coefficient σ_{eff}, absorption coefficient κ_{eff}, and scattering phase function ϕ_{eff}) from by considering the interaction of light with a spherical volume element of the material of diameter D, as illustrated in Figure 3. The spherical target, composed of the matrix and pore/particle phases (with complex refractive indexes denoted $m_m = n_m + i\kappa_m$ and $m_p = n_p + i\kappa_p$ respectively), is illuminated by a monochromatic plane wave traveling in the direction $\mathbf{u}$ in a non-absorbing surrounding medium for which we set the refractive index as $n_{\text{amb}} = n_m$.

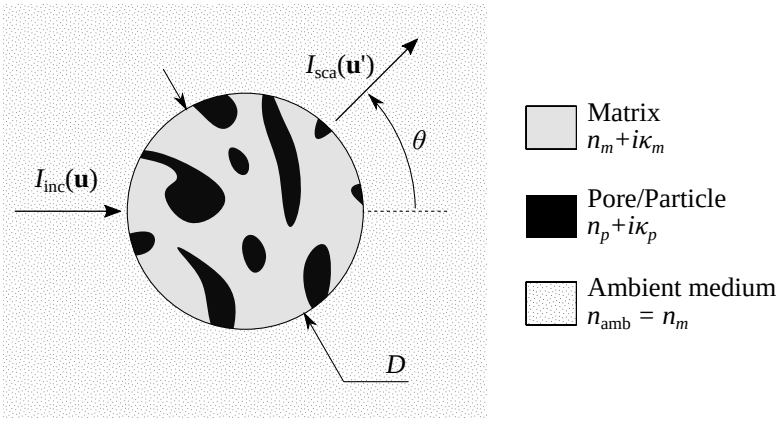

Figure 3: Computation of effective volume radiative properties from a spherical volume element of the material.

While we aim to model the extinction of light by scattering and absorption within the target volume, edge effects exist due to truncated pores/particles on the target boundary distorting the scattering behavior, and the mismatch between m_m and n_{amb} causing spurious reflections off the target boundary. To keep these edge effects to a minimum, we restrict our study to materials with a weakly absorbing matrix phase (low κ_m) having a significantly higher volume fraction than the pore/particle phases, and use targets much larger than the size of the heterogeneities as well as the wavelength of interest.

For every dipole j in the target volume, the matrix $\mathbf{A}_{jk}$ describing the influence of the k-th dipole on the local electric field is given by [20]:

$$\mathbf{A}_{jk} = \mathbf{A}'(\mathbf{x}_k - \mathbf{x}_j) \tag{15}$$

The interaction matrix $\mathbf{A}'$ is defined for a given distance vector $\mathbf{r}$ as:

$$\mathbf{A}'(\mathbf{r}) = \begin{cases} \mathbf{0}_3 & \text{if} \quad |\mathbf{r}| = 0 \\ \dfrac{\exp\left(i\mathcal{k}|\mathbf{r}|\right)}{4\pi\varepsilon_0|\mathbf{r}|}\left[\mathcal{k}^2\left(\dfrac{\mathbf{r}\mathbf{r}}{|\mathbf{r}|^2} - \mathbf{1}_3\right) + \dfrac{i\mathcal{k}|\mathbf{r}| - 1}{|\mathbf{r}|^2}\left(\dfrac{3\mathbf{r}\mathbf{r}}{|\mathbf{r}|^2} - \mathbf{1}_3\right)\right] & \text{otherwise} \end{cases} \tag{16}$$

where ε_0 is the permittivity of free space, $\mathbf{0}_n$ is the n-dimensional zero matrix, and $\mathbf{1}_n$ is the n-dimensional identity matrix.

P is then solved using equation (14), and used to calculate the extinction, absorption and scattering[1] cross sections C according to the relations proposed by Draine [41]:

$$C_{\text{ext}} = \frac{k}{\varepsilon_0 |\mathbf{E}_{\text{inc}}|^2} \sum_{j=1}^{N} \text{Im}\left(\overline{\mathbf{E}}_{\text{inc,j}} \cdot \mathbf{P}_j\right) \tag{17}$$

$$C_{\text{abs}} = \frac{k}{\varepsilon_0 |\mathbf{E}_{\text{inc}}|^2} \sum_{j=1}^{N} \left\{ \text{Im}\left(\mathbf{P}_j \cdot \overline{\boldsymbol{\alpha}}_j^{-1} \cdot \overline{\mathbf{P}}_j\right) - \frac{2}{3} k^3 \mathbf{P}_j \cdot \overline{\mathbf{P}}_j \right\} \tag{18}$$

$$C_{\text{sca}} = C_{\text{ext}} - C_{\text{abs}} \tag{19}$$

where $\overline{X}$ denotes the complex conjugate of a complex quantity X.

In the far field, the scattered intensity I_{sca} of unpolarized light at a distance r from the target in the $\mathbf{u}'$ direction may be expressed as a function of the incident intensity I_{inc} using the first principal element M_{11} of the Mueller scattering matrix [9]:

$$I_{\text{sca}}(r, \mathbf{u}') = \frac{M_{11}(\mathbf{u}')}{k^2 r^2} I_{\text{inc}}(\mathbf{u}) \tag{20}$$

where r is the distance from the target. Draine [41] computed $M_{11}(\mathbf{u}')$ from $\mathbf{u}$' and **P** as follows:

$$M_{11}(\mathbf{u}') = \frac{k^6}{(4\pi\varepsilon_0)^2 |\mathbf{E}_{\text{inc}}|^2} \left| \sum_{j=1}^{N} \left[\mathbf{P}_j - \mathbf{u}'\left(\mathbf{u}' \cdot \mathbf{P}_j\right)\right] \exp\left(-ik\mathbf{u}' \cdot \mathbf{x}_j\right) \right|^2 \tag{21}$$

Under azimuthal symmetry, M_{11} only depends on the angle θ between $\mathbf{u}$ and $\mathbf{u}'$.

The effective volume radiative properties are then calculated as follows [36]:

$$\sigma_{\text{eff}} = \frac{C_{\text{sca}}}{V} \tag{22}$$

$$\kappa_{\text{eff}} = \frac{C_{\text{abs}}}{V} \tag{23}$$

$$\phi_{\text{eff}}(\theta) = \frac{M_{11}(\theta)}{\int_{4\pi} M_{11}(\theta)\, \text{d}\Omega} \tag{24}$$

where V is the total volume of the spherical target (including pores, if any).

2.3.3. Bidirectional surface reflectivity

We consider that only heterogeneities from an optically thin region close to micro-scale rough surface contribute to macro-scale surface reflection. As such, we propose simulating a semi-infinite layer of thickness $h \ll 1/(\sigma_{\text{eff}} + \kappa_{\text{eff}})$ by applying periodic boundary conditions to a cuboidal volume

[1] Alternatively, C_{sca} may be directly calculated from **P** by injecting equations (20) and (21) into the definition: $C_{\text{sca}} I_{\text{inc}}(\mathbf{u}) = \int_{4\pi} I_{\text{sca}}(r, \mathbf{u}') r^2 \, \text{d}\Omega'$. Due to the higher computational complexity, this definition is usually preferred only when scattering is extremely weak and higher precision on C_{sca} is required [41].

element of the rough surface, illustrated in Figure 4a. The volume element is assumed aligned to the reference frame $\{\mathbf{e}_1, \mathbf{e}_2, \mathbf{e}_3\}$, and its dimensions along the principal directions are denoted h, L_2, and L_3 respectively.

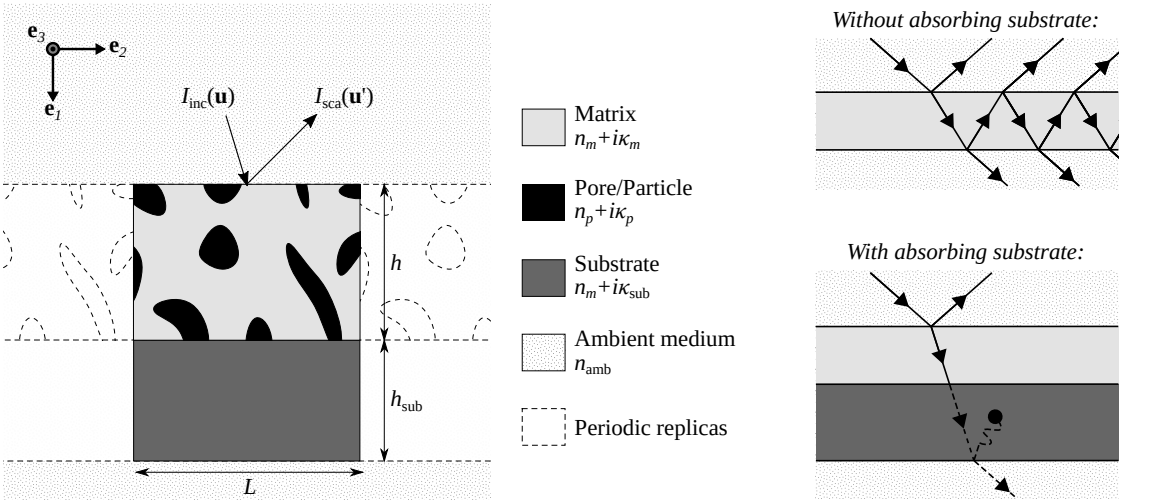

(a) Simulated configuration.

(b) Role of the absorbing substrate.

Figure 4: Computation of the bidirectional interface reflectivity from a semi-infinite layer of the material atop an absorbing substrate, via application of periodic boundary conditions to a cuboidal volume element of the material.

The top surface is illuminated by a monochromatic plane wave traveling in the $\mathbf{u}$ direction from the ambient medium of refractive index n_{amb}. As the fraction of light entering the heterogeneous layer and reaching the bottom surface should no longer contribute to reflection, we propose adding an absorbing substrate to the bottom of the heterogeneous layer to remove this fraction of light. With appropriately chosen substrate properties (refractive index n_{sub}, thickness h_{sub}, and absorption index κ_{sub}, see details in Appendix A), the interface between the top layer and the substrate becomes practically non-reflecting everywhere, save for the few locations where pores/particles are present. All light reaching the bottom surface of the top layer would then be transmitted into the substrate and absorbed, as illustrated in Figure 4b for the case of a homogeneous top layer.

Periodic boundary conditions in the DDA, first introduced by Chaumet et al. [48], are formulated by considering virtual replicas of the target volume in each direction where periodicity is enforced ($\mathbf{e}_2$ and $\mathbf{e}_3$ in the present case). For each dipole j, the 3×3 matrix $\mathbf{A}_{jk}$ describing the influence of the dipole k and all its replicas on the local electric field is written as [46]:

$$\mathbf{A}_{jk} = \sum_{v=-\infty}^{+\infty} \sum_{w=-\infty}^{+\infty} \mathbf{A}'(\mathbf{x}_{kvw} - \mathbf{x}_j) \exp\left[i k \mathbf{u} \cdot (v L_2 \mathbf{e}_2 + w L_3 \mathbf{e}_3)\right] \tag{25}$$

with $\mathbf{A}'$ as defined in equation (16), and $\mathbf{x}_{kvw} = \mathbf{x}_k + v L_2 \mathbf{e}_2 + w L_3 \mathbf{e}_3$. This infinite sum is numerically approximated by Draine and Flatau [46] through the introduction of a term containing an interaction

cut-off parameter $\gamma = 0.01$ that suppresses the influence of dipoles far apart:

$$\mathbf{A}_{jk} \approx \sum_{v,w} \mathbf{A}'(\mathbf{x}_{kvw} - \mathbf{x}_j) \exp\left[i\mathcal{k}\mathbf{u} \cdot (vL_2\mathbf{e}_2 + wL_3\mathbf{e}_3) - \left(\gamma\mathcal{k}|\mathbf{x}_{kvw} - \mathbf{x}_j|\right)^4 \right] \tag{26}$$

The sum is performed over all v and w for which $\gamma\mathcal{k}|\mathbf{x}_{kvw} - \mathbf{x}_j| \leq 2$.

$\mathbf{P}$ is then solved using equation (14), and used to compute the Mueller matrix element M_{11} according to equation (21). Draine and Flatau [46] demonstrated that for a given incident direction $\mathbf{u}$, M_{11} is defined only for directions $\mathbf{u}'$ satisfying all of the following conditions:

$$\mathbf{u}' \cdot \mathbf{u} < 0 \tag{27a}$$

$$\mathcal{k}\left(\mathbf{u}' - \mathbf{u}\right) \cdot L_2\mathbf{e}_2 = 2\pi v', \quad v' \in \mathbb{Z} \tag{27b}$$

$$\mathcal{k}\left(\mathbf{u}' - \mathbf{u}\right) \cdot L_3\mathbf{e}_3 = 2\pi w', \quad w' \in \mathbb{Z} \tag{27c}$$

$$\left(\mathbf{u}' \cdot \mathbf{e}_1\right)^2 = 1 - \left(\mathbf{u}' \cdot \mathbf{e}_2\right)^2 - \left(\mathbf{u}' \cdot \mathbf{e}_3\right)^2 > 0 \tag{27d}$$

The bidirectional reflectivity $\mathcal{R}(\mathbf{u}, \mathbf{u}')$ for unpolarized incident light is then calculated as follows [46]:

$$\mathcal{R}(\mathbf{u}, \mathbf{u}') = \frac{4\pi^2 M_{11}(\mathbf{u}')}{\mathcal{k}^4 (L_2 L_3)^2 |\mathbf{u} \cdot \mathbf{e}_1||\mathbf{u}' \cdot \mathbf{e}_1|} \tag{28}$$

2.3.4. Uncertainty analysis

We identify and comment on the most important sources of uncertainty in the proposed approach. The influence of the choice of model parameters on the accuracy of the results will be assessed in the convergence and sensitivity studies in section 3.

Uncertainty relating to cell size. In the DDA, the target geometry is approximated by finite volume cells each associated to a point dipole, leading to discretization errors as the quantities and fields within each cell are assumed constant. Shape errors also arise from meshing non-cubic geometries with a regular cubic mesh [49]. Both errors generally decrease with decreasing cell size d at higher computational cost in terms of N [18, 20, 49]. Past studies usually consider the discretization parameter y:

$$y = |m| d \frac{2\pi}{\lambda_0} \tag{29}$$

where $\lambda_0 = \lambda n_{\text{amb}}$ is the vacuum wavelength. Satisfactory results for the cross sections are generally reported for $y < 1$ [20, 49], although $y < 0.5$ may be required if directional scattering quantities are of interest [46].

In our present case, as we work with tomography-reconstructed microstructures, the input geometry has already been discretized into cubic voxels during the image acquisition process. Performing grid refinement by voxel subdivision (see illustration in Figure 5) thus reduces discretization errors only while maintaining the shape constant, which should improve grid convergence behavior.

Uncertainty relating to polarizability model. The DDA requires prescription of a polarizability model $\boldsymbol{\alpha}$, the choice of which remains an open question: while early work used the well-known Clausius-Mosotti relation [19], many improvements have been proposed over the past few

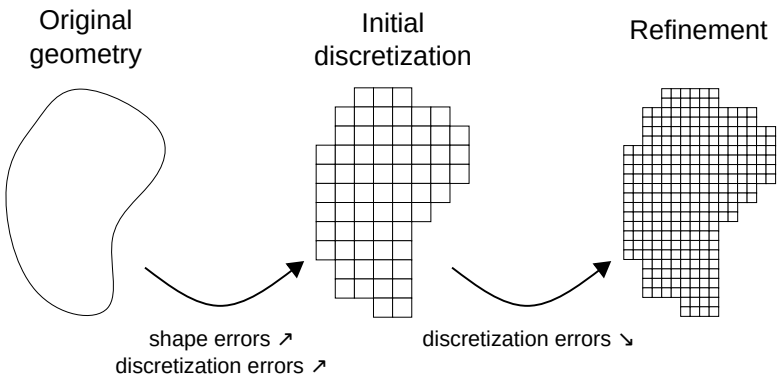

Figure 5: Shape and discretization errors in tomography-reconstructed geometries: true geometry, initial voxelization, and voxel refinement.

decades [42]. Performance of the different polarizabilities (in terms of grid convergence rate, accuracy at a given discretization, computational speed, etc.) depend on target geometry and refractive index [50] among other factors, and are usually assessed on a case-by-case basis with test microstructures, as done in section 3.

Uncertainty relating to volume element size. For random microstructures, the volume element should be large enough to minimize edge effects as well as ensure that the target microstructure and radiative behavior are truly representative of those of the material. Edge effects are mainly caused by truncated pores/particles on the target boundaries distorting the scattering behavior. Regarding material representativity, computation of deterministic effective properties from a single so-called representative volume element (RVE) is often prohibitive in random porous media due to the large memory required; instead, a large number of computations on smaller volume elements may be performed and used to deduce the statistical effective behavior of the material [51].

3. Validation on reference microstructures

In this section, we simulate the radiative characteristics of several reference microstructures to study the influence of model parameters on the accuracy of our proposed models. The influence of cell size d and volume element size V are assessed through grid and volume element size convergence studies. For the polarizability α, we compared two prescriptions that we deemed the most appropriate based on the review by Yurkin and Hoekstra [42]: the Lattice Dispersion Relation (LDR) by Gutkowicz-Krusin and Draine [43] and the Filtered Coupled Dipole (FCD) prescription by Piller and Martin [52].

Two reference microstructures of comparable composition and complexity to porous multiphase ceramics are considered for each type of model:

1. Volume radiative properties modeling on isolated spherical volume elements;
    - Scattering and absorption by a multilayered sphere with an absorbing matrix phase (section 3.1.1);
    - Scattering coefficient of a transparent solid containing random monodisperse non-overlapping spherical pores (section 3.1.2);

2. Reflectivity modeling using periodic boundary conditions on cuboidal volume elements;
    - Reflectance of a periodic ordered opal structure (section 3.2.1);
    - Specular interface reflectivity of a homogeneous semi-infinite surface (section 3.2.2).

3.1. Volume radiative properties modeling

3.1.1. Multilayered sphere with an absorbing matrix phase

We first consider the scattering and absorption behavior of a multilayered sphere for which reference solutions can be obtained with Mie theory [9, 53]. Figure 6b illustrates the radii and composition of the different layers, chosen such that the solid matrix phase m has a volume fraction of $f_m \approx 0.70$, while the pore (1) and particle (2) phases have fractions $f_1 \approx 0.18$ and $f_2 \approx 0.12$ respectively. The complex refractive indexes m of the three phases at selected wavelengths are given in Table 1. The refractive index of the ambient medium was set to $n_{\text{amb}} = n_m$ following the configuration defined in section 2.3.2.

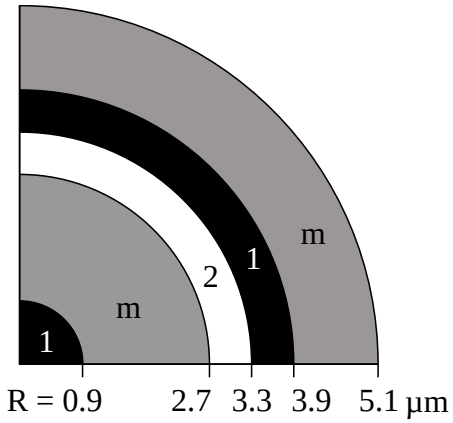

(a) Radii and composition.

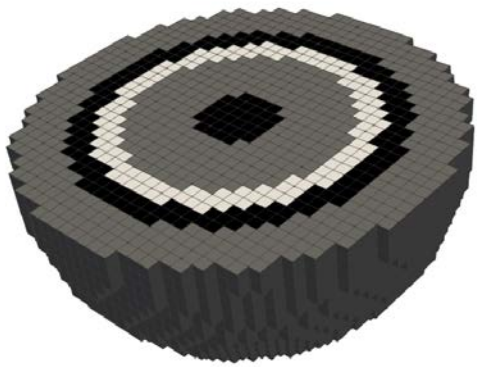

(b) Rough initial discretization with cell size $d_0 = 300$ nm.

Figure 6: Schema of the multilayered sphere. The matrix phase (m) is represented in gray, while the pore (1) and particle (2) phases are represented in black and white respectively.

To study the influence of discretization errors at constant shape errors, we first applied a rough initial discretization of $d_0 = 300$ nm to the multilayered sphere (see sectional view in Figure 6a), then subdivided each voxel the number of times necessary to obtain different desired final cell sizes. Three final cell sizes were studied in our grid convergence study: $d = 75$ nm, 60 nm, and 50 nm, corresponding to maximal discretization parameters y (see equation (29)) of 0.98, 0.78, and 0.65 respectively at $\lambda_0 = 1$ µm. In addition, we also performed computations on a finely discretized version of the multilayered sphere ($d_0 = d = 50$ nm) to study the influence of shape errors when the true geometry is known.

Figure 7 shows the reference scattering and absorption cross sections from Mie theory, and the errors in the DDA results obtained on the roughly discretized sphere ($d_0 = 300$ nm) using different polarizabilities and cell sizes. For vacuum wavelengths below 4 µm, errors in the scattering cross section are generally low, indicating a limited influence of shape errors. However, both the polarizability and the cell size have a significant influence. The LDR is preferred as it generally

λ_0 [µm]	$m_m = n_m + \kappa_m i$	$m_1 = n_1$	$m_2 = n_2 + \kappa_2 i$
1	$1.645 + 6.880 \times 10^{-7} i$	1.000	$2.079 + 1.428 \times 10^{-6} i$
2	$1.632 + 1.239 \times 10^{-6} i$	1.000	$2.068 + 1.208 \times 10^{-6} i$
3	$1.611 + 1.613 \times 10^{-6} i$	1.000	$2.048 + 1.092 \times 10^{-6} i$
4	$1.578 + 1.201 \times 10^{-5} i$	1.000	$2.020 + 4.538 \times 10^{-6} i$
5	$1.534 + 2.017 \times 10^{-4} i$	1.000	$1.982 + 7.110 \times 10^{-5} i$
6	$1.473 + 1.340 \times 10^{-3} i$	1.000	$1.933 + 5.458 \times 10^{-4} i$
7	$1.392 + 6.907 \times 10^{-3} i$	1.000	$1.870 + 2.489 \times 10^{-3} i$
8	$1.291 + 2.259 \times 10^{-2} i$	1.000	$1.800 + 1.016 \times 10^{-2} i$
9	$1.161 + 3.529 \times 10^{-2} i$	1.000	$1.707 + 6.246 \times 10^{-3} i$
10	$0.961 + 5.397 \times 10^{-2} i$	1.000	$1.581 + 8.728 \times 10^{-3} i$

Table 1: Complex refractive indexes m for the matrix (m), pore (1) and particle (2) phases of the multilayered sphere at selected vacuum wavelengths λ_0.

gives smaller errors than the FCD, with results insensitive to cell size. As for the absorption cross section, the high relative errors on this wavelength range merely reflect the significant numerical uncertainty due to the near-zero absorption, and are of little concern.

At vacuum wavelengths of 4 µm and higher, the absorption cross section shows excellent agreement with the Mie solution, while the scattering cross section differed by as high as 22%. As the DDA results are essentially independent of polarizability and cell size on this wavelength range, this error in the scattering cross section is mainly due to shape errors. Indeed, with the finely discretized sphere ($d_0 = d = 50$ nm), the discrepancy in the scattering cross section becomes lower than 5% on the whole wavelength range.

Similar conclusions can be drawn from Figure 8, in which the Mueller matrix element M_{11} at $\lambda_0 = 2$ µm obtained with the LDR on the roughly discretized sphere at different cell sizes are compared to the Mie solution. The results appear insensitive to cell size, with an excellent agreement in the forward scattering direction but with discrepancies elsewhere (especially in the backward scattering direction) mainly due to shape errors. This is confirmed by simulations on the finely discretized sphere, which gave greatly improved results everywhere save for a slight underestimation at scattering angles close to 180°.

These results indicate that when the true geometry is known, shape errors arising from the rough initial discretization have a non-negligible impact, especially on the scattering patterns. On the other hand, when shape errors are negligible such as on the wavelength range of $\lambda_0 = 1$ µm–4 µm for the present case study, a discretization parameter of $y \leq 0.98$ is sufficient for grid convergence when using the LDR polarizability model, while the FCD polarizability model does not provide converged results even for finer discretizations.

3.1.2. Transparent solid with random spherical pores

We next simulate the volume radiative properties at $\lambda_0 = 1$ µm of a transparent solid matrix ($n_m = 1.718 = n_{\text{amb}}$) containing monodisperse non-overlapping spherical pores ($n_p = 1$) of radius $a_p = 0.9$ µm, equivalent to a size parameter of $\chi_p = k a_p = 9.71$. The base microstructure is generated by successively adding spherical pores to random locations within a large cubic matrix

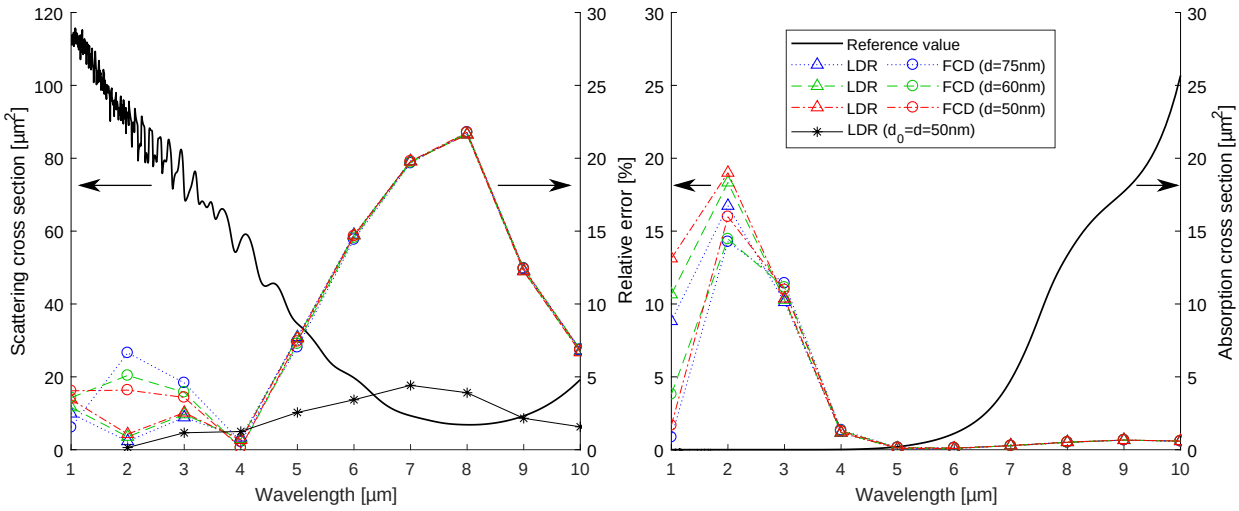

Figure 7: Scattering (left) and absorption (right) cross sections of a multilayered sphere: reference Mie solution (thick black lines) and errors in DDA results obtained on a roughly discretized sphere of initial cell size $d_0 = 300\,\text{nm}$, using the Lattice Dispersion Relation [43] (LDR, △) and Filtered Coupled Dipole [52] (FCD, ○) polarizabilities. Results are shown for three final cell sizes: $d = 75\,\text{nm}$ (dotted lines), $d = 60\,\text{nm}$ (dashed lines), and $d = 50\,\text{nm}$ (dash-dot lines). For the scattering cross section, additional results obtained with a finer initial discretization of $d_0 = d = 50\,\text{nm}$ are also given ($*$ connected with thin lines).

without any overlaps until a porosity of $f_p = 0.08$ is reached. The scattering coefficient of the material is then computed from spherical subvolumes according to the method presented in section 2.3.2. Due to memory constraints, it is generally prohibitive if not impossible to perform DDA calculations on a single target large enough to be considered a RVE [51] while maintaining a sufficiently fine discretization. Our goal here is to assess whether the effective scattering behavior of the material may still be estimated from the statistical behavior of a large number of smaller, non-representative volume elements, knowing that significant microstructural variability exists between each of them.

We performed DDA computations on volume elements with diameters ranging from $D = 6.6\,\mu\text{m}$ to $D = 13.5\,\mu\text{m}$ using the LDR [43] polarizability prescription and a discretization of $d = 75\,\text{nm}$ ($y = 0.81$). For each target size, between 27 and 125 targets were sampled from the base microstructure to assess the influence of microstructural variability on the results. As the porosity of each target generally differs from the base microstructure porosity of $f_p = 0.08$ due to the non-representative volume element sizes, each target effectively represents a slightly different base material. By considering the results of each target individually, we may observe how the DDA predictions vary statistically in response to small changes in porosity about the nominal value.

DDA results in Figure 9 show, for a given target size, a quasi-linear relation between the scattering coefficient of a target and its porosity. At a given porosity, the variation in scattering coefficient between targets of the same size decreases with increasing target size, and stabilizes at $\pm 4.9\%$ for targets with $D = 10.2\,\mu\text{m}$ and above. To judge convergence with respect to volume element size, we compare the DDA results at the nominal porosity $f_p = 0.08$ for different target sizes, and find a mere variation of -4.4% between $D = 10.2\,\mu\text{m}$ and $D = 12\,\mu\text{m}$, within the dispersion due to microstructural variability. We therefore consider that convergence with respect to volume

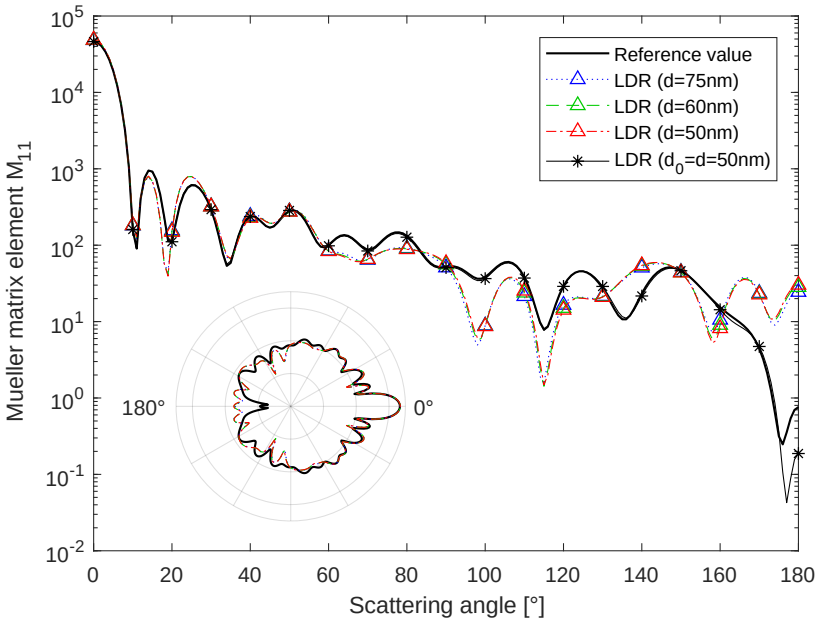

Figure 8: Mueller matrix element M_{11} of a multilayered sphere at a vacuum wavelength of $\lambda_0 = 2\,\mu\text{m}$: reference Mie solution (thick black line) and DDA results obtained on a roughly discretized sphere of initial cell size $d_0 = 300\,\text{nm}$ using the Lattice Dispersion Relation [43] (LDR, $\triangle$) polarizability. Results are shown for three final cell sizes: $d = 75\,\text{nm}$ (dotted lines), $d = 60\,\text{nm}$ (dashed lines), and $d = 50\,\text{nm}$ (dash-dot lines). In addition, results obtained with a finer initial discretization of $d_0 = d = 50\,\text{nm}$ are also given ($*$ connected with thin lines). Note that the angle 0° corresponds to forward scattering and 180° to backward scattering, and that scattering patterns are plotted on a logarithmic scale, both in the main graph and the inset.

element size is reached at $D = 10.2\,\mu\text{m}$.

Out of curiosity, we also compared the DDA results to the independent scattering solution (equation (9b)), with the scattering cross section of a single pore given by Mie theory [9, 53]. Two main sources of discrepancies between the present DDA results and the independent scattering hypothesis are expected:

1. Occurrences of smaller non-spherical pores truncated by the target boundary, which are more present in smaller targets. For the considered nominal porosity and wavelength, the total scattering cross section increases when a larger number of pores that are slightly smaller than the nominal pore size are present. As a result of these edge effects, DDA results for smaller targets tend to predict a higher scattering coefficient than the independent scattering solution.
2. Occurrences of pores close together, which are more present in larger targets and in targets with high porosity. These give rise to stronger dependent scattering effects such as shadowing that tend to diminish the scattering contribution of some pores [11], giving a lower scattering coefficient than the independent scattering solution.

Nevertheless, as the mean distance between pores [54] is large (about $7\,\mu\text{m} \approx 12\lambda$), the converged DDA results remain close to the independent scattering solution despite these sources of discrepancies.

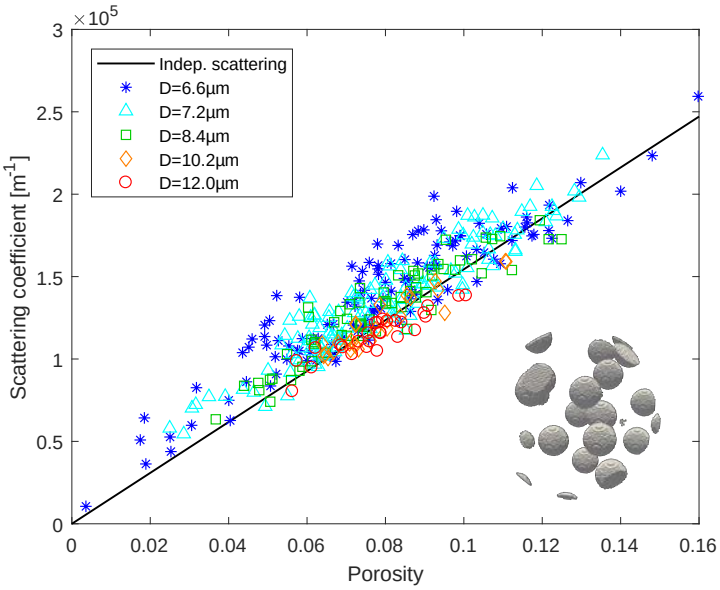

Figure 9: Scattering coefficient at $\lambda_0 = 1\,\mu$m as a function of porosity, computed from spherical targets containing a transparent solid matrix with monodisperse non-overlapping spherical pores. Each point represents DDA results for a single target of diameter D. The independent scattering solution (black line) is also given. An example target with $D = 10.2\,\mu$m is featured in the inset, with only the pores shown.

Our results indicate that the effective properties of a random material can indeed be estimated to good accuracy from samples of sub-RVE sizes, on the condition that the volume elements are sufficiently large to limit edge effects. Simulations over a large number of samples help gauge convergence with respect to volume element size D, and provides an estimate of the uncertainty due to microstructural variability. For example, in the present case study, convergence is reached at $D = 10.2\,\mu$m. The uncertainty in the scattering coefficient at $f_p = 0.08$ is estimated as $\pm 4.9\%$ based on simulations on 27 samples of the same size.

3.2. Reflectivity modeling

3.2.1. Periodic ordered opal structure

We next simulate the normal-hemispherical reflectance of a semi-infinite layer of the periodic ordered opal structure previously studied by Liu et al. [30]. The cuboidal periodic unit cell is composed of solid alumina spheres 1 µm in diameter arranged in a hexagonal close packed lattice (see Figure 10), and has a porosity of $f_p = 0.24$. The surrounding medium as well as the pore phase has refractive index $n_{\text{amb}} = n_p = 1$. Details on the geometry and solid phase complex refractive index n_m are given by Liu et al. [30], whose work provides reference numerical results obtained with the finite-domain-time-difference (FDTD) method. Note that unlike the FDTD which requires the simulation of a 2×2 tessellation of unit cells for convergence [30], in the DDA, only one unit cell needs to be simulated. The normal-directional reflectance is first computed from the polarization field $\mathbf{P}$ through equation (28), then used to calculate the normal-hemispherical reflectance via equation (6).

We first performed a grid convergence study by applying different levels of initial discretization without further refinement ($d = d_0$), which means that both shape and discretization errors decrease with decreasing cell size. In addition, we also compared two polarizability prescriptions (LDR [43] and FCD [52]) to assess their influence. Results for selected wavelengths are plotted as a function of discretization parameter y in Figure 10a. We observe a smooth grid convergence behavior for wavelengths of $\lambda_0 = 1.5\,\mu\text{m}$ and above, while for shorter wavelengths, a much higher sensitivity to cell size and polarizability is observed. A low discretization parameter y of between 0.15 and 0.09 depending on wavelength is required for grid convergence, of the same order as grid sizes used by Liu et al. [30] for their FDTD simulations on this microstructure. Note that this is much stricter than the $y < 0.5$ criterion that Draine and Flatau [46] found sufficient for DDA simulation on homogeneous thin slabs. Converged results for both the LDR and FCD polarizabilities are practically identical.

We also compared results obtained with $d = 12.5\,\text{nm}$ (which gives $y \leq 0.18$, maximal at $\lambda_0 = 0.76\,\mu\text{m}$) to reference results by Liu et al. [30] in Figure 10b. Excellent agreement in the results is found, especially on the wavelength range $\lambda_0 \geq 1.5\,\mu\text{m}$. This threshold of $\lambda_0 = 1.5\,\mu\text{m}$ corresponds in fact to the limit between the long-wavelength response of this structure where the reflectance varies smoothly with wavelength, and the short-wavelength response where sharp peaks and dips in the reflectance arise from resonance effects from the highly ordered microstructure. Shape errors due to discretization can have a large impact on the short-wavelength response, which explains the slow grid convergence for $\lambda_0 < 1.5\,\mu\text{m}$, as well as the discrepancies at certain resonance peaks between our results and the reference.

To conclude, the DDA gives accurate results for the reflectance of the ordered opal structure with a discretization of $y \approx 0.15$ for most wavelengths, although a much finer grid ($y \leq 0.09$) may be needed for grid convergence at short wavelengths due to resonance effects. It should be noted however that the extreme sensitivity to shape errors is mainly due to the high geometric regularity in addition to the spherical contours in the present microstructure, and should be less of a problem when performing simulations on tomography-reconstructed random porous ceramics.

3.2.2. Homogeneous semi-infinite surface

Our final case study aims to assess the accuracy of the surface reflectivity computed according to the method proposed in section 2.3.3, which involves simulating a semi-infinite layer of the material illuminated from above with non-reflecting boundary conditions for light transmitted into the material that reaches the bottom surface. The non-reflecting boundary conditions are simulated by adding an absorbing substrate with properties chosen according to Appendix A.

We consider the limiting case where the top layer is a smooth homogeneous slab of refractive index $n_m + i\kappa_m$, without any pores or particles. The model should then predict the interface reflectivity given by Fresnel's equations [25, 55]:

$$\mathcal{R}_{\text{/\!/}}(\mathbf{u}) = \mathcal{R}_{\text{Fr}}(\mathbf{u}) = \frac{(n_m - n_{\text{amb}})^2 + \kappa_m^2}{(n_m + n_{\text{amb}})^2 + \kappa_m^2} \tag{30}$$

For a top layer with $n_m = 1.718$, $\kappa_m = 0$, and $n_{\text{amb}} = 1$, the absorbing substrate properties are chosen as $n_{\text{sub}} = n_m$, $\kappa_{\text{sub}} = 0.09$, and $h_{\text{sub}} = 2.1\,\mu\text{m}$ (see Appendix A). Results for our grid

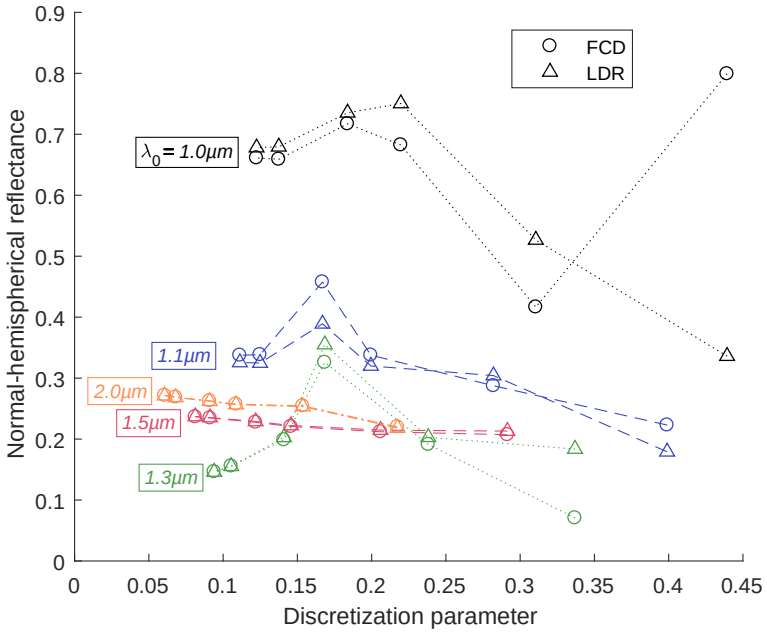

(a) Grid convergence results for selected wavelengths.

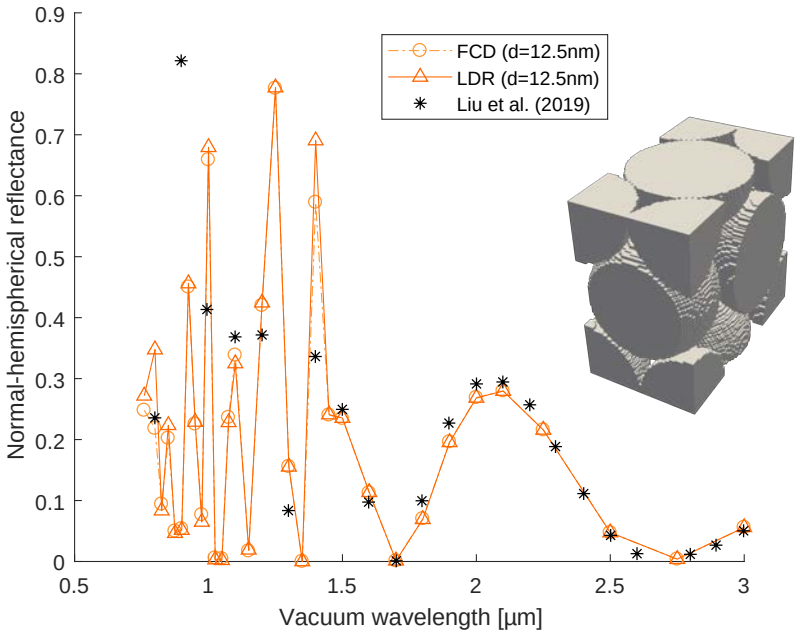

(b) Comparison with results by Liu et al. [30].

Figure 10: Spectral normal-hemispherical reflectance of an ordered opal structure [30] simulated with the DDA with the Lattice Dispersion Relation [43] (LDR, △) and Filtered Coupled Dipole [52] (FCD, ○) polarizability prescriptions. Converged results obtained with $d = 12.5$ nm are compared to reference results by Liu et al. [30] (∗), with the corresponding periodic unit cell illustrated in the inset.

convergence study for different top layer thicknesses h and with the LDR [43] and FCD [52] polarizabilities are shown in Figure 11. We observe that for different values of h, the simulated normal-normal reflectivity converges to different values at about $\pm 2.5\%$ of the normal-normal reflectivity. This is because the proposed implementation of non-reflecting boundary conditions at the bottom surface of the top layer only reduces the boundary reflectivity to an extremely low but non-zero value (see Figure A.17b). Interference effects due to the residual reflections thus cause extremely small oscillations about the target reflectivity.

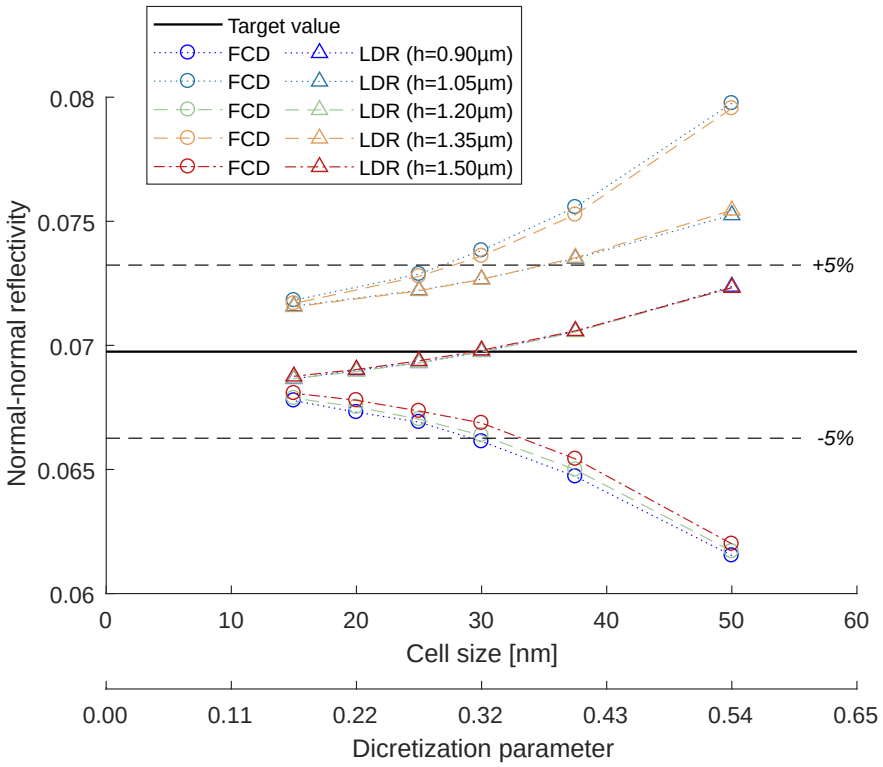

Figure 11: Normal-normal reflectivity of a homogeneous semi-infinite surface simulated from a thin layer of thickness h atop an absorbing substrate: DDA grid convergence results for different h and polarizability prescriptions (Lattice Dispersion Relation, LDR [43] and Filtered Coupled Dipole, FCD [52]), compared to the target reflectivity from Fresnel's equations [25] with a $\pm 5\%$ error band.

The variation of reflectivity with the discretization parameter y is well-described by a second-order polynomial as observed by Yurkin et al. [49], thanks to the absence of shape errors, with the FCD giving higher errors at equal cell sizes comapred to the LCD, as well as being more sensitive to cell size. While grid convergence is only reached for cell sizes $d < 15\,\text{nm}$ (corresponding to $y < 0.16$, as was observed for the ordered opal structure in section 3.2.1), using the LDR polarizability with a discretization of $y < 0.4$ is sufficient to ensure results within 5% of the target value, regardless of the top layer thickness h.

3.3. Summary of validation studies

Through convergence and sensitivity studies in this section on reference geometries, we were able to confirm the ability of our proposed models to obtain model-parameter-independent results

for the volume radiative properties and surface reflectivity, as well as estimate the error arising from the choice of model parameters: polarizability $\boldsymbol{\alpha}$, cell size d, and volume element size V. Key takeaways are summarized below:

- The influence of shape errors is shown to be non-negligible when simulating non-cubic shapes. As our model is intended for tomography-reconstructed microstructures, the actual geometry would already have been discretized during the imaging process. Assuming a sufficiently fine resolution has been used to obtain the input microstructure, we focus on choosing a level of grid refinement that gives a low enough discretization parameter y (defined in equation (29)) to keep discretization errors within 5%, while keeping the input shape constant (see discussion in section 2.3.4).

- For the considered geometries and refractive indexes, when the discretization is sufficiently fine such that the results are close to their grid-independent values, we found that the Lattice Dispersion Relation (LDR [43]) gave equal or more accurate results than the Filtered Coupled Dipole (FCD [52]) polarizability prescription at equal cell size. We also observed generally shorter computational times with the LDR. It must be noted that these observations are only valid for the considered refractive indexes, which are close to 1; Yurkin et al. [50] showed that the FCD outperforms the LDR at extremely high refractive indexes.

- Complete grid independence requires an extremely fine discretization (e.g. $y < 0.09$ for the ordered opal structure in section 3.2.1). At this discretization, results obtained with the LDR and FCD are practically identical. However, this level of discretization is impractical as it severely limits the volume element sizes that can be simulated.

- When shape errors are absent or negligible in the reference microstructures studied, using the LDR polarizability, an accuracy of within 5% of the reference solutions is achieved using a discretization of $y < 1$ for the computation of volume radiative properties, and $y < 0.4$ for the computation of interface reflectivity.

- For random materials, direct simulation on large representative volume elements (RVEs) is usually prohibitive due to memory limitations. Nevertheless, our results suggest that convergence of the statistical radiative properties with volume element sizes may still be reached at sub-RVE sizes. Convergence as well as the uncertainty due to microstructural variability may be evaluated by performing DDA computations on a large number of volume elements.

4. Application to a porous alumina ceramic

In this section, we apply the models proposed in section 2 to compute the effective radiative properties of a tomography-reconstructed porous α-alumina ceramic for selected wavelengths between $\lambda_0 = 1\,\mu\text{m}$ and $\lambda_0 = 7\,\mu\text{m}$. The material and its microstructure are first described in section 4.1. The choice of modeling parameters and procedure is then described in section 4.2, and results are discussed in section 4.3.

4.1. Material and microstructure

The studied material is a high-purity porous sintered alumina ceramic, composed of 99% α-alumina by mass. Grain boundary effects in the polycrystalline alumina phase may be neglected thanks to its high purity and large grain sizes: the volume median diameter of 2.9 µm before sintering, larger than the threshold of $\lambda_0/10$ below which grain boundary scattering is generally observed [56]. As such, the solid matrix, denoted with the subscript m, is assumed here to be isotropic and homogeneous. The refractive index n_m and absorption index κ_m are therefore calculated via the averaging relation proposed by Pajdzik and Glazer [57] from room-temperature birefringent optical data measured on alumina monocrystals [58]. Table 2 lists n_m and κ_m for selected wavelengths λ_0 between 1 µm and 7 µm.

λ_0 [µm]	n_m	κ_m
1.0	1.718	1.362×10^{-41}
1.5	1.712	8.119×10^{-21}
2.0	1.704	7.223×10^{-14}
3.0	1.680	4.251×10^{-9}
4.0	1.644	3.434×10^{-7}
5.0	1.594	2.775×10^{-5}
6.0	1.527	2.375×10^{-4}
7.0	1.435	1.942×10^{-3}

Table 2: Refractive index n_m and absorption index κ_m of the polycrystalline alumina matrix at 295 K at selected vacuum wavelengths λ_0.

The pore phase, denoted with the subscript p, is composed of air, thus $n_p = 1$ and $\kappa_p = 0$ at all wavelengths.

X-ray tomography (RX Solutions EasyTom Nano) was performed on a small ceramic sample at the MATEIS laboratory (Villeurbanne, France), followed by image processing with the Fiji software [59] to obtain a 3D binary reconstruction of a 60 µm × 60 µm × 60 µm volume of the material, shown in Figure 12. The resolution of the image is 0.3 µm per voxel. The porosity of the ceramic is $f_p = 0.12$, determined from the volume fraction of the void phase voxels. The characteristic pore size was estimated to voxel precision through the pore phase mean chord length [54] as $\langle\langle \ell_p \rangle\rangle = 1.8$ µm. Note that in the case of non-overlapping spherical pores of uniform radius a_p, Dirac's formula gives $a_p = 0.75\langle\langle \ell_p \rangle\rangle$ [60].

The low values of κ_m and f_p in the studied porous ceramic agree with the hypotheses behind our proposed approach in section 2.3. The material data in Table 2 and the image in Figure 12 was used as input data for the modeling procedure described in the next section. The tomography-reconstructed microstructure is converted into a dipole array by placing one dipole at the center of each voxel, eventually after one or more voxel subdivisions (see Figure 5) to ensure a sufficiently fine discretization.

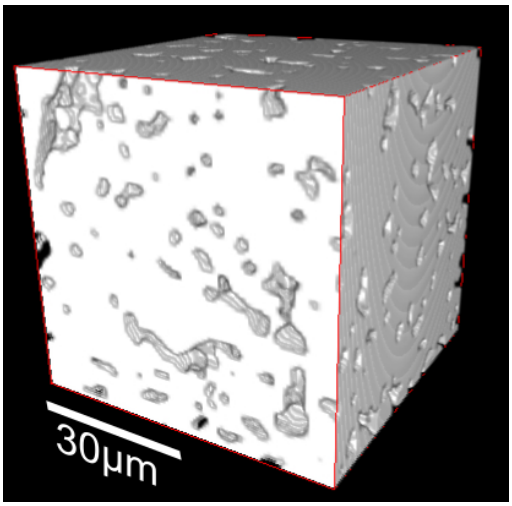

Figure 12: Tomography-reconstructed porous alumina ceramic with physical dimensions of 60 µm × 60 µm × 60 µm and a resolution of 0.3 µm per voxel. The alumina phase is in white while the voids are the air-filled pores.

4.2. Modeling procedure

4.2.1. Volume radiative properties

We compute the volume radiative properties for the wavelengths listed in Table 2 according to the method described in section 2.3.2. For wavelengths greater than 4 µm, the initial cell size $d_0 = 300\,\text{nm}$ is sufficient to ensure a discretization parameter y below 0.81, where results are essentially independent of grid size. For smaller wavelengths, voxel subdivision was performed to obtain a final cell size of $d = 75\,\text{nm}$ for $\lambda_0 < 2\,\mu\text{m}$ and $d = 150\,\text{nm}$ for $2\,\mu\text{m} \leq \lambda_0 < 4\,\mu\text{m}$. The uncertainty in the results due to choice of model parameters is estimated in section 3 to be lower than 5%.

Non-overlapping spherical volume elements of equal diameter D are then sampled from the reconstructed microstructure, with the number of volume elements ranging from 1 to 125 depending on D. The porosity f_p and mean pore phase chord length $\langle\langle \ell_p \rangle\rangle$ [54] of each volume element are also computed. As discussed in section 3.1.2, each volume element effectively represents a slightly different material since these microstructural parameters vary from one volume element to another. To ensure that numerical results are independent of volume element size D, we performed size convergence studies with $D > \langle\langle \ell_p \rangle\rangle$ and $D > \lambda_0$ while being capped at $D \leq 200d$ based on available computational resources ($N \approx 4.2$ million dipoles requiring approximately 16GB of memory and up to 20 CPU hours of iterative resolution).

Converged results are used to extract microstructure-property relations, which are then compared to analytical relations presented in section 2.2. In particular, the independent scattering hypothesis (equation (9b)) is applied by treating the tortuous pores within each volume element as if they were a equal-volume cluster of independently scattering spherical pores, of uniform radius a_p calculated from the mean chord length via Dirac's formula [60]: $a_p = 0.75\langle\langle \ell_p \rangle\rangle$.

4.2.2. Surface reflectivity

The surface of the sintered porous alumina contains asperities, grain boundaries, surface pores, and eventually subsurface pores that may contribute to non-specular surface scattering (reflection and refraction). Guévelou et al. [24] considered the Gaussian roughness parameters of dense ceramic surfaces composed of micron-sized grains, and concluded that scattering is specular on wavelengths from 0.4 µm to 20 µm. Applying this conclusion to the present case, we model our porous alumina surface as optically smooth everywhere except where pores are present, and simply extract non-overlapping slabs of dimensions $h \times L \times L$ at random from the reconstructed microstructure to simulate the surface layer. The low porosity in our ceramic means that large zones on the surface (of area fraction $\approx 1 - f_p$) would scatter specularly. However, some interference and diffraction effects from the surface and subsurface pores as well as Mie-type resonant effects at wavelengths close to the characteristic pore size $\langle\langle \ell_p \rangle\rangle = 1.8\,\mu\text{m}$ [28, 29] would lead to deviations from the geometrical optics approximation.

We wish to quantify the potential deviations between the physical optics solution and the prediction of several simplified analytical models based on the geometrical optics approximation, for an incidence configuration in which wave effects would be significant in the present porous ceramic. As such, we applied our method (presented in section 2.3.3) to study the case of normally incident light with $\lambda = \lambda_0 = 2\,\mu\text{m}$. Voxel refinement was performed to give a cell size of $d = 60\,\text{nm}$ corresponding to $y = 0.321$. The substrate parameters were chosen as $h_{\text{sub}} = 4.2\,\mu\text{m}$ and $\kappa_{\text{sub}} = 0.09$ following the method in Appendix A. With these model parameters, the uncertainty in the simulated reflectivity is estimated at 8.6% through the approach employed in section 3.2.2. Numerical results were then compared to three geometrical-optics-based analytical models, explained further in section 4.3.

4.3. Results and discussion

4.3.1. Effective absorption coefficient

Figure 13 shows the effective absorption coefficient κ_{eff} computed with the DDA for wavelengths $\lambda_0 = 6\,\mu\text{m}$ and 7 µm. Results for volume elements of different diameters D are compared, with the number of non-overlapping samples ranging from 64 at the smallest diameter to 1 for $D > 30\,\mu\text{m}$. As absorption in the present material happens only in the alumina matrix ($\kappa_{\text{eff}} = \kappa_{\text{eff},m}$), we also compare the results to equation (8) initially proposed by Dombrovsky et al. [6].

For $\lambda_0 = 6\,\mu\text{m}$ at which $\kappa_m = 2.375 \times 10^{-4}$, an excellent agreement between the numerical DDA results and the model of Dombrovsky et al. [6] is observed regardless of the volume element size D, with a root-mean-squared (RMS) deviation between the analytical and numerical results of 4.5% at $D = 15\,\mu\text{m}$ (64 samples) and 1.8% at $D = 30\,\mu\text{m}$ (8 samples). Equally good results were also observed for smaller wavelengths at which κ_m are several orders of magnitude lower; they are not represented in Figure 13 to preserve legibility.

On the other hand, for $\lambda_0 = 7\,\mu\text{m}$ at which $\kappa_m = 1.942 \times 10^{-3}$, the analytical model very slightly overestimates κ_{eff}. This is because scattering by heterogeneities modify the path lengths traveled by light in the matrix and thus the amount of light absorbed, which is neglected by the model of Dombrovsky et al. [6] leading to deviations at high enough matrix absorptivities. These deviations remain very small in the present material and wavelength, with a RMS value of 5.0%

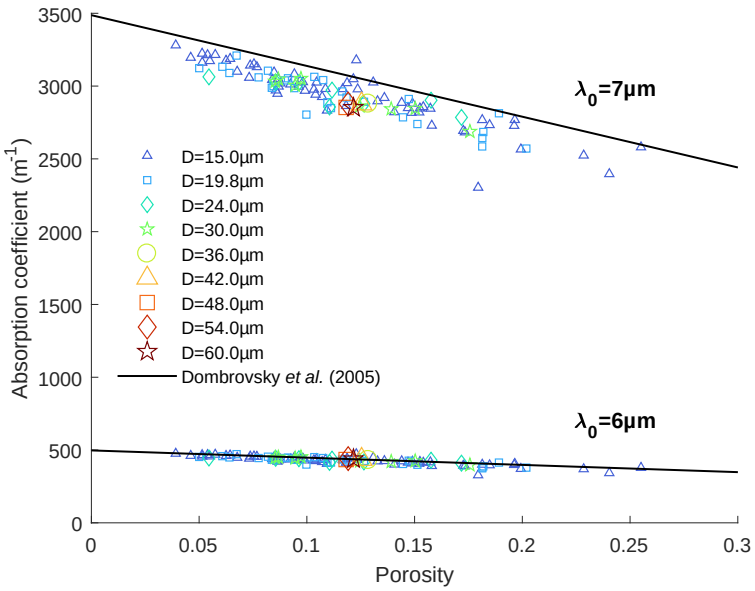

Figure 13: Effective absorption coefficient as a function of porosity computed with the DDA on volume elements of different diameters D (shown as different symbols) for wavelengths $\lambda_0 = 6\,\mu\text{m}$ and $7\,\mu\text{m}$, compared to the analytical relation for matrix absorption proposed by Dombrovsky et al. [6] (equation (8), thick lines).

over 8 samples of $D = 30\,\mu\text{m}$ and 6.9% for the single $D = 60\,\mu\text{m}$ sample. We thus consider the use of the model of Dombrovsky et al. [6] justified for the considered wavelengths.

While wavelengths greater than $\lambda_0 = 7\,\mu\text{m}$ are beyond the scope of this study, we note that the accuracy of this analytical model is expected to further degrade on this range, since the absorptivity of alumina increases while approaching the Christiansen wavelength ($\approx 10\,\mu\text{m}$) at which it exhibits blackbody-like behavior [58].

4.3.2. Effective scattering coefficient and phase function

Figure 14 shows, on the left, the variation of effective scattering coefficient σ_{eff} with porosity computed with the DDA on volume elements of different sizes D, and on the right, the scattering phase function ϕ_{eff} for different values of D averaged over volume elements of porosity $f_p = 0.12 \pm 0.01$. Results at wavelengths $\lambda_0 = 2\,\mu\text{m}$ and $\lambda_0 = 7\,\mu\text{m}$ are given. The number of non-overlapping samples ranging from 125 at the smallest diameter to 1 for $D > 30\,\mu\text{m}$. The independent scattering solution for monodisperse spherical pores is also given for different pore radii: the nominal value $a_p = 0.75\langle\langle \ell_p \rangle\rangle = 1.38\,\mu\text{m}$ estimated from the pore mean chord length [60], and $a_p = 1.6\,\mu\text{m}$ and $a_p = 1.15\,\mu\text{m}$ reflecting the uncertainty of $\pm 17\%$ in the determined mean chord length.

For the scattering coefficient σ_{eff}, results suggest that despite the huge simplifications to pore morphology in the proposed independent scattering solution, good results may be obtained for extremely low porosities ($f_p < 0.05$). However, deviations appear at higher values of f_p due to dependent scattering. In addition, volume element size dependence appears to be significant, without convergence even for the largest volume element sizes. This is likely due to forward-scattering interference effects [11, 12, 38] and can be seen from sharp lobe in the scattering phase

functions ϕ_{eff} for scattering angles close to 0°. This arises from constructive interference of coherent wavelets scattered in the forward direction when observed in the far field, and thus becomes more pronounced with increasing volume element sizes due to the higher number of scattered wavelets. For other scattering directions, the allure of ϕ_{eff} appears similar to that predicted by independent scattering theory, except they are several orders of magnitude lower due to the extremely high forward-scattering lobe.

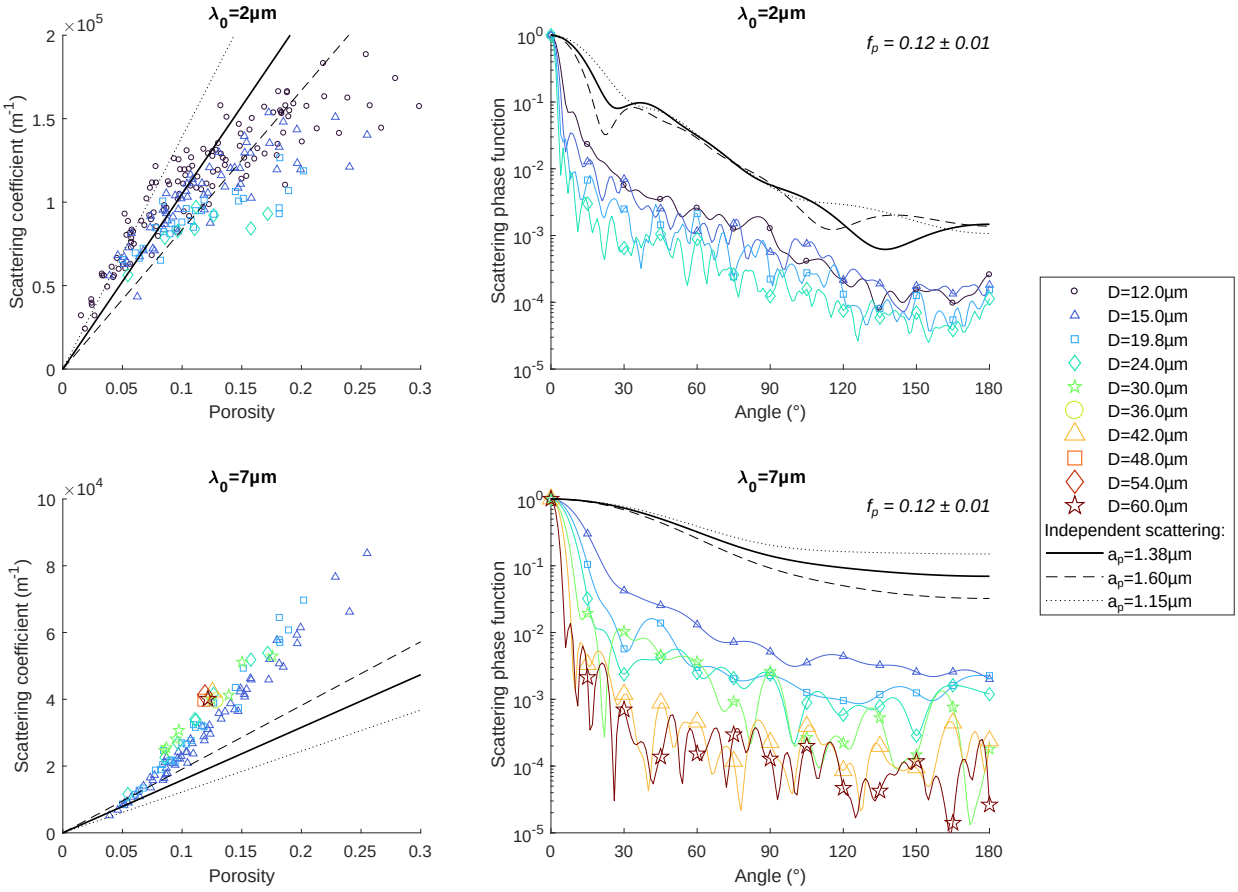

Figure 14: Left: Effective scattering coefficient as a function of porosity computed with the DDA on volume elements of different diameters D (shown as different symbols) for wavelengths $\lambda_0 = 2\,\mu m$ (top) and $7\,\mu m$ (bottom). Right: Scattering phase function ϕ_{eff}, averaged over volume elements of porosity $f_p = 0.12 \pm 0.01$ and normalized such that $\phi_{eff}(0) = 1$, for different volume element sizes. DDA results are compared to the independent scattering model applied to clusters of spherical pores of uniform radii a_p (equation (9b)). The influence of a slight variation about the nominal $a_p = 1.38\,\mu m$ is shown (thick lines vs. dotted lines).

In radiative transfer theory, as the forward-scattered intensity may simply be treated as unscattered radiation [12, 16], we invoke the transport approximation, which models a material with scattering coefficient σ_{eff} and anisotropic phase function ϕ_{eff} as a material of transport scattering coefficient σ_{tr} and an isotropic phase function [61]. Physically, this approximation considers that in an anisotropically scattering material, light "forgets" its initial direction after several consecutive scattering events spanning a characteristic distance of $1/\sigma_{tr}$. The transport scattering coefficient

σ_{tr} is calculated as:

$$\sigma_{tr} = \sigma_{\text{eff}}(1 - g_{\text{sca}}) \tag{31}$$

where g_{sca} is the asymmetry parameter defined below:

$$g_{\text{sca}} = \int_{4\pi} \phi_{\text{eff}}(\theta) \cos\theta \, \mathrm{d}\Omega' \tag{32}$$

Values for g_{sca} thus range from -1 for complete backscattering behavior, to +1 for complete forward-scattering. Notably, in the perfectly forward-scattering limit ($g_{\text{sca}} \to 1$), scattering under the transport approximation vanishes: $\sigma_{tr} \to 0$.

Figure 15 shows the values of σ_{tr} for all the considered wavelengths obtained on some of the largest volume element sizes. We observe significantly better convergence with increasing volume element size D, in that results for larger values of D generally fall within the dispersion observed for smaller values of D. This supports our hypothesis that the poor convergence with respect to volume element size observed in σ_{eff} is mainly due to the constructive interference of forward-scattered radiation. Rather surprisingly, the independent scattering solution for σ_{tr} describes the DDA result fairly well at wavelengths of $\lambda_0 \leq 1.5\,\mu\text{m}$, while at larger wavelengths it still fails beyond $f_p > 0.05$.

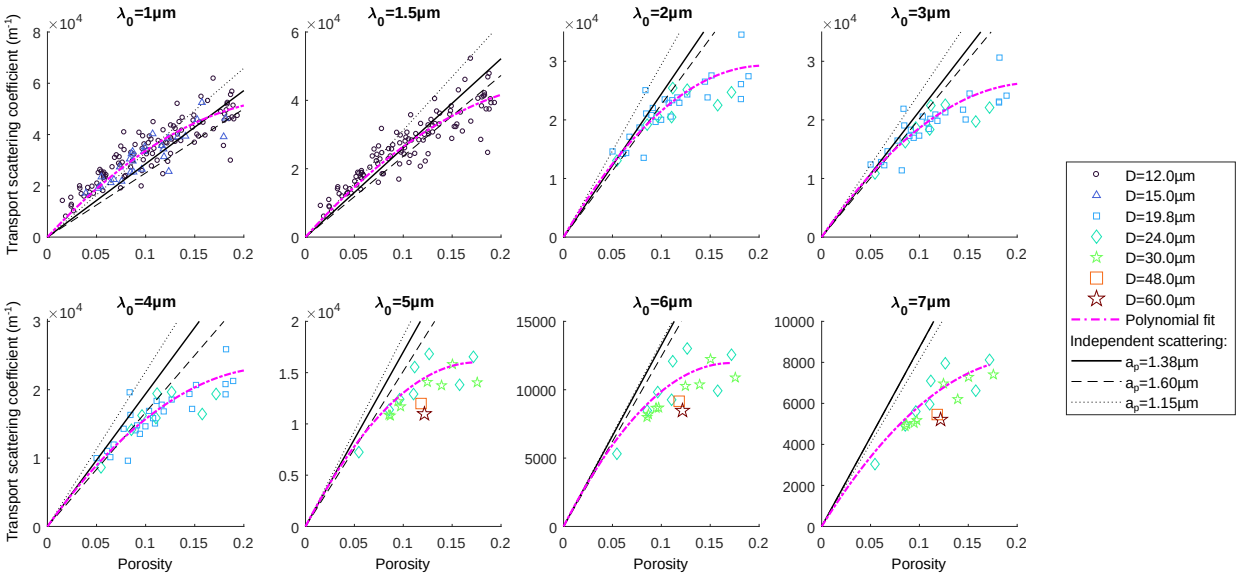

Figure 15: Effective transport scattering coefficient as a function of porosity computed with the DDA on volume elements of different diameters D (shown as different symbols) for wavelengths λ_0 between 1 μm and 7 μm. Converged results are fitted with a second-order polynomial function (thick dash-dotted lines), and compared to the independent scattering model applied to clusters of spherical pores of uniform radii a_p (equation (9b)). The influence of a slight variation about the nominal $a_p = 1.38\,\mu\text{m}$ is shown (thick continuous lines vs. thin dotted lines).

Our results suggest that for the considered porosities, σ_{tr} may be described fairly well by the second-order polynomial function below:

$$\sigma_{tr}(f_p, \lambda_0) = p_1(\lambda_0) f_p + p_2(\lambda_0) f_p^2 \tag{33}$$

Equation (33) satisfies the condition $\sigma_{tr} = 0$ at $f_p = 0$. Values of p_1 and p_2 for the considered wavelengths are given in Table 3. The confidence interval of the proposed correlations, determined from their RMS deviation with respect to the DDA results, reflects the variations in pore shapes and sizes at constant porosity, and ranges from 20.8% at $\lambda_0 = 1\,\mu m$ to 9.8% at $\lambda_0 = 5\,\mu m$.

λ_0 [µm]	p_2 [m^{-1}]	p_1 [m^{-1}]	D [µm]	N	$f_{p,\max}$	RMS deviation [%]
1.0	-7.9752×10^5	4.1620×10^5	12.0	125	0.31	20.8
1.5	-5.6131×10^5	3.2047×10^5	12.0	125	0.31	17.6
2.0	-6.9006×10^5	2.8421×10^5	19.8	27	0.20	12.0
3.0	-5.5285×10^5	2.4132×10^5	19.8	27	0.20	12.1
4.0	-4.3028×10^5	2.0015×10^5	19.8	27	0.20	13.1
5.0	-5.1739×10^5	1.8200×10^5	24.0	8	0.17	9.8
6.0	-4.0644×10^5	1.3940×10^5	24.0	8	0.17	12.5
7.0	-1.7899×10^5	7.6655×10^4	24.0	8	0.17	10.9

Table 3: Coefficients of second-order polynomial correlations describing the transport scattering coefficient σ_{tr} as a function of porosity f_p (see equation 33), extracted from DDA computations on N spherical volume elements of diameter D. The correlations are obtained on the domain $0 < f_p < f_{p,\max}$. The root-mean-squared (RMS) difference between the numerical results and the proposed correlations are also given.

4.3.3. Surface reflectivity

As mentioned in section 4.2.2, while the geometrical optics approximation should be appropriate for the considered wavelengths following the criterion of [27], Mie-type resonances may cause deviations at wavelengths close to the pore sizes. DDA computations are therefore performed for light of wavelength $\lambda_0 = 2\,\mu m$ at normal incidence and compared to several analytical models based on the geometric optics approximation.

In Figure 16, DDA results for the normal-normal ($\mathcal{R}_{\text{spec}}$) and normal-hemispherical ($\mathcal{R}_{fi}$) reflectivity obtained for volume elements of different dimensions are shown. The symbols ○, △, and □ represent volume elements of width $L = 5.1\,\mu m$ and thicknesses $h = 0.9\,\mu m$, $1.5\,\mu m$, and $2.1\,\mu m$ respectively, while ◇ represent volume elements of $L = 6.3\,\mu m$ and $h = 1.5\,\mu m$. As the volume element sizes are much smaller than those used for the volume radiative properties simulations, the large dispersion in results is a natural consequence of the higher microstructural variability. In particular, sharp peaks are observed at porosities $f_p > 0.2$ especially for the two smallest volume elements, which is likely due to edge effects: in particular, the periodic boundary conditions artificially introduce spatial microstructural correlations of length scale L, potentially leading to spurious resonance effects if L is too small.

The results for both $\mathcal{R}_{\text{spec}}$ and $\mathcal{R}_{fi}$ at $h = 1.5\,\mu m$ and $h = 2.1\,\mu m$ (for $L = 5.1\,\mu m$) are statistically similar, which suggests that subsurface pores at depths beyond $1.5\,\mu m$ have little effect on the reflectivity. On the other hand, when comparing results for different L at $h = 1.5\,\mu m$, the results for $\mathcal{R}_{\text{spec}}$ appear unaffected while the values for $\mathcal{R}_{fi}$ at $L = 6.3\,\mu m$ tends to be on the low end of the predictions obtained with $L = 5.1\,\mu m$, suggesting that $L = 5.1\,\mu m$ leads to a slight overestimation of the diffuse component of the reflected light.

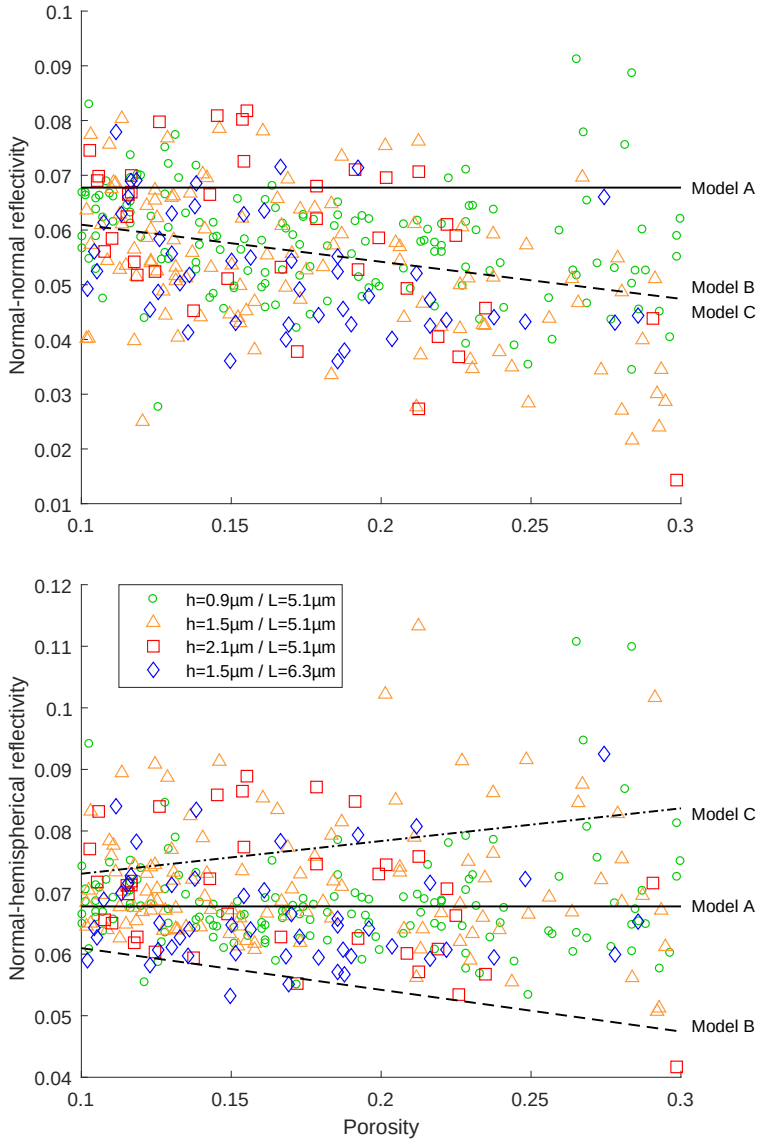

Figure 16: Normal-normal ($\mathcal{R}_{\text{spec}}$) and normal-hemispherical ($\mathcal{R}_{h}$) reflectivity for $\lambda = \lambda_0 = 2\,\mu\text{m}$ as a function of porosity. DDA results obtained on volume elements of various thickness h and width L (symbols) are compared to analytical models based on the geometrical optics approximation (lines).

DDA results in Figure 16 are also compared to three geometrical-optics-based analytical models presented below, with the specular reflectivity obtained from Fresnel's equations [25] using the solid phase complex refractive index $m_m = n_m + i\kappa_m$ denoted as $\mathcal{R}_{\text{Fr}}$:

"Model A" assumes perfectly smooth surfaces due to the relatively large distances between surface pores and small pore sizes, giving perfectly specular reflection everywhere according to Fresnel's equations:

$$\mathcal{R}_{h} = \mathcal{R}_{\text{spec}} = \mathcal{R}_{\text{Fr}} \tag{34}$$

This assumption has commonly been used in past work on radiative transfer in low porosity

media [2, 14, 15, 17, 24, 62].

"Model B" assumes an infinitesimally thin surface layer, smooth everywhere save where pores are present. As diffraction is neglected, only rays encountering the solid phase at the surface are reflected in the specular direction according to Fresnel's equations, while rays encountering surface pores are fully transmitted into the volume. The reflection is therefore also perfectly specular, and is proportional to the solid phase volume fraction f_m:

$$\mathcal{R}_{\hbar} = \mathcal{R}_{\text{spec}} = f_m \mathcal{R}_{\text{Fr}} \tag{35}$$

"Model C" assumes a smooth solid surface with pores modeled as locally smooth cavities, which produces diffuse reflection where pores are present on the surface, and specular reflection elsewhere. Diffuse reflection is assumed isotropic and modeled by the incident-cosine-weighted average reflectivity [61, 63]. This gives the following expression for $\mathcal{R}_{\hbar}$:

$$\mathcal{R}_{\hbar} = \mathcal{R}_{\text{spec}} + \mathcal{R}_{\text{diff}} = f_m \mathcal{R}_{\text{Fr}} + f_p \int_{\mathbf{u}'\cdot\mathbf{n}<0} 2\mathcal{R}_{\text{Fr}}(\mathbf{u}')|\mathbf{u}'\cdot\mathbf{n}|\,\mathrm{d}\Omega' \tag{36}$$

where $\mathbf{n}$ is the normal vector pointing outwards from the surface.

For the normal-normal reflectivity ($\mathcal{R}_{\text{spec}}$), a clear decreasing trend with porosity is observed in Figure 16, which renders Model A inapplicable. On the other hand, for the normal-hemispherical reflectivity ($\mathcal{R}_{\hbar}$), Model B appears to correspond to the statistical lower bound of the DDA results, which is a consequence of neglecting the effect of subsurface structure and diffraction. These observations are supported by the RMS deviations between each model and the DDA results obtained on different volume element sizes, listed in Table 4. Overall, Model C gives satisfactory agreement with the DDA results, with a dispersion of 19%–27% on $\mathcal{R}_{\text{spec}}$ and 17.7%–22.6% on $\mathcal{R}_{\hbar}$ due to microstructural variability as well as wave effects that are neglected in the geometrical-optics-based model.

Number of samples		h [μm]	L [μm]	RMS deviation in $\mathcal{R}_{\text{spec}}$ [%] Model A	Models B and C	RMS deviation in $\mathcal{R}_{\hbar}$ [%] Model A	Model B	Model C
172	○	0.9	5.1	23.21	19.96	12.07	93.13	17.74
136	△	1.5	5.1	36.04	27.00	18.98	92.75	17.83
99	□	2.1	5.1	31.74	26.16	18.14	93.24	22.61
62	◇	1.5	6.3	37.71	26.68	14.40	93.51	22.58

Table 4: Root-mean-squared (RMS) deviations between the normal-normal ($\mathcal{R}_{\text{spec}}$) and normal-hemispherical ($\mathcal{R}_{\hbar}$) reflectivity at $\lambda_0 = 2\,\mu\text{m}$ computed with the DDA on volume elements of different thicknesses h and widths L, and predictions of three analytical models based on the geometrical optics approximation.

5. Conclusion

We proposed a numerical approach based on the discrete dipole approximation (DDA) to predict the effective radiative properties of porous ceramics composed of a weakly absorbing solid

matrix containing low volume fractions of small pores or particles. The 3D microstructure and the complex refractive index of each phase were used as input. Validation studies on reference microstructures were performed to determine the optimal model parameters that reproduce known solutions to an accuracy within 5%.

We then applied our models to compute the volume and surface radiative properties of a tomography-reconstructed porous alumina ceramic with a nominal porosity of 12% and a mean pore size of 1.8 µm. Computations on a large number of small volume elements provided statistics of effective properties for small variations about the nominal microstructural parameters, which were used to validate and/or extract analytical microstructure-property relations. The uncertainty was also estimated via the root-mean-squared (RMS) deviation between all the DDA results and the analytical relations.

Simulations of volume scattering and absorption confirmed the applicability of the absorption coefficient κ_{eff} predicted using the analytical model by Dombrovsky et al. [6] for the considered wavelengths, with only a slight overestimation of 6.7% at $\lambda_0 = 7\,\mu\text{m}$ by the analytical model due to the high matrix absorption index ($\kappa_m = 1.942 \times 10^{-3}$). On the other hand, the simulated scattering coefficient σ_{eff} and phase function ϕ_{eff} converges poorly with volume element size due to strong forward-scattering interference effects. We show that by considering the transport scattering coefficient $\sigma_{tr} = \sigma_{\text{eff}}(1 - g_{\text{sca}})$ instead, results converge much better with increasing volume element size. The independent scattering solution computed from the mean pore chord length agrees well with simulated data for porosities below 5%. For larger porosities up to 20%, the variation of σ_{tr} can be described with a second-order polynomial function of the porosity, with a variation of up to 20.8% due to the high microstructural variability in the studied material.

The surface reflectivity of the porous alumina for 2 µm wavelength radiation at normal incidence was also modeled and used to assess the suitability of several geometrical-optics-based analytical models. By considering rays incident on the solid phase to be reflected specularly according to Fresnel's equations and rays incident on the pore phase to be diffusely reflected with the reflectivity given by Siegel and Spuckler [63], an agreement with simulated data to within 22.6% for the normal-hemispherical reflectivity $\mathcal{R}_{ft}$ and 27.0% for the specular component $\mathcal{R}_{\text{spec}}$ is achieved. Note that the high uncertainty in σ_{tr}, $\mathcal{R}_{ft}$ and $\mathcal{R}_{\text{spec}}$, estimated through the RMS deviation between all the DDA points and the analytical relations, is mainly due to microstructural variation.

Our proposed numerical method provides a powerful way to directly predict the effective volume and surface radiative properties of arbitrary microstructures while accounting for dependent scattering between heterogeneities that are small and close to each other compared to the wavelength. This paves the way for more accurate radiative transfer modeling at larger scales. Due to the small volume element sizes involved, special attention must be paid to verify the convergence of the results with respect to the volume element size, and to account for the potentially high microstructural variability. In the next part of our study presented in a companion paper [33], the predicted effective radiative properties of the studied porous ceramic are applied to the simulation of the reflectance, transmittance and emittance of thin slabs of the same material, which we then validate with spectroscopic measurements. The influence of the uncertainty in the effective radiative properties on the simulated quantities is also quantified through a sensitivity study.

6. Acknowledgments

This research was supported by Saint-Gobain Research (SGR) Provence and the French National Association for Research and Technology (ANRT) through the CIFRE grant number 2017/ 0775. The authors would like to express their gratitude to L. San Miguel (SGR Provence), L. Pierrot (SGR Provence) and J. Meulemans (SGR Paris) for their insight and discussions that greatly improved the research; to Y. Millot (SGR Provence) for sample preparation; to J. Adrien (MATEIS) and N. Naouar (LaMCoS) for assistance with X-ray tomography; and to D. De Sousa Meneses (CEMHTI) for provision of optical data and helpful discussions. Special thanks also go to authors who graciously made their codes available on the public domain: B.T. Draine and P. Flatau (DDSCAT), J. Schäfer (MatScat), S.J. Byrnes (TMM), and M.R. MacIver (chord length calculator).

Appendix A. Non-reflecting boundary conditions on semi-infinite layers using an absorbing substrate

The bidirectional surface reflectivity model proposed in section 2.3.3 considers reflection from a semi-infinite layer of the heterogeneous material (with a dominant matrix phase of complex refractive index $m_m = n_m + i\kappa_m$) illuminated from the top. Non-reflecting boundary conditions are applied to the bottom surface by the addition of an absorbing substrate of thickness h_{sub} and refractive index $m_{\text{sub}} = n_{\text{sub}} + i\kappa_{\text{sub}}$. This appendix explains how the amount of light reflected off the boundary between the top layer and the substrate depends on the substrate properties, and how an appropriate choice of said properties can be made to minimize this reflection.

Interface reflection [25], labeled as ① in Figure A.17a, occurs due to the mismatch in refractive indexes on both sides of the interface. To minimize the mismatch between the top layer and the substrate, we set $n_{\text{sub}} = n_m$ and limit the absorption index κ_{sub} of the substrate to small values (less than 0.1 [64]).

Some of the light entering the substrate may experience one or multiple reflections off the bottom surface of the substrate in contact with the ambient medium before traveling back to the top layer. This source of reflection is labeled as ② in Figure A.17a. For a given κ_{sub}, the substrate thickness h_{sub} should thus be as large as possible to maximize absorption, with memory constraints limiting the number of dipoles and thus the thickness that can be simulated.

This undesired reflection at the boundary between the top layer and the substrate may be estimated from the reflectance of a semi-infinite substrate of refractive index m_{sub} and thickness h_{sub}, placed between an infinite upper layer of refractive index m_m and an infinite bottom layer of refractive index n_{amb} and illuminated from above (same configuration as in Figure A.17a). Analytical solvers of Maxwell's equations for multi-layered systems, such as the Python "Transfer Matrix Method" package [55], can be used to simulate such a configuration. Figure A.17b plots the normal boundary reflectivity at $\lambda_0 = 1\,\mu\text{m}$ as a function of absorption index κ_{sub} for three different substrate thicknesses h_{sub}, with $n_m = 1.718 = n_{\text{sub}}$, $\kappa_m = 0$ and $n_{\text{amb}} = 1$. For a given thickness, we see that the boundary reflectivity initially decreases with increasing absorption index as the reflection from source ② diminishes, but then reaches a minimum and increases as the reflection from source ① becomes more significant. Furthermore, the results suggest that there exists a single combination of κ_{sub} and h_{sub} that minimizes the boundary reflectivity, which corresponds to $\kappa_{\text{sub}} = 0.09$ and $h_{\text{sub}} = 2.1\,\mu\text{m}$ among the investigated combinations.

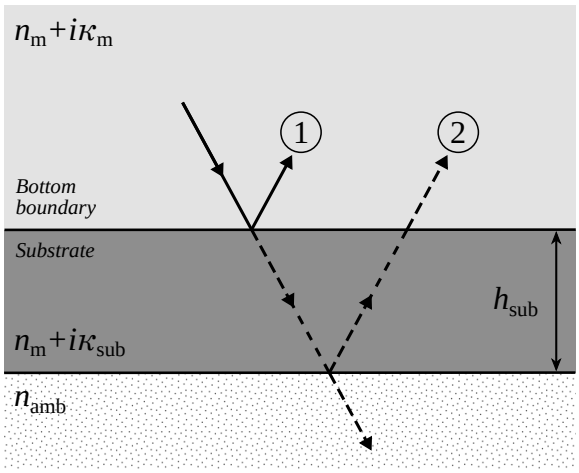

(a) Reflection at the bottom boundary.

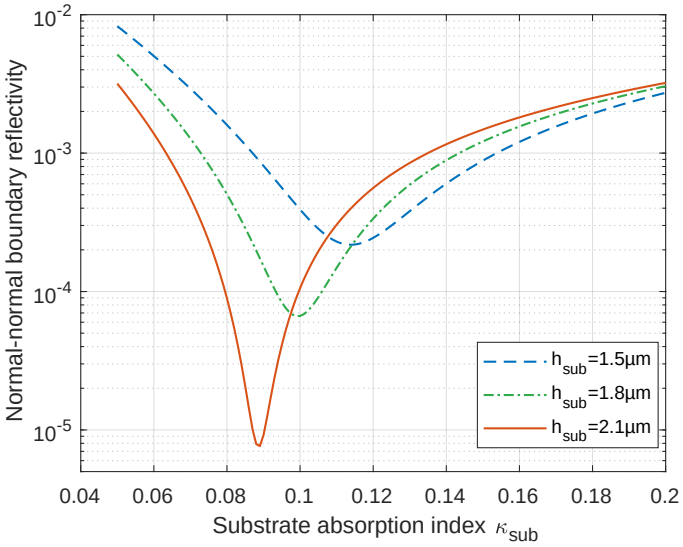

(b) Boundary reflectivity for different substrate parameters.

Figure A.17: Simulation of non-reflecting boundary conditions by the addition of an absorbing substrate: the substrate properties determine the amount of reflection at the boundary between the top layer and the substrate.

A limitation to this method lies in the fact that the optimal combination of substrate parameters varies with incidence angle. In simulations involving heterogeneous materials, light arrives at the bottom surface of the top layer at a wide range of incidence angles that is difficult to know beforehand. Simplifying assumptions (e.g., near-normal incidence) are therefore required when choosing the substrate parameters.

References

[1] X. Chen, C. Zhao, B. Wang, Microstructural effect on radiative scattering coefficient and asymmetry factor of anisotropic thermal barrier coatings, Journal of Quantitative Spectroscopy and Radiative Transfer 210 (2018)

116 – 126.

[2] O. Rozenbaum, C. Blanchard, D. De Sousa Meneses, Determination of high-temperature radiative properties of porous silica by combined image analysis, infrared spectroscopy and numerical simulation, International Journal of Thermal Sciences 137 (2019) 552–559.

[3] Y. Bao, Y. Huang, W. Li, K. Zhu, Combination of the monte carlo method and dda to evaluate the radiative properties of ito- pigmented and tio2-pigmented coatings, International Journal of Thermal Sciences 146 (2019) 106076.

[4] B. Zeghondy, E. Iacona, J. Taine, Experimental and RDFI calculated radiative properties of a mullite foam, International Journal of Heat and Mass Transfer 49 (2006) 3702–3707.

[5] L. A. Dombrovsky, D. Baillis, Thermal Radiation in Disperse Systems: An Engineering Approach, Begell House, 2010.

[6] L. Dombrovsky, J. Randrianalisoa, D. Baillis, L. Pilon, Use of Mie theory to analyze experimental data to identify infrared properties of fused quartz containing bubbles, Applied optics 44 (2005) 7021–7031.

[7] J. Randrianalisoa, D. Baillis, L. Pilon, Modeling radiation characteristics of semitransparent media containing bubbles or particles, J. Opt. Soc. Am. A 23 (2006) 1645–1656.

[8] A. Kaemmerlen, C. Vo, F. Asllanaj, G. Jeandel, D. Baillis, Radiative properties of extruded polystyrene foams: Predictive model and experimental results, Journal of Quantitative Spectroscopy and Radiative Transfer 111 (2010) 865–877.

[9] C. F. Bohren, D. R. Huffman, Absorption and Scattering of Light by Small Particles, John Wiley & Sons, Inc., 1983. doi:10.1002/9783527618156.

[10] Z. Ivezic, M. P. Menguc, An investigation of dependent / independent scattering regimes using a discrete dipole approximation, International Journal of Heat and Mass Transfer 39 (1996) 811–822.

[11] M. I. Mishchenko, L. Liu, D. W. Mackowski, B. Cairns, G. Videen, Multiple scattering by random particulate media: exact 3d results, Opt. Express 15 (2007) 2822–2836.

[12] B. Wang, C. Zhao, Effect of dependent scattering on light absorption in highly scattering random media, International Journal of Heat and Mass Transfer 125 (2018) 1069 – 1078.

[13] T. Galy, D. Huang, L. Pilon, Journal of Quantitative Spectroscopy & Radiative Transfer Revisiting independent versus dependent scattering regimes in suspensions or aggregates of spherical particles, Journal of Quantitative Spectroscopy and Radiative Transfer 246 (2020) 106924.

[14] B. Rousseau, D. De Sousa Meneses, P. Echegut, M. Di Michiel, J. F. Thovert, Prediction of the thermal radiative properties of an x-ray μ-tomographied porous silica glass, Applied Optics 46 (2007) 4266–4276.

[15] B. Rousseau, J.-y. Y. Rolland, P. Echegut, L. Del Campo, D. De Sousa Meneses, P. Echegut, Modelling of the Thermal Radiative Properties of Oxide Ceramics, in: Proceedings of the 14th International Heat Transfer Conference, 13, 2010, pp. 1–6.

[16] J. Randrianalisoa, D. Baillis, Radiative properties of densely packed spheres in semitransparent media: A new geometric optics approach, Journal of Quantitative Spectroscopy and Radiative Transfer 111 (2010) 1372 – 1388.

[17] B. Bouvry, L. Del Campo, D. De Sousa Meneses, O. Rozenbaum, R. Echegut, D. Lechevalier, M. Gaubil, P. Echegut, Hybrid Methodology for Retrieving Thermal Radiative Properties of Semi-Transparent Ceramics, Journal of Physical Chemistry C 120 (2016) 3267–3274.

[18] M. Kahnert, Numerical solutions of the macroscopic Maxwell equations for scattering by non-spherical particles: A tutorial review, Journal of Quantitative Spectroscopy and Radiative Transfer 178 (2016) 22–37.

[19] E. M. Purcell, C. R. Pennypacker, Scattering and Absorption of Light by Nonspherical Dielectric Grains, The Astrophysical Journal 186 (1973) 705.

[20] B. T. Draine, P. J. Flatau, Discrete-Dipole Approximation For Scattering Calculations, Journal of the Optical Society of America A 11 (1994) 1491.

[21] S. Lallich, F. Enguehard, D. Baillis, Experimental Determination and Modeling of the Radiative Properties of Silica Nanoporous, Journal of Heat Transfer 131 (2009) 082701.

[22] X. Dai, S. Haussener, Optical characterization of multi-scale morphologically complex heterogeneous media – application to snow with soot impurities, Journal of Quantitative Spectroscopy and Radiative Transfer 206 (2018) 378 – 391.

[23] R. Coquard, D. Baillis, D. Quenard, Energy & Buildings Numerical and experimental study of the IR opacification of polystyrene foams for thermal insulation enhancement, Energy & Buildings 183 (2019) 54–63.
[24] S. Guévelou, B. Rousseau, G. Domingues, J. Vicente, A simple expression for the normal spectral emittance of open-cell foams composed of optically thick and smooth struts, Journal of Quantitative Spectroscopy and Radiative Transfer 189 (2017) 329 – 338.
[25] Q. Brewster, Thermal Radiative Transfer and Properties, John Wiley & Sons, Inc., 1992.
[26] P. Beckmann, A. Spizzichino, The Scattering of Electromagnetic Waves from Rough Surfaces, Pergamon Press Ltd., 1963.
[27] K. Tang, R. A. DIMENNA, R. O. BUCKIUS, Regions of validity of the geometric optics approximation for angular scattering from very rough surfaces, International Journal of Heat and Mass Transfer 40 (1996) 49 – 59.
[28] J. ELSON, H. BENNETT, J. BENNETT, Chapter 7 - scattering from optical surfaces, volume 7 of *Applied Optics and Optical Engineering*, Elsevier, 1979, pp. 191 – 244. URL: http://www.sciencedirect.com/science/article/pii/B9780124086074500141. doi:https://doi.org/10.1016/B978-0-12-408607-4.50014-1.
[29] H. Ragheb, E. R. Hancock, Testing new variants of the beckmann–kirchhoff model against radiance data, Computer Vision and Image Understanding 102 (2006) 145 – 168.
[30] B. Liu, X. Xia, X. Zhang, C. Sun, Spectral radiative properties of skeleton inner structure of ceramic foam based on ordered opal structure model, Journal of Quantitative Spectroscopy and Radiative Transfer 224 (2019) 279 – 288.
[31] B. Liu, X.-l. Xia, C. Sun, X. Chen, Analysis on spectral radiative properties of micro-scaled rough ligament surface inside open-cell nickel foam, International Journal of Heat and Mass Transfer 145 (2019) 118773.
[32] F. Cabannes, D. Billard, Measurement of infrared absorption of some oxides in connection with the radiative transfer in porous and fibrous materials, International Journal of Thermophysics 8 (1987) 97–118.
[33] Z. Low, A. Novikov, D. De Sousa Meneses, D. Baillis, 2– radiative behavior of porous alumina up to high temperatures: experiments and physical optics-based modeling, 2020. In preparation.
[34] W. Lipiński, J. Petrasch, S. Haussener, Application of the spatial averaging theorem to radiative heat transfer in two-phase media, Journal of Quantitative Spectroscopy and Radiative Transfer 111 (2010) 253–258.
[35] R. Siegel, J. R. Howell, Thermal Radiation Heat Transfer, 3 ed., Hemisphere Publishing Corporation, 1992.
[36] R. Coquard, D. Baillis, Radiative Characteristics of Beds of Spheres Containing an Absorbing and Scattering Medium., Journal of Thermophysics and Heat Transfer 19 (2005) 226–234.
[37] M. I. Mishchenko, L. Liu, G. Videen, Conditions of applicability of the single-scattering approximation, Opt. Express 15 (2007) 7522–7527.
[38] M. I. Mishchenko, "independent" and "dependent" scattering by particles in a multi-particle group, OSA Continuum 1 (2018) 243–260.
[39] Q. Zhu, H. Lee, Z. M. Zhang, Radiative properties of materials with surface scattering or volume scattering: A review, Frontiers of Energy and Power Engineering in China 3 (2009) 60–79.
[40] M. Loretz, R. Coquard, D. Baillis, E. Maire, Metallic foams: Radiative properties/comparison between different models, Journal of Quantitative Spectroscopy and Radiative Transfer 109 (2008) 16–27.
[41] B. T. Draine, The discrete-dipole approximation and its application to interstellar graphite grains, The Astrophysical Journal 333 (1988) 848.
[42] M. Yurkin, A. Hoekstra, The discrete dipole approximation: An overview and recent developments, Journal of Quantitative Spectroscopy and Radiative Transfer 106 (2007) 558 – 589. IX Conference on Electromagnetic and Light Scattering by Non-Spherical Particles.
[43] D. Gutkowicz-Krusin, B. T. Draine, Propagation of Electromagnetic Waves on a Rectangular Lattice of Polarizable Points (2004) 1–17.
[44] R. D. da Cunha, T. Hopkins, The Parallel Iterative Methods (PIM) package for the solution of systems of linear equations on parallel computers, Applied Numerical Mathematics 19 (1995) 33–50.
[45] M. Petravic, G. Kuo-Petravic, ILUCG algorithm which minimizes in the Euclidean norm, Technical Report July, Princeton Plasma Physics Laboratory (PPPL), Princeton, NJ (United States), 1978. URL: http://www.osti.gov/servlets/purl/6611598-bsiTOx/. doi:10.2172/6611598.
[46] B. T. Draine, P. J. Flatau, Discrete-dipole approximation for periodic targets: theory and tests, Journal of the

Optical Society of America A 25 (2008) 2693.
[47] B. T. Draine, P. J. Flatau, User Guide for the Discrete Dipole Approximation Code DDSCAT 7.3, 2019.
[48] P. C. Chaumet, A. Rahmani, G. W. Bryant, Generalization of the coupled dipole method to periodic structures, Phys. Rev. B 67 (2003) 165404.
[49] M. A. Yurkin, V. P. Maltsev, A. G. Hoekstra, Convergence of the discrete dipole approximation. I. Theoretical analysis, Journal of the Optical Society of America A 23 (2006) 2578.
[50] M. A. Yurkin, M. Min, A. G. Hoekstra, Application of the discrete dipole approximation to very large refractive indices: Filtered coupled dipoles revived, Physical Review E 82 (2010) 036703.
[51] T. Kanit, S. Forest, I. Galliet, V. Mounoury, D. Jeulin, Determination of the size of the representative volume element for random composites: Statistical and numerical approach, International Journal of Solids and Structures 40 (2003) 3647–3679.
[52] N. B. Piller, O. J. Martin, Increasing the performance of the coupled-dipole approximation: A spectral approach, IEEE Transactions on Antennas and Propagation 46 (1998) 1126–1137.
[53] J.-P. Schäfer, Implementierung und Anwendung analytischer und numerischer Verfahren zur Lösung der Maxwellgleichungen für die Untersuchung der Lichtausbreitung in biologischem Gewebe, Doctoral thesis, Universität Ulm, 2011. doi:10.18725/OPARU-1914.
[54] M. R. MacIver, M. Pawlik, Analysis of in situ microscopy images of flocculated sediment volumes, Chemical Engineering & Technology 40 (2017) 2305–2313.
[55] S. J. Byrnes, Multilayer optical calculations (2016) 1–20.
[56] D. C. Harris, L. F. Johnson, L. Cambrea, L. Baldwin, M. Baronowski, E. Zelmon, W. B. Poston, J. D. Kunkel, M. Parish, M. R. Pascucci, J. J. Gannon, Jr, T.-c. Wen, Refractive index of infrared- transparent polycrystalline alumina, Optical Engineering 56 (2017) 077103.
[57] L. A. Pajdzik, A. M. Glazer, Three-dimensional birefringence imaging with a microscope tilting-stage. I. Uniaxial crystals, Journal of Applied Crystallography 39 (2006) 326–337.
[58] J. F. Brun, L. del Campo, D. De Sousa Meneses, P. Echegut, Infrared optical properties of alpha-alumina with the approach to melting: gamma-like tetrahedral structure and small polaron conduction, Journal of Applied Physics 114 (2013) 223501.
[59] J. Schindelin, I. Arganda-Carreras, E. Frise, V. Kaynig, M. Longair, T. Pietzsch, S. Preibisch, C. Rueden, S. Saalfeld, B. Schmid, J.-Y. Tinevez, D. J. White, V. Hartenstein, K. Eliceiri, P. Tomancak, A. Cardona, Fiji: an open-source platform for biological-image analysis, Nature Methods 9 (2012) 676–682.
[60] W. de Kruijf, J. Kloosterman, On the average chord length in reactor physics, Annals of Nuclear Energy 30 (2003) 549–553.
[61] L. A. Dombrovsky, The use of transport approximation and diffusion-based models in radiative transfer calculations, Computational Thermal Sciences: An International Journal 4 (2012) 297–315.
[62] B. Zeghondy, E. Iacona, J. Taine, Determination of the anisotropic radiative properties of a porous material by radiative distribution function identification (RDFI), International Journal of Heat and Mass Transfer 49 (2006) 2810–2819.
[63] R. Siegel, C. Spuckler, Approximate solution methods for spectral radiative transfer in high refractive index layers, International Journal of Heat and Mass Transfer 37 (1994) 403 – 413.
[64] P. C. Chang, J. G. Walker, K. I. Hopcraft, Ray tracing in absorbing media, Journal of Quantitative Spectroscopy and Radiative Transfer 96 (2005) 327–341.

2– Radiative behavior of porous alumina up to high temperatures: Experiments and physical-optics-based modeling

Z.K. Low[a,b,*], A. Novikov[b,c], D. De Sousa Meneses[c], D. Baillis[a]

[a] *Univ Lyon, INSA-Lyon, CNRS UMR5259, LaMCoS, F-69621 Villeurbanne, France.*
[b] *Saint-Gobain Research Provence, F-84306 Cavaillon, France.*
[c] *CEMHTI, CNRS UPR3079, Univ. Orléans, F-45071 Orléans, France.*

Abstract

We compare two methods of characterizing the radiative behavior of porous sintered alumina disks containing µm-sized pores on the 1 µm to 7 µm wavelength range up to very high temperatures. The first consists of direct spectroscopic measurements of the normal-hemispherical reflectance and transmittance at room temperature, as well as the normal emittance up to 1300 °C. The second is a multi-scale numerical approach that requires only the X-ray tomography-reconstructed microstructure and the complex refractive index of dense sintered alumina as input: the spectral effective radiative properties are first calculated using a novel physics-optics-based model to account for wave effects and dependent scattering, then applied to the resolution of the radiative transfer equation on an equivalent homogeneous medium to obtain the spectral reflectance, transmittance, and emittance. Uncertainties in the numerical results, mainly due to microstructural variability, are quantified through sensitivity studies. The good agreement between the experimental and numerical results confirm the ability of our proposed numerical approach to give accurate predictions of the effective radiative properties.

Keywords: Porous ceramics, Radiative properties, Infrared spectroscopy, Radiative transfer equation (RTE), High temperature

1. Introduction

The knowledge of radiometric quantities such as the spectral reflectance, transmittance, or emittance of materials are of great interest notably for high-temperature applications [1, 2], and a wide array of experimental methods have been developed for their characterization [3–5]. In the case of semi-transparent materials such as metal oxide ceramics, these quantities depend not only on material composition, but also on extrinsic parameters such as sample thickness, surface roughness, and the morphology of pores and other heterogeneities [6–9]. To account for the influence of some of these parameters, inverse methods based on minimizing the differences between theoretical predictions and experimental radiometric measurements are often used to identify the

*Corresponding author
Email address: zi.low@insa-lyon.fr (Z.K. Low)

Preprint written as part of the doctoral thesis number 2020LYSEI122, INSA Lyon, France

Nomenclature

First- and second-order tensors ("vectors" and "matrices") are written in **bold face**.

Latin

A	Area
$\mathfrak{E}$	Normal emittance
e	Basis vector
f	Volume fraction
h	Height
$\mathcal{I}$	Radiance
I	Intensity, $\int \mathcal{I}\,\mathrm{d}\Omega$
ℓ	Chord length
m	Complex refractive index, $n + i\kappa$
n	Real refractive index; Normal vector
p	Parameter
$\mathcal{R}$	Reflectivity
$\mathfrak{R}$	Normal-hemispherical reflectance
$\mathfrak{S}$	Sensitivity
$\mathcal{T}$	Transmissivity
$\mathfrak{T}$	Normal-hemispherical transmittance
u	Direction
X	Input variable
x	Position
Y	Output/Observed variable

Greek

Δ	Difference; interval; absolute uncertainty
δ	Kronecker delta
ϕ	Scattering phase function
φ	Azimuth angle
κ	Absorption index
κ	Absorption coefficient
λ	Wavelength
μ	Direction cosine
σ	Scattering coefficient
θ	Polar angle
Ω	Solid angle

Superscripts and Subscripts

$'$	Modified quantity
$+/-$	Positive/Negative neighbourhood
0	Reference, *in vacuo*
$*$	Basic radiance
abs	Absorption
amb	Ambient
diff	Diffuse
eff	Effective
int	Internal
Fr	Fresnel
$\hbar$	Hemispherical
inc	Incident
ext	External
m	Matrix
p	Pore/Particle
sca	Scattering
spec	Specular
sub	Substrate
tr	Transport
V	Per unit volume

Operators and accents

$\cdot$	Dot product
$\langle\bullet\rangle$	Weighted average
$\langle\langle\bullet\rangle\rangle$	Stochastic mean

Acronyms

DDA	Discrete dipole approximation
OH	Hydroxyl
RMS	Root-mean-squared
RTE	Radiative transfer equation

effective radiative properties [10–14]. Alternatively, numerical methods are increasingly used to predict the radiometric quantities of interest from tomography-reconstructed or digitally generated microstructures. These methods are more suitable for the study of microstructure-property relations compared to inverse methods, as a large number of microstructural different samples may be characterized at a lower cost [6, 15].

In the so-called "discrete-scale" approach [16], the propagation, scattering and absorption of radiation are simulated at the microstructural level. Direct Monte Carlo ray-tracing on 3D microstructures, usually assuming locally smooth interfaces that reflect and refract specularly [6, 14, 17–20], is a popular choice when heterogeneities are large and far apart compared to the wavelength. When this is not the case, numerical resolution of Maxwell's equations should be performed [9, 21], though the high computational cost limits its application to very small geometries. On the other hand, a less computationally demanding "continuum-scale" approach treats the heterogeneous material as an equivalent homogeneous medium [8, 22, 23], and solves for the radiometric quantities of interest using the radiative transfer equation (RTE). Accurate microstructure-based determination of the effective radiative properties is the challenge in this case: while ray-tracing can also be used to deduce these properties in the geometrical optics limit [24–27], when heterogeneities are small compared to the wavelength, the independent scattering hypothesis is often used to deduce the effective radiative properties of the material from the scattering and absorption cross sections of a single pore or particle [7, 8, 28–30]. This latter approach fails to account for dependent scattering between small heterogeneities when their volume fraction exceeds a mere few percent [31–33]. In addition, Fresnel's equations are often used to describe specular reflection and refraction at the boundary between the equivalent homogeneous medium and its surroundings [8, 22, 23, 30], which neglects the potential influence of surface heterogeneities on boundary scattering.

The present work is the second of two papers dealing with the infrared radiative behavior of porous ceramics containing pores and/or particles of sizes close to the wavelength of interest. In our first paper [34], we proposed a physical optics approach based on the discrete dipole approximation (DDA) to determine the effective volume radiative properties and surface reflectivity from 3D microstructures, while accounting for dependent scattering between the μm-sized pores. We also computed these properties on a tomography-reconstructed porous alumina ceramic, and compared our numerical results with analytical solutions. In the present paper, we characterize the normal reflectance, transmittance, and emittance of thin samples of the porous alumina ceramic from room temperature up to 1300 °C using two approaches. First, infrared spectroscopy measurements of the room-temperature normal-hemispherical reflectance and transmittance as well as the normal emittance up to 1300 °C are performed. These radiometric quantities are then simulated via the RTE-based equivalent homogeneous medium approach from the effective radiative properties computed with the DDA in our first paper [34] and compared to experimental results. Section 2 describes the samples used in this study, and the experimental methods used for microstructural and radiometric characterization. Section 3 briefly summarizes the numerical method and key results of our first paper [34], then presents the RTE-based model used to predict the reflectance, transmittance, and emittance of the samples. Section 4 then presents and compares the experimental and numerical results, with the uncertainties in numerical results quantified through a sensitivity study.

2. Experimental procedure

2.1. Material and microstructure

The studied material is a high-purity porous alumina ceramic, fabricated as plane-parallel disk samples for the infrared spectroscopy measurements (presented in section 2.2). A raw powder mix composed of 99% α-alumina by mass, with a volume median grain diameter of 2.9 µm, was first dispersed in water to form a homogeneous slurry, then air-dried and ground back up into powder form. Uniaxial pressing at 10 MPa in a cylindrical mold followed by sintering at 1650 °C for 6 hours gave porous sintered alumina cylinders 33 mm in diameter. Finally, plane-parallel cuts perpendicular to the cylinder axis were made with a precision saw to obtain disks of thickness $h = 2.0 \pm 0.1$ mm. The machined samples were heat-treated at 800 °C for 6 hours to remove all organic pollutants.

Scanning electron microscopy (Hitachi TM3030, 15 kV accelerating voltage, backscattered electrons mode) was performed at Saint-Gobain Research Provence (Cavaillon, France) on polished samples of the porous alumina ceramic (see Figure 1). The Fiji software [35] was then used to perform binarization, denoising, and microstructural analysis on the micrographs. Note that in our companion paper [34] we also presented the X-ray tomography and image processing protocol used to obtain the 3D microstructure.

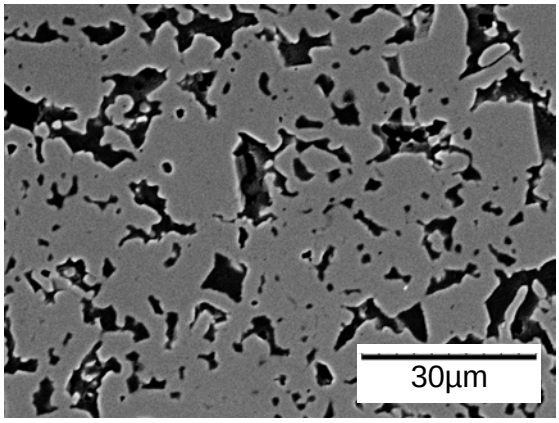

Figure 1: Scanning electron micrograph of a polished section of the porous alumina ceramic, with pores in black.

Physical measurements were also performed at Saint-Gobain Research Provence (Cavaillon, France) on the porous ceramic cylinders:

- A total porosity of $f_p = 0.22 \pm 0.02$ was measured on the cylinders by dividing their apparent density (caliper method) by the known density of the alumina powder mix. Open porosity measurements via the water immersion and saturation method [36] gave almost identical results, showing that little to no closed porosity is negligible (note that the porosity was also estimated through void pixel counting on 15 electron micrographs giving $f_p = 0.20 \pm 0.07$, which is in good agreement with the physical measurement). We thus consider $f_p = 0.22 \pm 0.02$ as the nominal porosity for the remainder of this study.

- We also performed pore size measurements just to check that the different methods and samples agree: the mean pore chord length [37] is estimated at $\langle\langle \ell_p \rangle\rangle = 1.8 \pm 0.3\,\mu m$ from the electron micrographs (which is in good agreement with value found on the tomographic reconstruction [34]). It agrees with the value of $\langle\langle \ell_p \rangle\rangle \approx 4f_p/A_V = 1.2 \pm 0.2\,\mu m$ measured using mercury intrusion porosimetry (A_V is the specific surface area) [38, 39]. The difference between the physical measurement and the image processing result may be attributed to the hypothesis of cylindrical pores in mercury intrusion porosimetry, which leads to underestimation when throats are present [39].

2.2. Infrared spectroscopy

The spectral radiometric quantities of interest (reflectance, transmittance, and/or emittance) are measured on the 2 mm thick disks of diameter 33 mm, for vacuum wavelengths λ_0 between 1 µm and 10 µm from room temperature up to 1300 °C using two setups developed at the CEMHTI laboratory (Orléans, France), briefly described here.

At room temperature, the normal-hemispherical reflectance $\mathfrak{R}$ and transmittance $\mathfrak{T}$ are acquired using a 6-inch integrating sphere with infragold coating and a liquid-nitrogen-cooled mercury cadmium telluride detector, both coupled to a Fourier transform infrared spectrometer (Bruker Vertex 70). Measurements were performed at least 4 times (both sides of two samples) and averaged to account for the influence of material variability, which incidentally is quite low in the present case: the absolute uncertainty is between 0.01 and 0.02 for both $\mathfrak{R}$ and $\mathfrak{T}$. According to Kirchhoff's law [2], the room-temperature normal emittance $\mathfrak{E}$, equal to the absorbance, is calculated from $\mathfrak{R}$ and $\mathfrak{T}$ as follows:

$$\mathfrak{E} = 1 - \mathfrak{R} - \mathfrak{T} \tag{1}$$

At high temperatures, the normal emittance $\mathfrak{E}$ of a sample maintained at a constant elevated temperature T is directly measured as the ratio of the spectral intensity emitted by the sample to that emitted by a blackbody at the same temperature [3]. The apparatus, shown in Figure 2 and described in detail in reference [5], consists of a reference blackbody furnace and a sample heating system mounted on a computer-controlled turntable within a purged enclosure. Two Fourier transform spectrometers (Bruker Vertex 80v working under vacuum, and Bruker Vertex 70 purged with dry air) enable measurements from the far infrared to the visible range. The flux emitted by the sample in the normal direction within an aperture of diameter 1 mm is measured and compared to the reference blackbody flux, with supplementary measurements to quantify and correct for the parasite fluxes from the instruments. To minimize the axial temperature gradient within the sample, a 500 W CO_2 laser (Coherent K500) separated equally by a beam splitter is used to heat the sample on both faces. The temperature of the sample is determined by using the spectrometer as a pyrometer at the known Christiansen wavelength of alumina ($\approx$ 10 µm) where it exhibits blackbody-like emissivity [40]. This methods allows the direct measurement of $\mathfrak{E}$ with an absolute uncertainty of 0.02 at extreme temperatures up to 2500 K.

Interested readers are invited to consult references [4] and [5] for more details on the apparatus used in this study.

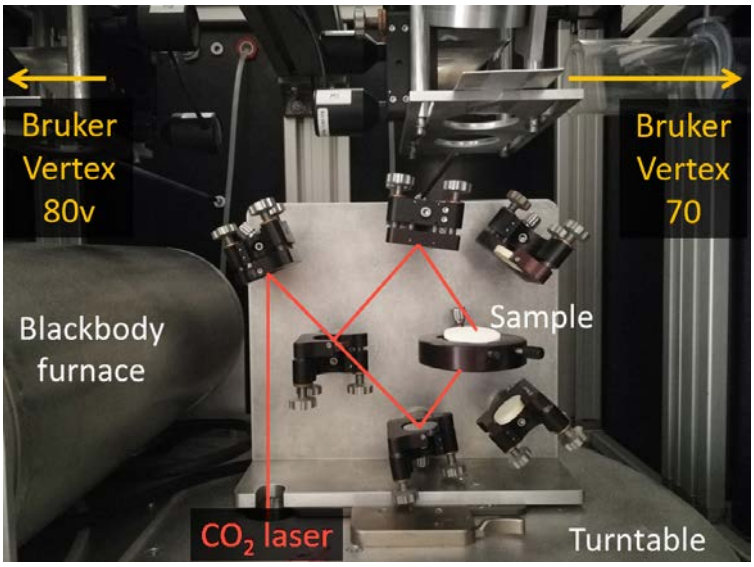

Figure 2: Apparatus at the CEMHTI laboratory (Orléans, France) used to measure the high-temperature emittance [5].

3. Numerical method

The normal-hemispherical reflectance $\mathfrak{R}$ and transmittance $\mathfrak{T}$ of the porous alumina samples are simulated using a multi-scale approach presented in this section, then used to calculate the normal emittance $\mathfrak{E}$ via equation (1). In this approach, effective volume and surface radiative properties of the porous alumina material are first calculated using analytical relations, deduced from microstructure-based-simulation results of a novel physical optics model proposed in our companion paper [34]. We calculated effective radiative properties at selected temperatures from room temperature up to 1300 °C, which covers common service temperatures for refractory alumina. These effective properties are then used to model the reflectance and transmittance of the porous alumina disks under normal collimated illumination, by resolving the radiative transfer equation (RTE) on an equivalent homogeneous medium.

3.1. Effective radiative properties modeling with a physical optics based approach

The effective radiative properties modeling approach proposed in our companion paper [34] has been developed for porous or multiphase materials with a homogeneous weakly absorbing dominant phase (henceforth referred to as the matrix, denoted with subscript m) having a much higher volume fraction compared to the other phases (pore or particle heterogeneities, denoted with subscript p). As the porous alumina samples in the present study contains 78% of high-purity α-alumina by volume, with grain sizes exceeding one-tenth of the wavelengths of interest allowing grain boundary effects to be neglected [41], they fit the description. The model simulates scattering and absorption in tomography-reconstructed volume elements of the material using the discrete dipole approximation (DDA) [42, 43], which takes into account dependent scattering when heterogeneities are small and close to each other compared to the wavelength.

We determined the effective radiative properties of the porous alumina at temperatures T = 22 °C, 800 °C, 1000 °C, and 1300 °C for selected wavelengths between λ_0 = 1 µm and λ_0 = 7 µm.

For each investigated temperature, we calculated the spectral complex refractive index $n_m + i\kappa_m$ of the sintered alumina matrix used as input, by directional averaging [44] the birefringent complex refractive indexes of α-alumina monocrystals [40]. Values are given in Table 1:

λ_0	T = 22 °C		T = 800 °C		T = 1000 °C		T = 1300 °C	
[µm]	n_m	κ_m	n_m	κ_m	n_m	κ_m	n_m	κ_m
1.0	1.718	1.36×10^{-41}	1.665	4.17×10^{-7}	1.645	6.88×10^{-7}	1.629	5.84×10^{-7}
1.5	1.712	8.12×10^{-21}	1.659	5.93×10^{-7}	1.640	9.86×10^{-7}	1.624	8.38×10^{-7}
2.0	1.704	7.22×10^{-14}	1.651	7.36×10^{-7}	1.632	1.24×10^{-6}	1.617	1.05×10^{-6}
3.0	1.680	4.25×10^{-9}	1.628	9.31×10^{-7}	1.611	1.61×10^{-6}	1.595	1.40×10^{-6}
4.0	1.644	3.43×10^{-7}	1.594	6.66×10^{-6}	1.578	1.20×10^{-5}	1.564	1.84×10^{-5}
5.0	1.594	2.78×10^{-5}	1.547	1.42×10^{-4}	1.534	2.02×10^{-4}	1.521	2.77×10^{-4}
6.0	1.527	2.37×10^{-4}	1.482	9.97×10^{-4}	1.473	1.34×10^{-3}	1.462	1.74×10^{-3}
7.0	1.435	1.94×10^{-3}	1.390	6.03×10^{-3}	1.392	6.91×10^{-3}	1.385	7.06×10^{-3}

Table 1: Complex refractive index of sintered alumina at the studied temperatures.

Due to the high computational cost of the proposed approach, we performed simulations on a large number of subvolumes (8 to 125 depending on wavelength and volume element size). This allowed us to extract analytical porosity-property relations for porosities ranging from a few percent up to $f_p \approx 0.3$, and also to quantify the uncertainty in the computed effective radiative properties as the root-mean-squared (RMS) deviation between DDA results on all subvolumes and the analytical relation. Key conclusions for the studied porous alumina ceramic are summarized below:

- DDA simulations confirmed that thanks to the low alumina absorptivity on the absorption coefficient κ_{eff} may be calculated to 7% uncertainty on the wavelength range of interest with the analytical relation proposed by Dombrovsky et al. [45] for porous ceramics with a weakly absorbing solid phase:

$$\kappa_{\text{eff}} = \frac{4\pi\kappa_m}{\lambda_0} f_m \tag{2}$$

  Indeed, as pure alumina monocrystal data is used as input for the solid matrix, κ_m very low for the considered temperatures and wavelengths ($\leq 6 \times 10^{-3}$) and κ_{eff} scales linearly with the matrix fraction f_m. The values of κ_{eff} at the nominal porosity $f_p = 0.22 = 1 - f_m$ of the porous alumina samples are plotted for the studied wavelengths and temperatures in Figure 3a. Note that as a logarithmic scale is used, the $\pm$7% error bars are barely visible. At room temperature, the extremely low κ_{eff} (less than 1 m^{-1}) for wavelengths between 1 µm to 4 µm are not represented to improve legibility (practically no absorption occurs in the mm-sized samples at this temperature and wavelength range).

- Based on our discussion in the companion paper [34], we found that the porous alumina material, initially with scattering coefficient σ_{eff} and anisotropic phase function ϕ_{eff}, is appropriately modeled with a transport scattering coefficient σ_{tr} associated with an isotropic

phase function $\phi_{tr} = (4\pi)^{-1}$ instead [46]:

$$\sigma_{tr} = \sigma_{\text{eff}}(1 - g_{\text{sca}}) = \sigma_{\text{eff}}\left(1 - \int_{4\pi} \phi_{\text{eff}}(\mathbf{u}, \mathbf{u}')|\mathbf{u} \cdot \mathbf{u}'|\, \mathrm{d}\Omega'\right) \tag{3}$$

where $\mathbf{u}$ and $\mathbf{u}'$ are the incident and scattered unit direction vectors respectively, $\mathrm{d}\Omega'$ is the elementary solid angle associated with $\mathbf{u}'$, and 4π is the solid angle of a sphere which represents the entire angular space. Note that in this work ϕ_{eff} is normalized such that $\int_{4\pi} \phi_{\text{eff}}(\mathbf{u}, \mathbf{u}')\, \mathrm{d}\Omega' = 1$.

The values of σ_{tr} simulated using the DDA were well described with a second-order polynomial function of the porosity:

$$\sigma_{tr} = p_1 f_p + p_2 f_p^2 \tag{4}$$

with coefficients $p_1(\lambda_0, T)$ and $p_2(\lambda_0, T)$ identified from DDA results for every temperature and wavelength. The values of σ_{tr} predicted with these correlations at the nominal porosity of $f_p = 0.22$ are plotted in Figure 3b. Error bars indicate the uncertainty of $\pm 20.8\%$, estimated by taking the RMS deviation between all DDA results and the analytical relation, and reflects the high microstructural variability.

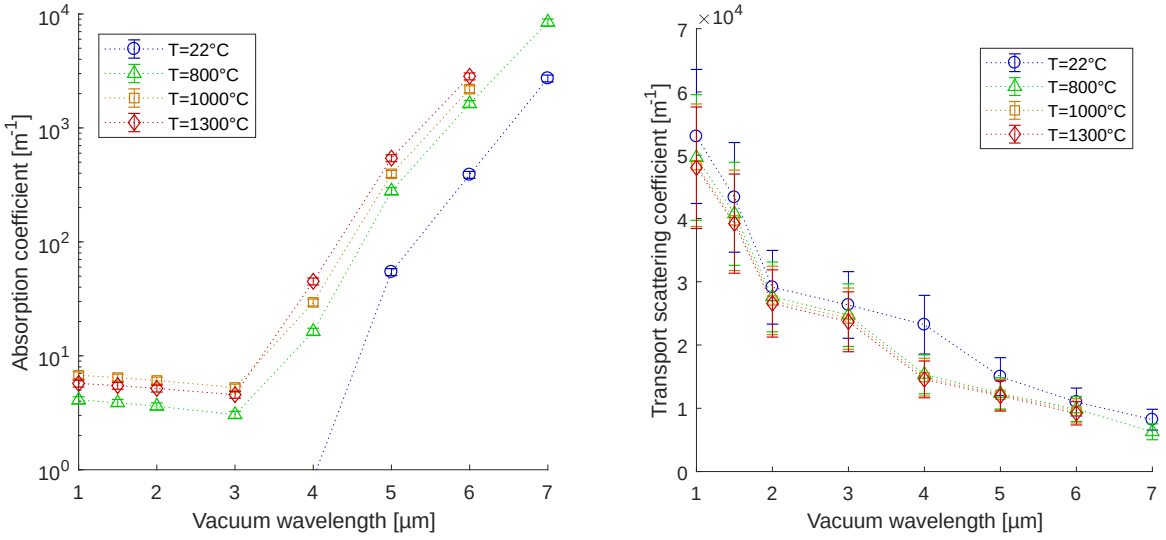

(a) Absorption coefficient.

(b) Transport scattering coefficient.

Figure 3: Spectral volume radiative properties of the porous alumina ceramic, evaluated at its nominal porosity $f_p = 0.22$, for four different temperatures T.

- For the surface reflectivity, we assume that the surface of the studied porous alumina is smooth everywhere save where pores are present. DDA numerical results in our companion paper [34] for the case of normal illumination by light of wavelength $\lambda = \lambda_0 = 2\,\mu\text{m}$ were rather well described by a geometrical-optics-based analytical model that simply considers perfectly diffuse reflection for incident radiation incident on the pore phase, and perfectly specular reflection according to Fresnel's equations for the remaining radiation.

The directional-hemispherical reflectivity $\mathcal{R}_{\hbar}$ and transmissivity $\mathcal{T}_{\hbar}$ for incidence direction $\mathbf{u}$ are then modeled as follows [34]:

$$\mathcal{R}_{\hbar}(\mathbf{u}) = \underbrace{f_m \mathcal{R}_{\mathrm{Fr}}(\mathbf{u})}_{\mathcal{R}_{\mathrm{spec}}(\mathbf{u})} + \underbrace{f_p \left\langle \mathcal{R}_{\mathrm{Fr}} \right\rangle}_{\mathcal{R}_{\mathrm{diff}}} \tag{5a}$$

$$\mathcal{T}_{\hbar}(\mathbf{u}) = \underbrace{f_m (1 - \mathcal{R}_{\mathrm{Fr}}(\mathbf{u}))}_{\mathcal{T}_{\mathrm{spec}}(\mathbf{u})} + \underbrace{f_p \left(1 - \left\langle \mathcal{R}_{\mathrm{Fr}} \right\rangle\right)}_{\mathcal{T}_{\mathrm{diff}}} \tag{5b}$$

$\mathcal{R}_{\mathrm{Fr}}(\mathbf{u})$ is the specular reflectivity given by Fresnel's equations [1], here computed for light in vacuum incident on an alumina surface of refractive index n_m. $\langle \mathcal{R}_{\mathrm{Fr}} \rangle$ is the diffuse reflectivity obtained by the following weighted average of $\mathcal{R}_{\mathrm{Fr}}$ [46, 47]:

$$\left\langle \mathcal{R}_{\mathrm{Fr}} \right\rangle \equiv \int_{\mathbf{u}' \cdot \mathbf{n} < 0} 2 \mathcal{R}_{\mathrm{Fr}}(\mathbf{u}') |\mathbf{u}' \cdot \mathbf{n}| \, \mathrm{d}\Omega' \tag{6}$$

where $\mathbf{n}$ is the normal vector pointing outwards from the surface. For normally incident light on a surface with $n_m = 1.718$ (corresponding to the sintered alumina phase at room temperature and $\lambda_0 = 1\,\mu\mathrm{m}$), equation (5a) gives $\mathcal{R}_{\hbar} = 0.0814$. Uncertainties are estimated at 22.6% on $\mathcal{R}_{\hbar}$ and 27% on $\mathcal{R}_{\mathrm{spec}}$, mainly due to neglected wave effects and microstructural variability.

In the next section, the effective radiative properties of the porous alumina ceramic evaluated at its nominal porosity ($f_p = 0.22$) is applied to simulate radiometric measurements on the 2 mm thick disks from room temperature to 1300 °C. While the uncertainties in some of the computed effective properties are rather high, sensitivity studies presented in section 4.2 show that they have limited influence on the simulated radiometric properties.

3.2. Reflectance, transmittance, and emittance modeling

In this section, the normal-reflectance $\mathfrak{R}$ and transmittance $\mathfrak{T}$ of the porous alumina disks at different temperatures are simulated with the radiative transfer equation (RTE) using the equivalent homogeneous approach. With these two quantities, the normal emittance $\mathfrak{E}$ can then be calculated using Kirchhoff's law (equation (1)).

We consider a semi-infinite plane-parallel slab of thickness h placed in vacuum ($n_{\mathrm{amb}} = 1$), illuminated on one face by a collimated beam at incidence angle θ_{inc} (= 0 in the present work). The slab, at uniform temperature T, is composed of a homogeneous absorbing-scattering material prescribed the absorption (κ_{eff}) and transport scattering (σ_{tr}) in Figure 3. Per classic assumptions [12, 28, 29] of 1D radiative transfer, azimuthal symmetry, and negligible self-emission, the RTE simplifies to [2]:

$$\mu \frac{\partial \mathcal{I}^*(x, \mu)}{\partial x} = -(\sigma_{tr} + \kappa_{\mathrm{eff}}) \mathcal{I}^*(x, \mu) + \frac{\sigma_{tr}}{4\pi} \int_{4\pi} \mathcal{I}^*(x, \mu') \, \mathrm{d}\Omega' \tag{7}$$

where x is the position along the thickness direction $\mathbf{e}_x$, and $\mu \equiv \mathbf{u} \cdot \mathbf{e}_x$ is the direction cosine for the unit direction vector $\mathbf{u}$ associated with the solid angle $\mathrm{d}\Omega$. Note we solve for the spectral basic

radiance $\mathcal{I}^*$ to account for the conservation of étendue [48] when light refracts at the boundary between the surrounding vacuum medium and the slab:

$$\mathcal{I}^* = \frac{\mathcal{I}}{n^2} \tag{8}$$

where $\mathcal{I}$ is the spectral radiance (intensity per unit solid angle per unit vacuum wavelength) and n is the local refractive index: $n = 1$ in vacuum and $n > 1$ within the slab.

To write the boundary conditions, we first define the incident radiance $\mathcal{I}^*_{\text{inc}}$ at $x = 0^-$ in terms of the spectral intensity I_{inc} concentrated in a narrow solid angle $\Delta\Omega$ about the normal direction $\mu = 1$:

$$I_{\text{inc}} = \int_{\mu>0} \mathcal{I}^*(x = 0^-, \mu)\mu \, \mathrm{d}\Omega = \int_{\Delta\Omega} \mathcal{I}^*(x = 0^-, \mu = 1) \, \mathrm{d}\Omega \equiv \int_{\Delta\Omega} \mathcal{I}^*_{\text{inc}} \, \mathrm{d}\Omega \tag{9}$$

Note that $\mathcal{I}^* = \mathcal{I}$ in vacuum; that is, for $x < 0$ and $x > h$.

In section 3.1, we chose to model the directional-hemispherical reflectivity $\mathcal{R}_h$ of the slab boundary under external illumination from the surrounding vacuum medium as the sum of a perfectly specular component $\mathcal{R}_{\text{spec}}$ and a perfectly diffuse component $\mathcal{R}_{\text{diff}}$ (equation (5a)). These terms are henceforth denoted with the superscript "ext" to distinguish them from their counterparts for radiation arriving at the boundary from within the material (internal illumination), denoted with the superscript "int". Based on microscopic reversibility principles [49], we assume that $\mathcal{R}^{\text{int}}$ is also modeled in the same manner as $\mathcal{R}^{\text{ext}}$ using equations (5a) and (6), with $\mathcal{R}^{\text{int}}_{\text{Fr}} = 1$ for incident angles exceeding the critical angle for total internal reflection.

The boundary conditions are then expressed using the definitions in equations (5a) and (5b),

- For $x = 0^+$:

$$\begin{aligned}\mathcal{I}^*(\mu > 0) = \mathcal{T}^{\text{ext}}_{\text{spec}}(\mu)\mathcal{I}^*_{\text{inc}}\delta_{1-\mu} + \frac{1}{\pi}\mathcal{T}^{\text{ext}}_{\text{diff}} \int_{\Delta\Omega} \mathcal{I}^*_{\text{inc}} \, \mathrm{d}\Omega' \\ + \mathcal{R}^{\text{int}}_{\text{spec}}(\mu'_{\mathcal{R}})\mathcal{I}^*(\mu'_{\mathcal{R}}) + \frac{1}{\pi}\mathcal{R}^{\text{int}}_{\text{diff}} \int_{\mu'<0} \mathcal{I}^*(\mu')\mu' \, \mathrm{d}\Omega'\end{aligned} \tag{10a}$$

  where δ represents the Kronecker delta, here defined as $\delta_X = 1$ if $X = 0$, and $\delta_X = 0$ otherwise;

- For $x = h^-$:

$$\mathcal{I}^*(\mu < 0) = \mathcal{R}^{\text{int}}_{\text{spec}}(\mu'_{\mathcal{R}})\mathcal{I}^*(\mu'_{\mathcal{R}}) + \frac{1}{\pi}\mathcal{R}^{\text{int}}_{\text{diff}} \int_{\mu'>0} \mathcal{I}^*(\mu')\mu' \, \mathrm{d}\Omega' \tag{10b}$$

where $\mu'_{\mathcal{R}} = -\mu$ represents the direction prior to a specular reflection event that reflected light towards the direction μ. These boundary conditions are illustrated in Figure 4.

Equations (7) and (10) were resolved with the Monte Carlo method [2, 20]: converged results were obtained using 10^6 equal-energy packets. The reflected and transmitted radiance fields are

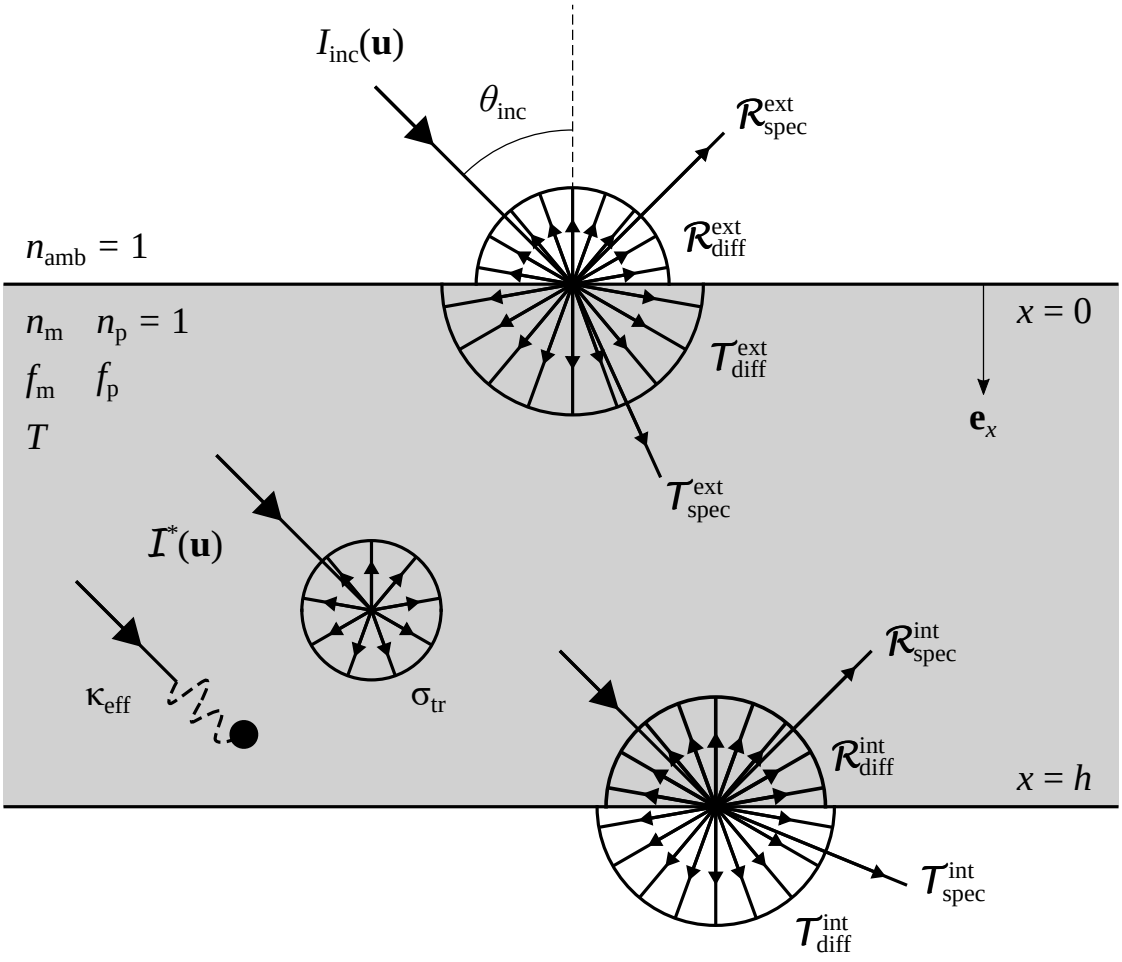

Figure 4: Diagram of the reflectance and transmittance model.

then calculated:

$$\begin{aligned}\mathcal{I}^*(x = 0^-, \mu < 0) = \mathcal{R}^{\text{ext}}_{\text{spec}}(\mu)\mathcal{I}^*_{\text{inc}}\delta_{1+\mu} + \frac{1}{\pi}\mathcal{R}^{\text{ext}}_{\text{diff}}\int_{\Delta\Omega}\mathcal{I}^*_{\text{inc}}\,\mathrm{d}\Omega' \\ + \mathcal{T}^{\text{int}}_{\text{spec}}(\mu'_{\mathcal{T}})\mathcal{I}^*(x = 0^+, \mu'_{\mathcal{T}}) + \frac{1}{\pi}\mathcal{T}^{\text{int}}_{\text{diff}}\int_{\mu'<0}\mathcal{I}^*(x = 0^+, \mu')\mu'\,\mathrm{d}\Omega'\end{aligned} \tag{11a}$$

$$\mathcal{I}^*(x = h^+, \mu > 0) = \mathcal{T}^{\text{int}}_{\text{spec}}(\mu'_{\mathcal{T}})\mathcal{I}^*(x = h^-, \mu'_{\mathcal{T}}) + \frac{1}{\pi}\mathcal{T}^{\text{int}}_{\text{diff}}\int_{\mu'>0}\mathcal{I}^*(x = h^-, \mu')\mu'\,\mathrm{d}\Omega' \tag{11b}$$

where $\mu'_{\mathcal{T}}$ represents the direction prior to an outgoing specular refraction event that refracted light towards the direction μ, calculated using the Snell-Descartes law [48]: $n_m^2(1-\mu'^2_{\mathcal{T}}) = n^2_{\text{amb}}(1-\mu^2)$.

The normal-hemispherical reflectance $\mathfrak{R}$ and transmittance $\mathfrak{T}$ are then obtained as follows:

$$\mathfrak{R} = \frac{1}{I_{\text{inc}}} \int_{\mu<0} \mathcal{I}^*(x = 0^-, \mu)\mu \, \mathrm{d}\Omega \tag{12a}$$

$$\mathfrak{T} = \frac{1}{I_{\text{inc}}} \int_{\mu>0} \mathcal{I}^*(x = h^+, \mu)\mu \, \mathrm{d}\Omega \tag{12b}$$

after which the normal emittance is simply calculated as $\mathfrak{E} = 1 - \mathfrak{R} - \mathfrak{T}$ per equation (1).

4. Results and Discussion

4.1. Comparison of experimental and numerical results

Figure 5 compares the experimentally measured reflectance ($\mathfrak{R}$) and transmittance ($\mathfrak{T}$) at room temperature to the ones simulated at selected wavelengths using our new physical-optics-based approach. An excellent agreement is found between the two results at wavelengths smaller than 2.5 µm and greater than 5 µm, well within experimental uncertainties (± 0.01), which is extremely encouraging for validation of our proposed numerical approach.

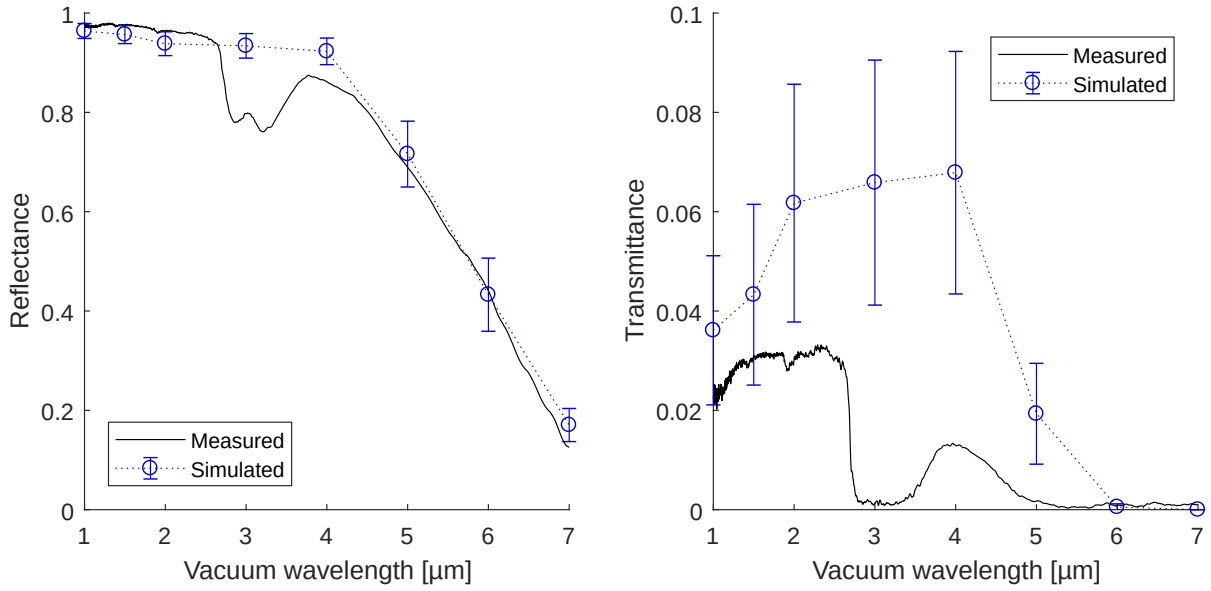

(a) Normal-hemispherical reflectance.

(b) Normal-hemispherical transmittance.

Figure 5: Measured (lines) and simulated (○) spectral normal-hemispherical reflectance and transmittance of the porous alumina disks at room temperature (T = 22 °C).

Note that the error bars represent numerical uncertainties denoted ΔY for an observed quantity $Y \in \{\mathfrak{R}, \mathfrak{T}, \mathfrak{E}\}$, evaluated assuming that the input parameters X vary independently of one another:

$$(\Delta Y)^2 = \sum_X \left(\mathfrak{S}_Y(X) \frac{\Delta X}{X_0} \times 100\% \right)^2 \tag{13}$$

where $(\Delta X/X_0) \times 100\%$ is the relative uncertainty in % on X, and $\mathfrak{S}_Y(X)$ is the sensitivity coefficient defined as the variation in Y per % increase in X, all other input parameters being constant:

$$\mathfrak{S}_Y(X) = \left.\frac{\partial Y}{\partial X}\right|_{X_0} \frac{X_0}{100\%} \tag{14}$$

Note that $\mathfrak{S}_Y(X)$ is studied later in section 4.2, with values given in Figure 7. Table 2 summarizes the input parameters X considered and their relative uncertainties. The computed uncertainties range from 0.01 to 0.07 depending on the radiometric quantity and wavelength.

$\frac{\Delta\kappa_{\text{eff}}}{\kappa_{\text{eff},0}}$	$\frac{\Delta\sigma_{tr}}{\sigma_{tr,0}}$	$\frac{\Delta\mathcal{R}^{\text{ext}}_{\text{spec}}}{\mathcal{R}^{\text{ext}}_{\text{spec},0}} = \frac{\Delta\mathcal{R}^{\text{int}}_{\text{spec}}}{\mathcal{R}^{\text{int}}_{\text{spec},0}}$	$\frac{\Delta\mathcal{R}^{\text{ext}}_{\text{diff}}}{\mathcal{R}^{\text{ext}}_{\text{diff},0}} = \frac{\Delta\mathcal{R}^{\text{int}}_{\text{diff}}}{\mathcal{R}^{\text{int}}_{\text{diff},0}}$	$\frac{\Delta h}{h_0}$
7%	21%	26%	40%	5%

Table 2: Uncertainties in input parameters: effective absorption coefficient (κ_{eff}), transport scattering coefficient (σ_{tr}), specular ($\mathcal{R}_{\text{spec}}$) and diffuse ($\mathcal{R}_{\text{diff}}$) components of the surface reflectivity (for both external/internal illumination), and sample thickness (h).

Between 2.5 µm and 5 µm, a sharp dip is observed in the measured spectra for both $\mathfrak{R}$ and $\mathfrak{T}$ but is absent from the numerical results. This difference between numerical and experimental results at room temperature is expected: it is due to the characteristic absorption by hydroxyl (OH) groups and adsorbed water molecules, which are almost always present on the surface of alumina ceramics [50] but are not taken into account in the input data for our numerical model. Recall that we worked with complex refractive indexes derived from measurements on impurity-free alumina monocrystals [40]. Precise determination of impurity content and its influence on radiometric quantities is generally challenging: Rozenbaum et al. [6] recently proposed an inverse method to identify the OH content in porous silica, which combines emittance measurements on dense and porous samples with discrete-scale ray-tracing simulations.

While this absorption peak is clearly seen on the room-temperature emittance curve in Figure 6, it is absent from the high-temperature emittance spectra since near-complete desorption of the OH groups occur at 800 °C and above [50]. With the increase in temperature, the absorption front (sharp increase in emittance between $\lambda_0 \approx 3\,\mu\text{m}$ and $\lambda_0 \approx 7\,\mu\text{m}$) shifts slightly towards shorter wavelengths under the influence of multiphonon processes [40]. The low emittance at wavelengths below 2.5 µm for all temperatures is a testament to the high purity of the alumina matrix.

In the absence of OH absorption peaks, the high-temperature emittance spectra are extremely well reproduced by the numerical models. The numerical results appear to slightly overestimate the experimental results at all wavelengths, though the differences still remain within their respective confidence intervals. Notably, uncertainties in the temperature and reference blackbody flux determination during high-temperature emittance measurements give an estimated absolute uncertainty of ± 0.02.

These results validate our numerical modeling approach, notably the DDA-based method proposed in our companion paper [34] to compute the effective radiative properties, the use of alumina monocrystal data as input while neglecting grain boundary scattering.

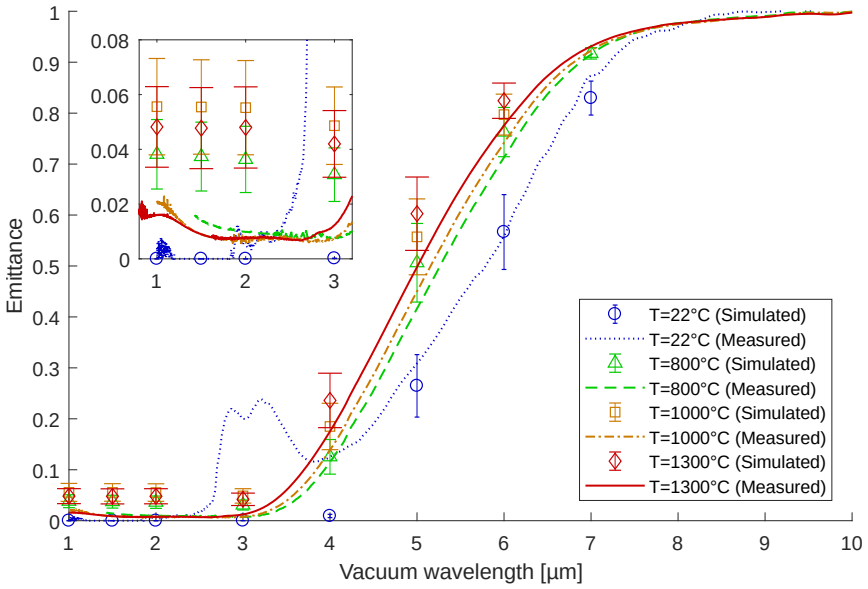

Figure 6: Measured (lines) and simulated (symols) spectral normal emittance of the porous alumina disks at different temperatures T: 22 °C (dotted lines vs. ○), 800 °C (dashed lines vs. △), 1000 °C (dash-dotted lines vs. □), 1300 °C (continuous lines vs. ◇). The inset shows the near-zero emittances at wavelengths between 1 µm and 3 µm.

4.2. Sensitivity study

Figure 7 shows the sensitivity coefficients $\mathfrak{S}_Y(X)$ defined in equation (14) as a function of wavelength $X = \left\{\sigma_{tr}, \kappa_{\text{eff}}, \mathcal{R}_{\text{spec}}, \mathcal{R}_{\text{diff}}, h\right\}$ and $Y = \{\mathfrak{R}, \mathfrak{T}, \mathfrak{E}\}$ at temperature $T = 800\,°\text{C}$ (note that similar trends are also observed at the other studied temperatures). The magnitude of $\mathfrak{S}_Y(X)$ indicates the sensitivity of Y to small changes in X, while its sign indicates whether a small increase in X leads to an increase ($\mathfrak{S}_Y > 0$) or decrease ($\mathfrak{S}_Y < 0$) in Y.

We observe that while $\mathfrak{S}_Y$ is generally quite low, it is always non-zero except when the observed quantity Y is null or very low. The non-zero value of $\mathfrak{S}_h$ shows the extrinsic nature of the radiometric quantities. Some interesting observations are summarized below:

- The signs of $\mathfrak{S}_Y(\sigma_{tr})$ and $\mathfrak{S}_Y(\kappa_{\text{eff}})$ are physically coherent: increasing σ_{tr} increases $\mathfrak{R}$, decreases $\mathfrak{T}$ and decreases $\mathfrak{E}$, while increasing κ_{eff} decreases $\mathfrak{R}$, decreases $\mathfrak{T}$ and increases $\mathfrak{E}$. The similar trends in their magnitudes suggest that the influence of σ_{tr} and κ_{eff} are correlated. This is discussed further in section 4.3.

- The sensitivity coefficients for $\mathcal{R}_{\text{spec}}$ and $\mathcal{R}_{\text{diff}}$ are very similar, since $\mathfrak{R}$, $\mathfrak{T}$ and $\mathfrak{E}$ are quite insensitive to the exact angular distribution of radiative energy. Surprisingly, an increase in either of these parameters decrease $\mathfrak{R}$ while increasing $\mathfrak{T}$ and $\mathfrak{E}$. This is because a large part of the total reflected radiation is actually composed of radiation initially transmitted into the slab before exiting it from the illuminated face. When $\mathcal{R}_{\text{spec}}$ or $\mathcal{R}_{\text{diff}}$ is increased, the fraction of incident radiation transmitted into the slab decreases, and the probability of internal radiation exiting the slab also decreases. This "trapping" effect by the slab boundaries [20] increases the emittance especially, and also the transmittance to a smaller extent.

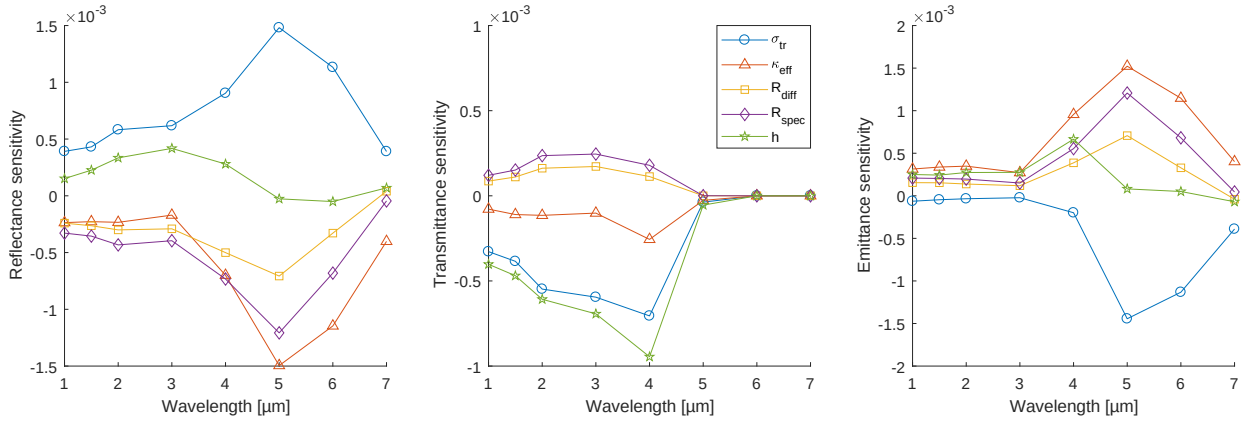

Figure 7: Spectral sensitivity coefficients (see equation (14)) for the normal-hemispherical reflectance (left), normal-hemispherical transmittance (center) and normal emittance (right) at 800 °C, with respect to five input parameters: transport scattering coefficient σ_{tr} (○), absorption coefficient κ_{eff} (△), diffuse reflectivity component $\mathcal{R}_{\text{diff}}$ (□), specular reflectivity component $\mathcal{R}_{\text{spec}}$ (◇), and slab thickness h (⋆).

- While the thickness h is the most influential parameter on $\mathfrak{T}$ on the semi-transparent range ($\lambda_0 < 5\,\mu\text{m}$), its effect on $\mathfrak{R}$ and $\mathfrak{E}$ on this range appears limited. Indeed, when scattering dominates, the optical paths traveled by radiation within the material is generally tortuous with multiple internal reflections off the boundary, and are therefore insensitive to small changes in h. In the opaque range ($\lambda_0 \geq 5\,\mu\text{m}$), h has practically no influence on all radiometric properties since radiation-matter interaction is limited to a small region close to the incident surface.

4.3. Influence of porosity

Before concluding, we study the influence of porosity on the radiometric properties by comparing the room-temperature reflectance ($\mathfrak{R}$), transmittance ($\mathfrak{T}$) and emittance ($\mathfrak{E}$) of our 22% porous alumina disks to those of a dense sintered alumina, modeled with Fresnel's equations using the same complex refractive index $n_m + i\kappa_m$ used in section 3.1. Figure 8 shows a remarkable increase in $\mathfrak{R}$ by more than 0.8 (and a corresponding decrease in $\mathfrak{T}$) due to the porosity of 22%. While the increase in reflectance and decrease in transmittance are natural when pores are present, the magnitude of these variations is much higher than past investigations on porous ceramics [6, 18]. This shows the interest in being able to incorporate physical optics effects in radiative transfer modeling.

In addition, between the wavelengths of 4 µm to 8 µm on the emittance (=absorbance) plot, we see that the absorption front is significantly modified by the presence of pores, with higher emittance in the porous material between 4 µm to 6 µm and higher emittance in the dense material beyond 6 µm. In fact, when the porosity increases, two competing mechanisms are in play: on one hand, the increased volume scattering within the porous material prolongs the optical paths traveled by light and thus the probability of being absorbed [18]; on the other hand, the probability of being absorbed for the same optical path length is lower in the porous material than in the dense material due to the lower matrix fraction. The prevalence of one over another depends on the relative magnitudes of the absorbing and scattering coefficients and also on the shape of the phase

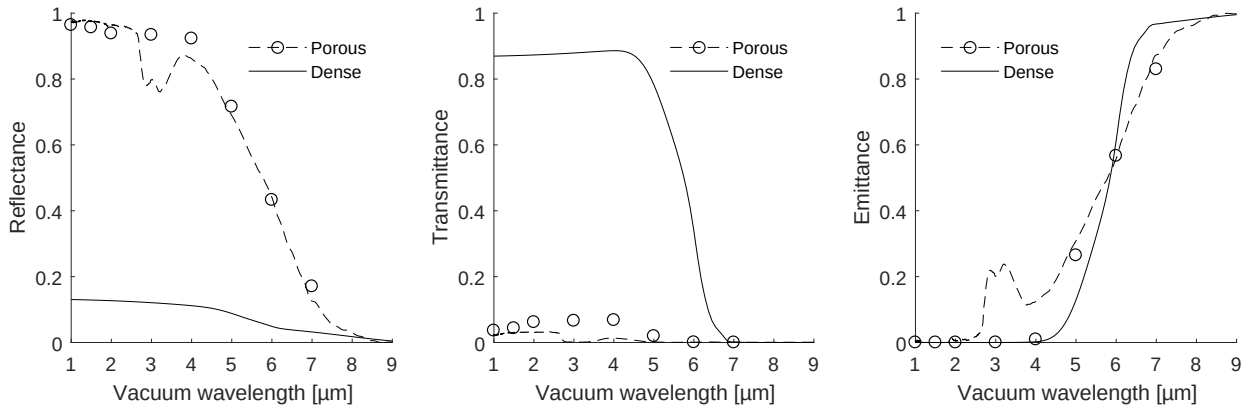

Figure 8: Room-temperature normal-hemispherical reflectance (left), normal-hemispherical transmittance (center), and normal emittance (right): measurements and physical-optics-based simulations on porous alumina disks (dashed lines and ○ respectively) compared to calculations with Fresnel's equations for a dense sintered alumina (continuous lines).

function, which explains the correlation observed between the sensitivity coefficients taken with respect to σ_{tr} and κ_{eff} (see section 4.2). In the present case, it would appear that the first mechanism dominates for wavelengths below 6 µm, while for wavelengths beyond this threshold the second mechanism dominates.

5. Conclusion

The reflectance, transmittance and emittance of porous alumina disks are measured from room temperature up to 1300 °C are compared to numerical results obtained using a novel multi-scale approach: effective radiative properties are first computed from the material microstructure using physical optics models based on the discrete dipole approximation (DDA), then applied to the simulation of an equivalent homogeneous medium using the radiative transfer equation (RTE).

A sensitivity study using the RTE-based model was performed to quantify the uncertainties in numerical results, mainly arising from microstructural variability due to the small volume elements used in physical optics modeling. Uncertainties in the radiometric quantities (reflectance, transmittance and emittance)are generally low, varying from 0.01 to 0.07 depending on wavelength. The sensitivity coefficients also provided insight to the influence of different input parameters and the physical phenomena in play.

The excellent agreement between experimental and numerical results confirm the validity of the proposed multi-scale approach. The extremely high reflectance and low transmittance in the present porous alumina samples for such a low porosity is never observed in the geometrical optics limit. It illustrates the strong influence of small heterogeneities on the macro-scale radiative properties, and highlights the need for more accurate physical-optics-based radiative transfer models.

Future work should focus on using the DDA numerical results to establish more accurate analytical modeling of microstructure-property relations, taking into account not just the porosity as we did, but also other parameters such pore size or pore shape. Application of the present DDA-RTE approach to the simulation and validation on other types of materials (e.g., multiple

particle phases), or other types of radiometric quantities (e.g., bidirectional quantities) would also be of great interest to test the capabilities of the proposed approach.

6. Acknowledgments

This research was supported by Saint-Gobain Research (SGR) Provence and the French National Association for Research and Technology (ANRT) through the CIFRE grant number 2017/0775. The authors would like to express their gratitude to L. San Miguel (SGR Provence), L. Pierrot (SGR Provence) and J. Meulemans (SGR Paris) for their insight and discussions that greatly improved the research; to Y. Millot (SGR Provence) for sample preparation and physical microstructural characterization; to J. Adrien (MATEIS) and N. Naouar (LaMCoS) for assistance with X-ray tomography; and last but not least, to R. Coquard (EC2 Modélisation) and S. Cunsolo (ex-LaMCoS) for helpful discussions on radiative transfer modeling.

References

[1] Q. Brewster, Thermal Radiative Transfer and Properties, John Wiley & Sons, Inc., 1992.
[2] R. Siegel, J. R. Howell, Thermal Radiation Heat Transfer, 3 ed., Hemisphere Publishing Corporation, 1992.
[3] J. M. Palmer, The measurement of transmission, absorption, emission and reflection, in: M. Bass (Ed.), Handbook of Optics, Optical Society of America, Volume II, 2 ed., McGraw-Hill, 1994, pp. 25.1–25.25.
[4] D. De Sousa Meneses, M. Balat-Pichelin, O. Rozenbaum, L. del Campo, P. Echegut, Optical indices and transport scattering coefficient of pyrolytic boron nitride: a natural thermal barrier coating for solar shields, Journal of Materials Science 51 (2016) 4660–4669.
[5] D. De Sousa Meneses, P. Melin, L. Del Campo, L. Cosson, P. Echegut, Apparatus for measuring the emittance of materials from far infrared to visible wavelengths in extreme conditions of temperature, Infrared Physics and Technology 69 (2015) 96–101.
[6] O. Rozenbaum, C. Blanchard, D. De Sousa Meneses, Determination of high-temperature radiative properties of porous silica by combined image analysis, infrared spectroscopy and numerical simulation, International Journal of Thermal Sciences 137 (2019) 552–559.
[7] R. Coquard, D. Baillis, D. Quenard, Energy & Buildings Numerical and experimental study of the IR opacification of polystyrene foams for thermal insulation enhancement, Energy & Buildings 183 (2019) 54–63.
[8] Y. Bao, Y. Huang, W. Li, K. Zhu, Combination of the monte carlo method and dda to evaluate the radiative properties of ito- pigmented and tio2-pigmented coatings, International Journal of Thermal Sciences 146 (2019) 106076.
[9] X. Chen, C. Zhao, B. Wang, Microstructural effect on radiative scattering coefficient and asymmetry factor of anisotropic thermal barrier coatings, Journal of Quantitative Spectroscopy and Radiative Transfer 210 (2018) 116 – 126.
[10] R. Lopes, L. M. Moura, D. Baillis, J. F. Sacadura, Directional spectral emittance of a packed bed: Correlation between theoretical prediction and experimental data, Journal of Heat Transfer 123 (2001) 240–249.
[11] B. Zeghondy, E. Iacona, J. Taine, Experimental and RDFI calculated radiative properties of a mullite foam, International Journal of Heat and Mass Transfer 49 (2006) 3702–3707.
[12] L. A. Dombrovsky, H. K. Tagne, D. Baillis, L. Gremillard, Near-infrared radiative properties of porous zirconia ceramics, Infrared Physics & Technology 51 (2007) 44 – 53.
[13] L. A. Dombrovsky, D. Baillis, Thermal Radiation in Disperse Systems: An Engineering Approach, Begell House, 2010.
[14] B. Bouvry, L. Del Campo, D. De Sousa Meneses, O. Rozenbaum, R. Echegut, D. Lechevalier, M. Gaubil, P. Echegut, Hybrid Methodology for Retrieving Thermal Radiative Properties of Semi-Transparent Ceramics, Journal of Physical Chemistry C 120 (2016) 3267–3274.

[15] O. Rozenbaum, D. De Sousa Meneses, P. Echegut, Texture and porosity effects on the thermal radiative behavior of alumina ceramics, International Journal of Thermophysics 30 (2009) 580–590.
[16] J. Petrasch, S. Haussener, W. Lipiński, Discrete vs. continuum-scale simulation of radiative transfer in semitransparent two-phase media, Journal of Quantitative Spectroscopy and Radiative Transfer 112 (2011) 1450–1459.
[17] B. Singh, M. Kaviany, Independent theory versus direct simulation of radiation heat transfer in packed beds, International Journal of Heat and Mass Transfer 34 (1991) 2869 – 2882.
[18] B. Rousseau, J.-y. Y. Rolland, P. Echegut, L. Del Campo, D. De Sousa Meneses, P. Echegut, Modelling of the Thermal Radiative Properties of Oxide Ceramics, in: Proceedings of the 14th International Heat Transfer Conference, 13, 2010, pp. 1–6.
[19] J. Randrianalisoa, S. Haussener, D. Baillis, W. Lipiński, Radiative characterization of random fibrous media with long cylindrical fibers: Comparison of single- and multi-rte approaches, Journal of Quantitative Spectroscopy and Radiative Transfer 202 (2017) 220 – 232.
[20] S. Cunsolo, D. Baillis, N. Bianco, Improved Monte Carlo methods for computational modelling of thermal radiation applied to porous cellular materials, International Journal of Thermal Sciences 137 (2019) 161–179.
[21] B. Liu, X. Xia, X. Zhang, C. Sun, Spectral radiative properties of skeleton inner structure of ceramic foam based on ordered opal structure model, Journal of Quantitative Spectroscopy and Radiative Transfer 224 (2019) 279 – 288.
[22] J. Randrianalisoa, D. Baillis, L. Pilon, Modeling radiation characteristics of semitransparent media containing bubbles or particles, J. Opt. Soc. Am. A 23 (2006) 1645–1656.
[23] S. Haussener, J. Randrianalisoa, Radiative characterization of ceramic foams with microporosity, Journal of Physics: Conference Series 676 (2016) 012010.
[24] M. Tancrez, J. Taine, Direct identification of absorption and scattering coefficients and phase function of a porous medium by a Monte Carlo technique, International Journal of Heat and Mass Transfer 47 (2004) 373–383.
[25] R. Coquard, D. Baillis, Radiative characteristics of opaque spherical particles beds: A new method of prediction, Journal of Thermophysics and Heat Transfer 18 (2004) 178–186.
[26] W. Lipiński, J. Petrasch, S. Haussener, Application of the spatial averaging theorem to radiative heat transfer in two-phase media, Journal of Quantitative Spectroscopy and Radiative Transfer 111 (2010) 253–258.
[27] J. Randrianalisoa, D. Baillis, Radiative properties of densely packed spheres in semitransparent media: A new geometric optics approach, Journal of Quantitative Spectroscopy and Radiative Transfer 111 (2010) 1372 – 1388.
[28] S. Lallich, F. Enguehard, D. Baillis, Experimental Determination and Modeling of the Radiative Properties of Silica Nanoporous, Journal of Heat Transfer 131 (2009) 082701.
[29] A. Kaemmerlen, C. Vo, F. Asllanaj, G. Jeandel, D. Baillis, Radiative properties of extruded polystyrene foams: Predictive model and experimental results, Journal of Quantitative Spectroscopy and Radiative Transfer 111 (2010) 865–877.
[30] X. Dai, S. Haussener, Optical characterization of multi-scale morphologically complex heterogeneous media – application to snow with soot impurities, Journal of Quantitative Spectroscopy and Radiative Transfer 206 (2018) 378 – 391.
[31] Z. Ivezic, M. P. Menguc, An investigation of dependent / independent scattering regimes using a discrete dipole approximation, International Journal of Heat and Mass Transfer 39 (1996) 811–822.
[32] M. I. Mishchenko, L. Liu, D. W. Mackowski, B. Cairns, G. Videen, Multiple scattering by random particulate media: exact 3d results, Opt. Express 15 (2007) 2822–2836.
[33] T. Galy, D. Huang, L. Pilon, Journal of Quantitative Spectroscopy & Radiative Transfer Revisiting independent versus dependent scattering regimes in suspensions or aggregates of spherical particles, Journal of Quantitative Spectroscopy and Radiative Transfer 246 (2020) 106924.
[34] Z. Low, D. Baillis, 1– a physical optics approach to predict the radiative properties of semi-transparent porous ceramics, 2020. In preparation.
[35] J. Schindelin, I. Arganda-Carreras, E. Frise, V. Kaynig, M. Longair, T. Pietzsch, S. Preibisch, C. Rueden, S. Saalfeld, B. Schmid, J.-Y. Tinevez, D. J. White, V. Hartenstein, K. Eliceiri, P. Tomancak, A. Cardona, Fiji: an open-source platform for biological-image analysis, Nature Methods 9 (2012) 676–682.
[36] U. Kuila, D. K. McCarty, A. Derkowski, T. B. Fischer, M. Prasad, Total porosity measurement in gas shales by

the water immersion porosimetry (wip) method, Fuel 117 (2014) 1115 – 1129.
[37] M. R. MacIver, M. Pawlik, Analysis of in situ microscopy images of flocculated sediment volumes, Chemical Engineering & Technology 40 (2017) 2305–2313.
[38] W. de Kruijf, J. Kloosterman, On the average chord length in reactor physics, Annals of Nuclear Energy 30 (2003) 549–553.
[39] P. A. Webb, An introduction to the physical characterization of materials by mercury intrusion porosimetry with emphasis on reduction and presentation of experimental data, Technical Report, Micromeritics Instrument Corp, Norcross, Georgia, 2001.
[40] J. F. Brun, L. del Campo, D. De Sousa Meneses, P. Echegut, Infrared optical properties of alpha-alumina with the approach to melting: gamma-like tetrahedral structure and small polaron conduction, Journal of Applied Physics 114 (2013) 223501.
[41] D. C. Harris, L. F. Johnson, L. Cambrea, L. Baldwin, M. Baronowski, E. Zelmon, W. B. Poston, J. D. Kunkel, M. Parish, M. R. Pascucci, J. J. Gannon, Jr, T.-c. Wen, Refractive index of infrared- transparent polycrystalline alumina, Optical Engineering 56 (2017) 077103.
[42] B. T. Draine, P. J. Flatau, Discrete-Dipole Approximation For Scattering Calculations, Journal of the Optical Society of America A 11 (1994) 1491.
[43] B. T. Draine, P. J. Flatau, Discrete-dipole approximation for periodic targets: theory and tests, Journal of the Optical Society of America A 25 (2008) 2693.
[44] L. A. Pajdzik, A. M. Glazer, Three-dimensional birefringence imaging with a microscope tilting-stage. I. Uniaxial crystals, Journal of Applied Crystallography 39 (2006) 326–337.
[45] L. Dombrovsky, J. Randrianalisoa, D. Baillis, L. Pilon, Use of Mie theory to analyze experimental data to identify infrared properties of fused quartz containing bubbles, Applied optics 44 (2005) 7021–7031.
[46] L. A. Dombrovsky, The use of transport approximation and diffusion-based models in radiative transfer calculations, Computational Thermal Sciences: An International Journal 4 (2012) 297–315.
[47] R. Siegel, C. Spuckler, Approximate solution methods for spectral radiative transfer in high refractive index layers, International Journal of Heat and Mass Transfer 37 (1994) 403 – 413.
[48] J. Chaves, Introduction to Nonimaging Optics, 2 ed., CRC Press, 2017.
[49] B. H. Mahan, Microscopic reversibility and detailed balance. an analysis, Journal of Chemical Education 52 (1975) 299.
[50] Z. Łodziana, J. K. Nørskov, P. Stoltze, The stability of the hydroxylated (0001) surface of α-Al2O3, Journal of Chemical Physics 118 (2003) 11179–11188.

Chapitre III

Modélisation des propriétés radiatives de la mousse et du transfert thermique conducto-radiatif

Sommaire

Experimental and numerical characterization of high-temperature heat transfer in a ceramic foam with dual-scale porosity

Z.K. Low[a,b,*], N. Blal[a], D. Baillis[a]

[a] *Univ Lyon, INSA-Lyon, CNRS UMR5259, LaMCoS, F-69621 Villeurbanne, France.*
[b] *Saint-Gobain Research Provence, F-84306 Cavaillon, France.*

Abstract

Numerical predictions of the high-temperature conductive-radiative heat transfer in an alumina foam with dual-scale porosity are compared to experimental data. The influence of the dual-scale porosity, consisting of 100 µm-sized spheroidal cells and a network of µm-sized pores within the foam skeleton, is taken into account through simulations on tomography-reconstructed microstructures. The effective thermal conductivity of the foam (without radiative contributions) is computed using a finite element homogenization technique with the measured thermal conductivity of the foam skeleton as input. The foam effective radiative properties at high temperatures are computed with a Monte Carlo ray-tracing approach, adapted to account for volume and interface scattering within the semi-transparent foam skeleton. Conductive-radiative heat transfer through an equivalent homogeneous slab is then simulated with the control volume method, coupled to the discrete ordinates method for resolution of the radiative transfer equation. The radiative contribution is well-described by the Rosseland radiative conductivity at sufficiently large slab thicknesses. The angular distribution of reflected and refracted radiation at the foam skeleton surface is shown to have a significant effect on radiative transfer at the macro-scale. Numerical results show good agreement with the measured apparent thermal conductivity when perfectly diffuse reflection and refraction at the interface between the foam cells and the foam skeleton are assumed.

Keywords: Foams, Dual-scale porosity, Finite element homogenization, Monte Carlo ray-tracing, Radiative transfer equation (RTE)

1. Introduction

Cellular materials are a source of interest in many heat transfer applications thanks to their attractive thermal and mechanical properties [1–3], with ceramic foams in particular often developed for use at extreme temperatures [4, 5]. Accurate experimental characterization of their high-temperature thermal properties is often challenging due to the significant contribution of radiative transfer [6–9]. While radiative transfer may be modeled via an equivalent thermal conductivity for optically thick semi-transparent materials [10], that is not always the case for foams

*Corresponding author
Email address: zi.low@insa-lyon.fr (Z.K. Low)

Preprint written as part of the doctoral thesis number 2020LYSEI122, INSA Lyon, France

Nomenclature

First-order tensors (vectors) are indicated in **bold face**.

Latin

a	Thermal diffusivity
$\mathcal{B}$	Spectral blackbody radiance
c	Specific heat capacity; Speed of light
d	Distance
f	Volume fraction
g	Asymmetry
h	Thickness; Planck's constant
$\mathcal{I}$	Spectral radiance
k_B	Boltzmann constant
k	Thermal conductivity
ℓ	Free path
L	Length
N	Number
n	Refractive index; Normal direction
p	Parameter
$\mathbb{P}$	Probability
Q	Heat flow
q	Heat flux
$\mathcal{R}$	Reflectivity
s	Distance variable
$\mathcal{T}$	Transmissivity
T	Temperature
t	Time
u	Direction
x	Position

Greek

β	Extinction coefficient, $\kappa + \sigma$
Δ	Difference
ϵ	Residual
ϕ	Scattering phase function
φ	Azimuth angle
κ	Absorption coefficient
$\varkappa$	Absorption index
λ	Wavelength
ρ	Density
σ_{SB}	Stefan-Boltzmann constant
σ	Scattering coefficient
τ	Optical thickness
θ	Polar angle
θ	Relative temperature
Ω	Solid angle
Ω	Domain
ω	Albedo, κ/β

Superscripts and Subscripts

$'$	Modified quantity
0	Reference, *in vacuo*
sca	Absorption
app	Apparent
a	Air; Foam cells
diff	Diffuse
eff	Effective
ext	Extinction
Fr	Fresnel
$\hbar$	Hemispherical
inc	Incident
m	Sintered alumina matrix
p	Porosity within foam skeleton
sca	Scattering
spec	Specular
s	Foam skeleton
tr	Transport approximation

Operators and accents

∇	Del operator
$\cdot$	Dot product
$\langle\bullet\rangle$	Weighted average
$\langle\!\langle\bullet\rangle\!\rangle$	Stochastic mean

Acronyms

CDF	Cumulative distribution function
RDFI	Radiative Distribution Function Identification
RTE	Radiative transfer equation

in which coupled conductive-radiative heat transfer usually takes place, with an extrinsic radiative contribution [11]. Significant effort has therefore gone towards the development of numerical models to predict the contribution of different heat transfer modes in service conditions, with X-ray tomography allowing computations based on real foam morphologies [1, 3, 12].

Foams are traditionally modeled as two-phase media composed of a cell phase and a skeleton phase, both often assumed homogeneous and isotropic [1, 2]. Based on scale separation principles, heat transfer in foams may be considered at two distinct length scales: a micro-scale at which the foam cellular structure is treated explicitly, and a macro-scale at which the foam is treated as a single equivalent homogeneous medium [13]. Conductive heat transfer at the macro-scale is usually represented with an intrinsic effective thermal conductivity, which can be predicted through resolving Fourier's law on tomography-reconstructed foams under appropriate boundary conditions [14]. The contribution of thermal radiation at the macro-scale is usually described using the Radiative Transfer Equation (RTE), which requires knowledge of the foam effective radiative properties. Among the direct and inverse methods available to determine these properties [11, 15], microstructure-based Monte Carlo ray-tracing [16–19] is the most popular technique, as most foams have characteristic heterogeneity sizes greater than the wavelengths of interest (in the μm-range for high temperature radiative heat transfer) allowing the geometrical optics approximation to be made.

In the present work, we perform numerical simulations of the high-temperature conductive-radiative heat transfer of a tomography-reconstructed alumina ceramic foam [4], and compare them to experimental results. A specificity and complexity of the studied foam is the presence of a dual-scale porosity (see Figure 1): apart from the 100 μm-sized spheroidal cells forming the macrocellular network, tortuous μm-sized pores are also present within the foam skeleton. As these pores reduce conductive heat transfer through the foam skeleton, the effective thermal conductivity (without radiative contributions) of the porous foam skeleton is first characterized through laser Flash measurements [20] on porous alumina samples of equivalent microstructure, before being used to estimate the effective thermal conductivity of the foam through a finite element homogenization approach [14]. The influence of the μm-sized pores on radiative heat transfer is more complex to predict, since scattering no longer follows geometrical optics laws in view of the small pore sizes compared to the wavelengths of interest. Past studies represented this type of foam skeleton as a semi-transparent phase with its own set of radiative properties: Zeghondy et al. [21] identified the foam skeleton effective radiative properties from bidirectional reflectance measurements, while Haussener and Randrianalisoa [12] calculated them directly using the independent scattering theory. We recently proposed and validated a new physical-optics-based approach [22, 23] to directly compute the effective volume radiative properties and non-specular surface reflection of the foam skeleton material through tomography-reconstructed microstructures, which accounts for dependent scattering and wave effects. These computed foam skeleton radiative properties are used in the present work within an adapted ray-tracing algorithm [24–26] to simulate the effective radiative properties of the foam. The foam effective thermal conductivity and radiative properties are then applied to simulate the apparent thermal conductivity including radiative contributions. Numerical results are then compared to high-temperature measurements performed with the parallel hot-wire technique [8].

Section 2 describes the experimental methods used to characterize the dual-scale foam porosity,

and to measure the high-temperature thermal conductivity of the foam and foam skeleton. Section 3 describes the numerical method used to compute the effective thermal conductivity and effective radiative properties of the foam, before applying them to the simulation of coupled conductive-radiative heat transfer through a foam slab at high temperatures. Section 4 presents the numerical results and compares them with experimental data before concluding.

1.1. Definitions and mathematical notation

Throughout this work, tensorial notation is used in equations, with scalars written in regular font and first- and second-order tensors ("vectors" and "matrices") written in bold face. To distinguish the different porosity scales, we define the following terminology for use in the rest of this paper:

- At the cellular scale, the foam is assumed to be composed of two homogeneous phases: a skeleton phase (denoted with the subscript *s*), and air-filled cells (denoted with the subscript *a*);
- When the microstructure of the foam skeleton is explicitly considered, it is also assumed to be composed of two homogeneous phases: a sintered polycrystalline alumina matrix (denoted with the subscript *m*), and µm-sized pores (denoted with the subscript *p*).

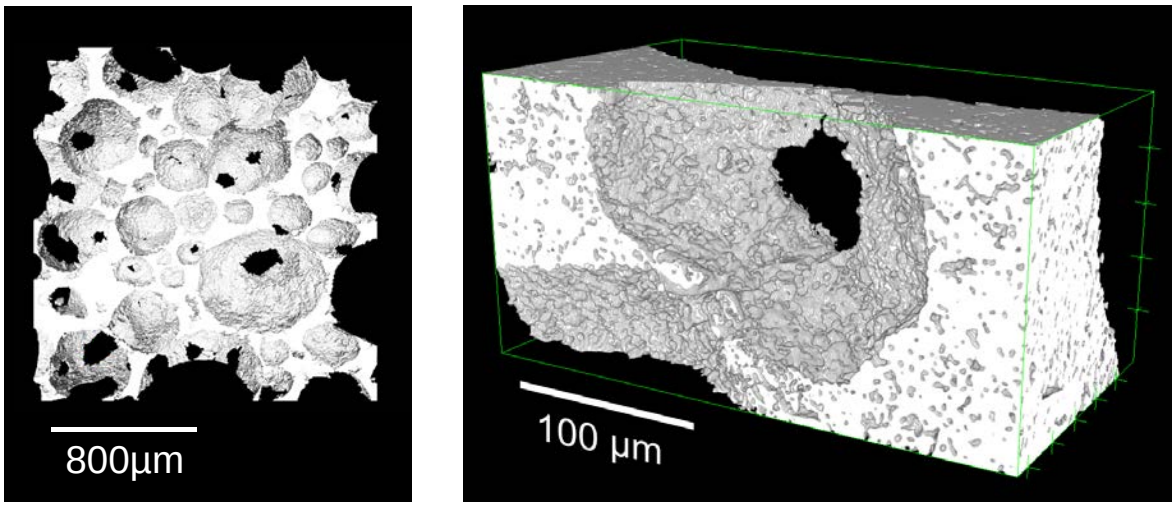

(a) Macrocellular network ($\sim$ 100 µm). (b) Foam skeleton containing µm-sized pores.

Figure 1: Tomographic reconstructions of NorFoam showing the dual-scale porosity.

2. Experimental procedure

2.1. Material and microstructure

The studied material is NorFoam XPure by Saint-Gobain, a high-purity (99% α-alumina by mass) alumina foam for high temperature thermal insulation [4]. Figure 1 shows the 3D microstructure of the foam with its dual-scale porosity.

To characterize the macrocellular porosity, X-ray tomography (GE Phoenix v|tome|x s, MATEIS laboratory, Villeurbanne, France) and image analysis (Fiji [27]) were performed on a foam sample according to the protocol described in our previous study [14]. A 3D reconstruction of the foam spanning a volume of 4.515 mm × 4.515 mm × 4.515 mm with a voxel size of 8.75 µm is obtained; an extract is shown in Figure 1a. An open-cell network comprised of spheroidal cells with a lognormal size distribution [14] is observed, with a macrocellular porosity of $f_a = 0.74 \pm 0.02$ and a median diameter of 590 µm based on pore volume. An extremely low anisotropy in the foam structure is also observed based on the covariance range [28], which only varies slightly between 333 µm to 373 µm along the three principal directions of the cubic tomography-reconstructed foam [14].

We also characterized the porosity within the foam skeleton via scanning electron microscopy (Hitachi TM3030, Saint-Gobain Research Provence, Cavaillon, France) and X-ray tomography (RX Solutions EasyTom Nano, MATEIS laboratory, Villeurbanne, France): a reconstructed foam skeleton segment with a voxel size of 0.3 µm is shown in Figure 1b. A tortuous network of µm-sized pores is observed, with an extremely high local microstructural variability due to the small observation scale. To facilitate experimental characterization of foam skeleton properties, 2 mm thin slabs of porous sintered alumina were fabricated and verified to be of equivalent microstructure to the foam skeleton (see protocols in our previous studies [22, 23]). The nominal porosity of the foam skeleton material is $f_p = 0.22 \pm 0.2$, while the characteristic pore size, estimated from the mean pore chord length [29], was 1.8 ± 0.3 µm.

2.2. Foam skeleton thermal diffusivity and conductivity

The thermal diffusivity α_s of the foam skeleton was measured at Saint-Gobain Research Paris (Aubervilliers, France) using the laser Flash technique [20] (Netzsch LFA 457 MicroFlash apparatus). 10 mm × 10 mm × 2 mm thin slabs of the foam skeleton material were fabricated according to the protocol described in our previous study [23]. After coating the slabs in graphite paint, measurements were performed from room temperature to 800 °C under nitrogen atmosphere . As illustrated in Figure 2a, one face of the slab was heated by a short energy pulse $Q(t)$, while the temperature rise $\theta(t)$ on the opposite face over the next ~ 3 s was measured with an InSb infrared detector. The thermal diffusivity (excluding radiative contributions) was then estimated by minimizing the least-squares error between the measured temperature rise and that predicted by an analytical model [30, 31] that explicitly accounts for radiative transfer. Thickness variations over the considered temperature range, smaller than 0.6% according to Touloukian et al. [32], were neglected in the analytical model.

The thermal conductivity k_s of the foam skeleton was then computed as:

$$k_s = \alpha_s \rho_s c_s \tag{1}$$

where $\rho_s = 3.07\ \mathrm{g{\cdot}cm^{-3}}$ is the density of the foam skeleton material, and c_s is the foam skeleton specific heat capacity, equal to that of alumina given by Touloukian and Buyco [33]:

$$c_s(T) = 1.0446 + 1.742 \times 10^{-4}\, T - \frac{2.796 \times 10^4}{T^2} \tag{2}$$

The variation of k_s with temperature T is plotted in Figure 3, which shows a monotonous

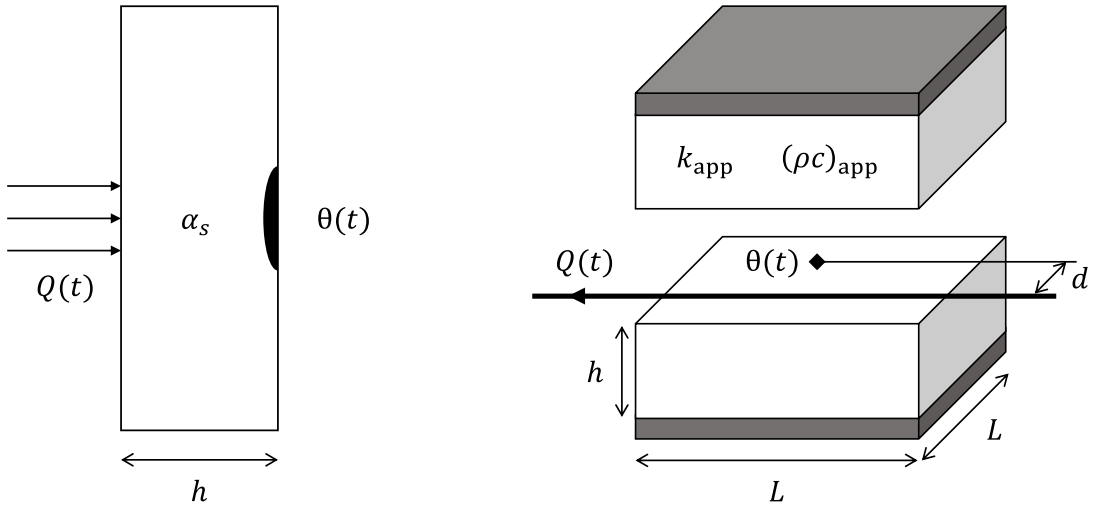

(a) Laser Flash technique [30].

(b) Parallel hot-wire technique [8].

Figure 2: Illustrations of experimental configurations, with samples in white. Key dimensions are indicated: thickness h, length L, distance d. The measured evolution of heat flow $Q(t)$ and temperature rise $\theta(t)$ are used to estimate the thermal diffusivity α_s in (a), and the apparent thermal conductivity k_{app} and volumetric heat capacity $(\rho c)_{\text{app}}$ in (b).

decrease with temperature resulting from the decrease in phonon heat conduction within the polycrystalline alumina matrix at higher temperatures [34] (uncompensated by the increase in thermal conductivity of air [35]). The error bars reflect the experimental uncertainty on k_s, estimated at 7.5%. The relation between the inverse thermal conductivity k_s^{-1} of the foam skeleton and T (in K) is also plotted below, along with its linear fit ($R^2 = 0.999$):

$$k_s^{-1} = p_1 T + p_0 \quad \text{with} \quad \begin{cases} p_1 = (2.13 \pm 0.03) \times 10^{-4}\ \text{m·W}^{-1} \\ p_0 = (-2.8 \pm 2.0) \times 10^{-3}\ \text{m·K·W}^{-1} \end{cases} \tag{3}$$

Equation (3) is consistent with past observations on low-porosity sintered alumina [34], and the value of p_0 lies within the range of $\pm 10^{-3}$ reported by Smith et al. [34] for polycrystalline alumina samples in which grain boundary resistance is negligible. This is expected from the high purity and large grain sizes in the present samples (volume median grain diameter of 2.9 µm before sintering) [36].

Although *ab initio* demonstration of equation (3) was only performed for temperatures below the Debye temperature of alumina of $T \approx 1000$ K [34], we assume in the following sections that it applies to the whole range of temperatures investigated in this study, up to 1300 °C.

2.3. Foam apparent thermal conductivity at high temperatures

The apparent thermal conductivity of NorFoam from 400 °C to 1000 °C was measured at the LEMTA laboratory in Nancy, France using the parallel hot-wire method [8]. The experimental configuration, which involves two identical 300 mm × 300 mm × 30 mm foam samples, is illustrated in Figure 2b and described by Jannot and Degiovanni [8]. An 80/20 Nickel-Chromium resistance heating wire (thick black line) is embedded in a groove cut into the top surface of the bottom

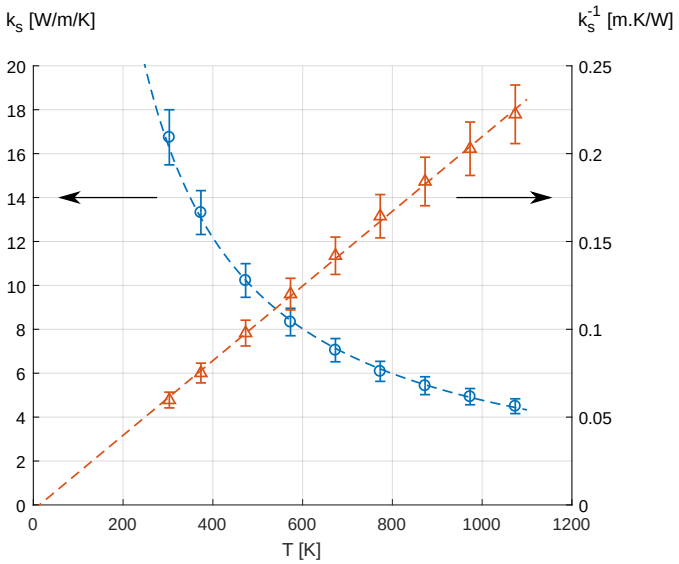

Figure 3: Foam skeleton effective thermal conductivity k_s (without radiative contributions) and its inverse k_s^{-1} as a function of temperature T in K: laser Flash measurements (points) and the correlation proposed by Smith et al. [34] (dashed lines, equation (3)).

sample, while a type K sheath thermocouple is inserted in another groove running parallel to the heating wire at a distance $d = 15$ mm. A second sample is placed on top, and the assembly is clamped between two 10 mm thick stainless steel plates (grey slabs). A heat flow step $Q(t)$ is applied with the heating wire, and the temperature rise $\theta(t)$ at the thermocouple is measured over the next ~ 300 s.

Assuming negligible material orthotropy, the analytical quadrupolar model of Jannot and Degiovanni [8] is then used to estimate the apparent thermal conductivity k_{app} and volumetric heat capacity $(\rho c)_{\text{app}}$ of the foam from the measured temperatures. The model accounts explicitly for several important parameters (radius and thermal capacity of the heating wire, thermal capacity of the thermocouple, heating wire-sample and thermocouple-sample thermal resistances), which prevents errors when estimating the thermal conductivity of low-density insulators [6]. Radiative heat transfer is however not modeled explicitly. The term "apparent" instead of "effective" is therefore used to denote the measured thermal conductivity of the foam, since it includes the contributions of both conductive and radiative heat transfer and is generally speaking an extrinsic quantity. The experimental uncertainty of the present hot-wire method is estimated at 5%.

The measured high-temperature apparent thermal conductivity of the foam is presented in section 4.3, and compared to numerical predictions obtained with a multi-scale approach detailed in the next section.

3. Numerical modeling

Considering the extremely small characteristic heat transfer length scales at the micro-scale (cellular structure with morphological features between 10 µm to 1 mm) compared to the the macro-scale (samples or parts typically of cm sizes), a multi-scale numerical procedure is used to simulate

high-temperature conductive-radiative heat transfer in this work. The proposed approach consists of three components. The first simulates the effective thermal conductivity of the foam without radiative contributions using a finite element homogenization technique (section 3.1). The second simulates the effective radiative properties of the foam via a microstructure-based Monte Carlo ray-tracing algorithm (section 3.2). The third solves for the coupled macro-scale conductive-radiative heat transfer on an equivalent homogeneous slab that possesses the computed effective thermal conductivity and effective radiative properties of the foam (section 3.3).

Note that at the micro-scale, the foam is considered to be composed of two homogeneous and isotropic phases: the foam skeleton denoted with "s" and air-filled cells denoted with "a", with the tomography-reconstructed microstructure shown in Figure 1a.

3.1. Determination of the foam effective thermal conductivity

The following finite element homogenization technique used to predict the effective thermal conductivity tensor $\boldsymbol{k}_{\text{eff}}$ (excluding radiative contributions) has been studied and validated for the case of highly porous tomography-reconstructed foams in our previous study [14]. Given a reference temperature T_0, the 3D steady-state heat equation (4) is resolved on a cubic foam volume denoted as Ω:

$$\forall \mathbf{x} \in \Omega, \quad \boldsymbol{q} = -k\boldsymbol{\nabla}\theta \quad \text{with} \quad \boldsymbol{\nabla} \cdot \boldsymbol{q} = 0 \tag{4}$$

where $\boldsymbol{q}$ is the local heat flux vector, $\theta = T - T_0$ is the local relative temperature, and k is the local scalar thermal conductivity equal to $k_s(T_0)$ (equation (3)) in the foam skeleton and $k_a(T_0)$ (given by Coquard and Baillis [35]) in the air-filled foam cells. We consider small temperature variations across the foam volume, such that k may be assumed temperature-independent. The following conditions are enforced on the boundary $\partial\Omega$ of the cubic foam volume:

$$\forall \mathbf{x} \in \partial\Omega, \qquad \begin{cases} \theta = \boldsymbol{G_0} \cdot \mathbf{x} & \text{if} \quad \mathbf{n} \parallel \boldsymbol{G_0} \\ q_n = 0 & \text{if} \quad \mathbf{n} \perp \boldsymbol{G_0} \end{cases} \tag{5}$$

where $\mathbf{n}$ is the local unit normal vector pointing outwards, $q_n = \boldsymbol{q} \cdot \mathbf{n}$ is the normal heat flux, and $\boldsymbol{G_0}$ is an arbitrary temperature gradient vector oriented along one of the principal directions $\mathbf{e}_1, \mathbf{e}_2, \mathbf{e}_3$ of the cubic volume. The volume-averaged heat flux and temperature gradient vectors are then linked by an apparent thermal conductivity tensor $\boldsymbol{k}_{\text{app}}$:

$$\langle \boldsymbol{q} \rangle = -\boldsymbol{k}_{\text{app}} \cdot \langle \boldsymbol{\nabla}\theta \rangle \tag{6}$$

where $\langle \bullet \rangle = \int_\Omega \bullet \, \mathrm{d}V / V_\Omega$ is the volume averaging operator over the entire cubic foam volume V_Ω. Here the term "apparent" is used to emphasize the dependence of $\boldsymbol{k}_{\text{app}}$ on volume element size and boundary conditions. As equation (6) only provides 3 scalar equations, three orthogonal configurations (i.e., permuting $\boldsymbol{G_0} = G_0\mathbf{e}_j$ for $j \in \{1, 2, 3\}$) have to be resolved to obtain the full $\boldsymbol{k}_{\text{app}}$ tensor containing 9 unknowns.

The classic schema considers either periodic microstructures or microstructures large enough to be considered as representative volume elements, for which $\boldsymbol{k}_{\text{app}}$ is equal to the intrinsic $\boldsymbol{k}_{\text{eff}}$ of the heterogeneous material [37, 38]. As tomography-reconstructed microstructures are generally not representative volume elements in this sense [28], $\boldsymbol{k}_{\text{app}}$ is dependent on V_Ω and may also vary

from one realization of the microstructure to another. In addition, due to the slight anisotropy in the studied foam, $\boldsymbol{k}_{\text{app}}$ may also be anisotropic. In the present work, we assumed an isotropic effective thermal conductivity ($\boldsymbol{k}_{\text{eff}} = k_{\text{eff}}\mathbf{1}_3$, where $\mathbf{1}_N$ is the N-dimensional identity tensor). The scalar k_{eff} is estimated from the different $\boldsymbol{k}_{\text{app}}$ obtained on 8 different tomography-reconstructed foams of $V_\Omega = (1.8\,\text{mm})^3$:

$$k_{\text{eff}} \approx \langle\langle k_{j,N}^{\text{app}} \rangle\rangle \tag{7}$$

where $\langle\langle \bullet \rangle\rangle$ represents the stochastic mean, j represents the 3 principal directions of anisotropy, and N represents the 8 different foam realizations.

Numerical resolution of equations (4), (5), and (6) was performed for reference temperatures T_0 between 25 °C and 1800 °C using the preconditioned Krylov-based iterative finite element solver in Abaqus/Standard 2017 [39] on foam volumes meshed with linear (P1) brick elements (1 element per voxel). The standard variation in $k_{\text{eff}}(T_0)$ estimated from equation (7) lies between 7.6% (at $T_0 = 25$ °C) and 3.5% (at $T_0 = 1800$ °C) of the mean value, mainly due to material anisotropy.

3.2. Determination of the spectral effective radiative properties of the foam

3.2.1. Theory and definitions

The spectral distribution of radiative energy at a given temperature T_0 (in K) is described by Planck's law [40]:

$$\mathcal{B}(T_0, \lambda_0) = \frac{2hc_0^2}{\lambda_0^5\left[\exp\left(\frac{hc_0}{k_B T_0 \lambda_0}\right) - 1\right]} \tag{8}$$

where $\mathcal{B}(\lambda_0, T_0)$ is the spectral blackbody radiance in vacuum (power emanating from an ideal emitter per unit area per unit solid angle per unit vacuum wavelength λ_0), h is the Planck constant, k_B is the Boltzmann constant, and c_0 is the speed of light in vacuum.

In this work, we focus on computing the spectral properties of the foam at three temperatures: 800 °C, 1000 °C, and 1300 °C. For each considered temperature, the wavelength λ_{peak} at which blackbody radiance is maximal, the wavelength range $\Delta\lambda_0$ on which radiative properties are computed and the fraction of blackbody radiative energy represented is summarized in Table 1.

T_0 [°C]	λ_{peak} [µm]	$\Delta\lambda_0$ [µm]	Fraction of radiative energy [%]
800	2.70	[1,7]	83.5
1000	2.28	[1,6]	83.9
1300	1.84	[1,6]	88.8

Table 1: Temperatures T_0, wavelength of peak blackbody radiance λ_{peak}, and wavelength range $\Delta\lambda_0$ on which spectral radiative properties of the foam are computed, with the fraction of radiative energy represented by $\Delta\lambda_0$.

The foam is represented at the macro-scale by a single equivalent homogeneous and isotropic medium, with effective radiative properties determined through simulating the interaction of radiation with the foam microstructure. As the wavelengths of interest are in the µm-range, much smaller than the morphological features of the cellular foam structure (cells and struts well above the 10 µm scale), we apply the geometrical optics approximation and treat radiation propagating in the foam are treated as energy bundles or rays. Ray history effects are assumed negligible due to the

absence of plane-parallel, specular interfaces (unlike in some closed-cell foams [26] or cylindrical fibrous media [41]). The probability distribution of distance ℓ traveled by a ray within the foam before undergoing extinction, henceforth referred to as the free path, can therefore be assumed to follow the Beer-Lambert law:

$$\mathbb{P}(\ell \leq s) = 1 - \exp(-\beta_{\text{eff}} s) = 1 - \exp[-(\kappa_{\text{eff}} + \sigma_{\text{eff}})s] \tag{9}$$

where β_{eff} is the extinction coefficient, equal to the sum of the effective absorption and scattering coefficients (κ_{eff} and σ_{eff} respectively).

The effective scattering albedo ω_{eff} is defined as the ratio of scattering to extinction:

$$\omega_{\text{eff}} = \frac{\sigma_{\text{eff}}}{\beta_{\text{eff}}} = \frac{\sigma_{\text{eff}}}{\kappa_{\text{eff}} + \sigma_{\text{eff}}} \tag{10}$$

The effective scattering phase function ϕ_{eff} describes the angular distribution of scattered radiation:

$$\mathbb{P}(\theta \leq \Theta) = \int_{\theta=0}^{\Theta} \phi_{\text{eff}}(\theta)\, \mathrm{d}\Omega \tag{11}$$

where θ is the angle between the incident and scattered rays, and $\mathrm{d}\Omega = \sin\theta\, \mathrm{d}\theta\, \mathrm{d}\varphi$ is the elementary solid angle. Here ϕ_{eff} is assumed independent of the angle φ (azimuthal symmetry) due to the random microstructure.

By simulating the interaction of a sufficiently large number of rays with the foam microstructure, using random numbers and appropriate probability models to determine the outcome of each interaction, the effective radiative properties β_{eff}, ω_{eff}, and ϕ_{eff} may be determined from the relevant ray statistics. This is the principle of the microstructure-based ray-tracing Monte Carlo algorithm presented in the next section.

3.2.2. Microstructure-based Monte Carlo ray-tracing algorithm

The Monte Carlo ray-tracing algorithm used in the present work improves on several past developments [17, 19, 24–26, 35] to handle the particularities in the studied foam: namely, the fact that the foam skeleton is itself semi-transparent, composed of a weakly absorbing alumina matrix in which a low but significant fraction of µm-sized pores ($f_p = 0.22$) is present. As the pore sizes are close to the wavelengths of interest, wave effects occur when light is reflected off or scattered within the foam skeleton.

Our previous work [22, 23] showed that these wave effects may be taken into account by modeling the foam skeleton as a homogeneous absorbing, emitting, and isotropically scattering phase, with the absorption coefficient κ_s and transport scattering coefficient σ_s computed via a physical optics-based approach (values and uncertainties are given in reference [23]). We also showed that reflection and refraction of light at the interface between the foam skeleton and cells, characterized by the directional-hemispherical reflectivity $\mathcal{R}_{fi}$ and transmissivity $\mathcal{T}_{fi}$, may be

modeled as follows:

$$\mathcal{R}_{fi}(\mathbf{u}) = \underbrace{p_{\text{spec}}\mathcal{R}_{\text{Fr}}(\mathbf{u})}_{\mathcal{R}_{\text{spec}}(\mathbf{u})} + \underbrace{(1-p_{\text{spec}})\left\langle\mathcal{R}_{\text{Fr}}\right\rangle}_{\mathcal{R}_{\text{diff}}} \tag{12a}$$

$$\mathcal{T}_{fi}(\mathbf{u}) = \underbrace{p_{\text{spec}}(1-\mathcal{R}_{\text{Fr}}(\mathbf{u}))}_{\mathcal{T}_{\text{spec}}(\mathbf{u})} + \underbrace{(1-p_{\text{spec}})\left(1-\left\langle\mathcal{R}_{\text{Fr}}\right\rangle\right)}_{\mathcal{T}_{\text{diff}}} \tag{12b}$$

In equation (12), the so-called "specularity parameter" p_{spec} is introduced to describe the non-specular interface reflection and transmission[1]. We consider that a fraction p_{spec} of incident radiation along direction $\mathbf{u}$ undergoes specular reflection and refraction with a reflectivity $\mathcal{R}_{\text{Fr}}$ calculated with Fresnel's equations [42] for a smooth air-alumina interface. The rest is assumed to undergo isotropic diffuse reflection and transmission with a reflectivity $\langle\mathcal{R}_{\text{Fr}}\rangle$ defined as follows [10, 43]:

$$\left\langle\mathcal{R}_{\text{Fr}}\right\rangle \equiv \int_{\mathbf{u}'\cdot\mathbf{n}<0} 2\mathcal{R}_{\text{Fr}}(\mathbf{u}')|\mathbf{u}'\cdot\mathbf{n}|\,\mathrm{d}\Omega' \tag{13}$$

where $\mathbf{n}$ is the local unit normal vector at the interface, oriented such that $\mathbf{u}\cdot\mathbf{n} < 0$. Per our past work [22, 23], we consider that the interface is smooth everywhere save where pores are present, and equate p_{spec} with f_m, the volume fraction of the alumina matrix within the foam skeleton.

For a given wavelength and temperature, the effective radiative properties of them foam may then be computed with the foam skeleton radiative properties (κ_s, σ_s, $\phi_s = (4\pi)^{-1}$, and $p_{\text{spec}} = f_m$), the alumina phase refractive index n_j, and a triangle mesh of the interface between the foam skeleton and cells (generated from a 2.27 mm × 2.27 mm × 2.27 mm tomography-reconstructed foam using iso2mesh [44], see Figure 4) given as input. The Monte Carlo ray-tracing algorithm used to obtain the necessary ray statistics consists of launching a large number of rays ($N_{\text{rays}} \sim 10^5$) from random points within the foam volume (cells or skeleton) in random directions, and tracking each of them until their first extinction (absorbing or scattering) event.

The rays interact with the foam microstructure independently of one another following the algorithm described below:

- Rays may be cast in the cell phase or the skeleton phase, with probabilities equal to their respective volume fractions f_a and $f_s = 1 - f_a$ [24, 26, 45].
- Pseudo-periodic boundary conditions are applied to the RVE: rays leaving one face of the RVE are recast in the same direction from a randomly chosen point on the opposite face in the same phase, and treated as a continuation of the initial ray [46]. Therefore, every ray necessarily undergoes extinction ($N_{\text{rays}} = N_{\text{ext}}$), sometimes after traveling the span of multiple foam volumes.
- The initial location of each ray is chosen as if it were the location of the ray following a previous extinction event [19], determined as follows:

[1] Note that the present definition of p_{spec} is adapted for the case of semi-transparent foam skeletons, and thus differs from the parameter of the same name introduced by Loretz et al. [25] for opaque foam skeletons.

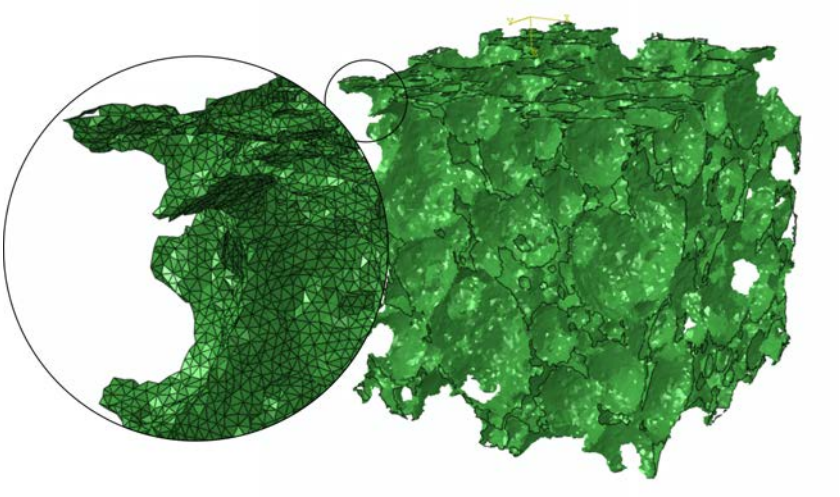

Figure 4: Triangle mesh of the interface between the foam skeleton and cells within a 2.27 mm × 2.27 mm × 2.27 mm foam volume, containing 169015 elements.

  - Each ray cast in the transparent air phase necessarily undergoes extinction by scattering at the first interface it encounters (with the probability of being reflected or refracted determined from equations (12)). Rays cast in the air phase are therefore always launched from random points on the interface, as they follow either cell-cell reflection or skeleton-cell refraction events.
  - Each ray cast in the solid phase may either undergo interface scattering or volume extinction. This is resolved by choosing the closest of two possible extinction points: a volume extinction point randomly generated based on the skeleton extinction coefficient $\beta_s = \kappa_s + \sigma_s$ and the Beer-Lambert law (equation (9)), and an interface extinction point at the first interface it would encounter if no volume extinction occurs [24].
    * If the volume extinction point is chosen, the ray undergoes volume absorption or isotropic scattering, with the probability of being scattered equal to the skeleton albedo $\omega_s = \kappa_s/\beta_s$. The next ray cast in the solid phase is then launched from a random point within the skeleton volume.
    * If the interface extinction point is chosen, the ray undergoes interface reflection or refraction according to equations (12). The next ray cast in the air phase is therefore always launched from a random point on the interface.

- The initial direction of each ray at its source point is chosen randomly assuming isotropic angular distribution [35].

For each ray, the free path ℓ, the type of extinction event (scattering or absorption), and—if the ray is scattered—the scattering angle θ between the initial and scattered directions are recorded. While the effective scattering phase function ϕ_{eff} is directly obtained from equation (11), the effective extinction coefficient β_{eff} and albedo ω_{eff} may be obtained through one of two ways:

1. The Radiative Distribution Function Identification (RDFI) method proposed by Tancrez and Taine [17] seeks β_{eff} and then ω_{eff} that minimize the residuals in equations (14a) and (14b) respectively, defined according to the Beer-Lambert law (equation (9)):

$$\epsilon_{\text{ext}}(\beta) = \sqrt{\sum_i \left[1 - \exp(-\beta s_i) - \mathbb{P}\left(\ell \leq s_i\right)\right]^2} \tag{14a}$$

$$\epsilon_{\text{abs}}(\omega) = \sqrt{\sum_i \left[(1-\omega)\left(1 - \exp(-\beta_{\text{eff}} s_i)\right) - \mathbb{P}\left((\ell \leq s_i) \cap (\ell \in \{\ell_{\text{abs}}\})\right)\right]^2} \tag{14b}$$

$\{\ell_{\text{abs}}\}$ denotes the set of all the absorbed rays, and (s_i) are discretized distances covering the useful range on which RDFI is performed, which Tancrez and Taine [17] chose to correspond to optical thicknesses between 0 and 3, i.e., $\mathbb{P}(\ell \leq s_i) \leq 1 - \exp(-3) \approx 95\%$.

2. Building on the work of [16], Randrianalisoa and Baillis [19] proposed a direct calculation of β_{eff} and ω_{eff} from the stochastic mean free path $\langle\langle \ell \rangle\rangle$ and the fraction of scattered rays:

$$\beta_{\text{eff}} = \langle\langle \ell \rangle\rangle^{-1} \tag{15a}$$

$$\omega_{\text{eff}} = \frac{N_{\text{sca}}}{N_{\text{ext}}} = \frac{N_{\text{sca}}}{N_{\text{rays}}} \tag{15b}$$

It can be noted that definitions (14) and (15) are rigorously identical when radiative propagation in the heterogeneous medium verifies the Beer-Lambert law [40, 46], which is often used to describe the radiative behavior of real porous microstructures. The Beer-Lambert law has been shown to be a good approximation for many isotropic random foams [1, 24, 26]. Deviations have been observed in rare cases, for example in materials with high anisotropy [45]. We propose here to study the applicability of the Beer-Lambert law and to compare the two definitions ((14) and (15)) of the extinction coefficient β_{eff} and albedo ω_{eff}. Figure 5 shows an example of the extinction CDF obtained through ray-tracing on the studied foam, compared to the Beer-Lambert law (9) expressed in terms of β_{eff} obtained via RDFI (14a) and the inverse mean free path (15a). We see that the simulated extinction behavior in the present foam is fairly well approximated by the Beer-Lambert law. For the considered temperatures and wavelengths, the maximal difference observed between definitions (14) and (15) was only 7.4% for β_{eff} and 2.0% for ω_{eff}. We thus conclude that the choice between these two definitions has little influence on the computed effective radiative properties of the present foam. In the next section (3.3), the effective radiative properties obtained via RDFI are applied to the simulation of macro-scale conductive-radiative heat transfer.

3.3. Simulation of coupled conductive-radiative heat transfer through a foam slab

Following typical steady-state thermal conductivity measurement and simulation configurations [35, 48], we consider a plane-parallel foam slab with a small thickness h relative to its lateral dimensions, held at a reference temperature T_0 with a small temperature gradient in the thickness direction by maintaining the two faces at constant uniform temperatures with a difference of ΔT between one another.

By modeling the foam as an equivalent homogeneous and isotropic semi-infinite slab with 1D

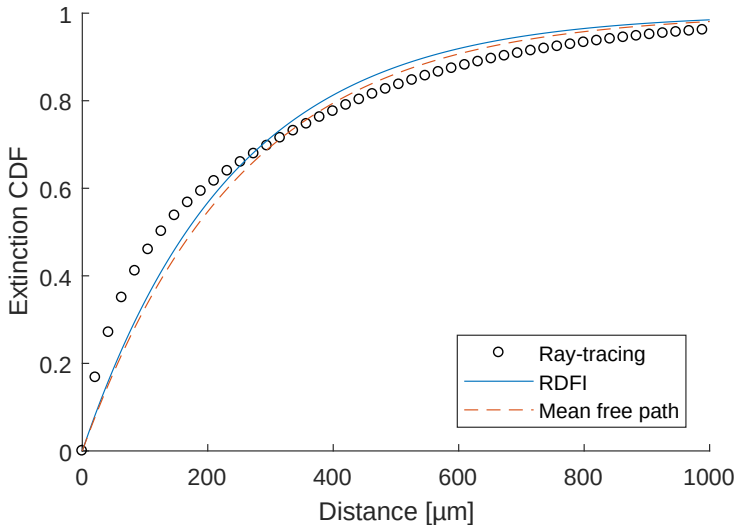

Figure 5: Extinction CDF $\mathbb{P}(\ell \leq s)$ as a function of distance s: comparison of ray-tracing result for $T = 1000\,°C$ and $\lambda_0 = 6\,\mu m$ (○) to the Beer-Lambert distributions with extinction coefficients β_{eff} obtained via Radiative Distribution Function Identification (RDFI [47], lines) and from the inverse mean free path [19] (dashes).

heat transfer along the thickness direction $\mathbf{e}_x$, and neglecting the contribution of convection in the pores (a common and valid assumption in foams with sub-mm cells [11]), the macro-scale heat flux $\boldsymbol{q}$ and its divergence are written as follows:

$$\boldsymbol{q} = (q_{cond} + q_{rad})\mathbf{e}_x \tag{16a}$$

$$\boldsymbol{\nabla} \cdot \boldsymbol{q} = \frac{\partial q_{cond}}{\partial x} + \frac{\partial q_{rad}}{\partial x} = 0 \tag{16b}$$

Equation (16b) is the macro-scale heat equation describing the energy balance on an elementary volume of the slab far from the boundaries, under steady-state conditions, with no heat sources.

The macro-scale 1D conductive heat flux q_{cond} may be expressed in terms of the isotropic effective thermal conductivity k_{eff} computed in section 3.1, which is assumed constant across the slab due to the small temperature gradient. This gives the following:

$$q_{cond} = -k_{eff}(T_0)\frac{\partial T}{\partial x} \tag{17a}$$

$$\frac{\partial q_{cond}}{\partial x} = -k_{eff}(T_0)\frac{\partial^2 T}{\partial x^2} - \frac{\partial k_{eff}}{\partial x}\frac{\partial T}{\partial x} \approx -k_{eff}(T_0)\frac{\partial^2 T}{\partial x^2} \tag{17b}$$

On the other hand, the macro-scale radiative heat flux q_{rad} and its divergence within the slab is expressed in terms of the homogenized spectral radiance $\mathcal{I}$, defined as the radiative flux per unit

solid angle per unit vacuum wavelength λ_0:

$$q_{\text{rad}} = \int_0^\infty \int_{4\pi} \mathcal{I}(x, \mathbf{u}, \lambda_0)\mathbf{u} \cdot \mathbf{e}_x \, \mathrm{d}\Omega \, \mathrm{d}\lambda_0 \tag{18a}$$

$$\frac{\partial q_{\text{rad}}}{\partial x} = \int_0^\infty \int_{4\pi} \frac{\partial \mathcal{I}(x, \mathbf{u}, \lambda_0)}{\partial x}\mathbf{u} \cdot \mathbf{e}_x \, \mathrm{d}\Omega \, \mathrm{d}\lambda_0 \tag{18b}$$

where $\mathbf{u}$ is the unit direction vector associated with the elementary solid angle $\mathrm{d}\Omega$, and 4π is the solid angle of a sphere which represents the entire angular space. To account for the conservation of étendue in a multiphase material [49], we consider the basic radiance $\mathcal{I}^*$ defined as follows:

$$\mathcal{I}^*(x, \mathbf{u}, \lambda_0) = \frac{\mathcal{I}(x, \mathbf{u}, \lambda_0)}{n_{\text{eff}}^2(\lambda_0)} \tag{19}$$

As $n = 1$ giving $\mathcal{I}^* = \mathcal{I}$ in vacuum, $\mathcal{I}^*$ in a refractive medium may be understood as the equivalent radiance in vacuum. The effective refractive index n_{eff} is obtained via the volume-averaging definition [18, 45]:

$$\begin{aligned} n_{\text{eff}}^2 &= f_a n_a^2 + f_s n_s^2 \\ &= f_a n_a^2 + f_s \left(f_p n_p^2 + f_m n_m^2\right) \end{aligned} \tag{20}$$

Recall that the subscripts a and s denote the foam cells and foam skeleton respectively ($f_a + f_s = 1$), with the skeleton phase composed of a sintered alumina matrix containing µm-sized pores, denoted respectively with m and p ($f_m + f_p = 1$). As the pores in the present material are filled with air, $n_a = n_p = 1$.

Given the effective radiative properties (extinction coefficient β_{eff}, albedo ω_{eff}, and scattering phase function ϕ_{eff}) for the reference temperature T_0 and a wavelength λ_0 within the range of interest, the spectral basic radiance field is calculated through the radiative transfer equation (RTE):

$$\frac{\partial \mathcal{I}^*(x, \mathbf{u})}{\partial x}\mathbf{u} \cdot \mathbf{e}_x = -\beta_{\text{eff}}\mathcal{I}^*(x, \mathbf{u}) + (1 - \omega_{\text{eff}})\beta_{\text{eff}}\mathcal{B}(T(x)) + \omega_{\text{eff}}\beta_{\text{eff}} \int_{4\pi} \mathcal{I}^*(x, \mathbf{u}')\phi_{\text{eff}}(\theta') \, \mathrm{d}\Omega' \tag{21}$$

where $\mathcal{B}$ is the blackbody radiance in vacuum given by Planck's law (equation (8)), and θ' is the angle between directions $\mathbf{u}$ and $\mathbf{u}'$ (the latter being associated with the elementary solid angle $\mathrm{d}\Omega'$).

Assuming black isothermal walls at the two faces with a temperature difference of $\Delta T = 10\,^\circ\text{C}$, the following thermal and radiative boundary conditions are enforced:

$$T(x = 0) = T_0 - \frac{\Delta T}{2} \tag{22a}$$

$$\mathcal{I}^*(x = 0, \mathbf{u} \cdot \mathbf{e}_x > 0) = \mathcal{B}(T(x = 0)) \tag{22b}$$

$$T(x = h) = T_0 + \frac{\Delta T}{2} \tag{22c}$$

$$\mathcal{I}^*(x = h, \mathbf{u} \cdot \mathbf{e}_x < 0) = \mathcal{B}(T(x = h)) \tag{22d}$$

We resolved the heat equation (16b) with the control volume method and RTE (21) with the discrete ordinates method in a coupled manner, following the iterative numerical scheme of Coquard and Baillis [35]. The slab was meshed with a 30-element 1D Chebyshev grid, which gives finer spatial discretization near the boundaries. The angular space was discretized with 181 directions covering $\theta = 0°$ to $\theta = 180°$ at 1° intervals, θ being the angle between $\mathbf{u}$ and $\mathbf{e}_x$. For the spectral discretization, we considered 30 equal-energy wavelength bands that together represent 99.9% of the total blackbody radiative energy at T_0. Since the wavelength range considered is greater than the interval $\Delta\lambda_0$ on which effective radiative properties were computed explicity (see Table 1), we attributed blackbody-radiance-weighted-averages to the wavelengths outside of $\Delta\lambda_0$:

$$X(T_0, \lambda_0 \notin \Delta\lambda_0) = \frac{\displaystyle\int_{\Delta\lambda_0} X(T_0, \lambda_0)\mathcal{B}(T_0, \lambda_0)\,\mathrm{d}\lambda_0}{\displaystyle\int_{\Delta\lambda_0} \mathcal{B}(T_0, \lambda_0)\,\mathrm{d}\lambda_0} \tag{23}$$

where X denotes an arbitrary effective radiative property.

Three reference temperatures T_0 are investigated: 800 °C, 1000 °C and 1300 °C. For each temperature, we simulated slabs of thicknesses h between 5 mm and 50 mm. The apparent thermal conductivity k_{1D} under steady-state 1D heat flow is computed for each case:

$$\boldsymbol{q} = -k_{1D}\boldsymbol{\nabla}T \approx -k_{1D}\frac{\Delta T}{h}\mathbf{e}_x \quad \Longleftrightarrow \quad k_{1D} = \left|(q_{cond} + q_{rad})\frac{h}{\Delta T}\right| \tag{24}$$

3.3.1. Diffusion and transport approximation: the Rosseland radiative conductivity

In an optically thick region of the foam far from the boundaries, the conductive and radiative heat transfer modes may be decoupled through the introduction of a radiative conductivity k_{rad} (called the diffusion approximation [10]):

$$\boldsymbol{q} = -(k_{eff} + k_{rad})\boldsymbol{\nabla}T \tag{25}$$

For a given temperature T (in K), the Rosseland radiative conductivity gives k_{rad} as a function of the effective radiative properties only:

$$k_{rad} = \frac{4\pi}{3}\int_0^\infty \frac{n_{eff}^2}{\beta_{tr}}\frac{\partial\mathcal{B}}{\partial T}\,\mathrm{d}\lambda_0 = \frac{16}{3}\left\langle\frac{n_{eff}^2}{\beta_{tr}}\right\rangle\sigma_{SB}T^3 \tag{26}$$

where σ_{SB} is the Stefan-Boltzmann constant, and β_{tr} is the transport extinction coefficient:

$$\beta_{tr} = \kappa_{eff} + \sigma_{eff}(1 - g_{sca}) = \beta_{eff}(1 - \omega_{eff}g_{sca}) \tag{27}$$

The asymmetry parameter g_{sca}, calculated from the scattering phase function, gives $g_{sca} = -1$ for perfect backward scattering, $g_{sca} = 0$ for isotropic scattering, and $g_{sca} = +1$ for perfect forward scattering:

$$g_{sca} = \int_{4\pi}\phi_{eff}(\theta)\cos\theta\,\mathrm{d}\Omega \tag{28}$$

The definition of β_{tr} relies on the transport approximation, which considers that in an anisotropically scattering medium, light "forgets" its initial direction after several consecutive scattering events. A medium with scattering coefficient σ_{eff} and phase function ϕ_{eff} is then modeled as an isotropically scattering medium with scattering coefficient $\sigma_{\text{eff}}(1 - g_{\text{sca}})$.

As good results have been reported using the diffusion and transport approximations in optically thick media with high scattering compared to absorption [10], the Rosseland radiative conductivity k_{rad} will be compared in section 4.2 to the radiative contribution evaluated through full numerical modeling.

4. Results and discussion

4.1. Effective radiative properties of the foam: influence of the specularity parameter

The Monte Carlo ray-tracing approach in section 3.2 computes the effective radiative properties of the foam from the tomography-reconstructed foam microstructure and the foam skeleton radiative properties (obtained through a physical-optics-based approach in our previous work [22]). Due to the high microstructural variability within the foam skeleton, significant uncertainties were present in the foam skeleton radiative properties provided as input, notably the scattering coefficient σ_s and the interface directional-hemispherical reflectivity $\mathcal{R}_h$ (along with the specular and diffuse components) [22, 23].

In our previous work [22, 23] and also in section 3.2.2, we assumed that the interface is smooth everywhere save where pores are present; as such, p_{spec} (which represents the fraction of rays undergoing specular reflection at the interface) was set to $p_{\text{spec}} = f_m = 0.78$ for the considered foam skeleton material. However, as this parameter should be very sensitive to the actual surface roughness of the foam skeleton within the foam, we also considered the extreme values of $p_{\text{spec}} = 0$ (perfectly diffuse interface scattering) and $p_{\text{spec}} = 1$ (perfectly specular interface scattering). The resulting foam extinction coefficient β_{eff}, albedo ω_{eff}, and scattering asymmetry g_{sca} at $T_0 = 1000\,°\text{C}$ are shown in Figure 6.

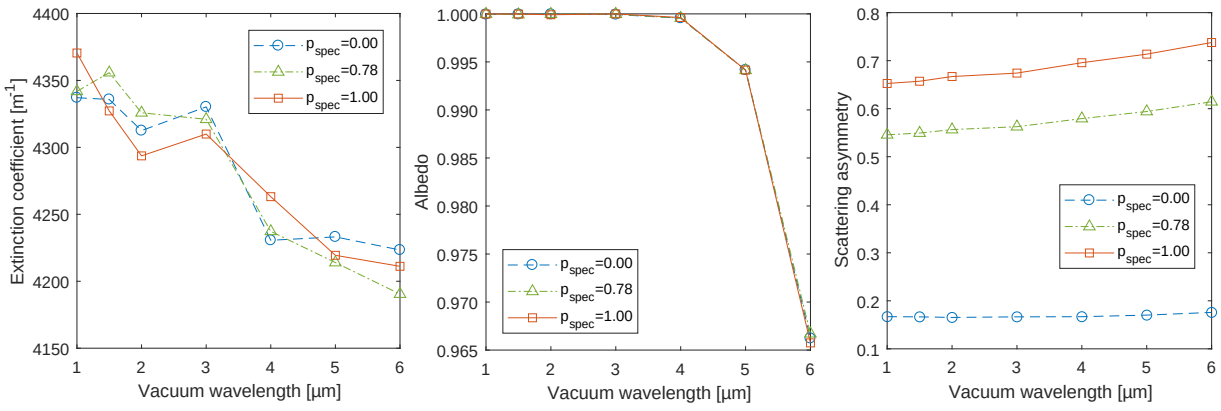

Figure 6: Effective radiative properties at $T_0 = 1000\,°\text{C}$ for different specularity parameter values: $p_{\text{spec}} = 0$ (○), $p_{\text{spec}} = 0.78$ (△, nominal value), $p_{\text{spec}} = 1$ (□).

We first note that p_{spec} has a low influence on β_{eff} and ω_{eff}, since these two properties mainly depend on the destinies of rays launched in the foam cell phase, which depend in turn on the macro-

cellular morphology of the foam (independent of p_{spec}) and $\mathcal{R}_{fi}$ (weakly dependent on p_{spec}). On the other hand, the effective scattering phase function ϕ_{eff} and the resulting asymmetry parameter g_{sca} are highly dependent on p_{spec}: the higher the fraction of specularly reflected radiation ($p_{\text{spec}} \to 1$), the sharper the forward scattering peak ($g_{\text{sca}} \to 1$). This is because according to Fresnel's equations for specular reflection off weakly absorbing dielectric surfaces, rays with large incidence angles θ_{inc} are more likely to be reflected [42], leading to smaller scattering angles $\theta = \pi - 2\theta_{\text{inc}}$, i.e., stronger forward scattering. This has been observed for example by Zeghondy et al. [24], who assumed $p_{\text{spec}} = 1$ in their work on mullite foams.

As we see over the next sections, the influence of p_{spec} on ϕ_{eff} and g_{sca} has strong repercussions on radiative heat transfer at the macro-scale.

4.2. Applicability of the Rosseland radiative conductivity

We next study the applicability of the Rosseland radiative conductivity introduced in section 4.2. In Figure 7a, the difference between the radiative contribution computed through numerical simulation ($k_{1D} - k_{\text{eff}}$) and the Rosseland radiative conductivity (k_{rad}) is plotted for the investigated slab thicknesses h. Different values of the specularity parameter p_{spec} are considered. We observe that the radiative contribution computed numerically increases monotonously with slab thickness h, converging to an asymptote lying only within a few percentage points of the Rosseland radiative conductivity.

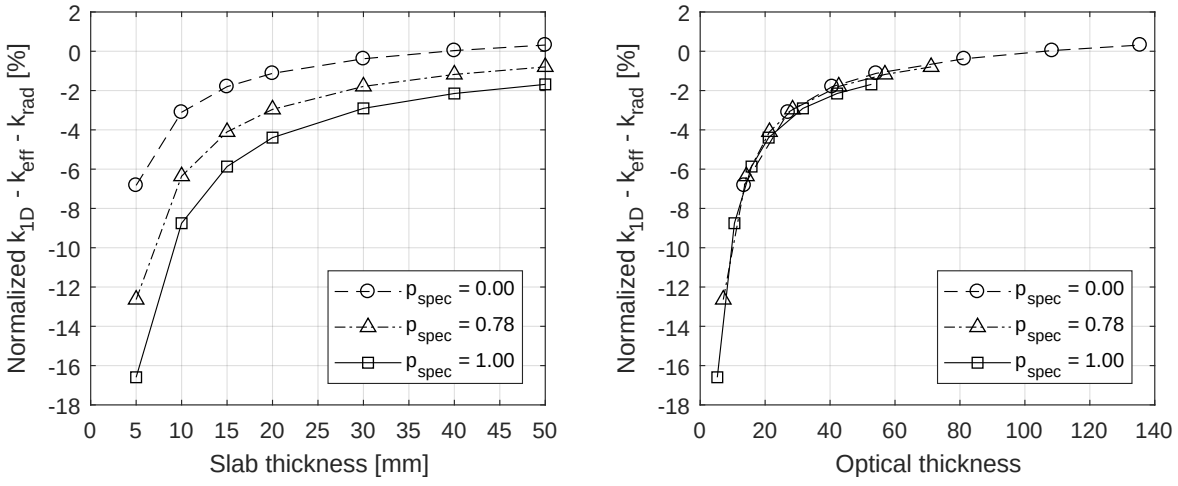

(a) As a function of physical thickness h.

(b) As a function of optical thickness τ.

Figure 7: Radiative contribution to heat transfer at $T_0 = 1000\,°\text{C}$: difference between simulation results ($k_{1D} - k_{\text{eff}}$) and the Rosseland radiative conductivity (k_{rad}) normalized with respect to k_{rad}, for specularity parameters $p_{\text{spec}} = 0$ (○), $p_{\text{spec}} = 0.78$ (△), and $p_{\text{spec}} = 1$ (□).

It is interesting here to consider the dimensionless optical thickness τ:

$$\tau = h \left\langle \frac{n_{\text{eff}}^2}{\beta_{tr}} \right\rangle^{-1} \tag{29}$$

where $\left\langle n_{\text{eff}}^2/\beta_{tr}\right\rangle^{-1}$ is the average transport extinction coefficient defined in equation (26), given for $T_0 = 1000\,°\text{C}$ as:

$$T_0 = 1000\,°\text{C}: \quad \left\langle \frac{n_{\text{eff}}^2}{\beta_{tr}} \right\rangle^{-1} = \begin{cases} 2719\,\text{m}^{-1} & \text{for} \quad p_{\text{spec}} = 0 \\ 1434\,\text{m}^{-1} & \text{for} \quad p_{\text{spec}} = 0.78 \\ 1066\,\text{m}^{-1} & \text{for} \quad p_{\text{spec}} = 1 \end{cases} \tag{30}$$

In Figure 7b, we observe differences of less than 3% between numerical results and the Rosseland radiative conductivity for $\tau > 30$, which corresponds to slab thicknesses between 10 mm and 30 mm depending on p_{spec}. This shows that for small temperature gradients over cm-range thicknesses, the radiative contribution to heat transfer can indeed be modeled with the Rosseland radiative conductivity, i.e., it can be considered an intrinsic property that depends only on the effective radiative properties.

4.3. Experimental validation of simulated high-temperature thermal conductivity

Last but not least, in Figure 8, we compare the numerically calculated high-temperature thermal conductivity to the foam apparent thermal conductivity measured using the parallel hot-wire technique (section 2.3).

Two numerically simulated curves are compared to the experimental results (◇). The first shows the foam effective thermal conductivity k_{eff} without radiative contributions (○) calculated in section 3.1 for the whole range of temperatures of interest. A monotonous decrease with temperature is observed, which follows the trend measured on the foam skeleton samples (see Figure 3). The error bars reflect both the uncertainties in the measured foam skeleton thermal conductivity, as well as the microstructural variability and slight anisotropy of the foam cellular structure. Good agreement is found with the measured apparent thermal conductivity at 400 °C and 600 °C, where radiative heat transfer is indeed negligible. This validates the finite element homogenization technique [14] used to predict k_{eff}.

The second curve is the sum of k_{eff} and the Rosseland radiative conductivity k_{rad} (△), and represents the thermal conductivity including conductive and radiative contributions of an optically thick region of the foam. The points represent the values of $k_{\text{eff}} + k_{\text{rad}}$ at the nominal specularity parameter $p_{\text{spec}} = 0.78$, with the error bars representing the uncertainty in the radiative properties of the foam skeleton due to microstructural variability [22] in addition to the uncertainty in k_{eff}. We see that this is dwarfed by the uncertainty arising from the choice of p_{spec}, represented by the large error band. The experimental results at 800 °C and 1000 °C lie below the nominal $k_{\text{eff}} + k_{\text{rad}}$ curve, which can be explained by:

- The diffusion approximation made in the hot wire measurements that may not necessarily be verified due to an optically thin distance between the hot wire and the thermocouple;
- Potential uncertainties on k_s and thus on the computed k_{eff} from extrapolating equation (3) to temperatures beyond 800 °C;
- A rougher foam skeleton surface than assumed, which would decrease p_{spec} from its nominal value of 0.78. Indeed, a good agreement between experimental results and numerical

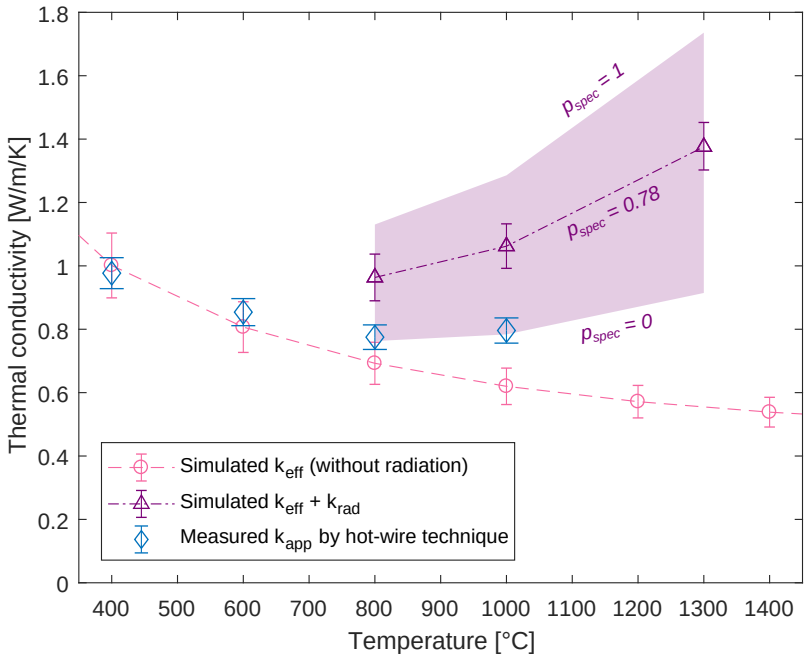

Figure 8: High-temperature thermal conductivity of the studied foam: simulated effective thermal conductivity k_{eff} (○, conductive heat transfer only), sum of k_{eff} with the Rosseland radiative conductivity k_{rad} (△), and measured apparent thermal conductivity k_{app} via the parallel hot-wire technique (◇, includes radiative contributions). Numerical results are calculated for discrete temperature points joined by straight dashed line segments. The error band about the $k_{\text{eff}} + k_{\text{rad}}$ curve represents the uncertainty arising from the choice of specularity parameter p_{spec}.

predictions can be obtained by assuming perfectly diffuse reflection and refraction at the foam skeleton surface ($p_{\text{spec}} = 0$).

This results confirms the predictive capability of the present model, and highlights the importance of precise characterization of the surface roughness and its influence on the angular distribution of reflected and transmitted rays.

5. Conclusion

In this work, we compared the measured apparent thermal conductivity of an alumina foam up to 1000 °C with numerical predictions based on tomography-reconstructed foam microstructures. The numerical model uses a multi-scale approach accounting for the influence of µm-sized pores within the semi-transparent foam skeleton, which notably leads to non-specular reflection and refraction at the foam skeleton surface. We found that the Rosseland radiative conductivity can be used to model radiative heat transfer for optical thicknesses above 40, which correspond to dimensions of foam parts in the cm range. Good agreement between numerical and experimental results are achieved when perfectly diffuse interface reflection and refraction are assumed.

Our results confirm the ability of the proposed model to provide accurate microstructure-based predictions of high-temperature conductive-radiative heat transfer. An interesting possibility for

future work would be to apply this model to parametric studies on virtual microstructures with prescribed dual-scale porosity, which would provide valuable understanding of microstructure-property relations for the design of high-performance materials.

6. Acknowledgments

This research was supported by Saint-Gobain Research (SGR) Provence and the French National Association for Research and Technology (ANRT) through the CIFRE grant number 2017/ 0775. The authors would like to express their gratitude to L. San Miguel and L. Pierrot (SGR Provence) for discussions that greatly improved the research; to J. Meulemans (SGR Paris) for laser Flash measurements and valuable insights, to Y. Millot (SGR Provence) for sample preparation; to Y. Jannot and V. Schick (LEMTA) for hot-wire measurements and helpful discussions, to J. Adrien (MATEIS) and N. Naouar (LaMCoS) for assistance with X-ray tomography; and last but not least, to R. Coquard (EC2 Modélisation) and S. Cunsolo (ex-LaMCoS) for enriching discussions on radiative transfer modeling.

References

[1] J. Petrasch, P. Wyss, A. Steinfeld, Tomography-based monte carlo determination of radiative properties of reticulate porous ceramics, Journal of Quantitative Spectroscopy and Radiative Transfer 105 (2007) 180 – 197.

[2] D. Baillis, R. Coquard, J. Randrianalisoa, L. A. Dombrovsky, R. Viskanta, Thermal Radiation Properties of Highly Porous Cellular Foams, Special Topics & Reviews in Porous Media - An International Journal 4 (2013) 111–136.

[3] S. Ackermann, M. Takacs, J. Scheffe, A. Steinfeld, Reticulated porous ceria undergoing thermochemical reduction with high-flux irradiation, International Journal of Heat and Mass Transfer 107 (2017) 439–449.

[4] M. Schumann, L. San Miguel, Fiber-Free Ceramic Insulation Foam for Highest Temperatures – a New Generation of HSE-friendly Refractory Products with Multiple Application Possibilities, refractories WORLDFORUM 9 (2017) 50–58.

[5] J. Mora-Monteros, C. Suter, S. Haussener, Effective conductivity of porous ceramics in a radiative environment, Ceramics International 46 (2020) 2805–2815.

[6] R. Coquard, D. Baillis, D. Quenard, Experimental and theoretical study of the hot-wire method applied to low-density thermal insulators, International Journal of Heat and Mass Transfer 49 (2006) 4511–4524.

[7] B. Hay, J. Hameury, N. Fleurence, P. Lacipiere, M. Grelard, V. Scoarnec, G. Davee, New facilities for the measurements of high-temperature thermophysical properties at LNE, International Journal of Thermophysics 35 (2014) 1712–1724.

[8] Y. Jannot, A. Degiovanni, An improved model for the parallel hot wire: Application to thermal conductivity measurement of low density insulating materials at high temperature, International Journal of Thermal Sciences 142 (2019) 379–391.

[9] Y. Jannot, A. Degiovanni, V. Schick, J. Meulemans, Thermal diffusivity measurement of insulating materials at high temperature with a four-layer (4L) method, International Journal of Thermal Sciences 150 (2020) 106230.

[10] L. A. Dombrovsky, The use of transport approximation and diffusion-based models in radiative transfer calculations, Computational Thermal Sciences: An International Journal 4 (2012) 297–315.

[11] J. Randrianalisoa, D. Baillis, Thermal conductive and radiative properties of solid foams: Traditional and recent advanced modelling approaches, Comptes Rendus Physique 15 (2014) 683–695.

[12] S. Haussener, J. Randrianalisoa, Radiative characterization of ceramic foams with microporosity, Journal of Physics: Conference Series 676 (2016) 012010.

[13] J. Petrasch, S. Haussener, W. Lipiński, Discrete vs. continuum-scale simulation of radiative transfer in semitransparent two-phase media, Journal of Quantitative Spectroscopy and Radiative Transfer 112 (2011) 1450–1459.

[14] Z. Low, N. Blal, N. Naouar, D. Baillis, Influence of boundary conditions on computation of the effective thermal conductivity of foams, International Journal of Heat and Mass Transfer 155 (2020) 119781.
[15] D. Baillis, J.-F. Sacadura, Thermal radiation properties of dispersed media: theoretical prediction and experimental characterization, Journal of Quantitative Spectroscopy and Radiative Transfer 67 (2000) 327 – 363.
[16] R. Coquard, D. Baillis, Radiative characteristics of opaque spherical particles beds: A new method of prediction, Journal of Thermophysics and Heat Transfer 18 (2004) 178–186.
[17] M. Tancrez, J. Taine, Direct identification of absorption and scattering coefficients and phase function of a porous medium by a Monte Carlo technique, International Journal of Heat and Mass Transfer 47 (2004) 373–383.
[18] W. Lipiński, J. Petrasch, S. Haussener, Application of the spatial averaging theorem to radiative heat transfer in two-phase media, Journal of Quantitative Spectroscopy and Radiative Transfer 111 (2010) 253–258.
[19] J. Randrianalisoa, D. Baillis, Radiative properties of densely packed spheres in semitransparent media: A new geometric optics approach, Journal of Quantitative Spectroscopy and Radiative Transfer 111 (2010) 1372 – 1388.
[20] W. J. Parker, R. J. Jenkins, C. P. Butler, G. L. Abbott, Flash method of determining thermal diffusivity, heat capacity, and thermal conductivity, Journal of Applied Physics 32 (1961) 1679–1684.
[21] B. Zeghondy, E. Iacona, J. Taine, Experimental and RDFI calculated radiative properties of a mullite foam, International Journal of Heat and Mass Transfer 49 (2006) 3702–3707.
[22] Z. Low, D. Baillis, 1– a physical optics approach to predict the radiative properties of semi-transparent porous ceramics, 2020. In preparation.
[23] Z. Low, A. Novikov, D. De Sousa Meneses, D. Baillis, 2– radiative behavior of porous alumina up to high temperatures: experiments and physical optics-based modeling, 2020. In preparation.
[24] B. Zeghondy, E. Iacona, J. Taine, Determination of the anisotropic radiative properties of a porous material by radiative distribution function identification (RDFI), International Journal of Heat and Mass Transfer 49 (2006) 2810–2819.
[25] M. Loretz, R. Coquard, D. Baillis, E. Maire, Metallic foams: Radiative properties/comparison between different models, Journal of Quantitative Spectroscopy and Radiative Transfer 109 (2008) 16 – 27.
[26] S. Cunsolo, D. Baillis, N. Bianco, Improved monte carlo methods for computational modelling of thermal radiation applied to porous cellular materials, International Journal of Thermal Sciences 137 (2019) 161 – 179.
[27] J. Schindelin, I. Arganda-Carreras, E. Frise, V. Kaynig, M. Longair, T. Pietzsch, S. Preibisch, C. Rueden, S. Saalfeld, B. Schmid, J.-Y. Tinevez, D. J. White, V. Hartenstein, K. Eliceiri, P. Tomancak, A. Cardona, Fiji: an open-source platform for biological-image analysis, Nature Methods 9 (2012) 676–682.
[28] T. Kanit, S. Forest, I. Galliet, V. Mounoury, D. Jeulin, Determination of the size of the representative volume element for random composites: Statistical and numerical approach, International Journal of Solids and Structures 40 (2003) 3647–3679.
[29] M. R. MacIver, Analysis of In Situ Microscopy Images of Flocculated Sediment Volumes, Chemical Engineering & Technology 40 (2017) 2305–2313.
[30] H. Mehling, G. Hautzinger, O. Nilsson, J. Fricke, R. Hofmann, O. Hahn, Thermal diffusivity of semitransparent materials determined by the laser-flash method applying a new analytical model, International Journal of Thermophysics 19 (1998) 941–949.
[31] J. Blumm, J. Opfermann, Improvement of the mathematical modeling of flash measurements, High Temperatures - High Pressures 34 (2002) 515–521.
[32] Y. Touloukian, R. Kirby, R. Taylor, T. Lee, Vol. 13. Thermal Expansion - Nonmetallic Solids., Thermophysical Properties of Matter - The TPRC Data Series, Plenum Publishing Corp., New York, 1977.
[33] Y. Touloukian, E. Buyco, Vol. 5. Specific heat - Nonmetallic solids, Thermophysical Properties of Matter - The TPRC Data Series, Plenum Publishing Corp., New York, 1970.
[34] D. S. Smith, F. Puech, B. Nait-Ali, A. Alzina, S. Honda, Grain boundary thermal resistance and finite grain size effects for heat conduction through porous polycrystalline alumina, International Journal of Heat and Mass Transfer 121 (2018) 1273–1280.
[35] R. Coquard, D. Baillis, Modeling of Heat Transfer in Low-Density EPS Foams, Journal of Heat Transfer 128 (2006) 538.
[36] H. Dong, B. Wen, R. Melnik, Relative importance of grain boundaries and size effects in thermal conductivity

of nanocrystalline materials, Scientific Reports 4 (2014) 7037.
[37] R. Hill, Elastic properties of reinforced solides: Some theoretical principles, Journal of the Mechanics and Physics of Solids 11 (1963) 357–372.
[38] I. Özdemir, W. A. M. Brekelmans, M. G. D. Geers, Computational homogenization for heat conduction in heterogeneous solids, International Journal for Numerical Methods in Engineering 73 (2008) 185–204.
[39] Dassault Systèmes Simulia Corp., Abaqus Analysis User's Guide, in: Abaqus 2017 Documentation Collection, 2017.
[40] R. Siegel, J. R. Howell, Thermal Radiation Heat Transfer, 3 ed., Hemisphere Publishing Corporation, 1992.
[41] Y. Dauvois, D. Rochais, F. Enguehard, J. Taine, Statistical radiative modeling of a porous medium with semi transparent and transparent phases: Application to a felt of overlapping fibres, International Journal of Heat and Mass Transfer 106 (2017) 601 – 618.
[42] Q. Brewster, Thermal Radiative Transfer and Properties, John Wiley & Sons, Inc., 1992.
[43] R. Siegel, C. Spuckler, Approximate solution methods for spectral radiative transfer in high refractive index layers, International Journal of Heat and Mass Transfer 37 (1994) 403 – 413.
[44] Q. Fang, D. A. Boas, Tetrahedral mesh generation from volumetric binary and grayscale images, Proceedings - 2009 IEEE International Symposium on Biomedical Imaging: From Nano to Macro, ISBI 2009 (2009) 1142–1145.
[45] J. Taine, F. Enguehard, Statistical modelling of radiative transfer within non-Beerian effective phases of macro-porous media, International Journal of Thermal Sciences 139 (2019) 61–78.
[46] S. Cunsolo, R. Coquard, D. Baillis, N. Bianco, Radiative properties modeling of open cell solid foam: Review and new analytical law, International Journal of Thermal Sciences 104 (2016) 122–134.
[47] J. Taine, F. Bellet, V. Leroy, E. Iacona, Generalized radiative transfer equation for porous medium upscaling: Application to the radiative Fourier law, International Journal of Heat and Mass Transfer 53 (2010) 4071–4081.
[48] ISO 8302, Thermal insulation – Determination of steady-state thermal resistance and related properties – Guarded hot plate apparatus, International Organization for Standardization, 1991.
[49] J. Chaves, Introduction to Nonimaging Optics, 2 ed., CRC Press, 2017.

Conclusion générale

Synthèse

La modélisation directe de la conductivité thermique haute température des matériaux cellulaires à partir de leur microstructure est un levier fondamentale pour maîtriser la performance de ces derniers en service. Dans le cas des mousses comme NorFoam XPure®présentant un volume poreux élevé avec une porosité hiérarchique, il est important d'appliquer les modèles physiques appropriés pour tenir compte de l'influence de la porosité à différentes échelles sur le transfert thermique, qui se fait principalement par conduction et par rayonnement. Dans cette thèse, des modélisations numériques des propriétés thermiques et radiatives ont été effectuées à partir des reconstructions tomographiques de la mousse NorFoam et de son squelette poreux, et comparées aux mesures réalisées à haute température. Cette démarche a permis de clarifier le caractère approprié des différentes approches de modélisation existantes, ainsi que d'en proposer des nouvelles quand aucune n'est convenable.

La méthode d'homogénéisation numérique par éléments finis a été employée pour simuler la conductivité thermique effective de NorFoam, en considérant dans un premier temps que le squelette est homogène. Les microstructures tomographiées n'étant généralement ni périodiques ni suffisamment grandes pour être des VER, la conductivité simulée est une valeur apparente dépendant de la taille de volume élémentaire et des conditions aux limites. Dans le **Chapitre I**, quatre jeux de conditions aux limites ont été étudiés : des conditions de flux thermique homogène, des conditions de gradient de température homogène, des conditions périodiques, et des conditions mixtes. Les conditions mixtes ne vérifient pas forcément la condition de macrohomogénéité, qui assure la conservation des grandeurs thermodynamiques fondamentales lors du changement d'échelle. Les résultats théoriques et numériques indiquent que dans le cas des mousses tomographiées à haute porosité comme NorFoam, l'application des conditions aux limites mixtes permet non seulement de vérifier *a posteriori* la condition de macrohomogénéité, mais aussi d'obtenir les estimations de conductivité effective les plus justes et précises parmi les conditions aux limites étudiées.

Une approche multi-échelle a été adoptée pour la prédiction des propriétés radiatives effectives de mousse NorFoam, afin de tenir compte de l'influence de la double porosité sur le transfert radiatif. Le squelette de mousse est composé de l'alumine intrinsèquement peu absorbante à l'infrarouge proche et moyen, et possède un caractère fortement diffusant en raison d'une présence significative de pores de tailles proches des longueurs d'onde d'intérêt [1]. Dans le **Chapitre II**, une nouvelle approche numérique a été proposée pour prédire les propriétés radiatives volumiques et

1. Entre 1000 °C et 1700 °C, plus de 83% d'énergie utile est comprise entre 1 µm et 6 µm.

surfaciques du squelette. Basée sur l'approximation dipolaire discrète, elle permet de tenir compte de la diffusion dépendante et des phénomènes ondulatoires dans le transfert radiatif à l'échelle du squelette. Cette approche a d'abord été validée sur des microstructures de référence, puis appliquée à un grand nombre de petits volumes tomographiés du matériau du squelette de NorFoam. Les résultats de simulation ont permis d'établir des relations analytiques entre les propriétés radiatives effectives du squelette et sa porosité, et de quantifier les incertitudes liées principalement au caractère aléatoire de la morphologie de pores.

Afin de valider les propriétés radiatives prédites, des propriétés radiométriques (réflectance, transmittance, et émettance) des disques composés du matériau du squelette ont été simulées, puis comparées aux mesures spectroscopiques réalisées au laboratoire CEMHTI (Orléans). Le bon accord entre les résultats numériques et expérimentaux de l'ambiante jusqu'à 1300 °C valide les propriétés radiatives du squelette à ces températures prédites par l'approche proposée. Notamment, le choix de négliger l'influence des joints de grains de l'alumine sur les propriétés radiatives a été justifié. L'hypothèse des réflexion et réfraction mixtes à la surface du matériau, comprenant une part spéculaire égale à la fraction d'alumine et une part diffuse isotrope égale à la fraction de pores, paraît également appropriée dans le cas de ces disques.

Connaissant les propriétés radiatives du squelette, ce dernier peut alors être modélisé comme une phase homogène absorbante-émettante-diffusante lors de la simulation des propriétés radiatives effectives de NorFoam dans le **Chapitre III**. Par approche de Monte Carlo, les propriétés radiatives de la mousse sont déduites à partir d'une procédure de lancer de rayons, adaptée pour prendre en compte la semi-transparence du squelette et les réflexion et réfraction non-spéculaires aux interfaces. Enfin, la résolution numérique couplée de l'équation de chaleur et de l'équation de transfert radiatif permet de calculer la conductivité thermique équivalente de NorFoam, sous l'hypothèse d'un transfert unidirectionnel en régime stationnaire à travers une plaque de mousse. Ce calcul a permis de vérifier que la contribution du rayonnement est bien représentée par la conductivité radiative de Rosseland avec l'approximation de transport pour des épaisseurs optiques supérieurs à 40, correspondant à des épaisseurs de plaque centimétriques.

Pour conclure ce manuscrit, la conductivité thermique apparente de NorFoam mesurée au LEMTA (Nancy) par technique de fil chaud parallèle entre 400 °C et 1000 °C a été comparée aux prédictions numériques de la conductivité thermique effective (conduction seulement) et la conductivité thermique équivalente (conduction et rayonnement). La conductivité thermique effective simulée affiche un très bon accord avec les mesures au-dessous de 600 °C, ce qui confirme la contribution négligeable du rayonnement à ces températures et valide l'approche d'homogénéisation numérique pour quantifier le transfert par conduction. À des températures plus élevées où la contribution du rayonnement est significative, les prédictions numériques affichent une sensibilité très élevée à la répartition angulaire du rayonnement réfléchi et transmis aux interfaces, qui elle dépend essentiellement de la rugosité de surface du squelette. Ces travaux mettent en évidence l'importance de caractériser finement l'état de surface du squelette, afin de modéliser plus précisément les propriétés radiatives. Il est néanmoins possible de constater que l'hypothèse des réflexion et transmission diffuses aux interfaces (correspondant à une rugosité de surface de squelette élevée) semble adaptée dans le cas de NorFoam, car elle permet d'avoir un très bon accord entre la conductivité thermique équivalente simulée et les mesures, sous réserve que incertitude expérimentale reste faible. En effet, les mesures fil chaud présentées considèrent un transfert thermique par conduction

pure, or l'approximation de Rosseland reste à vérifier dans cette configuration expérimentale.

Perspectives

Les travaux de cette thèse ont permis de développer des modèles numériques de prédiction de propriétés thermiques et radiatives des mousses à partir de leur microstructure poreuse hiérarchique., et les résultats numériques ont systématiquement été comparés à des mesures haute température. Ces outils prédictifs peuvent ensuite être appliqués à l'étude de l'influence de la microstructure sur les propriétés effectives du matériau, permettant ainsi de trouver l'architecture optimale permettant de répondre aux critères de performance, d'efficacité énergétique, et de sûreté des systèmes qu'il compose. Trois pistes étroitement liées à cet objectif seraient intéressantes à poursuivre dans le court terme :

— À partir des paramètres morphologiques tels que la porosité, la distribution de taille de pores, et la forme des pores, des matériaux numériques stochastiques peuvent être générés et appliqués à l'étude de l'influence de ces paramètres sur les propriétés d'intérêt. Des algorithmes de génération des "jumeaux numériques" de mousses, qui ont fait l'objet d'une présentation au Congrès Français de Mécanique en 2019 [17] Pour simuler le squelette poreux, des développements s'avèrent nécessaires mais peuvent être inspirés des algorithmes basées sur les diagrammes de Voronoï [18].

— Des relations analytiques entre les différents paramètres morphologiques et les propriétés d'intérêt (notamment les conductivités thermiques effective et équivalente) peuvent ensuite être établies sur la base des résultats d'études paramétriques. Les études passées sur la conductivité thermique effective des mousses ont donné lieu à de nombreuses relations analytiques [13, 14, 16], qu'il conviendrait d'étudier afin d'identifier celles qui conviennent. Des modèles analytiques basées sur les théories de milieux effectifs [14] sont d'un intérêt particulier, tel le modèle d'Archie présenté dans le **Chapitre I** et validé pour la mousse NorFoam à température ambiante. L'applicabilité de ce type de modèles à plus hautes températures mérite d'être étudiée. Pour décrire la contribution du rayonnement dans la mousse, même si l'approximation de Rosseland permet de simplifier en fournissant une conductivité radiative équivalente, elle fait appel à un coefficient d'extinction moyen qui reste difficile à prédire analytiquement. Une première étape a déjà été effectuée dans le **Chapitre II**, en établissant des relations entre la porosité du squelette et ses propriétés radiatives. Ces travaux devront donc être poursuivis, en commençant notamment par prendre en compte non seulement la porosité mais aussi la taille et la morphologie des pores au sein du squelette. L'étape suivante serait d'établir des relations analytiques pour prédire le coefficient d'extinction moyen décrivant le transfert radiatif à l'échelle de la mousse.

— Une extension de l'étude aux autres propriétés, par exemple aux propriétés élastiques du matériau pour lesquelles la méthode d'homogénéisation présentée dans le **Chapitre I** peut être directement appliquée, serait également d'intérêt pour l'optimisation multi-critères du matériau. Dans ce contexte, il est intéressant de mentionner les travaux de Pabst and Gregorová [19] sur les relations thermiques-mécaniques croisées, fondées sur le principe que

la connaissance d'une propriété effective d'un matériau poreux (telle la conductivité thermique) puisse aider à calculer directement une autre propriété effective (telle la matrice de rigidité effective). Les modèles développés dans cette étude peuvent également être appliqués à l'étude des céramiques d'autres compositions, à condition que les propriétés intrinsèques de chacune des phases soient connues.

Les résultats issus de cette thèse ont également montré quelques pistes importantes qui nécessitent une étude approfondie à plus long terme :

— Le lien entre l'état de surface et la répartition angulaire du rayonnement réflechi et transmis, qui selon les résultats du **Chapitre III** a une influence importante sur le transfert radiatif, doit être clarifié. Dans un premier temps, une caractérisation de la réflectivité bidirectionnelle de surface du squelette doit être effectuée, afin de confirmer l'hypothèse des réflexion et transmission diffuse isotropes retenue dans le **Chapitre III**. Dans un second temps, une étude avec des modèles analytiques ou numériques appropriés [20–22] permettrait d'obtenir la réflectivité bidirectionnelle de la surface du squelette en connaissant sa rugosité.

— L'une des limites majeures dans la modélisation numérique sur des microstructures poreuses est la grande taille de volume élémentaire représentatif nécessaire, souvent supérieure aux ressources de calcul disponibles. Cette limite est présente notamment au niveau des calculs d'homogénéisation par éléments finis sur des mousses non-périodiques, pour lesquelles des méthodes numériques basées sur la Transformée de Fourier Rapide [23, 24] peuvent être une alternative moins gourmande, et aussi au niveau de la résolution des équations de Maxwell à l'échelle du squelette poreux, pour laquelle les besoins importants en mémoire et temps de calculs peuvent être comblés en partie par des techniques de parallélisation plus robustes [25].

— Les techniques d'homogénéisation de propriétés thermiques et radiatives présentées dans cette thèse sont adaptées pour des matériaux de type "composite", constitués de plusieurs phases distinctes dont les propriétés intrinsèques sont supposées homogènes et connues. Dans le cas où les phases sont elles-mêmes hétérogènes à des échelles bien plus petites (nanostructurés, dopés, ou contenant des impuretés [12]), la détermination de ces propriétés peut être assujettie à des difficultés et des incertitudes importantes. Les années récentes ont vu le début des travaux sur la prédiction *ab initio* de ces propriétés pour des matériaux de base de compositions plus complexes, en faisant intervenir par exemple des modèles de dynamique moléculaire [1]. Des recherches dans ce sens peuvent fournir des méthodes intéressantes pour l'étude d'une gamme plus large de matériaux.

Bibliographie

[1] M. A. Badri, A. Biallais, G. Domingues, Y. Favennec, G. Fugallo, A. Mekeze Monthe, B. Rousseau, Combining micro- meso- and macro-scopic numerical methods for multiscale radiative transfer modeling of SiC-based foams up to very high temperatures, International Heat Transfer Conference 2018-Augus (2018) 8209–8216.

[2] M. Sans, Caractérisation des propriétés thermophysiques de mousses céramiques à haute température, Thèse de doctorat, Univeristé de Lorraine, 2019.

[3] J. Mora-Monteros, C. Suter, S. Haussener, Effective conductivity of porous ceramics in a radiative environment, Ceramics International 46 (2020) 2805–2815.

[4] S. Haussener, J. Randrianalisoa, Radiative characterization of ceramic foams with microporosity, Journal of Physics : Conference Series 676 (2016).

[5] S. Gauthier, E. Lebas, D. Baillis, SFGP 2007 - Natural gas/hydrogen mixture combustion in a porous radiant burner, International Journal of Chemical Reactor Engineering 5 (2007).

[6] B. Zeghondy, E. Iacona, J. Taine, Determination of the anisotropic radiative properties of a porous material by radiative distribution function identification (RDFI), International Journal of Heat and Mass Transfer 49 (2006) 2810–2819.

[7] M. Schumann, L. San Miguel, Fiber-Free Ceramic Insulation Foam for Highest Temperatures – a New Generation of HSE-friendly Refractory Products with Multiple Application Possibilities, refractories WORLDFORUM 9 (2017) 50–58.

[8] J. Randrianalisoa, D. Baillis, Thermal conductive and radiative properties of solid foams : Traditional and recent advanced modelling approaches, Comptes Rendus Physique 15 (2014) 683–695.

[9] B. Hay, J. Hameury, N. Fleurence, P. Lacipiere, M. Grelard, V. Scoarnec, G. Davee, New facilities for the measurements of high-temperature thermophysical properties at LNE, International Journal of Thermophysics 35 (2014) 1712–1724.

[10] Y. Jannot, A. Degiovanni, An improved model for the parallel hot wire : Application to thermal conductivity measurement of low density insulating materials at high temperature, International Journal of Thermal Sciences 142 (2019) 379–391.

[11] Y. Jannot, A. Degiovanni, V. Schick, J. Meulemans, Thermal diffusivity measurement of insulating materials at high temperature with a four-layer (4L) method, International Journal of Thermal Sciences 150 (2020) 106230.

[12] O. Rozenbaum, C. Blanchard, D. De Sousa Meneses, Determination of high-temperature radiative properties of porous silica by combined image analysis, infrared spectroscopy and numerical simulation, International Journal of Thermal Sciences 137 (2019) 552–559.

[13] P. Ranut, On the effective thermal conductivity of aluminum metal foams : Review and improvement of the available empirical and analytical models, Applied Thermal Engineering 101 (2016) 496–524.

[14] W. Pabst, E. Gregorová, Conductivity of porous materials with spheroidal pores, Journal of the European Ceramic Society 34 (2014) 2757–2766.

[15] S. Suter, A. Steinfeld, S. Haussener, Pore-level engineering of macroporous media for increased performance of solar-driven thermochemical fuel processing, International Journal of Heat and Mass Transfer 78 (2014) 688–698.

[16] Z. K. Low, N. Blal, N. Naouar, D. Baillis, Influence of boundary conditions on computation of the effective thermal conductivity of foams, International Journal of Heat and Mass Transfer 155 (2020) 119781.

[17] Z. K. Low, N. Blal, N. Naouar, L. San Miguel, D. Baillis, Techniques de génération de mousses virtuelles pour le calcul de conductivité thermique effective, in : 24ème Congrès Français de Mécanique, Association Française de Mécanique, Brest, France, 2019, pp. 1–7.

[18] T. Kanit, Notion de Volume Elémentaire Représentatif pour les Matériaux Hétérogènes : Approche Statistique et Numérique, Doctoral thesis, Ecole Nationale Supérieure des Mines de Paris, 2003.

[19] W. Pabst, E. Gregorová, Critical Assessment 18 : Elastic and thermal properties of porous materials -rigorous bounds and cross-property relations, Materials Science and Technology (United Kingdom) 31 (2015) 1801–1808.

[20] M. Nieto-Vesperinas, J. A. Sánchez-Gil, Light scattering from a random rough interface with total internal reflection, Journal of the Optical Society of America A 9 (1992) 424.

[21] K. Tang, R. A. Dimenna, R. O. Buckius, Regions of validity of the geometric optics approximation for angular scattering from very rough surfaces, International Journal of Heat and Mass Transfer 40 (1996) 49–59.

[22] H. Ragheb, E. R. Hancock, The modified Beckmann-Kirchhoff scattering theory for rough surface analysis, Pattern Recognition 40 (2007) 2004–2020.

[23] H. Moulinec, P. Suquet, A numerical method for computing the overall response of nonlinear composites with complex microstructure, Computer Methods in Applied Mechanics and Engineering 157 (1998) 69–94.

[24] S. Brisard, K. Sab, L. Dormieux, New boundary conditions for the computation of the apparent stiffness of statistical volume elements, Journal of the Mechanics and Physics of Solids 61 (2013) 2638–2658.

[25] M. A. Yurkin, A. G. Hoekstra, The discrete-dipole-approximation code ADDA : Capabilities and known limitations, Journal of Quantitative Spectroscopy and Radiative Transfer 112 (2011) 2234–2247.

FOLIO ADMINISTRATIF

THÈSE DE L'UNIVERSITÉ DE LYON OPÉRÉE AU SEIN DE L'INSA LYON

NOM : LOW
(avec précision du nom de jeune fille, le cas échéant)

DATE de SOUTENANCE : 27/11/2020

Prénoms : Zi Kang

TITRE : Matériaux cellulaires isolants haute température : Relation microstructure–propriétés

NATURE : Doctorat

Numéro d'ordre : 2020LYSEI122

École doctorale : Mécanique, Énergétique, Génie Civil, Acoustique (n°162)

Spécialité : Génie Mécanique

RÉSUMÉ :
Cette thèse CIFRE réalisée en collaboration avec Saint-Gobain Research Provence porte sur la modélisation des propriétés thermiques d'une mousse d'alumine NorFoam XPure®, conçue pour l'isolation thermique haute température (1200 °C–1700 °C). L'objectif est de développer et valider des modèles numériques multiéchelles pour calculer le transfert de chaleur par conduction et rayonnement dans cette mousse, à partir des microstructures 3D tomographiées et des propriétés intrinsèques des composants. La mousse étant composée des cellules ouvertes et d'un squelette solide lui-même poreux, la prise en compte de l'influence de cette double porosité est particulièrement novatrice.
Dans un premier temps, le transfert thermique par conduction à travers la mousse est modélisé avec des techniques d'homogénéisation par éléments finis. Il est démontré que des conditions aux limites périodiques couramment utilisées ne sont pas adaptées aux mousses tomographiées, et qu'un jeu de conditions aux limites mixtes permet d'obtenir des résultats plus précis sur ces dernières.
Quant au transfert radiatif à travers le squelette poreux, qui présente une forte diffusion volumique avec des phénomènes ondulatoires, le développement d'une nouvelle approche de modélisation basée sur l'approximation dipolaire discrète permet de prendre en compte l'influence desdits phénomènes.
Les propriétés radiatives de la mousse sont ensuite calculées par méthode de lancer de rayons en tenant compte du comportement radiatif complexe du squelette poreux. L'influence des phénomènes de réflexion et réfraction non-spéculaires aux interfaces entre le squelette et les cellules a été étudiée. Enfin, une modélisation numérique basée sur les techniques d'homogénéisation permet de calculer le transfert thermique à travers la mousse, avec couplage de la conduction et du rayonnement.
Le bon accord entre les résultats issus de chaque modèle et les mesures thermiques et optiques réalisées sur la mousse et le squelette poreux confirme le caractère prédictif des modèles développés.

MOTS-CLÉS : Mousse céramique, Conductivité thermique haute température, Homogénéisation numérique, Optique physique, Couplage conduction-rayonnement

Laboratoire(s) de recherche : Laboratoire de Mécanique des Contacts et des Structures
INSA de Lyon – CNRS UMR5259
Bâtiment Sophie Germain
27bis Avenue Jean Capelle
69621 Villeurbanne Cedex FRANCE

Directeur de thèse : Dominique BAILLIS

Président du jury : Samuel FOREST

Composition du jury : Sophia HAUSSENER Benjamin RÉMY Laurent PIERROT
Dominique BAILLIS Nawfal BLAL